MANIPULATING SUPERCONDUCTIVITY IN CUPRATES WITH SELECTIVE ULTRAFAST EXCITATION

BY

CASSANDRA RENÉE HUNT

DISSERTATION

Submitted in partial fulfillment of the requirements
for the degree of Doctor of Philosophy in Physics
in the Graduate College of the
University of Illinois at Urbana-Champaign, 2015

Urbana, Illinois

Doctoral Committee:

Professor Peter Abbamonte, Chair
Professor Laura H. Greene, Director of Research
Professor Philip W. Phillips
Professor John J. Thaler

Abstract

Ultrafast techniques allow an unprecedented look at the electronic and bosonic interactions that govern the macroscopic properties of materials. These processes can now be accessed on their fundamental timescale—the attosecond to picosecond range. Most ultrafast measurements involve using high energy excitation to bring a system out of equilibrium and then probing the subsequent relaxation processes. The development of ultrafast methods to selectively target collective excitations promises to transform ultrafast science into a tool not just of observation, but of precise control over material behavior.

Two examples of selective excitation will be explored in this thesis. Both studies involve targeting phonon modes of cuprate materials in order to manipulate their superconducting behavior. However, the pathway by which the light interacts with the phonon and electronic degrees of freedom is distinct in each case.

First, in Chapter 4, I present a study of resonant mid-infrared excitation of the lanthanide cuprate $La_{1.8-x}Eu_{0.2}Sr_xCuO_4$. This family of compounds exhibits a strong suppression of superconductivity near the doping $x = 0.125$, the so-called "1/8th anomaly." The suppression appears to be due to competition with charge and spin stripe order. This study expands on a previous investigation that found that superconducting transport appears to be restored by selective excitation of a phonon mode that couples to the electronic charge order. The transient superconducting behavior is characterized in the THz optical response by the appearance of a plasma mode associated with intrinsic Josephson tunneling in the material.

Here, I report that the transient plasma mode can be generated up to 65 K, near the charge ordering temperature. Two key observations are extracted from the relaxation dynamics. First, the plasma mode relaxes through a collapse of the carrier coherence length and not the carrier density, consistent with a Josephson

plasmon. Second, the relaxation dynamics were found to be quite different above and below the spin ordering temperature T_{SO}, with the regime below T_{SO} showing an anomalous temperature-independent lifetime. These results will be discussed in the context of recent theories that propose the 1/8th regime hosts an intertwined order of superconducting and charge ordered components.

The second study, introduced in Chapter 5, attempts to directly target the superconducting condensate of $YBa_2Cu_3O_x$, rather than aim at destroying a competing order. The superconducting response of cuprates has been found to be sensitive to the position of certain atoms in the unit cell, including the apical oxygen atoms that sit above and below the bilayer of CuO_2 planes in $YBa_2Cu_3O_x$. Selectively driving a *c*-axis apical oxygen mode (perpendicular to the planes) results in a stiffening of the Josephson plasma mode associated with Cooper pair tunneling between sets of planes.

Above T_c, the same excitation induces a transient plasma mode at frequencies comparable with the Josephson mode. Five compounds were investigated, four in the underdoped regime and one at optimal doping. The transient plasma mode could be induced in all underdoped compounds, with a plasma mode that blue shifts towards optimal doping, tracking the blue shift of the Josephson mode. The mid-infrared excitation targets the apical oxygen atoms only at sites that are undoped, therefore the lack of response in the optimally doped compound may be tied to the resonant nature of the excitation.

This non-uniform excitation, perhaps along with intrinsic inhomogeneity of the compound, is reflected in an inhomogeneous optical response of the system. The response above T_c is captured quantitatively by an effective medium of a superconductor and the unperturbed bulk. Below T_c, the blue shift of the Josephson plasmon is seen to be inhomogeneous as well, with one component remaining near the equilibrium plasma frequency.

The relaxation pathway of the transient mode is explored in Chapter 7. The principal finding is that the relaxation of the transient plasmon is driven by a loss of coherence, characterized by a decrease in carrier mobility, rather than a drop in carrier density as one might expect from quasiparticle excitation. Furthermore, during the relaxation, the transient plasmon splits, with one component centered near the equilibrium Josephson frequency and one component shifted to the blue. This may be related to the generation of (zero field) vortices, in a manner similar to the thermal vortex regime that forms an extended dome above T_c in the cuprate phase diagram in equilibrium.

I close this thesis by returning to the topic of research I pursued at the start of my graduate career. Chapter 8 presents a departure from the area of ultrafast science, turning to another (equilibrium) probe of superconductivity, point contact spectroscopy. Point contact spectroscopy (PCS) probes the superconducting order parameter via Andreev reflection and is sensitive to bosonic modes that couple to the quasiparticle spectrum. Recent work has shown that PCS can be used to detect a variety of correlated states that couple to electronic degrees of freedom. The technique has been widely applied to the study of order parameter symmetry, and has proven sensitive to the d-wave order parameter of cuprates and heavy fermion compounds, the multigap s_{++}-wave order of MgB_2, as well as p-wave and anisotropic s-wave symmetries.

I will present some work exploring the superconducting state of the pnictide superconductor $Sr(Fe_{1-x}Co_x)_2As_2$. The iron-based high temperature superconductors are unique in that multiple Fermi surfaces, with either electron-like or hole-like character, participate in the condensate. They are believed to exhibit a novel pairing mechanism, mediated by spin fluctuations and an s-wave order parameter that changes sign between each type of Fermi surface. Detecting this $s_{\pm}$-wave order has become one goal of recent point contact measurements and theoretical developments. I describe the multigap behavior of $Sr(Fe_{1-x}Co_x)_2As_2$ and find that the point contact spectra can be well-described by two independent bands, placing restrictions on proposed models of $s_{\pm}$-wave order. Additional modes, detected in the electron-boson spectrum $\alpha^2F(\omega)$, have been ascribed in literature to possible spin excitations. I show that these modes can in fact be tied to Raman-active phonon modes of the 122 structure.

To Laura, Bill, Ryan, and Stefan
(in the order that we met)

Acknowledgments

I have many people to acknowledge for making this thesis a reality. In practice it is impossible to put a name to every person who has shaped the course of your thoughts, opinions, and pursuits. Therefore I will necessarily leave out many individuals–teachers, friends, family–who have been influential to my development as a person and as a scientist. However incomplete, I would like to acknowledge some of those who have guided me into pursuing my present course and thank them for their contribution to the production of this thesis and for being a welcome part of my life.

First and foremost I thank my parents, Laura McGlasson and Bill Hunt. My mother Laura always stressed to me the importance of a good education as the foundation of a successful life. In a community where many did not go on to university, she made it clear that getting a college education was an absolute must. But *words* alone do not leave the impact that *action* imparts so forcefully. I watched my mother, who had gone straight to work after high school, return to college and complete her Associate's degree. Her determination to expand her education, with perfect grades to boot, showed me how serious she was about education as a route to self-improvement.

My father Bill taught me by example as well. Taking care of our family often meant long work hours and maintaining an exhausting schedule. Through him I learned that meeting your personal goals and getting ahead in life require sustained hard work—there are no easy roads to success. He showed me both how to keep forging ahead when your situation gets tough, and how to let yourself unwind and enjoy your triumphs along the way. While working full time, he also turned one of his side interests into a successful business. Watching his business develop showed me in a tangible way how ideas and ambitions can be made into your reality, and

that your career can be more than just a job, but a source of intellectual and personal enjoyment.

I have been fortunate to have had many passionate educators that have shown me how to enthusiastically engage with science and the world. This was perhaps especially crucial when I was young, a time when affecting disinterest was the fashionable attitude, regardless of the subject. In particular, my sixth and seventh grade science teachers, Mrs. Huels and Ms. Goebel, each in their own way encouraged me to pursue creative scientific inquiry inside and outside the classroom. Educators are not always teachers. I have fond early memories of taking hikes through the woods with my uncle Gary, who to my young mind knew just everything there was to know about each tree, bush, and flower we passed along the way. Perhaps then the idea first began to form that someday *I* wanted to know just everything there was to know about, well, *something*.

I must mention three writers whose books helped turn my attention to physics in particular. The first was *The Collapsing Universe: The Story of the Black Holes* by Isaac Asimov, who has an indisputable knack for story telling in fiction or non-fiction form. The second was *A Brief History of Time* by Stephen Hawking which cemented my sense of wonder and fascination with the universe. The third was *The God Particle* by Leon Lederman, who I credit (blame?) for convincing me that experimental physics had a certain rock star quality—who can resist a chapter title as alluring as "How We Violated Parity in a Weekend"? By the end of my undergraduate education I was convinced that I wanted to pursue condensed matter physics. I liked the idea of smaller-scale, table-top experiments in which I could play an active role from experimental design to data collection and analysis. Condensed matter systems, I came to believe, can be universes unto themselves, where the fundamental particles of the system change depending on the details of the material properties.

I first encountered my advisor Laura Greene at a public lecture and she immediately captured my attention with her enthusiasm for the field of superconductivity and her evident enjoyment of her work. I would come to learn that Laura also exemplifies with her lifestyle the energy that she puts into her words. I hope that I will be able to pursue both my career and personal life with half the passion that she infuses into hers. She has been truly an excellent advisor, both professionally and personally, and her words of wisdom and encouragement will be remembered no matter where my career takes me.

In particular, I thank her over and over for the support, understanding, and advice she provided when my now-husband Stefan had to move to Germany during his own graduate studies. Thanks to her I was able to spend some time doing research in Hamburg, which in the end became a large part of my thesis. I can confidently say that Stefan and I owe our marriage in some part to Laura's assistance.

I must acknowledge the patient and helpful support of Wan Kyu Park and Xin Lu when I first joined Laura's group. Wan Kyu impressed me from the first with both his abilities in the lab and the breadth and depth of his knowledge of recent literature. Since then I have developed the highest respect for his understanding and insight.

My years at Urbana will always rate amongst the happiest periods of my life, thanks to the friendship and camaraderie of my fellow graduate students. In particular, I'd like to mention Hamood, Yewon, Braden, Adam, Cory, Tyler, Katie, William, Tony, Yun, and Amanda.

My graduate school experience was made especially dear to me thanks to Hamood Arham. Whether it be late nights in the lab, exploring conferences, or just hanging out in our office, Hamood made each day brighter and more entertaining. He is gifted with both excellent technical ability in the lab and a strong work ethic, and I feel lucky to call him a friend.

Girls nights and trips to the gym with Yewon, Katie, and Amanda were some of the highlights of graduate school. These ladies are so impressive and talented, inside and outside the lab. (Someday I will learn how to crochet, I promise!) I particularly want to thank Yewon Gim for being an awesome friend and sometimes housemate. I wish we'd had more time in Urbana together.

I thank Andrea Cavalleri for giving me the opportunity to join his group in Hamburg and for introducing me to the exciting and growing field of ultrafast spectroscopy. Although we have had our disagreements, I will always admire Andrea's enthusiasm for his work as well as his ability to keep the big picture in mind, with regard to both his own research and the direction of ultrafast science in general.

The transition to ultrafast science made for a steep learning curve, and I benefited greatly from the experience and guidance of Daniele Nicoletti and Stefan Kaiser. The long hours in lab and sometimes intense measurement schedule were made easier having Daniele around. He is one of the talented few who manage to maintain full days in lab and keep an active nightlife going as well. I am still not certain when or if he sleeps. Stefan has the uncanny ability to breeze in and solve an intractable

problem in lab with a quick application of his "magic fingers"; I can only hope to someday to develop such skill.

The members of the Cavalleri group have been a pleasure to work with, whether it be a lunchtime chat or asking for advice in lab. Particularly I want to mention Ivanka Grguras. Though we have never worked together, I can speak with firsthand experience to Ivanka's talent as a graduate student—evidenced by the frequent visitors that would peak through our door to ask her for advice or assistance in lab. Ivanka's wit and dry humor made sharing an office fun. I will miss our shopping trips and sushi outings. I also want to mention Matteo Mitrano, whose enthusiasm and work ethic are truly admirable. Grabbing a beer together was always a welcome end to a long work day—we should have done it more often.

Finally, what would I do without the unflagging support of my wonderful husband, Stefan Pabst? Without my ever realizing a piece was missing, Stefan has managed to make my life whole. He has kept me sane through every twist and turn of our unconventional graduate school experience, even while devoting his boundless energy to driving me crazy. Thank you for bringing that energy into my life. Thank you for following me to the US, and thank you for helping make Germany feel like home afterwards. And finally, thank you for your infinite patience while I typed away at this thesis for the last three months. It's over now. We did it.

Role of the Author

This thesis would not have been possible without the help of many collaborators. Therefore I will attempt to lay out in some detail my contribution to this work.

All measurement and analysis of $La_{1.8-x}Eu_{0.2}Sr_xCuO_4$ shown in Chapter 4 were performed by the author, unless otherwise specifically stated. The low frequency THz optics set-up (shown in Section 2.4) that was used for these measurements and the measurements in Chapters 5 and 7 was developed by Stefan Kaiser and Daniele Nicoletti, based on designs by Matthias Hoffmann. The set-up was modified by the author and Yannis Laplace in order to probe with an antenna THz source. The pump beamline was modified by Daniele Nicoletti and Eliza Casandruc for measurements with 800 nm pump (see Appendix B.2).

Calculation of the full transient optical conductivity was performed using a MATLAB code package developed by the author[1]. This software implements the multilayer models discussed in Sections 2.5 and 2.6 to describe the response the excited material and account for the pump-probe penetration depth mismatch. This software has become a standard tool in the Cavalleri group for analyzing THz reflectivity data.

The data presented in Chapter 5 on $YBa_2Cu_3O_x$ (YBCO x) was measured over the course of several years by the author and Daniele Nicoletti, with assistance from Stefan Kaiser. Above T_c, the YBCO 6.5 data—which constitute the earliest measurements—were performed in collaboration amongst Daniele, Stefan, and the author; the YBCO 6.45 data (above T_c) were measured by the author with assistance from Daniele; the YBCO 6.6 data were measured by Daniele and Stefan with assistance from the author; the YBCO 6.3 data were measured by the author. Fluence

[1]The MATLAB code was originally developed for the $YBa_2Cu_3O_x$ project discussed in Chapters 5 and 7.

dependence data were measured by the author; wavelength dependence data were measured by Daniele. Below T_c, the YBCO 6.5 data were measured by the author; the YBCO 6.45 data were measured by Daniele and the author; the YBCO 6.6 data were measured by Stefan and Daniele. The author developed a method of *in situ* measurement of the absolute equilibrium optical response below T_c to reference the transient response (see Appendix B.3). The author adapted LabView programs in order to perform some of the measurements.

All analysis and fitting presented in Chapter 5 is the work of the author. Calculation of the full transient optical response was performed using a MATLAB code package developed by the author, as mentioned above. The author contributed the idea to use a mean field fit of the inductive response to extract a temperature scale T' for the transient state (see discussion in Section 5.4.2). The author and Daniele recognized the possible suppression of the transient state below the T'' scale and the author confirmed this suppression with more extensive measurements. The author contributed the idea to use a Bruggeman effective medium approach to quantitatively analyze the transient response above T_c (see Section 5.5). The author wrote a MATLAB code package to perform the effective medium fits and used this package to perform the effective medium analysis. Daniele assisted in using the code package to perform fits.

Chapter 6 covers three separate experiments that were inspired by the discovery of the transient plasma mode reported in Chapter 5 and Refs. [1, 2]. The broadband measurements of $YBa_2Cu_3O_x$ discussed in Section 6.2 began roughly a year after the initial finding of the transient plasma mode discussed in Chapter 5. However in the course of the development of the initial manuscript reporting the transient plasma mode, the broadband data eventually became integrated into the first published paper of this project, Ref. [1]. The broadband THz set-up was developed primarily by Wanzheng Hu and Isabella Gierz, who also performed the measurements. The author assisted in the effective medium analysis of the broadband data and in discussions of the interpretation.

The measurements of the transient lattice distortion, discussed in Section 6.3 and published in Ref. [3], were performed by a collaboration led by Roman Mankowsky and Michael Först, with extensive analysis and theoretical work performed by Alaska Subedi. The author was not involved with this project, except for some discussion. Section 6.3 also contains some of the author's own meta-analysis of data published by Jin, *et al.* [4].

Finally, Section 6.4 covers measurements of transient charge density wave (CDW) order suppression in $YBa_2Cu_3O_{6.6}$. These measurements were led by Sarnjeet Dhesi and Michael Först. The transient measurements of the CDW peak were performed at the soft x-ray beamline at the Stanford Linac Coherent Light Source (LCLS) free electron laser. The author's role involved on-the-fly acquisition and analysis of data to guide data collection during the beamtime.

The data presented in Chapter 7 were acquired together with the data presented in Chapter 5. The analysis presented in Chapter 7 is the work of the author, with helpful insights from Stefan Kaiser and Daniele Nicoletti. Particularly, Stefan pointed out the similarity between splitting of the transient plasma mode above T_c, which was first identified by the author, and the splitting of a Josephson plasma mode in an applied magnetic field.

Finally, the point contact spectra on $Sr(Fe_{1-x}Co_x)_2As_2$ presented in Chapter 8 were measured and analyzed by the author. The author performed all sample preparation of the soft point contact junctions. The author developed MATLAB code to implement point contact junction models by Blonder, Tinkham and Klapwijk [5], Golubov, *et al.* [6], and Sperstad, *et al.* [7]. The author contributed the idea that the above-gap features can be related to the phonon spectrum.

Table of Contents

List of Figures

Chapter 1

Introduction

Femtosecond lasers mostly operate in the near-infrared (NIR), making this excitation regime a popular target for ultrafast excitation. In unconventional superconductors, like most correlated systems, excitations in the eV range generally lead to a redistribution of quasiparticles into the conduction bands of the material. The resulting relaxation dynamics can reveal information about the underlying ground state [8–10] and unveil competing orders [11–15]. The transfer of charges can also lead to highly modified exchange interactions [16] and even produce crystallographic distortions [17–19].

The development of ultrafast methods to selectively target collective excitations promises to transform ultrafast science into a toolset not just of observation, but of precise control over material behavior. The goal of targeted pumping schemes is to populate a specific excitation channel without delivering excess energy to other excitation pathways.

Collective modes of complex materials have resonant frequencies that extend from GHz frequencies to deep in the mid-infrared. Tools for extending the frequency range of femtosecond lasers (see Chapter 2) now allow direct access to some of these excitations. Optical parametric amplification and difference frequency generation techniques can reach excitations down to ∼16 THz (550 cm^{-1}). This range covers phonon modes of light atoms such as oxygen, which play an important role in determining the macroscopic behavior of complex oxides like manganites and cuprates. Advances in THz sources have made it possible to also drive modes in the ∼0.5-3 THz range, where phonons of heavier atoms lie and where interesting collective excitations occur, for example the Josephson plasma resonance which we will encounter often in this thesis.

In this chapter I will provide some context for the work presented in this thesis by discussing a few examples of recent research that utilize targeted optical excitation to modify the properties of superconductors and manganites. These materials host collective charge, magnetic, and superconducting orders that are highly sensitive to small perturbations of the system's electronic and lattice properties. I will also discuss methods to probe the transient electronic and lattice response.

1.1 Controlling lattice deformation

Targeting phonon modes is the most direct way to trigger atomic motion in materials. Exciting infrared active modes does not produce a net distortion of the lattice, but rather generates resonant oscillations around the equilibrium atomic positions. However, nonlinear coupling of an infrared (IR) active mode to a Raman-active mode can indirectly excite oscillations of the Raman mode as well as produce a rectified, displacive distortion of the lattice along the Raman coordinate [20]. The mechanism for this coupling is discussed in more detail in Chapter 6.

The matrix elements that govern the coupling amplitude between IR and Raman modes are generally quite small; however, for many correlated materials, the macroscopic state of the system is highly sensitive to the underlying lattice structure. Changes in atomic positions of just a few percent can drive metal-insulator transitions [21], and control magnetic [21, 22], charge [23], and superconducting [24–27] orders. A recent review on using resonant IR-active phonon excitation to couple to Raman excitations can be found in Ref. [28].

The intimate connection between lattice and electronic order can be seen from the resonant excitation of manganite $La_{0.7}Sr_{0.3}MnO_3$ [20]. Like in the cuprates, manganites exhibit many competing magnetic and electronic orders that are highly sensitive to the position of atoms in the lattice [21]. In this case, the Mn-O-Mn bond angle of the MnO_6 octehedra tunes orbital overlap and can drive the system between ferromagnetic metallic and antiferromagnetic insulating behavior. The authors found that exciting an IR active Mn-O stretching mode leads to a coupling with a Raman mode that distorts this bond angle. See Figure 1.1 for an illustration of the modes. In the related compound $Pr_{0.7}Sr_{0.3}MnO_3$, the same excitation generates a insulator to metal transition, with the quasi-dc conductivity jumping over 4 orders of magnitude [29].

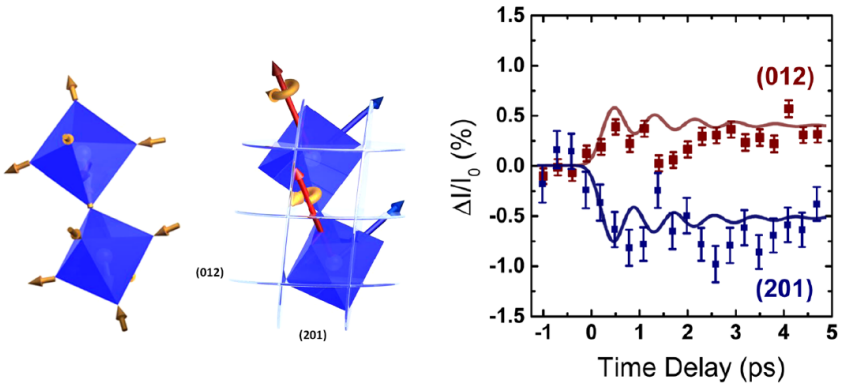

Figure 1.1: **Coupling of manganite E_u mode to an E_g Raman distortion. Left:** Two MnO_6 octehedra with arrows indicating the E_u-symmetric mode (left) and E_g mode (right). Figure from Ref. [20]. **Right:** Intensity changes of two Bragg peaks associated with the E_g mode. Lines indicate the expected shift from $Q_{IR}^2 Q_R$ coupling (see Section 6.3). Figure from Ref. [28].

In $YBa_2Cu_3O_x$, it is the relative positions of the Cu and O atoms in the CuO_2 planes—and the apical oxygen atoms that surround the planes—which has been shown to be closely tied to superconductivity. As we will see in Chapters 5, 6, and 7, excitation of a B_{1u} mode, which resonantly drives the apical oxygen atoms along the c-axis, leads to the formation of a c-axis plasma mode which appears to be tied to Josephson coupling. The Josephson plasma resonance is a collective mode produced by the resonant tunneling of Cooper pairs between layers in a stack of two-dimensional superconducting sheets. These modes occur in cuprates due to the intrinsic organization of the lattice, with superconductivity organized in the CuO_2 planes.

Mankowsky, *et al.* [3] showed that this B_{1u} mode couples with A_g-symmetric Raman modes, distorting the lattice on the same timescale as the formation of the transient plasma resonance. The positions of the planar CuO_2 atoms and apical O are rectified along these A_g coordinates, perhaps in a manner that supports superconductivity (see discussion in Chapter 6).

1.2 Controlling electronic response

1.2.1 Resonant pumping of infrared-active phonons

Rectified lattice distortions are just one way phonon excitation can drive changes in electronic order. The oscillating motion of a driven IR-active phonon can couple closely to electronic order. For example, resonantly driving the Mn-O stretching mode the manganite $La_{0.5}Sr_{1.5}MnO_4$ [30], in the same manner as discussed for $La_{0.7}Sr_{0.3}MnO_3$ above, was shown to drive the electronic system from a low temperature orbitally ordered phase into a high temperature unordered insulating state. The cause was initially supposed to be related to a phonon-driven relaxing of the Jahn-Teller distortion, however soft x-ray measurements of the spin and orbital orders showed only a partial reduction of orbital order [31]. Instead, the Mn-O excitation directly drives total destruction of antiferomagnetic spin order.

As we will see in Chapter 4, a similar stretching mode of Cu-O atoms in the lanthanides resides in the CuO_6 octehedra, analogous to the MnO_6 octehedra. Excitation of this mode leads to a suppression of the static charge stripe order that forms within the CuO_2 planes [32] (see Figure 1.2). The same excitation generates a high mobility plasma mode perpendicular to the CuO_2 planes in $La_{1.8-x}Eu_{0.2}Sr_xCuO_4$. As with $YBa_2Cu_3O_x$, this plasma mode can be tied to Josephson coupling, which appears to be restored by the destruction of stripe order [33, 34].

1.2.2 Other collective mode excitations

So far I have focused on driving phonon modes to trigger electronic and lattice excitations. Other collective modes, such as the Josephson plasma resonance, can also be selectively driven with light. The amplitude and phase of the superconducting order parameter, and the coherence length scale of the condensate, influence the shape of the Josephson plasmon response.

Excitations of bound vortex-antivortex pairs, called Josephson plasma solitons, have been predicted to form in the presence of high electromagnetic fields [35, 36]. This has now been experimentally realized in the optimally-doped lanthanide superconductor $La_{1.84}Sr_{0.16}CuO_4$. By driving the system with single-cycle pulses centered at the 2 THz Josephson plasma resonance, Dienst, *et al.* [37] could observe optical signatures of soliton formation.

THz radiation has also been shown to couple to another collective excitation, the Higgs amplitude mode [38, 39]. Papenkort, Axt, and Kuhn [40] showed theoretically

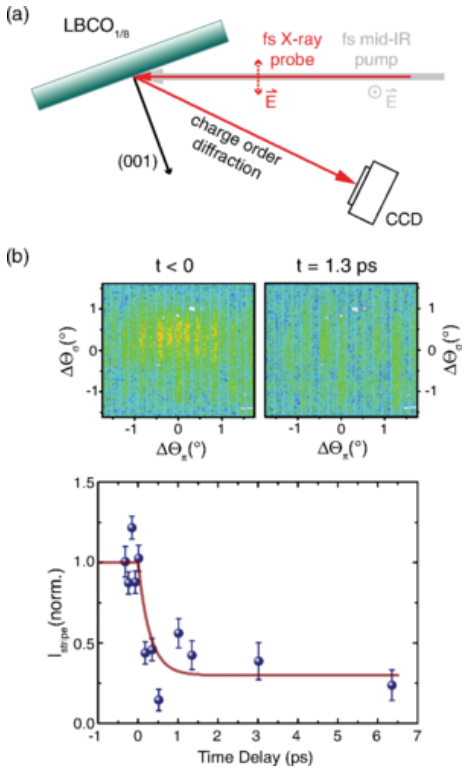

Figure 1.2: **Suppression of charge stripe order in $La_{2-x}Ba_xCuO_4$. (A)** Schematic diagram of the mid-infrared pump, resonant soft x-ray probe setup. **(B,top)** Intensity map of the charge order peak before and after excitation. **(B, bottom)** Time evolution of the charge order peak intensity. Red line is a fit to an exponential function with time constant 300 fs, the time resolution of the experiment. Figure from Ref. [32].

that ultrashort pulses could be used to excite the amplitude mode in a BCS superconductor. The condensate must be excited non-adiabatically, with pulses shorter than the response time of the BCS state, $\tau_\Delta = \hbar/\Delta$. They worked out that the resulting coherence between the excited quasiparticle states would cause an oscillation of the order parameter amplitude.

Matsunaga, *et al.* [41] used single cycle THz pulses with $\tau_{pump} = 1.5$ ps $(= 0.57\tau_\Delta)$ to excite the Higgs amplitude mode in the BCS superconductor $Nb_{1-x}Ti_xN$. They chose THz pulses centered at the superconducting gap energy since higher frequency light, such as near-infrared pulses, would excite other electronic and phonon degrees of freedom that would cause additional pair breaking. They found that the excitation produced an oscillation in the THz response at a frequency that agreed well with theoretical predictions for the amplitude mode.

1.3 Probing transient dynamics of correlated systems

We have seen that optical excitation of phonons can couple directly to electronic order. The electronic excitation may also be indirect, with the pumped phonon mode first driving additional modulation of the lattice. Disentangling the excitation pathways and their causal relationships in shaping the transient dynamics can require several complementary probing methods.

Direct time-resolved measurements of lattice structure dynamics are now possible thanks to free electron lasers (FELs). The experiments discussed in Section 1.1 were performed at the Linac Coherent Light Source (LCLS) at Stanford, which is capable of delivering a high flux of x-rays with a pulse length of 50 ps. The x-ray probe is synchronized with a femtosecond Ti:Sapphire laser that can be tuned from the near- to the mid-infrared in order to selectively pump the sample (see Chapter 2).

In a similar vein, an FEL can be used for time-resolved resonant soft x-ray scattering, which is sensitive to collective charge order [32, 42]. As discussed above, excitation of a B_{1u} phonon mode in $YBa_2Cu_3O_x$ gives rise to a transient plasma mode associated with superconductivity. Soft x-ray scattering has revealed that the B_{1u} excitation also suppresses charge density wave (CDW) order [42]. By comparing the timescales of the optical response and the charge density wave dynamics, we could determine that while the CDW suppression occurs alongside the formation of the transient plasmon, the suppression of charge order sets in too slowly to be the driving mechanism behind the generation of the mode (see Chapter 6 for details).

The projects presented in this thesis mostly entail probing the optical response of cuprates in the THz range. Definitions of the THz frequency regime vary, but it extends roughly between ∼0.1-30 THz (3-1000 cm^{-1}, 0.5-120 meV), covering the resonant frequencies of most phonons. This is also the energy scale of the superconducting gap, and gapping due to collective charge and spin orders. Other collective modes, such as the Josephson plasmon, also reside in this spectral range.

The electronic behavior of cuprates is highly momentum-dependent. Certain regions of their k-space are associated with superconductivity and with the pseudogap. Angle-resolved photoemission spectroscopy (ARPES) can be used to map the Fermi surface of a material and has become a crucial probe of high T_c superconductors. This technique has been successfully extended into the time domain and is just beginning to be utilized to investigate coherent excitation processes [43].

Chapter 2

Experimental methods for pump-probe time domain spectroscopy

2.1 Introduction

This chapter focuses on the subset of ultrafast tools and analysis techniques used in the experiments described in Chapters 4, 5, and 7. First, I introduce nonlinear optical processes. Most commercial ultrafast lasers are designed to generate narrowband pulses at a single frequency in the near infra-red (NIR). In order to access a broader range of frequencies, nonlinear optical processes are employed to convert the NIR pulses. The full range of nonlinear optics theory has filled books in itself [44], and as such, the discussion here will be restricted to those areas relevant to this thesis, primarily optical parametric amplification and difference frequency generation. These processes are used to produce mid-infrared and THz frequency radiation.

I will then introduce time-domain THz spectroscopy, the primary probe used in the experiments presented in this thesis. I describe three methods for THz generation: optical rectification in nonlinear crystals, photoconductive switches, and two-color plasma generation. The full amplitude and phase of the THz field can be measured with electro-optic sampling (EOS) detection. I will describe the EOS method and how to combine EOS detection with pump-probe measurements. Then I will discuss the experimental set-up used for most of the measurements covered in this thesis.

Finally, I will present several models used to extract the pump-induced (transient) optical response from THz spectra. For a homogeneous sample, the THz response is related to the refractive index through the Fresnel equations. However, an excited material has an optical response that changes with distance from the sample surface, depending on how deeply into the material the pump can penetrate.

If the pump penetrates much farther into the material than the THz, then the response is said the be in the "bulk" limit, and the Fresnel equations can still be applied. In non-metallic materials, the THz radiation often penetrates 10-100 μm or deeper into the sample. Resonant excitations on the other hand, for example at the frequency of IR-active phonon modes, are very effectively screened, leading to pump penetration depths on order 10-100 times less than the THz regime.

Models of layered materials can be used to account for the penetration depth mismatch. The transient response is defined by the response near the surface of the material, where the pump-induced changes are greatest. For very large penetration depth mismatches, analytic models of thin excited layers can be applied. In both the bulk and thin film limits, the characteristic matrix approach, described in Section 2.6, can effectively describe the response of the excited states of cuprates that are considered in later chapters. In Appendix C, I reproduce the Matlab code used to implement the models described in this chapter. I have combined this code into a software package that has become a standard tool used in the Cavalleri group to model the transient THz optical response.

2.2 Optical parametric amplification

2.2.1 Second order optical processes

An external electric field E will induce a polarization P within a medium. Typically, the two are linearly related by the susceptibility of the medium, $P = \chi^{(1)}E$. Certain media also respond non-linearly to an applied field, which we express by expanding the response as a power series in E,

$$\begin{aligned} P &= \chi^{(1)}E + \chi^{(2)}E^2 + \chi^{(3)}E^3 + ... + \chi^{(n)}E^n, \\ &= P^{(1)} + P^{(2)} + P^{(3)} + ... + P^{(n)}. \end{aligned} \tag{2.1}$$

The nonlinear susceptibility terms, $\chi^{(n>1)}$, are much smaller than the linear response term $\chi^{(1)}$ in almost all materials and generally only become relevant in the presence of intense fields. Light interactions involving higher order terms in the susceptibility are called "nonlinear" processes and several of these effects are key to ultrafast spectroscopy.

Second harmonic generation is the simplest nonlinear process, involving the $\chi^{(2)}$ term in the susceptibility. For a laser field,

$$E(t) = E_0 e^{i\vec{k}.\vec{x}-i\omega t} + \text{c.c.} \tag{2.2}$$

the second order polarizability becomes

$$P^{(2)} = \chi^{(2)}(E_0 E_0^* + E_0^2 e^{i(2\vec{k}.\vec{x}-2\omega t)} + \text{c.c.}), \tag{2.3}$$

with a dc term, which represents a rectification of the applied field, and a second field that propagates at 2ω. Sum and difference frequency mixing work in a similar manner. Rather than use the self-interaction of a monochromatic beam, these processes rely on mixing two frequencies, ω_1 and ω_2, which may be either picked from the spectrum of a single laser beam or from two overlapping beams. An external field,

$$E(t) = E_1 e^{i\vec{k}_1.\vec{x}-i\omega_1 t} + E_2 e^{i\vec{k}_2.\vec{x}-i\omega_2 t} + \text{c.c.}, \tag{2.4}$$

produces a nonlinear polarization of the form,

$$\begin{aligned} P^{(2)} \;=\; & \chi^{(2)}(E_1 E_1^* + E_2 E_2^* + E_1^2 e^{i2\vec{k}_1.\vec{x}-i2\omega_1 t} + E_2^2 e^{i2\vec{k}_2.\vec{x}-i2\omega_2 t} + \\ & 2E_1 E_2 e^{i(\vec{k}_1+\vec{k}_2).\vec{x}-i(\omega_1-\omega_2)t} + 2E_1 E_2^* e^{i(\vec{k}_1-\vec{k}_2).\vec{x}-i(\omega_1+\omega_2)t} + \text{c.c.}), \end{aligned} \tag{2.5}$$

where sum terms $\omega_1 + \omega_2$ and difference terms $\omega_1 - \omega_2$ join the second harmonic terms of the single frequency case. Conservation of momentum between the three fields, also referred to as phase matching, requires that $\vec{k}_3 = \vec{k}_1 + \vec{k}_2$ for the process $\omega_3 = \omega_1 - \omega_2$. The wavevector k of a field in a medium is related to the frequency ω via the refractive index $k = n(\omega)\omega/c$. Since the refractive index $n(\omega)$ is generally frequency dependent, achieving the phase matching condition is not trivial, but it is crucial to the efficiency of the nonlinear process.

2.2.2 Optical parametric amplifier

Optical parametric amplification uses difference frequency mixing of a high intensity pump beam at ω_p and a second "signal" beam at ω_s in order to amplify ω_s and generate a third "idler" beam at $\omega_i = \omega_p - \omega_s$ in the process. The name "parametric" amplification refers to any driven amplification process where a parameter, in this case ω_s, is populated in proportion to its amplitude by a driving pump at another frequency, in this case ω_p.

For the experiments described in this thesis, the laser source was a commercial Ti:Sapphire laser[1] which emits ∼80 fs pulses centered at 800 nm wavelength (1.55 eV) at a repetition rate of 1 kHz. Typical power output is 3-4 W. Optical parametric amplification was used to convert the 800 nm pulses to NIR light in the 1.2-1.5 μm range. The optical parametric amplifier (OPA) was a commercial TOPAS from Coherent. It is a two-stage OPA which uses 800 nm light to generate a near-infrared (NIR) signal beam in the first stage, then uses a second stage to amplify the NIR light.

A schematic layout of such an OPA is shown in Figure 2.1. The input beam is split in two, with the majority of the beam power reserved for the second stage. In the first stage, the beam is split in two again. Part of the beam is sent through a sapphire crystal to generate "white light". This white light consists of a supercontinuum of frequencies generated by a highly nonlinear process that is not yet completely understood [45]. Self-phase modulation is one key part of the process [46]. The optical Kerr effect in the sapphire results in an intensity-dependent refractive index (a $\chi^{(3)}$ process), which, for ultrashort pulses, means that the refractive index varies in time, adding an instantaneous phase to the pulse. This phase shift $\phi(t)$ shifts the frequency of the field $\omega = d\phi(t)/dt$, broadening the spectrum. The early part of the pulse is redshifted, while the trailing edge is blueshifted. Dispersion further increases the chirp of the pulse.

The temporal dispersion of the white light allows the selection of just a portion of the continuum for amplification. The white light is mixed with the rest of the first stage 800 nm beam in a nonlinear crystal, timing the arrival of the 800 nm pulse using a delay stage to correspond with the chosen color of the white light spectrum. Phase matching for optical parametric amplification can be achieved with a birefringent crystal, where the refractive index depends both on the light polarization and direction of propagation. Phase matching is optimized by selecting the optimal polarization of the pump and signal beams and tuning the orientation of the crystal. In the NIR regime, β-barium borate (BBO) is a popular choice for the nonlinear crystal due to its efficient phase matching in this frequency range. In Figure 2.1, the mixing is illustrated in a non-colinear geometry, which has the advantage of spatially separating the signal beam from the pump and idler.

The signal beam is sent on to the second stage, where it is mixed again in a second BBO crystal with the higher power 800 nm beam. This stage is depicted in Figure 2.1

[1]Coherent Libra series amplifier with integrated oscillator and pump lasers.

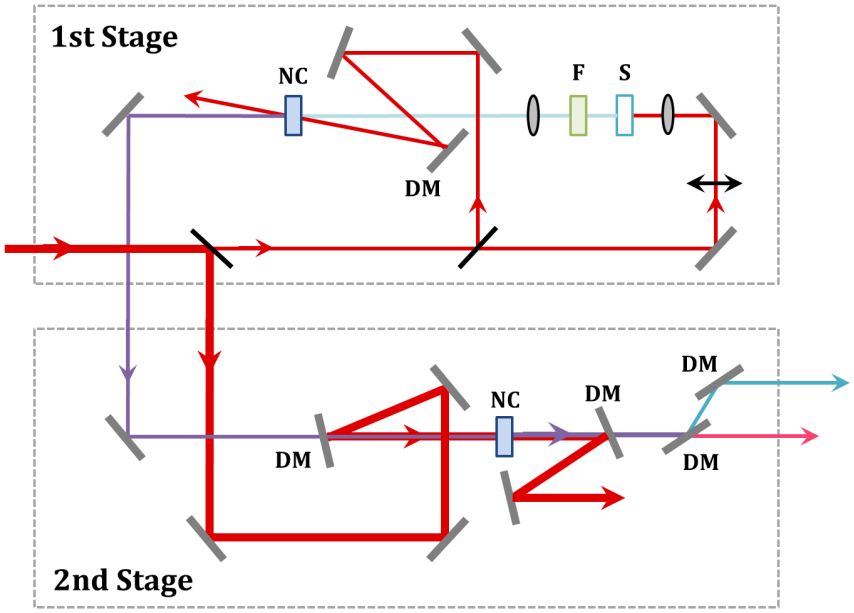

Figure 2.1: **General schematic diagram of an optical parametric amplifier for the near-infrared.** Red lines indicate 800 nm pump path, blue indicates the white light path, and purple indicates the path of the NIR (signal in pink and idler in blue). S = sapphire, F = filter, DM = dichroic mirror, and NC = nonlinear crystal.

in a collinear arrangement, which maximizes the signal and idler amplification. The pump beam is then separated from the NIR beams using a dichroic mirror.

Dichroic mirrors can also be used to separate the signal and idler beams if desired, as pictured in Figure 2.1, or, if the beams are cross-polarized, a waveplate can be used to select a single beam. For mid-infrared generation, we leave the signal and idler colinear and the OPA output is guided onward to the difference frequency set-up.

Optical parametric amplifiers have become a standard part of the ultrafast spectroscopy toolkit and commercial OPAs are capable of being tuned to generate narrowband, high fluence pulses over a broad spectral range. The typical spectral capabilities of the TOPAS system are plotted in Figure 2.2. The TOPAS OPA used in the experiments described in this thesis, combined with difference frequency generation, is capable of producing pulses up to 17 μm (~17 THz) in wavelength.

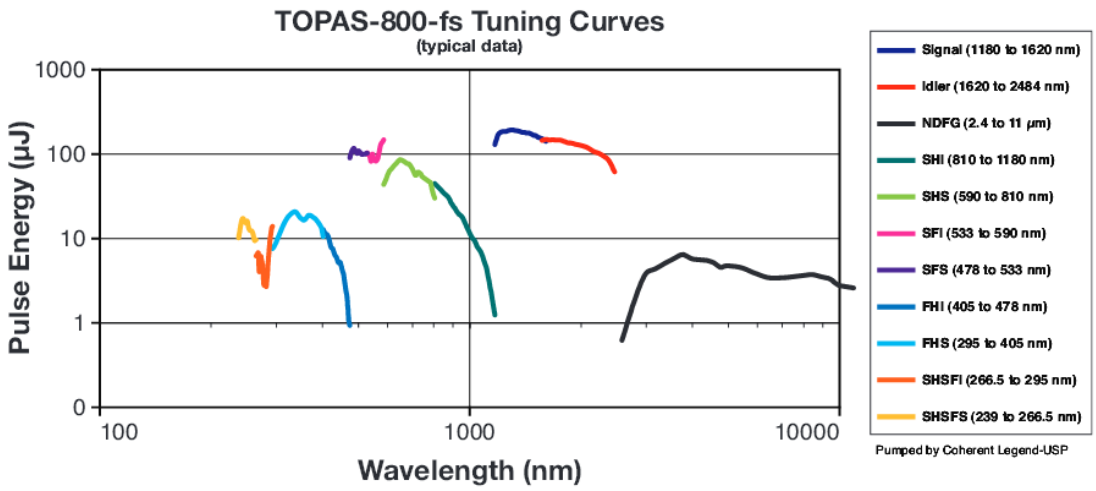

Figure 2.2: **Spectral range for the TOPAS optical parametric amplifier.** Typical output pulse energies over the tunable range of a commercial Coherent TOPAS (+NDFG) system. System is pumped by 1 mJ, < 40 fs pulses at 800 nm generated by a Coherent Legend series laser operating at 1 kHz. Figure from [47].

2.2.3 Difference frequency generation

Difference frequency generation (DFG) uses the $\chi^{(2)}$ process described in Section 2.2.1 to generate the difference frequency between the signal and idler beams produced by optical parametric amplification. This process extends the spectral range of the OPA into the mid-infrared (MIR). The DFG process can be performed in a colinear or non-colinear geometry. For the experiments reported here, we use a commercial Coherent NDFG system that operates in a non-collinear geometry, so the mid-infrared light can be separated from the remaining signal and idler beams by allowing the beams to spatially separate as they propagate.

Measuring the pulse spectrum in the mid-infrared range is not feasible with a commercial spectrometer. Instead, we employ a Michaelson interferometer setup. An example diagram of a Michaelson interferometer is shown in Figure 2.3. The MIR beam is split between two arms, one on a micron delay stage. The beams propagate along each arm and then are made colinear again at the beamsplitter before being focused onto a mercury-cadmium-telluride (MCT) detector. The MIR beam is modulated by a chopper before the interferometer and the MCT signal is amplified by a boxcar integrator triggered by the chopper before being sent through a lock-in amplifier and on to the computer for readout. By tuning the relative length

of each arm with the delay stage, the intensity of the MIR beam is modulated based on the phase difference between the two beams, beating at the frequency of the light.

The resulting interferogram is shown in Figure 2.4 for mid-infrared light centered at 15 μm. Taking the absolute value of the Fourier transform of the time profile produces the spectrum of the mid-infrared beam. The spectrum can be fit to a Gaussian form,

$$I = I_0 \exp\left(\frac{-(\lambda - \lambda_0)^2}{2\sigma^2}\right), \tag{2.6}$$

where for the spectrum shown in Figure 2.4, the central frequency is $\lambda_0 = 15.1$ μm and $\sigma = 1.1$ μm.

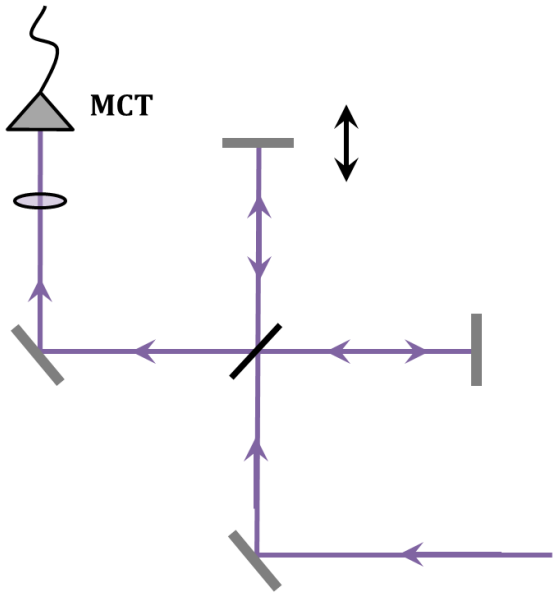

Figure 2.3: **Diagram of a Michaelson interferometer for measuring the mid-infrared spectrum.** The black arrows indicate the delay stage on one arm of the interferometer. After passing through the interferometer, the MIR beam is focused with a ZnSe lens onto an MCT detector.

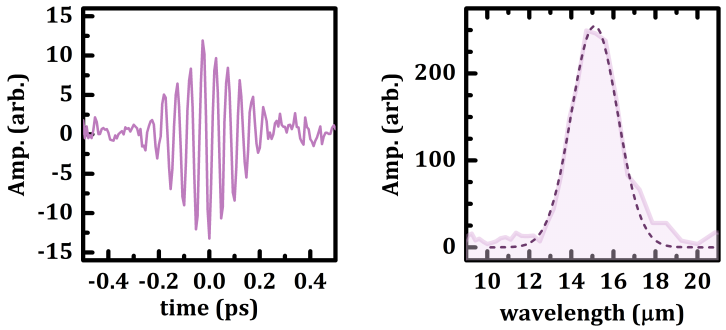

Figure 2.4: **Mid-infrared spectrum centered at 15 μm measured with Michaelson interferometry. Left:** The time-domain interferogram measured with 1 μm precision. A constant background has been subtracted. **Right:** The amplitude of the Fourier transform of the interferogram, reflecting the spectrum of the mid-infrared pulse. The spectrum is fit to a Gaussian profile with $\sigma = 1.1$ μm.

2.3 Time-domain THz spectroscopy

2.3.1 Optical rectification

Optical rectification utilizes ultrashort pulses to generate phase-stable, few- and single-cycle THz pulses. It is a $\chi^{(2)}$ process in which an optical pulse undergoes difference frequency mixing of its spectral components within a nonlinear crystal. The shape of the resulting THz field is determined by the envelope of the pump field. As such, the phase matching condition for rectification requires matching the *group* velocity wavevector of the optical pump with the *phase* velocity wavevector of the THz pulse.

The most widely used material is ZnTe, which naturally has good phase matching for NIR light. This material produces a spectrum between 0.2-2.7 THz, with the window determined partially by the pump beam characteristics and the thickness of the material. Typically, crystals used for optical rectification require excitation by sub-100 fs NIR pulses with pulse energies on order 1 mJ. Thicker crystals yield higher field intensities, at the sacrifice of bandwidth. This is due to balancing the benefit of having a larger optical path for rectification, and the detriment of a longer path length over which phase matching is lost. The distance for which the phase mismatch can be tolerated is called the coherence length. It is a material-specific value determined by the refractive index mismatch between THz and optical pump frequencies [48].

Other popular materials for optical rectification are GaP [49] and GaSe [50], which can produce higher frequency broadband spectrums, extending even above 100 THz [51], effectively bridging the gap to the NIR. Higher field, narrow bandwidth pulses have been made using $LiNbO_3$ [52, 53] and certain organic crystals, such as 4-N-methyl stilbazolium tosylate (DAST) [54]. The THz pulses made with these sources have fields high enough that they have been used even as pump sources. DAST has been shown to produce narrowband pulses centered at 2 THz with field strengths of 1.0 MV/cm. By tuning the pump[2] duration and crystal thickness, DAST can also be used to generate broadband pulses, with a spectral range of 0.1-10 THz reported [55].

2.3.2 Photoconductive antennae

Photoconductive antennae work on a different principle than optical rectification. A photoconductive, or "Auston", switch consists of a semiconductor device patterned with electrodes that apply a bias across a small (μm scale) strip of semiconductor. A femtosecond laser pulse transiently excites carriers from the valence band into the conductance band of the semiconductor. The applied bias accelerates the charges across the electrode, releasing dipole radiation. The timescale of this process is closely linked with the frequency of the emitted light. The limiting factor in determining the spectral range of the THz is the rise time of the photocurrent.

The Auston switch was first pioneered by Auston and collaborators [56–58] for generating THz along a stripline. They found that they could generate radiation between 0.1-1 THz [59] by using a colliding-pulse passively modelocked (CPM) dye laser to pump a dipole antenna fabricated on a substrate of radiation damaged silicon-on-sapphire. Today, low temperature grown gallium arsenide (LT-GaAs) [60] and In-doped GaAs have become the materials of choice for photoconductive antennas. Although some novel materials, such as graphene [61], are being actively researched for their potential as THz emitters.

The first time domain THz spectroscopy measurement was reported by van Exter, *et al.* [62], who looked at the THz absorption lines of water vapor. They used an antenna set-up adapted for free space THz radiation by the addition of a lens behind the antenna. Typically a hemispherical lens made of Si is used for free space antennas.

[2]DAST crystals were pumped at 1.35-1.5 μm wavelength, with 2.4 mJ energy per pulse and ~70 fs transform-limited pulse duration.

The geometry of antennae patterns has grown more sophisticated, with designs borrowed from earlier research on microwaves. The photoconductive antenna used in Chapter 4 is a commercial GaAs-based Tera-SED antenna produced by Laser Quantum. This is a large area antenna which is designed as an array of alternating positive and negative biased electrode strips. The gap between every other strip is covered by an opaque layer. Thus the light impinges only on areas of the semiconductor with the same static electric field direction and all of the emitted THz interferes constructively, generating a single coherent pulse in the far field. The design of the antenna is shown in Figure 2.5.

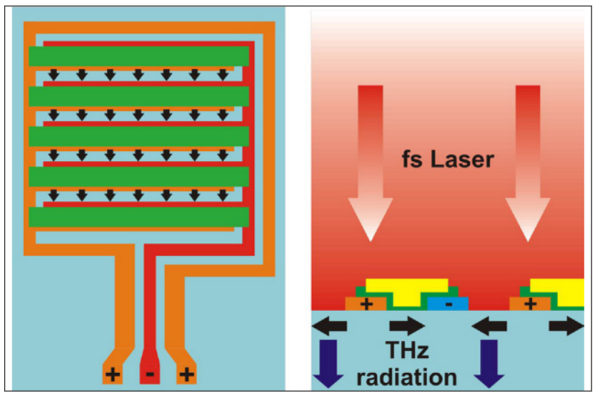

Figure 2.5: **Large area photoconductive antenna.** A diagram of a commercial photoantenna. Image from Ref. [63]. **Left:** An aerial view of the antenna, with arrows indicating the electric field direction across the semiconductor (light blue). The antenna array covers a 10×10 mm^2 area. **Right:** A side view of the antenna, with collimated 800 nm, fs laser light (red) impinging on the surface of the array. Electrodes are in orange and blue. Black arrows indicate the field direction along the semiconductor surface. Parts of the surface with counter-aligned fields are protected (yellow and green) from exposure to the beam. The direction of propagation of the emitted THz is indicated with blue arrows.

2.3.3 Generating broadband THz in a two color plasma

The spectral range of optical rectification is ultimately limited by the absorption spectrum of the nonlinear crystal. Even crystals such as GaSe that are capable of

generating broadband radiation show significant absorption lines within their spectrum. THz generation by plasma in air is another method of producing broadband radiation throughout the mid-infrared [64–66].

There are several methods for plasma generation. The two color plasma scheme uses tunnel ionization to accelerate electrons in a laser field, releasing broadband radiation with no sharp absorption lines. The generation scheme works as follows. An 800 nm beam is passed through a nonlinear crystal (generally, BBO) to generate second harmonic light at 400 nm. The remaining co-propagating 800 nm beam and the 400 nm beam are focused in air to create a volume with a fluence beyond the ionization threshold of the air. Mixing with the 2nd harmonic light introduces an asymmetry in the electric field, which accelerates the ionized electrons and produces THz radiation.

2.3.4 Electro-optic sampling

Electro-optic sampling is a detection technique for directly measuring the electric field profile of a THz pulse. The general procedure involves the use of an optical pulse with a duration much shorter than that of the THz field to sample the field profile. (In practice, a beam-splitter reserves a fraction of the femtosecond laser beam that is used to generate the THz in order to sample the resulting pulse.) The THz field interacts with the sampling beam in a nonlinear crystal via the Pockels effect, in which the electric field due to the THz pulse generates birefringence proportional to the field strength.[3] This birefringence leads to a rotation of the polarization of the sampling beam. The magnitude of the induced rotation depends on which part of the THz spectrum is timed with the arrival of the sampling beam. Iterative measurements, shifting the delay of the sampling pulse, allows the recovery of the full spectrum.

An electro-optic sampling (EOS) scheme is depicted in Figure 2.6. The sampling beam is initially polarized such that, in the absence of an applied field, a Wollaston prism will split the beam into two pulses of equal intensity but opposing polarization. These pulses are detected in two photodiodes, whose signals are subtracted. This "balanced detection" scheme ensures that whatever net signal is detected reflects the polarization imbalance produced by the THz field. A linear polarization scheme is depicted in Figure 2.6, where a half-wave ($\lambda/2$) plate rotates the sampling beam

[3] Note that this is different from the better-known Kerr effect, in which birefringence is proportional to the field *intensity*.

into equal horizontal (H) and vertical (V) components. It is also common to use an elliptical polarization scheme, replacing the $\lambda/2$-plate with a quarter-wave ($\lambda/4$) plate, which circularly polarizes the light in the absence of a field.

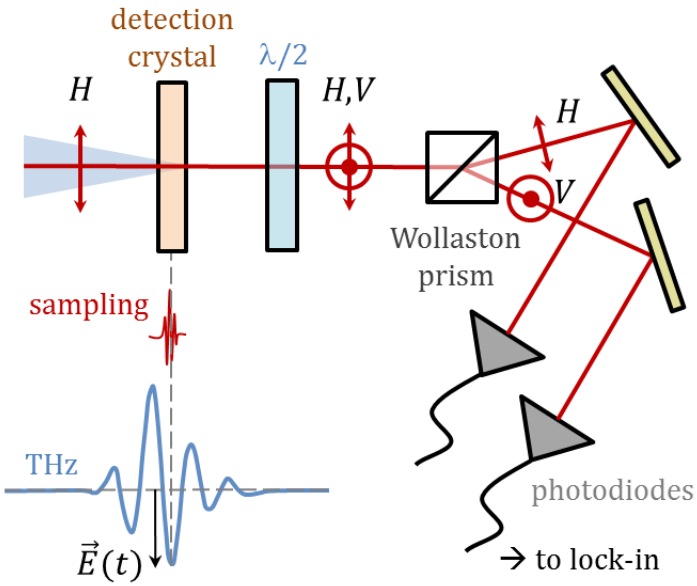

Figure 2.6: **Electro-optic sampling.** A depiction of the electro-optic sampling scheme in which THz light (blue) and a sampling beam (red) are focused into a nonlinear crystal, which rotates the polarization of the sampling beam in proportion to the applied THz field $E(t)$ at the arrival time t of the sampling pulse. The rotation of the polarization is measured by splitting the polarization components and measuring with a balanced detection scheme. By varying the arrival time t of the sampling pulse, the full THz spectrum can be measured.

A THz field generated by optical rectification in ZnTe, then reflected from n-doped GaAs, is plotted in Figure 2.7. The THz profile was measured via electro-optic sampling with 1 mm thick ZnTe used as the nonlinear detection crystal. This detection crystal was used for all the work presented in this thesis. Fourier transform of the field $E(t)$ yields the complex quantity $\tilde{E}(\omega)$, the absolute value of which corresponds to the spectral range of the field.

This technique is very useful for material characterization as it allow the full recovery of the complex amplitude and phase response of a material, even over a

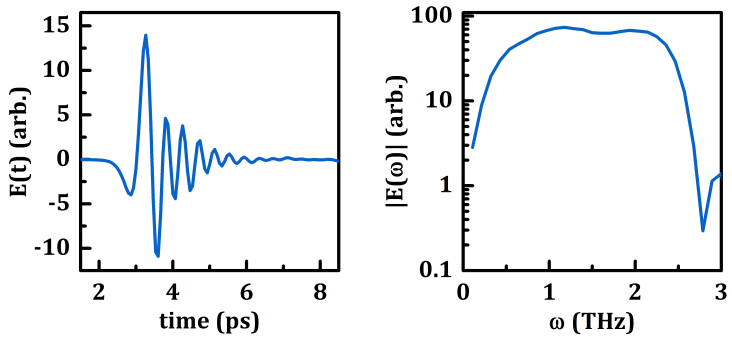

Figure 2.7: **THz reflectivity spectrum. Left:** The profile of a THz pulse reflected from n-doped GaAs. **Right:** The spectrum of the THz field produced by fast Fourier transform of the field profile.

narrow frequency region. A probe of the reflected or transmitted *intensity* of the field, by contrast, requires measuring a very broad spectrum in order to perform a Kramers-Kronig transform to deduce the phase component of the response. As with intensity measurements, the THz field reflected or transmitted from a sample of interest must be normalized with respect to a known material in order to recover the absolute magnitude and phase of the field.

There are several methods to do this *in situ*. In reflection, the challenge is referencing the sample without losing phase information, which is extremely sensitive to the sample position. Moving the sample in a way that changes the arrival *time* of the THz pulse translates to a shift in the *phase* in Fourier space. The evaporation of a thin Au layer on the sample surface provides one reliable way to reference the sample without losing phase information, though it can be potentially damaging to the sample.

In transmission, the phase information is not sensitive to the sample position, but the risk is rather that it can be distorted by the choice and alignment of a reference sample. For thin films on a substrate, measuring the bare substrate is an obvious choice for referencing, however care must be taken to ensure that the thickness and orientation of the reference precisely match that of the sample substrate.

2.3.5 Pump-probe with THz spectroscopy

As time-domain THz spectroscopy already utilizes ultrashort pulses for material characterization, it is the ideal tool to probe the far-infrared response of a system

after optical stimulation. The use of one or more optical pulses to excite, or "pump" the system, and a subsequent pulse or pulses to "probe" the dynamics is referred to as a "pump-probe" configuration. Here I will describe a three pulse pump-probe scheme, where a single pulse is used to pump the system and two pulses, the THz and sampling beams, are used to probe the transient optical response.

The pump-probe scheme is illustrated in Figure 2.8. There are two time delays to keep track of.

1. The time t between the sampling pulse and the THz pulse, which maps out the THz spectrum and is the Fourier conjugate of the THz frequency ω.

2. The time delay τ, which refers to the delay between the sampling pulse and pump beam and reflects the time after excitation of the sample.

Generally, $\tau = 0$ is defined as when the pump pulse arrives at the sample surface, though it is sometimes also defined by the peak of the transient response. Throughout this thesis, we will use the former definition.

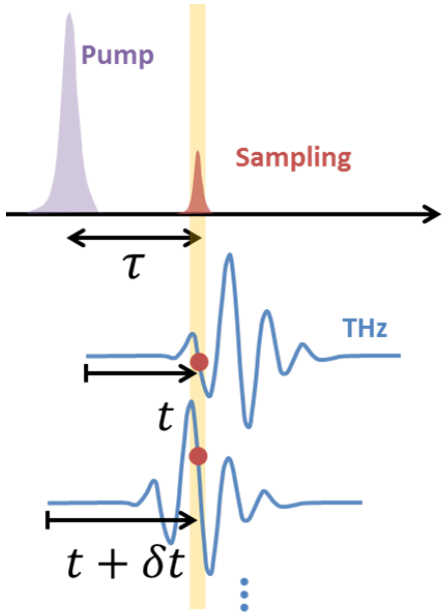

Figure 2.8: **Timing pump excitation with THz probe.**

It is common for those unfamiliar with this technique to initially assume that the broad spectrum of the THz, which can extend in time for several picoseconds, sets the time resolution of the experiment. However, this is not the case. The THz profile is *not* a reflection of a "single shot" measurement, in which different parts of the THz pulse interact with the sample at different delays with respect to the pump arrival time. Rather, the THz spectrum is measured over many "shots", with each time t measured with the same delay τ between the pump and sampling beam. In this way, the THz profile encodes the full response of the sample only at time delay τ. The time resolution of the experiment is limited instead by the spectral content of the THz.

As with equilibrium measurements, the THz field of the sample after pumping, $E_{on}(t)$, must be referenced by the equilibrium reflected field, $E(t)$. The two fields can be measured directly, using a chopper to modulate the THz beam and a lock-in amplifier to read out the balanced EOS diodes. However, in practice, when the pump-induced changes to the field $\Delta E(t) = E_{on}(t) - E(t)$ are small compared to $E(t)$, the amplifier may not be sensitive enough to detect them with a sufficient signal-to-noise ratio (SNR). In this case, we instead use the chopper to modulate the pump beam and acquire the differential changes $\Delta E(t)$ directly, at a higher lock-in sensitivity.

Figure 2.9 shows the THz reflectivity profile of n-doped GaAs with (purple) and without (grey) mid-infrared excitation. The pump-induced changes in the field are large enough, in this case, to directly measure by THz chopping (left-hand panel). The differential changes $\Delta E(t)$ are shown in the center panel, measured both by $E_{on}(t) - E(t)$ (purple) and direct acquisition (blue). The error bars indicate the average over several scans, with the direct acquisition technique resulting in far smaller noise. The normalized, Fourier transformed reflectivity spectrum,

$$\frac{\Delta E(\omega)}{E(\omega)} = \frac{E_{on}(\omega) - E(\omega)}{E(\omega)} \tag{2.7}$$

is shown for each case (right-hand panel), and are in good agreement.

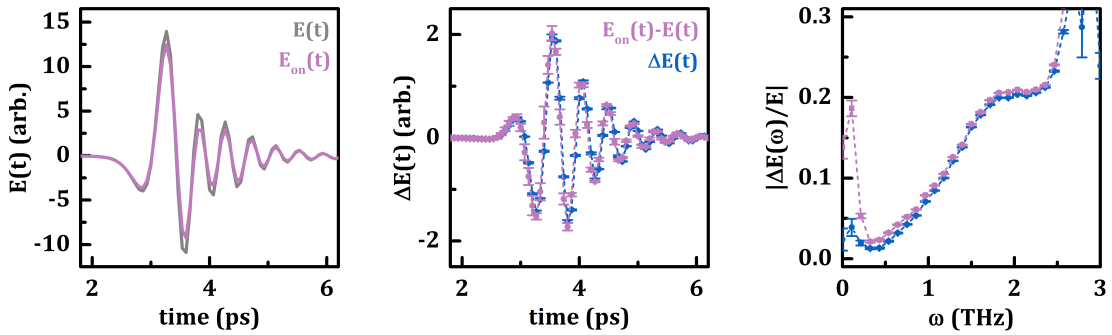

Figure 2.9: **Comparison of differential chopping with direct probe. Left:** The THz field reflected from GaAs after pump excitation (purple) and in equilibrium (grey). **Center:** The differential changes to the spectrum measured as the difference between the profiles in the left-hand panel (purple) or measured directly by modulation of the pump (blue). **Right:** The normalized Fourier transformed reflectivity spectra for the two cases.

2.3.6 Potential sources of artifacts

The referencing of the transient changes to the field $\Delta E(t)$ to the equilibrium field $E(t)$ is subject to the same sensitivity to phase as the absolute measurements described in Section 2.3.4. However, since the sample does not need to be moved or otherwise altered, the risk of introducing artifacts during referencing is low, although there are certain scenarios to be careful of. One source of phase error that can occur during cryogenic measurements is the shifting of the sample position due to thermal contraction of the sample stage. An example of this is illustrated in Figure 2.10.

Using a double chopping, two lock-in scheme, both $\Delta E(t)$ and $E(t)$ can be acquired simultaneously, preventing these sorts of issues. However, the increase in stability comes at the sacrifice of SNR. By maintaining a stable environment, sequential measurement of the transient and equilibrium fields can be performed consistently and with high SNR.

Convolution of the THz profile with the detector response can be another source of artifacts [67]. The detector bandwidth can act as a low-pass filter, broadening the THz pulse. This distortion can even lead to apparent pump-induced changes appearing before $\tau = 0$. The effect is generally only a problem when the pump-induced changes are very fast compared with the detector response time. A method of deconvolving the detector response is described in the supplementary material of Ref. [67].

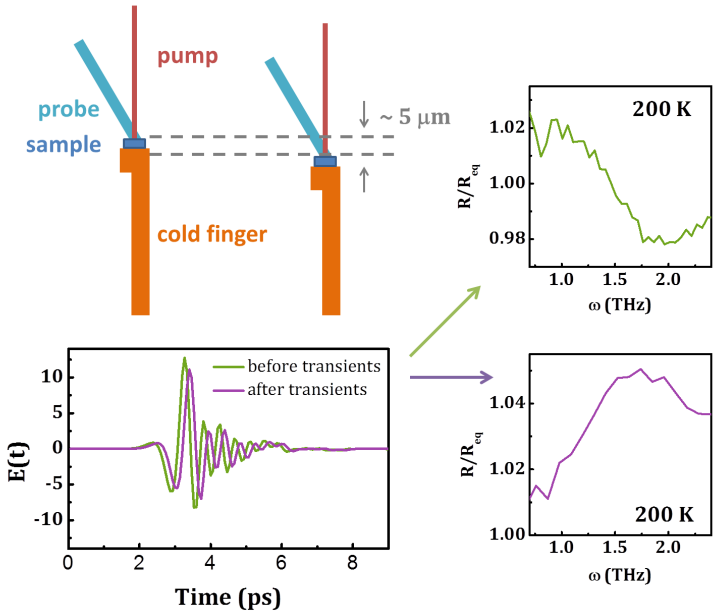

Figure 2.10: **Phase error introduced by thermal contraction.** An example of the effect of thermal contraction on the recalculated transient optical properties of YBCO 6.5. A schematic diagram (**top left**) shows a cold finger cryostat with a sample mounted at the end. After cooling from 295 K to 200 K, thermal contraction over a several hour period shrinks the length of the cold finger, increasing the optical path of the pump and THz probe. While the motion is small enough not to disrupt the pump probe overlap, the timing difference is enough to introduce an artificial phase shift between a THz field measured ∼1-2 hours after cooling (green) and a second spectrum measured a few hours later (purple), shown on the **lower left**. The transient field $\Delta E(t)$ was measured shortly after the first equilibrium spectrum. The transient reflectivity R/R_{eq}, has been calculated by referencing $\Delta E(t)$ with the first spectrum (textbftop right, green) and second spectrum (**lower right**, purple). The top figure represents the actual response.

2.4 Experimental design used for the work presented in this thesis

All time-domain THz spectroscopy measurements presented in this thesis were performed on single crystals in a reflection geometry. The THz was generated and detected within a vacuum chamber, shown in Figure 2.11, in order to reduce water absorption, minimize the focal length, and allow the full THz beam to access the sample without passing through windows. The chamber is capable of reaching base

pressures as low as 5×10^{-7} mbar. A base pressure of 5×10^{-6} mbar or lower at 295 K was necessary to prevent ice formation at cryogenic temperatures. The samples sat at the end of a cold finger cryostat affixed to the vacuum chamber. The cryostat is able to reach temperatures of 3.5 K with active helium pumping. The sample and cold finger were allowed to sit for typically 4 or more hours before measurement in order to reach thermal equilibrium.

Delay stages (not pictured) were set along the pump and sampling probe paths. The relative change between the pump and sampling beams set the pump-probe delay τ. The transient changes in the reflectivity $\Delta E(t)$ were captured by moving both stages together to set the relative delay between sampling beam and THz probe.

Rotating the orientation of a $\lambda/2$-plate (on the 800 nm probe path in Figure 2.11) and the ZnTe generation crystal allowed control over the polarization of the THz light. For the photoconductive switch, alignment of the switch determined the THz polarization. The THz polarization was checked with a MIR polarizer placed in the path of the THz before the EOS optics. The focal size of the THz beam was minimized by adjusting the cold finger (and sample) position to maximize the low frequency THz response.

The pump beam profile was measured by sending the MIR light down a path, outside the chamber, with the same distances and focal lengths as the set-up in the vacuum chamber. A razor blade was used to measure the profile and optimize the focusing lens position to match the THz beam width.

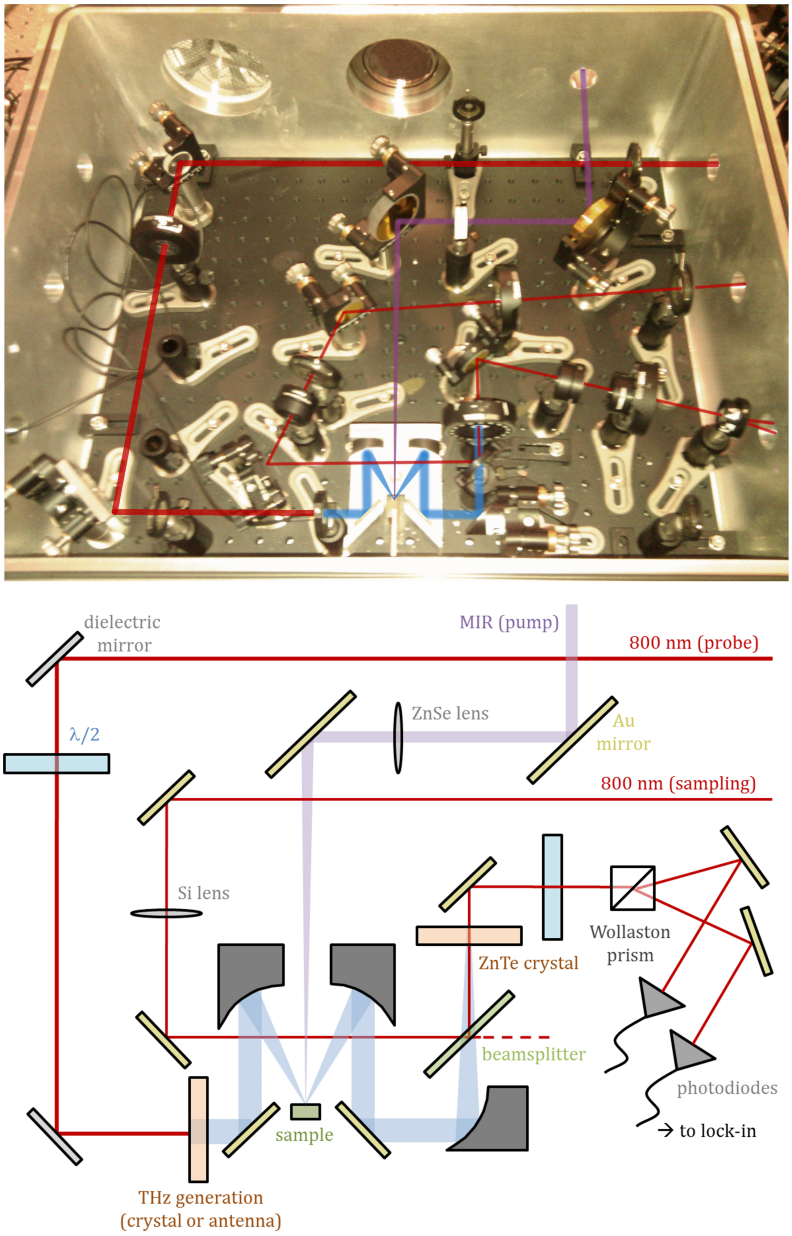

Figure 2.11: **The vacuum chamber containing the THz generation and detection optics.** The vacuum chamber is depicted in a photograph **(top)** and as a diagram **(bottom)**. The mid-infrared pump (purple) enters the chamber via a polypropylene window and is focused onto the sample at normal incidence. The sample sits at the end of a cold finger cryostat. The probe is generated from pulses of 800 nm light (thick red line) incident on a ZnTe crystal or photoconductive antenna. The THz beam (blue) is impinges on the sample at 30° incidence and the reflected beam is focused into a second ZnTe crystal. A second beam (thin red line) is focused on the same position for detection via electro-optic sampling. The photodiodes used to detect the difference signal are located outside the vacuum chamber and are not shown in the photograph.

2.5 Analytic models of photo-excited materials

2.5.1 Bulk excitation

The simplest approximation for calculating the optical response of a photo-excited material is to assume the sample is homogeneously transformed by the pump. This is a reasonable approximation in the limit that the pump penetration depth is much larger than that of the probe. In this regime, the reflection coefficient of the excited material, $\tilde{r}'$, can be related to its refractive index $\tilde{n}$ via the Fresnel equations,

$$\tilde{r}' = \frac{\cos\theta_0 - \tilde{n}\sqrt{1 - \left(\frac{\sin\theta_0}{\tilde{n}}\right)^2}}{\cos\theta_0 + \tilde{n}\sqrt{1 - \left(\frac{\sin\theta_0}{\tilde{n}}\right)^2}}, \qquad \text{(TE wave)} \tag{2.8}$$

and

$$\tilde{r}' = \frac{\sqrt{1 - \left(\frac{\sin\theta_0}{\tilde{n}}\right)^2} - \tilde{n}\cos\theta_0}{\sqrt{1 - \left(\frac{\sin\theta_0}{\tilde{n}}\right)^2} - \tilde{n}\cos\theta_0}, \qquad \text{(TM wave)} \tag{2.9}$$

where θ_0 is the angle of incidence on the sample and we have assumed the refractive index at the sample interface is $n = 1$.

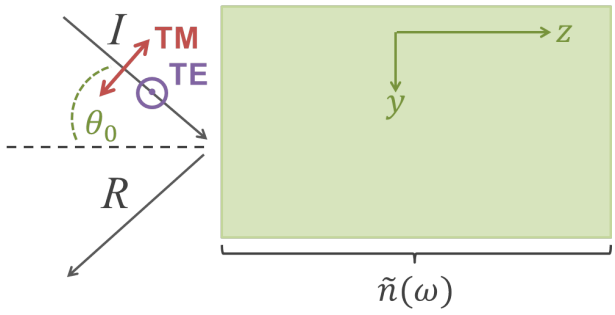

Figure 2.12: **Bulk model.** The simplest approximation of a photo-excited media is to assume we are probing a homogeneously transformed bulk.

The complex reflection coefficient $\tilde{r}'$ is related to the measured change in the electric field as,

$$\frac{\Delta E(\omega)}{E(\omega)} \equiv \frac{\Delta \tilde{r}}{\tilde{r}} = \frac{\tilde{r}' - \tilde{r}}{\tilde{r}}. \tag{2.10}$$

The *relative* changes in the electric field $\Delta E/E$ are not enough to determine the *absolute* optical properties of the excited state $\tilde{r}'$. We require an additional measurement of the equilibrium reflection coefficient, $\tilde{r}$. This can be calculated from an independent measurement of the broadband reflectivity using Kramers-Kronig analysis, or from referenced time domain THz spectra. Given the equilibrium response $\tilde{n}_0$, $\tilde{r}$ can be calculated using Equations 2.8 or 2.9. Once we determine $\tilde{r}'$, inverting Equations 2.8 or 2.9 yields the transient refractive index,

$$\begin{aligned}
\tilde{n}(\tilde{r'}) &= \sqrt{\sin^2\theta_0 + \cos^2\theta_0 \left(\frac{1-\tilde{r}'}{1+\tilde{r}'}\right)}, && \text{(TE wave)} \\
\tilde{n}(\tilde{r'}) &= \frac{1}{\sqrt{2}}\left(\frac{1+\tilde{r}'}{1-\tilde{r}'}\right)\sqrt{1+\sqrt{1-4\sin^2\theta_0\cos^2\theta_0\left(\frac{1-\tilde{r}'}{1+\tilde{r}'}\right)^2}}, && \text{(TM wave)}
\end{aligned} \tag{2.11}$$

Many important effects are measured with small signal-to-noise ratios, it is therefore worthwhile to look at how the measurement uncertainty propagates to our calculated optical properties. In Appendix A.1, I derive how to analytically propagate the standard deviation due to noise in the measured THz field, $\sigma_{\tilde{r}'}$, to the standard deviation of the refractive index, $\sigma_{\tilde{n}}$.

2.5.2 High pump-probe penetration depth mismatch: the thin film limit

An analytical model of the transient response can also be developed in the opposing limit, when the pump penetration depth d is much less than the probe penetration depth L. In this limit, we take the THz field to be constant through the film. The boundary conditions of the electromagnetic field between the vacuum (medium 1) and the unperturbed bulk of the sample (medium 2) can be written,

$$\begin{aligned}
\hat{z} \times (\vec{H}_1 - \vec{H}_2) &= j_s d, \\
\hat{z} \times (\vec{E}_1 - \vec{E}_2) &= 0,
\end{aligned} \tag{2.12}$$

where j_s is the surface current density, $j_s = \sigma E$, and $\hat{z}$ is the unit normal from the sample surface.

For the TE case, this becomes,

$$\begin{aligned} (H_i - H_r)\cos\theta_0 - H_t \cos\theta_t &= j_s d, \\ E_i + E_r &= E_t, \end{aligned} \tag{2.13}$$

for the incident (i), reflected (r), and transmitted (t) fields. The light is incident at angle θ_0 and the transmitted light propagates with angle θ_t from surface normal.

We solve Equations 2.13 in terms of the sample admittance $Y = H/E$, which is the inverse of the impedance $Z = Z_0/\tilde{n}$ and proportional to the complex refractive index $\tilde{n}$. The constant Z_0 is the impedance of free space, which in SI units is $Z_0 = \sqrt{\mu_0/\varepsilon_0} \approx 377\ \Omega$. The equation for the reflected field becomes

$$E_r = \frac{(Y_1 \cos\theta_0 - Y_2 \cos\theta_t)\, E_i - j_s d}{Y_1 \cos\theta_0 + Y_2 \cos\theta_t}. \tag{2.14}$$

The reflectivity of the excited film $\tilde{r}' = E_r/E_i$ can be expressed just in terms of the admittance and conductivity by using the definition of the surface current, $j_s d = \sigma E d = \sigma(E_i + E_r)d$,

$$\tilde{r}' = \frac{Y_1 \cos\theta_0 - Y_2 \cos\theta_t - \sigma d}{Y_1 \cos\theta_0 + Y_2 \cos\theta_t + \sigma d}, \tag{2.15}$$

or, in terms of the refractive index,

$$\tilde{r}' = \frac{\tilde{n}_1 \cos\theta_0 - \tilde{n}_2 \cos\theta_t - Z_0 \sigma d}{\tilde{n}_1 \cos\theta_0 + \tilde{n}_2 \cos\theta_t + Z_0 \sigma d}. \tag{2.16}$$

I now take the case that $\tilde{n}_1 = 1$ (vacuum) and $\tilde{n}_2 = \tilde{n}_0$ where $\tilde{n}_0$ is the bulk refractive index following the same notation used in Section 2.5.1. The transmitted angle θ_t can be written in terms of the refractive index using Snell's law, $\tilde{n}_0 \cos\theta_t = \sqrt{\tilde{n}_0^2 - \sin^2\theta_0}$. The refractive index of the unexcited material $\tilde{r}$ follows the Fresnel form given by Equation 2.8. So for the measured changes in the THz field, $\Delta\tilde{E}/\tilde{E} \equiv \Delta\tilde{r}/\tilde{r}$,

$$\frac{\Delta\tilde{r}}{\tilde{r}} = \left(\frac{\cos\theta_0 - \sqrt{\tilde{n}_0^2 - \sin^2\theta_0} - Z_0\sigma d}{\cos\theta_0 + \sqrt{\tilde{n}_0^2 + \sin^2\theta_0} + Z_0\sigma d} \right) \left(\frac{\cos\theta_0 + \sqrt{\tilde{n}_0^2 - \sin^2\theta_0}}{\cos\theta_0 - \sqrt{\tilde{n}_0^2 + \sin^2\theta_0}} \right) - 1. \tag{2.17}$$

Equation 2.17 can be inverted to solve for the conductivity term σ, which actually represents the pump-induced changes to the conductivity $\Delta\tilde{\sigma}(\omega)$. Finally we end up with,

$$\Delta\tilde{\sigma}(\omega) = \left(\frac{1}{Z_0 d}\right) \frac{\dfrac{\Delta\tilde{E}(\omega)}{\tilde{E}(\omega)}\left(\tilde{n}_0^2 - 1\right)}{\dfrac{\Delta\tilde{E}(\omega)}{\tilde{E}(\omega)}\left(\cos\theta_0 - \sqrt{\tilde{n}_0^2 - \sin^2\theta_0}\right) + 2\cos\theta_0} \tag{2.18}$$

2.6 Models with intermediate pump-probe penetration depth mismatch

2.6.1 The characteristic matrix

I will now derive a model for the intermediate pump-probe penetration depth regime which takes into account that the refractive index changes as a function of depth, $\tilde{n}(\omega, z)$. The first step in this analysis is to define the *characteristic matrix* of a material. The discussion in this section follows the derivation found in Born and Wolf's *Principles of Optics*, Section 1.6 [68].

We are interested in deriving the reflectivity of a beam incident on a slab of material that has been optically excited and thus has a refractive index that varies with depth. From Maxwell's equations, we can describe a TE wave incident on the y-z plane of a medium by

$$\begin{aligned} E_x &= U(z)\mathrm{e}^{i(k_0\beta y - \omega t)} \\ H_y &= V(z)\mathrm{e}^{i(k_0\beta y - \omega t)} \\ H_z &= W(z)\mathrm{e}^{i(k_0\beta y - \omega t)} \end{aligned} \tag{2.19}$$

where $\beta = \tilde{n}\sin\theta$ for a homogeneous plane wave, and $k_0 = 2\pi/\lambda_0$, where λ_0 is the incident wavelength propagating *in vacuo*. Note that, in accordance with Snell's law, β is a constant.[1]

We define the *characteristic matrix*, M, of the media which will map the EM field at some thickness z back to $z = 0$,

$$\begin{pmatrix} U_0 \\ V_0 \end{pmatrix} = M \begin{pmatrix} U(z) \\ V(z) \end{pmatrix} \tag{2.20}$$

[1] The term β is labeled as α in Born and Wolf.

where $U(0) = U_0$ and $V(0) = V_0$. We begin by using Maxwell's equations to define second order differential equations for U and V (note that $\beta U + \mu W = 0$).

$$\begin{aligned} \frac{d^2U}{dz^2} - \frac{d\left[\ln \mu\right]}{dz}\frac{dU}{dz} + k_0\left(\tilde{n}^2 - \beta^2\right)U &= 0 \\ \frac{d^2V}{dz^2} - \frac{d\left[\ln\left(\varepsilon - \beta^2/\mu\right)\right]}{dz}\frac{dV}{dz} + k_0\left(\tilde{n}^2 - \beta^2\right)V &= 0 \end{aligned} \tag{2.21}$$

The solutions to these differential equations may be expressed as a weighted sum of two solutions, U_1,U_2 and V_1,V_2, which satisfy the first order differential equations,

$$\begin{aligned} U_1' &= ik_0\mu V_1, & U_2' &= ik_0\mu V_2, \\ V_1' &= ik_0\left(\varepsilon - \frac{\beta^2}{\mu}\right)U_1, & V_2' &= ik_0\left(\varepsilon - \frac{\beta^2}{\mu}\right)U_2. \end{aligned} \tag{2.22}$$

For convenience, we define the initial conditions as $U_1(0) = V_2(0) = 0$ and $U_2(0) = V_1(0) = 1$. Note that throughout the following discussion we will assume $\mu = 1$. Then the solutions to Equations (2.22) have the form,

$$\begin{aligned} U(z) &= U_2(z)U_0 + U_1(z)V_0, \\ V(z) &= V_2(z)U_0 + V_1(z)V_0, \\ \Rightarrow \begin{pmatrix} U(z) \\ V(z) \end{pmatrix} &= \begin{bmatrix} U_2 & U_1 \\ V_2 & V_1 \end{bmatrix}\begin{pmatrix} U_0 \\ V_0 \end{pmatrix}. \end{aligned} \tag{2.23}$$

From Equations (2.22) we can derive $\partial_z(U_1V_2 - U_2V_1) = 0$ and thus that the matrix above must have a constant determinant, independent of z. We can use our initial conditions to explicitly solve that $\det(M^{-1}) = 1$ at $z = 0$.

Finally, we invert Equation (2.23) and arrive at our characteristic matrix,

$$\begin{pmatrix} U_0 \\ V_0 \end{pmatrix} = \begin{bmatrix} V_1 & -U_1 \\ -V_2 & U_2 \end{bmatrix}\begin{pmatrix} U(z) \\ V(z) \end{pmatrix}. \tag{2.24}$$

Equations (2.21) can be simplified by assuming $\tilde{n}$, the complex refractive index, is constant throughout the medium,

$$\begin{aligned} \frac{d^2U}{dz^2} + (k_0^2\tilde{n}^2\cos^2\theta)\,U &= 0, \\ \frac{d^2V}{dz^2} + (k_0^2\tilde{n}^2\cos^2\theta)\,V &= 0. \end{aligned} \tag{2.25}$$

Solving these equations using the initial conditions given above leads us to the final form of our characteristic matrix,

$$\boxed{M(z) = \begin{bmatrix} \cos(k_0\tilde{n}z\cos\theta) & -\dfrac{i}{p}\sin(k_0\tilde{n}z\cos\theta) \\ -ip\sin(k_0\tilde{n}z\cos\theta) & \cos(k_0\tilde{n}z\cos\theta) \end{bmatrix},} \tag{2.26}$$

where $p = \sqrt{\varepsilon/\mu}\cos\theta \equiv \tilde{n}\cos\theta$.

The above matrix form can be applied to the TM case as well if we make the substitution $p \to \cos\theta/\tilde{n}$.

2.6.2 Single excited layer model

The characteristic matrix has been derived assuming a uniformly excited media. In this section I will use the characteristic matrix to describe a uniformly excited single layer of thickness d on an unperturbed bulk. The terms of the characteristic matrix can be used to calculate the reflectivity coefficient, $\tilde{r}'$, for the excited medium. Defining I, R, and T as the amplitude of the incident, reflected, and transmitted waves, respectively, then

$$\begin{aligned} U_0 &= I + R, & U(d) &= T, \\ V_0 &= p_1(I - R), & V(d) &= p_d T. \end{aligned} \tag{2.27}$$

where we define p_1 for the material from which the field enters the medium and p_d for the material a distance d into the medium. So $p_1 = \cos\theta_0$, where θ_0 is the angle of incidence, and $p_d = \tilde{n}(d)\cos\theta_d = \tilde{n}_0\cos\theta_d$, where θ_d is the angle at which the field leaves the pumped region. Using Snell's law, $\cos\theta_d = \sqrt{1 - (\sin\theta_0/\tilde{n}_0)^2}$.

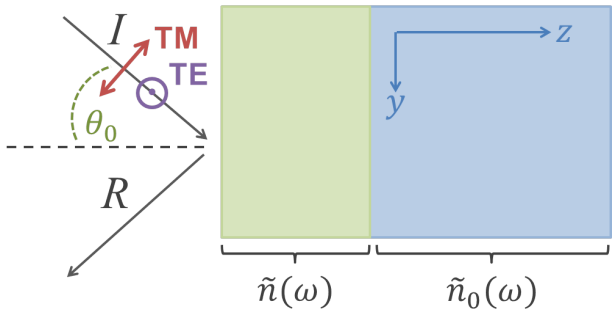

Figure 2.13: **Single layer model.** The material is modeled as a single excited layer on an unperturbed bulk.

Using M to solve Equations (2.27), we find that the reflectivity coefficient for the excited layer is,

$$\boxed{\tilde{r}' = \frac{R}{I} = \frac{(m_{11} + m_{12}p_d)\,p_1 - (m_{21} + m_{22}p_d)}{(m_{11} + m_{12}p_d)\,p_1 + (m_{21} + m_{22}p_d)},} \tag{2.28}$$

where m_{ij} is the i,jth component of the matrix M.

The code implementing this model can be found in Appendix C. The experimentally obtained $\tilde{r}'$ is expressed as a function of the pump-induced refractive index, $\tilde{n}$. The form of the matrix M makes explicit calculation of $\tilde{n}(\tilde{r}')$ not analytically feasible. However, we can recursively "guess" $\tilde{n}$ and try to fit the resulting $\tilde{r}'$ to our data. The method used to fit $\tilde{r}'$ is discussed in Section 2.6.4.

2.6.3 Multilayer model

In order to model a material with a refractive index that evolves as a function of z, we consider the case of many thin layers stacked together, where $\tilde{n}(z) = \textit{constant}$ for each layer. The characteristic matrix of this total medium is just a product of the matrices for each layer,

$$M(z_N) = M_1(z_1)M_2(z_2 - z_1)...M_N(z_N - z_{N-1}). \tag{2.29}$$

The surface is an excited layer with a refractive index, $\tilde{n}$, that exponentially decays to the bulk, $\tilde{n}_0$,

$$\tilde{n}(z) = \tilde{n}_0 + \Delta\tilde{n}\mathrm{e}^{-\alpha z}, \tag{2.30}$$

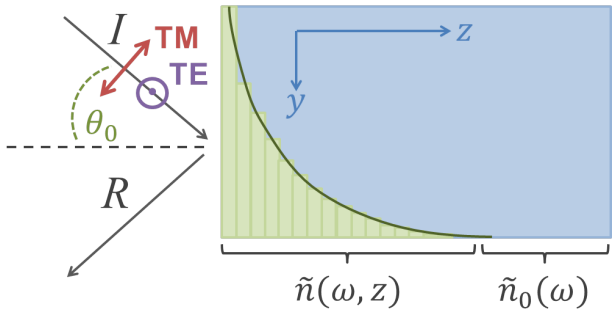

Figure 2.14: **Multilayer model.** The system is modeled as a multilayer, with the the pumped volume described as a stack of thin layers with z-independent refractive index, $\tilde{n}$. From layer to layer, the refractive index decays exponentially to the bulk value.

where the penetration depth of the pump, d, sets the decay rate, $\alpha = 1/d$. So $p_1 = \cos\theta_0$, where θ_0 is the angle of incidence, and $p_L = \tilde{n}(L)\cos\theta_L$, where θ_L is the angle at which the field would leave the probed region. Using Snell's law, $\cos\theta_L = \sqrt{1-(\sin\theta_0/\tilde{n}(L))^2}$.

This model has been implemented in Matlab and can be found in Appendix C. In order to improve calculation speed, the program sets a tolerance for the value for $\tilde{n}(z_{i+1}) - \tilde{n}(z_i)$ at which it assumes the bulk refractive index has been reached. In this limit, where the probe penetrates much deeper than the pump, the program produces quantitatively similar answers to the single film model.

For thin layers, $\delta z << k_0$, the characteristic matrix form can be approximated and the matrix elements solved for analytically. This is described in Appendix A.3. An analytic version of the multilayer model was derived for the TE polarization case and is discussed in Appendix A.4.

2.6.4 Implementing the non-analytic models

The code for each of the non-analytic models is given in Appendix C. They are designed to take as an input the guess value of the transient changes to the refractive index at the sample surface, $\Delta\tilde{n}$ at a single frequency ω. They also take the equilibrium refractive index $\tilde{n}_0$ at frequency ω as well as other necessary parameters, as described in the code. The output is the resulting transient reflectivity $\tilde{r}'(\tilde{n})$ for a refractive index $\tilde{n} = \tilde{n}_0 + \Delta\tilde{n}$. The reflectivity is related back to the measured quantity $\Delta\tilde{E}/\tilde{E}$ via Equation 2.10.

The key is to choose a good quantity to optimize in order to match the model value of $\Delta\tilde{E}/\tilde{E}$ at each frequency to the experimentally measured value. I implemented an algorithm in Matlab which uses the built-in minimization function fsolve() and the Levenberg-Marquardt fitting algorithm. The algorithm minimizes the set of two quantities $[\delta_{\Re}(\tilde{n}), \delta_{\Im}(\tilde{n})]$ which I have defined as,

$$\begin{aligned} \delta_{\Re}(\tilde{n}) &= \left|\frac{\Delta\tilde{E}}{\tilde{E}}\right|^{-1} \left|\Re\left(\frac{\Delta\tilde{E}}{\tilde{E}} - \frac{\tilde{r}'(\tilde{n}) - \tilde{r}}{\tilde{r}}\right)\right|, \\ \delta_{\Im}(\tilde{n}) &= \left|\frac{\Delta\tilde{E}}{\tilde{E}}\right|^{-1} \left|\Im\left(\frac{\Delta\tilde{E}}{\tilde{E}} - \frac{\tilde{r}'(\tilde{n}) - \tilde{r}}{\tilde{r}}\right)\right|, \end{aligned} \tag{2.31}$$

where $\tilde{r}'(\tilde{n})$ is calculated by the model and $\Delta\tilde{E}/\tilde{E}$ is the experimentally measured changes in the THz field.

2.7 Model comparison

Finally, I present a comparison of the various models derived here. The example case is the a-axis and c-axis response of $YBa_2Cu_3O_{6.5}$ (YBCO 6.5) after MIR excitation along the c-axis. See Chapter 5 for the experimental details. YBCO is highly anisotropic; in the pseudogap phase, the optical response in the 0-3 THz range is dominated by extended Drude metal-like behavior [69] along the a, b-axes while the c-axis response is gapped. The penetration depth of the THz regime reflects this anisotropy. The pump penetration depth, $d = 0.7$ μm, is much higher than the THz probe in-plane, where the THz is effectively screened. Along the c-axis, however, the THz probes on order 10 times as deeply as the pump, putting the excitation well into the thin film limit.

We examine first the response in the bulk limit, shown in Figures 2.15 and 2.16. The multilayer model (Section 2.6.3) and the single layer model (Section 2.6.2) both reproduce the bulk response calculated from the Fresnel equations (Section 2.5.1). In Appendix A.3 I derive an approximate form of the multilayer model. This model also works well in the bulk limit. Figure 2.15 shows the optical conductivity calculated by these methods, and the residuals between these methods and the bulk response.

The analytical model, based on the approximate multilayer model, (Appendix A.4) over-exaggerates the response, while the thin film model (Section 2.5.2) under-reports the magnitude of the pump-induced changes to the optical response. The

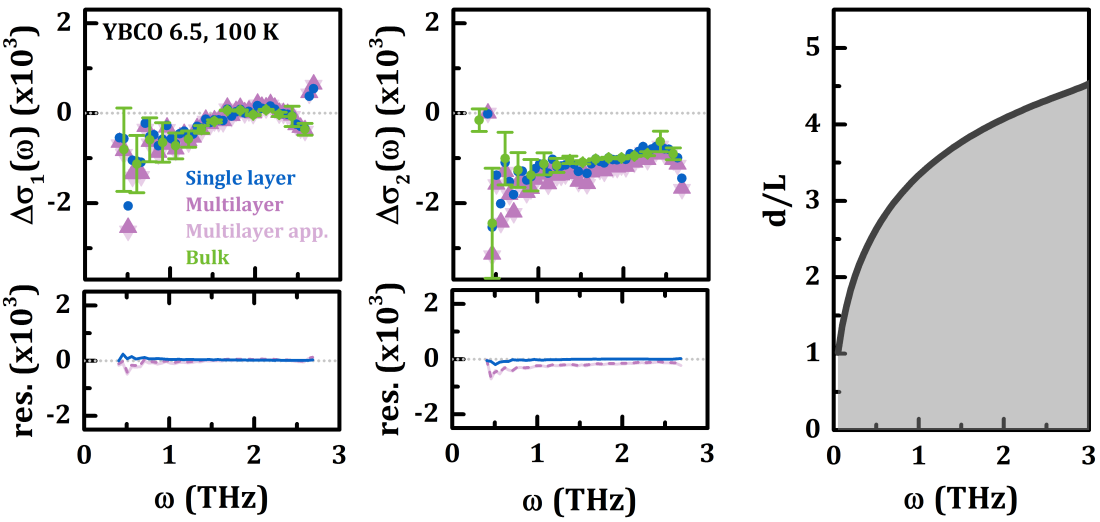

Figure 2.15: **Model comparison in the bulk limit: accurate models.** The a-axis response of YBCO 6.5 at 100 K after 15 μm excitation along the c-axis. The changes in the optical conductivity $\Delta\tilde{\sigma}(\omega) = \tilde{\sigma}(\omega) - \tilde{\sigma}_{\mathrm{eq}}(\omega)$ are shown in the left and center panels, as calculated by four models described in the main text. The residuals are plotted with respect to the response calculated with the bulk model (green dots). The penetration depth mismatch between pump d and probe $L(\omega)$ is plotted at right.

calculations using these methods, and their residuals with respect to the bulk response, are shown in Figure 2.16.

The thin film limit is shown in Figures 2.17 and 2.18. Here, the thin film model redeems itself. Both the single layer model and multilayer model also reproduce the response well. We find that in this limit, the approximations made to the multilayer model and the analytic solution both fail to capture the transient response, showing constant offsets from the single layer model response (plotted for comparison in Figure 2.18). The bulk model also fails to capture the transient response in this regime.

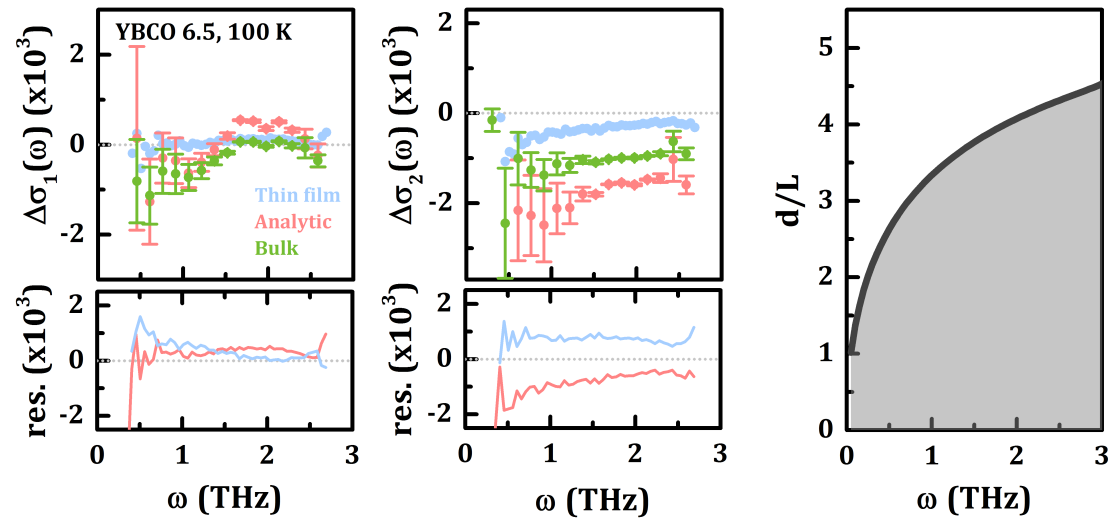

Figure 2.16: **Model comparison in the bulk limit: inaccurate models.** The a-axis response of YBCO 6.5 at 100 K after 15 μm excitation along the c-axis. The changes in the optical conductivity $\Delta\tilde{\sigma}(\omega) = \tilde{\sigma}(\omega) - \tilde{\sigma}_{\mathrm{eq}}(\omega)$ are shown in the left and center panels, as calculated by three models described in the main text. The residuals are plotted with respect to the response calculated with the bulk model (green dots). The penetration depth mismatch between pump d and probe $L(\omega)$ is plotted at right.

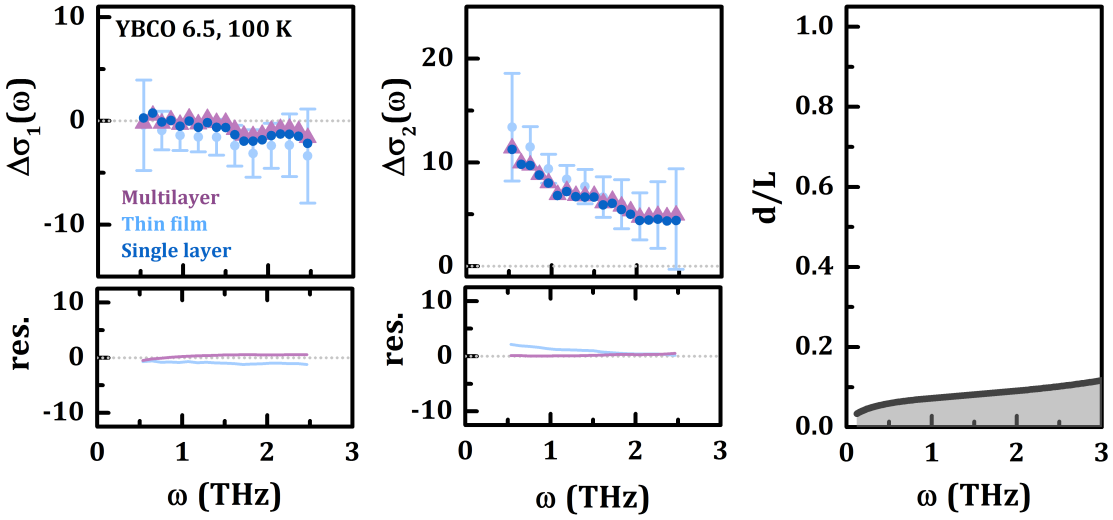

Figure 2.17: **Model comparison in the thin film limit: accurate models.** The c-axis response of YBCO 6.5 at 100 K after 15 μm excitation along the c-axis. The changes in the optical conductivity $\Delta\tilde{\sigma}(\omega) = \tilde{\sigma}(\omega) - \tilde{\sigma}_{\mathrm{eq}}(\omega)$ are shown in the left and center panels, as calculated by three models described in the main text. The residuals are plotted with respect to the response calculated with the single layer model (dark blue dots). The penetration depth mismatch between pump d and probe $L(\omega)$ is plotted at right.

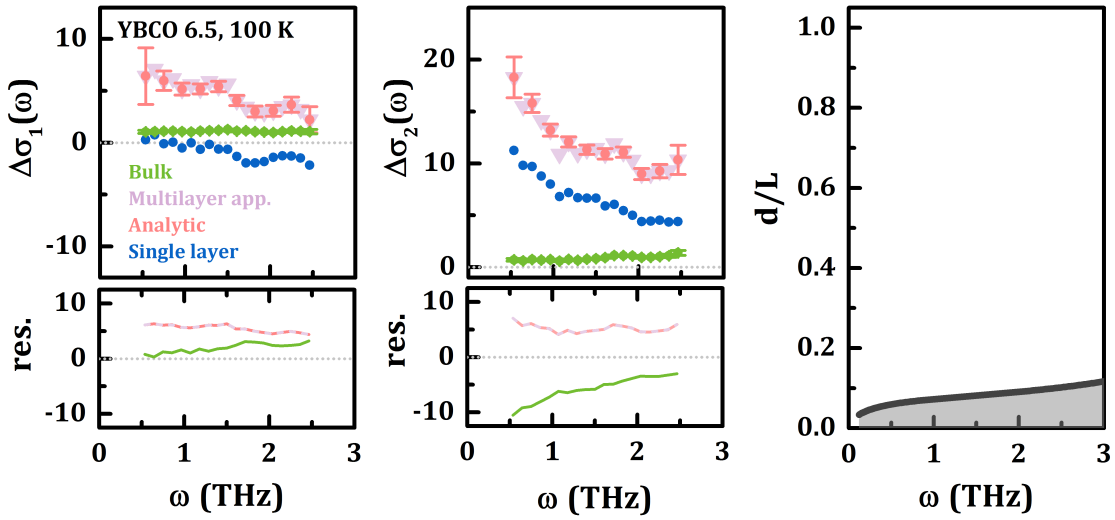

Figure 2.18: **Model comparison in the thin film limit: inaccurate models.** The c-axis response of YBCO 6.5 at 100 K after 15 μm excitation along the c-axis. The changes in the optical conductivity $\Delta\tilde{\sigma}(\omega) = \tilde{\sigma}(\omega) - \tilde{\sigma}_{\mathrm{eq}}(\omega)$ are shown in the left and center panels, as calculated by four models described in the main text. The residuals are plotted with respect to the response calculated with the single layer model (dark blue dots). The penetration depth mismatch between pump d and probe $L(\omega)$ is plotted at right.

Chapter 3

The Josephson plasma resonance

The Josephson plasma resonance (JPR) is one unique signature of superconductivity in the optical response of cuprates [70, 71]. The appearance and behavior of this plasma mode is intimately tied to the amplitude and phase of the superconducting order parameter and the coherence lengthscale of the condensate. In this chapter I will introduce the theoretical concept of the Josephson plasmon and present how this collective mode can be measured. The experiments described in Chapters 4, 5, and 7 use the physics of the Josephson plasmon to describe and interpret the transient states generated by optical excitation. In Chapter 5, I discuss more details of the equilibrium JPR in the context of the optical response of the cuprate superconductor $YBa_2Cu_3O_x$.

3.1 A stack of intrinsic Josephson junctions

Cuprates are organized as stacks of quasi two-dimensional (2D) superconductors, with pairs primarily occupying the Cu d-orbitals and O p-orbitals of the CuO_2 planes [72, 73]. The anisotropy of the system geometry means that while Coulomb interactions between carriers are three-dimensional (3D), electronic motion is confined to be mostly 2D. In the superconducting state, intrinsic Josephson coupling between CuO_2 planes along the c-axis allows full, 3D superconductivity [74, 75]. This Josephson tunneling between these planes produces, amongst other collective excitations [76], a longitudinal mode polarized along the c-axis. The organization of the $La_{1.8-x}Eu_{0.2}Sr_xCuO_4$ (LESCO x) lattice is illustrated in Figure 3.1. The illustration highlights the CuO_6 octehedra, in blue, with the CuO_2 planes bisecting their center in the ab-plane.

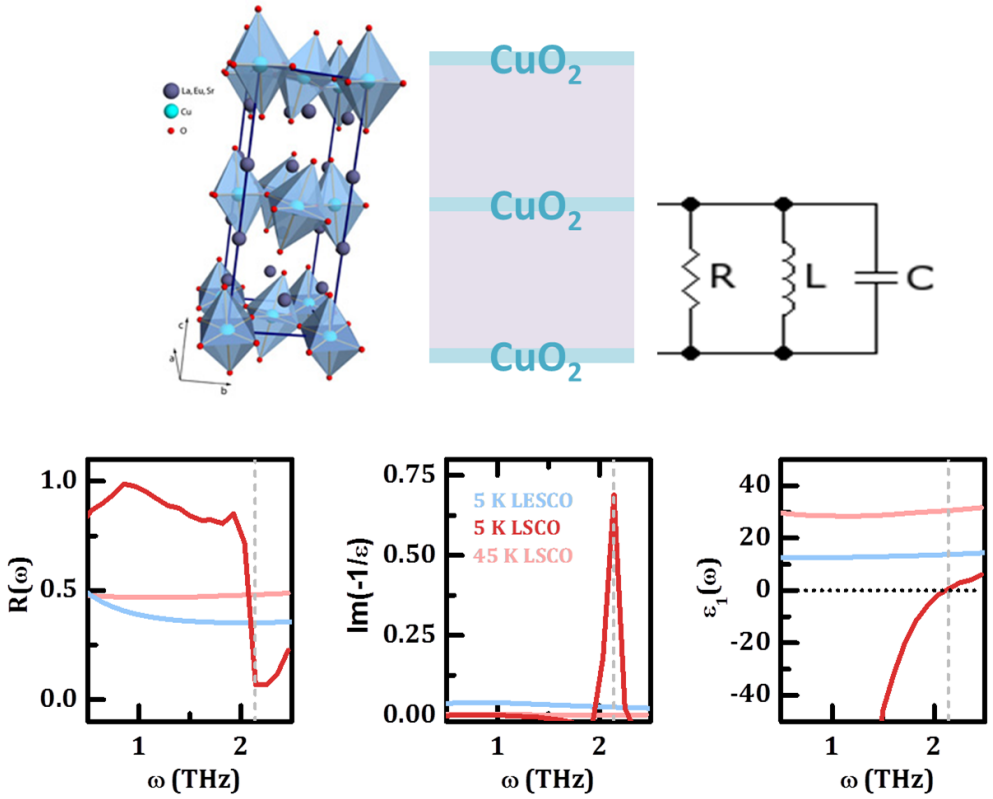

Figure 3.1: **The optical response due to a Josephson plasma mode. Top row:** The LESCO crystal structure (left) is organized as stacks of CuO_2 planes (illustrated at center). In the superconducting state, the crystal response is analogous to a stack of RLC circuits, with Josephson coupling providing the inductive channel. **Bottom row:** The Josephson plasma resonance appears as an edge in the optical reflectivity (left), a peak in the energy loss function $\Im(-1/\tilde{\varepsilon})$, and a zero crossing in the real dielectric response $\varepsilon_1(\omega)$.

The optical signature of a Josephson plasma mode is a c-axis reflectivity edge near the plasma frequency ω_p, as shown in the lower lefthand panel of Figure 3.1 for the near-optimally doped superconductor $La_{0.85}Sr_{0.15}CuO_4$ (red). The mode is also distinguishable in the energy loss function $\Im(-1/\tilde{\varepsilon}(\omega))$ as a peak in the response (center panel) and in $\varepsilon_1(\omega)$ as a zero crossing near the plasma frequency (right-hand panel).

The JPR frequency depends upon several factors, including the crystal geometry, superfluid density, and compressibility of the material [77]. However, within a single family of compounds, the relative position of the resonance can be related

to the superfluid density, $n_S \propto \omega_p^2$. Therefore as one approaches optimal doping, the resonance blue shifts as more carriers are available to condense.[1] The plasmon frequency falls in the 0-3 THz range for lanthanides. This frequency regime is free from other IR-active excitations, with the response remaining flat above T_c in superconducting compounds and featureless at all temperatures in non-superconducting LESCO 12.5% (see responses in pink and blue respectively in Figure 3.1).

The optical response for the Josephson plasmon can be described by the Lawrence-Doniach model for a Josephson junction between two 2D superconducting layers [74, 75]. The Josephson plasma resonance in cuprates can be modeled as a stack of 2D superconducting sheets [78], where Josephson coupling produces a resonant plasma mode with a dispersion,

$$\omega_p^2(\vec{k}, q) = \omega_{ab}^2 \left(\left(\frac{\lambda_{ab}}{\lambda_c} \right)^2 + \frac{k^2}{Q(q)^2 + \lambda_{ab}^{-2}} \right), \tag{3.1}$$

where $\vec{k}$ is the ab-plane wavevector and $-\pi \leq q \leq \pi$ is the dimensionless momentum along the c-axis, with $Q(q)^2 = 2(1 - \cos q)/L^2$, where L relates to the length of a single junction. The frequency $\omega_{ab} = c/\lambda_{ab}\sqrt{\varepsilon_0}$ is just the plasma frequency for a field in-plane and λ_{ab} (λ_c) is the in-plane (c-axis) penetration depth. In the limit that $q = 0$, Equation 3.1 reduces to that of a Josephson junction.

We will limit our discussion to the small $\vec{k}$ regime, $\vec{k} \to 0$. The dielectric function has the form,

$$\tilde{\varepsilon}_p = \tilde{\varepsilon}_c - \frac{\omega_p(q)^2}{\omega^2 - i\omega\Gamma}, \tag{3.2}$$

where for a bare plasmon, $\tilde{\varepsilon}_c$ is the high-frequency dielectric constant, $\varepsilon_\infty = 4.5$, a standard value for cuprates [79]. The response of a Josephson stack is analogous to that of a Drude metal, described by a single longitudinal mode. The effective mobility of the collective mode is described by Γ. In the original derivation for a Josephson stack, Γ is determined by thermally activated quasiparticles; however, generically, this term encompasses all processes that impact mobility along the c-axis. Fluctuations in the superconducting correlation length and time scale, for instance, have been shown to give rise to an effective Γ term near T_c in superconducting $La_{2-x}Sr_xCuO_4$ [80] and $Bi_2Sr_2CaCu_2O_{8+x}$ [81].

In the limit $\Gamma \to 0$, this equation gives rise to a pole at $\omega = 0$, which has a transverse polarized character and represents the "effective" condensate density

[1] This relationship is discussed in more detail in the context of $YBa_2Cu_3O_x$ in Section 5.3.1.

along the c-axis. The condensate density is effective in the sense that it comprises only those pairs that contribute to Josephson tunneling.

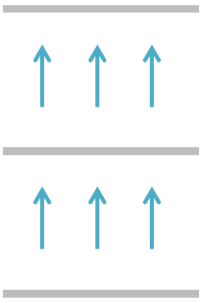

Figure 3.2: **Current flow across a stack of equivalent Josephson junctions.** The superconducting planes are depicted as grey lines, with the arrows depicting the direction of current flow. The longitudinal mode has $\vec{k} \perp$ planes and a zero frequency transverse "mode" with $\vec{k} \parallel$ planes describes the effective condensate along the perpendicular direction.

3.2 A stack of inequivalent junctions

If the stack of intrinsic junctions are not identical, then multiple Josephson resonances can form. Three distinct situations involving the formation of two resonances in $YBa_2Cu_3O_x$ will be encountered in this thesis.

1. The equilibrium $YBa_2Cu_3O_x$ crystal intrinsically has two plasma modes due to its bilayer structure. The response of only one mode, the interbilayer plasmon, is considered in Chapters 5 and 7. In Section 6.2, I will present the response of the higher frequency bilayer plasmon.

2. The transient blue shift of the interbilayer Josephson resonance which is seen below T_c is actually inhomogeneous, with a resonance also remaining near the equilibrium plasma frequency. (Discussed in Section 7.2.)

3. The transient plasmon induced above T_c splits into two modes as it relaxes. (Discussed in Section 7.3.)

Although the origin of the two plasmons is different in each case, their theoretical description is effectively the same. In this section, I will first introduce methods of modeling two inequivalent junctions. I will then show how a split resonance impacts the optical response when the geometry of the planes leads to an intrinsic splitting of the resonance, as in the case of bilayer cuprates.

3.2.1 Theoretical picture

Not long after this intrinsic Josephson plasma mode began to be understood, attention was drawn to the case of two inequivalent junctions [82]. $YBa_2Cu_3O_x$ was the first cuprate discovered to have a bilayer structure, naturally containing two inequivalent junctions. Compounds in the Bi, Tl, and Hg families can also contain two or more CuO_2 planes per unit cell. The simplest model for such a stack was proposed by van der Marel and Tsvetkov [82], effectively summing the junctions in series,

$$\tilde{\varepsilon} = \left(\sum_m \frac{z_m}{\tilde{\varepsilon}_m} \right)^{-1}, \tag{3.3}$$

where the weighting factor z_m is predominantly determined by the relative length of each junction. They described the normal state contribution to c-axis transport as a parallel component to the conductivity, $4\pi\tilde{\sigma}_0 = \Gamma_0$, replacing Equation 3.2 with the form,

$$\tilde{\varepsilon} = \varepsilon_\infty \left(1 - \frac{\omega_p^2}{\omega^2} \right) + \frac{i\Gamma_0}{\omega}. \tag{3.4}$$

For two junctions a and b, this yields a response [77],

$$\boxed{\frac{\varepsilon_\infty}{\tilde{\varepsilon}} = \frac{\omega^2 z_a}{\omega^2 - \omega_a^2 + i\omega\Gamma_a} + \frac{\omega^2 z_b}{\omega^2 - \omega_b^2 + i\omega\Gamma_b}.} \tag{3.5}$$

Immediately striking is the similarity between this response and that of two RLC circuits in series,

$$\frac{\varepsilon_\infty}{\tilde{\varepsilon} - \varepsilon_\infty} = \frac{\omega^2(\epsilon_\infty/4\pi C_a)}{\omega^2 - (1/L_a C_a) + i\omega\,(1/R_a C_a)} + \frac{\omega^2(\epsilon_\infty/4\pi C_b)}{\omega^2 - (1/L_b C_b) + i\omega\,(1/R_b C_b)}. \tag{3.6}$$

where the $\Gamma_{a,b}$ term describes the resistive channel. The relationship between the weight factors $z_{a,b}$ and the geometry of the junction becomes clear (recall that for a parallel plate capacitor with plates separated by a distance d, $C \propto 1/d$). In this

picture, the Josephson coupling can be thought of as an inductive coupling between planes.

The two junction case has two poles in the response, the zero frequency pole and a finite frequency transverse mode. This can be visualized by inverting Equation 3.5,

$$\frac{\tilde{\varepsilon}}{\varepsilon_\infty} = \frac{(\omega^2 - \omega_a^2)(\omega^2 - \omega_b^2)}{\omega^2(\omega^2 - \omega_T^2)}. \tag{3.7}$$

We've taken $\Gamma_{a,b} \to 0$ for clarity. The frequency of the transverse mode can be related to the longitudinal modes by $\omega_T^2 = z_b\omega_a^2 + z_a\omega_b^2$. The longitudinal and transverse modes can both be visualized in terms of the current flow across the junction, as depicted in Figure 3.3.

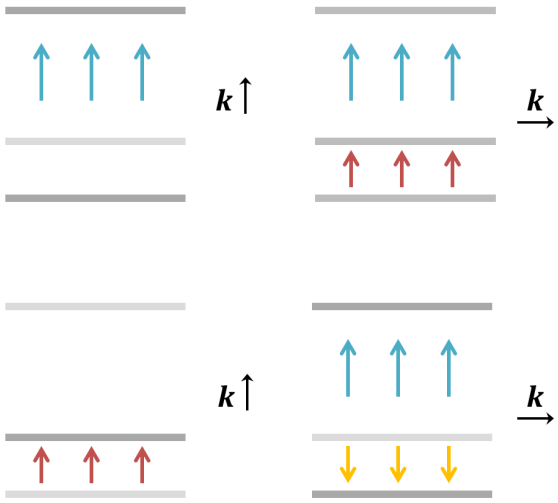

Figure 3.3: **Plasma modes of two inequivalent junctions.** The superconducting planes are depicted as grey lines, with the arrows depicting the direction of current flow. The shading of the lines is meant to represent the relative charging of the planes. **Left:** The two longitudinal modes have $\vec{k} \perp$ planes. **Right:** The two transverse modes with $\vec{k} \parallel$ planes. The top excitation is a zero frequency pole in the response, describing the effective condensate along the perpendicular direction. The lower mode is a finite frequency excitation that shares spectral weight with the zero frequency mode.

The two longitudinal modes are depicted as decoupled excitations; however they are generated by the response of coupled charge planes. We see how these modes arise by following the derivation of Equation 3.7 from Ref. [77] which starts from the Hamiltonian for the charge fluctuations on two inequivalent planes, $Q_{2m} = Q_2 e^{im\phi}$ and $Q_{2m+1} = Q_1 e^{im\phi}$, with periodic boundary conditions and with the addition of a Josephson coupling term $H_J = -\sum_m J_m^{m+1} \cos(\phi_m - \phi_{m+1})$,

$$H = -\sum_{m>n} \frac{|x_m - x_n|}{2C_0} Q_m Q_n + H_J. \tag{3.8}$$

The separation of planes m and n is $L|x_m - x_n|$ and the capacitance term is $C_0 = A/(4\pi L)$. The internal charge of plane m, $Q_m^i = Q_m - Q_m^e$, forms a conjugate variable with the Josephson phase of the plane, ϕ_m, giving the equations of motion,

$$\begin{aligned} \frac{\hbar}{2e}\frac{d\phi_m}{dt} &= \frac{\partial H}{\partial Q_m^i} \\ \frac{\hbar}{2e}\frac{dQ_m^i}{dt} &= -\frac{\partial H}{\partial \phi_m} \end{aligned} \tag{3.9}$$

These coupled equations can be diagonalized by recasting the charged planes in a new basis, $Q_a = Q_1 + Q_2$ and $Q_b = Q_1 + Q_2 e^{i\varphi}$. In this basis, we have separated out the voltage potential across junctions a and b, $V_a \propto z_a Q_a$ and $V_b \propto z_b Q_b$. Solving Equations 3.9, the charge response to an external charge Q^e is then,

$$\begin{aligned} Q_a^e &= \varepsilon_a Q_a, \quad \varepsilon_a = 1 - \omega_a^2/\omega^2, \\ Q_b^e &= \varepsilon_b Q_b, \quad \varepsilon_b = 1 - \omega_b^2/\omega^2, \end{aligned} \tag{3.10}$$

where the Josephson plasma frequency ω_i of junction $i = a, b$ can be related to the Josephson energies, J_i, of each junction,

$$\omega_i^2 = \left(\frac{2e}{\hbar}\right)^2 \frac{z_i J_i}{C_{av}}, \tag{3.11}$$

with the average capacitance defined as $C_{av} = A\varepsilon_{av}/4\pi L$. The average dielectric constant is a mixing of the dielectric constants of each junction, $\varepsilon_{i,0}$, such that $1/\varepsilon_{av} = x_a/\varepsilon_{a,0} + x_b/\varepsilon_{b,0}$. The relative weights for each junction are $z_i = x_i \varepsilon_{av}/\varepsilon_{i,0}$.

3.2.2 Josephson plasmon in bilayer cuprates

Because YBCO has a bilayer structure, with two CuO_2 planes per unit cell, the tunneling across each gap–the smaller *bilayer* and larger *interbilayer*–both determine the effective c-axis carrier density and thus the macroscopic superconducting behavior.

We have seen that two inequivalent Josephson junctions in series gives rise to a finite frequency transverse plasma mode. In equilibrium YBCO 6.5, this transverse mode appears as a broad peak in the Ohmic conductivity $\sigma_1(\omega)$ at about 400 cm^{-1} (12 THz). This mode shares spectral weight with the condensate at $\omega = 0$ [83]. The equilibrium broadband response of YBCO 6.5 at 5 K is shown in Figure 3.4 (grey lines) along with a fit to the two longitudinal Josephson plasma modes at 33 and 570 cm^{-1} (1 and 17 THz) using Equation 3.5 (red lines). The transverse mode is highlighted in blue, along with an arrow indicating the delta function distribution of the $\omega \approx 0$ condensate[2].

The Hamiltonian in Equation 3.8 is missing one term relevant for cuprates, the potential energy due to the electronic compressibility [77]. The compressibility leads to a mixing of the bare plasmons and, importantly, a reduction of the effective volume fraction of the short junction and a corresponding reduction in the magnitude and frequency of the transverse plasmon from what would be predicted from geometrical considerations alone.

Interestingly, there is evidence that Josephson coupling within the bilayer junction survives even above T_c. This is illustrated in Figure 3.5, with YBCO 6.5 at 60 K ($T_c = 51$ K). The fit is the same as that in Figure 3.4, but with the interbilayer plasma frequency $\omega_{IB} = 0$. The transverse mode still survives as long as the bilayer plasmon $\omega_B > 0$. A careful study of the transverse mode in a range of compounds $R\mathrm{Ba_2Cu_3O_x}$ (R = Y, Gd, Eu) [85] found a dome that extends deep into the pseudogap state in which bilayer coupling survives (see Figure 3.6). The existence of this regime indicates that even after global phase coherence is lost, the closely-spaced bilayer planes may retain local coherent coupling.

[2]The condensate would form a perfect London-like delta function distribution in the Ohmic conductivity, $\sigma_1(\omega) \propto n_S\delta(0)$ if there were no pair-breaking processes.

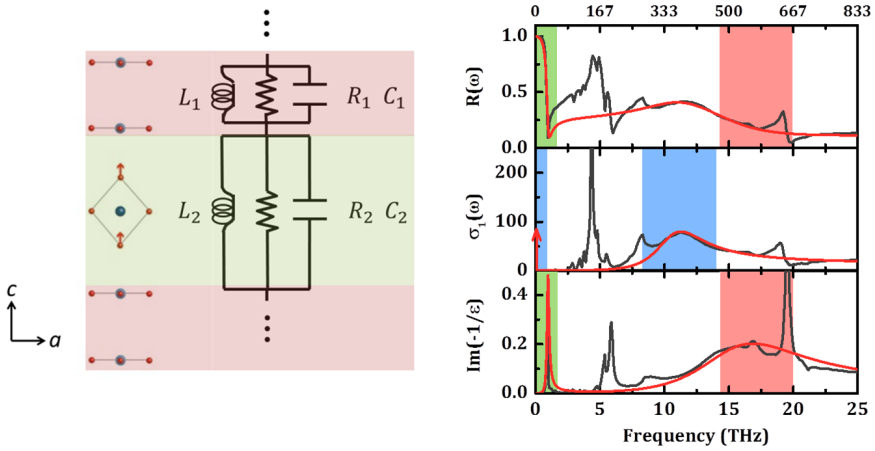

Figure 3.4: **The bilayer and interbilayer Josephson plasmons. Left:** The Cu (blue) and O (red) atoms of YBCO, organized into pairs of CuO_2 planes (pink) separated by an interbilayer gap (green). The coupling between planes can be considered using the analogy of an RLC circuit. **Right:** Calculations (red) of the bilayer and interbilayer tunneling contributions to the optical response of YBCO 6.5 (grey). The two peaks in the loss function $\Im(-1/\varepsilon)$ correspond to interbilayer Josephson tunneling (low frequency, green) and tunneling within the bilayer (high frequency, pink). A transverse plasmon appears as a peak in the Ohmic conductivity $\sigma_1(\omega)$ (blue) and shares spectral weight with the condensate at $\omega = 0$ (red arrow). Static YBCO 6.5 data from [84].

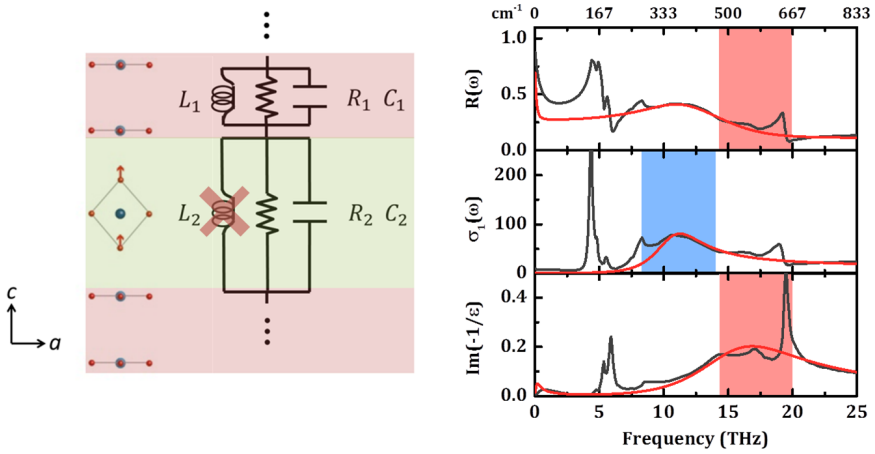

Figure 3.5: **The bilayer Josephson plasmon above T_c. Left:** To calculate the optical response, Josephson coupling across the interbilayer gap (green) is turned off above T_c, though tunneling within the bilayer (red) remains. **Right:** Calculations (red) of the bilayer and interbilayer tunneling contributions to the optical response of YBCO 6.5 (grey). Only one peak remains in the loss function $\Im(-1/\epsilon)$, corresponding to *intra*bilayer Josephson tunneling (high frequency, pink). The transverse plasma mode remains, though the condensate at $\omega = 0$ is fully depleted.

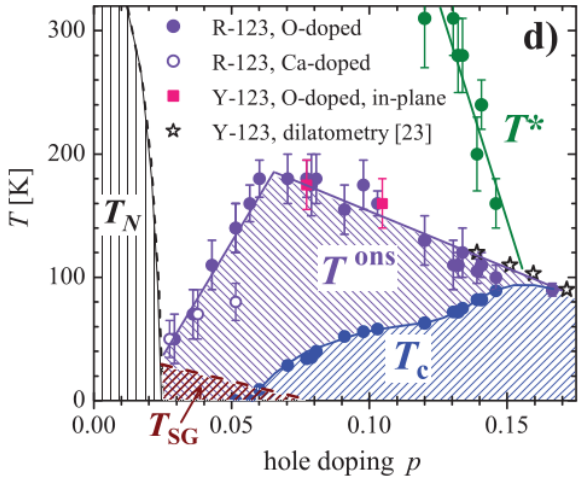

Figure 3.6: **Regime of bilayer coupling in R-123 compounds.** The regime beneath T^{ons} shows evidence of coupling within the bilayer.

Chapter 4

Generating Josephson coupling in $La_{1.675}Eu_{0.2}Sr_{0.125}CuO_4$ by the suppression of charge order

4.1 Introduction

In materials for which the electronic behavior is confined to be quasi two-dimensional, superconductivity is often found to lie in close proximity to various forms of charge order, for example in the BCS superconductor $2H$-$NbSe_2$ [86, 87], cuprates [88], and even certain organic compounds [89] and pnictides [90]. In cuprates, while the proximity of antiferromagnetic spin ordering was long understood to be ubiquitous across all families of compounds, evidence of charge ordering was found to be confined to a few materials, notably the lanthanum copper-oxides. Recently, the discovery of charge density wave behavior in $YBa_2Cu_3O_x$ [91] and then—all in the past year—in $Bi_2Sr_2CaCu_2O_{8+x}$ [92], $Bi_2Sr_{2-x}La_xCu_2O_{6+\delta}$ [93], and $HgBa_2CuO_{4+\delta}$ [94], has established that the charge ordering instability is in fact a generic feature of cuprates.

However, the nature of the interplay between superconductivity and charge order remains a subject of much debate. Superconductivity in cuprates is thought to be supported in two-dimensional CuO_2 planes and made three dimensional by Josephson tunneling between planes. Both in-plane and out-of-plane coherence can be strongly affected by ordering of charges and spins, which also organize within the CuO_2 planes. Small perturbations in doping, applied field, or pressure can tune the energy landscape between orders, suppressing or supporting the superconducting state.

This phase competition is especially dramatic in the lanthanum copper oxides, which exhibit striped spin and charge-ordered states, typically stabilized by an underlying lattice distortion [95, 96]. Static stripe order was first discovered in $La_{1.6-x}Nd_{0.4}Sr_xCuO_4$ (LNSCO x) [88, 97] and has since been detected in $La_{2-x}Ba_x$-

CuO_4 (LBCO x) [98, 99] and $La_{1.8-x}Eu_{0.2}Sr_xCuO_4$ (LESCO x) [23, 100]. Charge stripes are associated with the suppression of superconductivity in this family of compounds, with bulk superconductivity completely destroyed at $x = 1/8$ (12.5%) doping [101, 102], where the lattice spacing and charge order enter into lock-step and charge stripes develop at every fourth CuO_2 plaquette. This is illustrated in the top part of Figure 4.1, with the copper and oxygen atoms depicted in blue and red respectively and yellow highlighting indicating the plaquettes that host the charge stripes.

Recent theoretical [103–105] and experimental [15, 102, 106] work suggests that this suppression is not due to simple competition between orders, but instead that superconductivity may coexist with charge stripes. In this framework, charge ordering imposes a space dependence on the superconducting order parameter phase [104]. The spatial modulation—often referred to as a "pair density wave" state—suppresses the total Josephson tunneling by disruptive interference [105]. Stripes in neighboring planes alternate between alignment along the a and b crystallographic axes, and aligned stripes in next-nearest planes shift by half a period to reduce Coulomb interactions (see Figure 4.1) [106]. This stripe orientation effectively quadruples the unit cell to four CuO_2 planes, with Josephson coupling only possible between every fourth plane. Two-dimensional superconducting fluctuations would still be supported, and 3D superconductivity achieved below the temperature at which the superconducting c-axis coherence length exceeds the quadrupled unit cell spacing.

This assessment is supported by susceptibility [102] as well as resistivity and thermopower [106] measurements which suggest a fluctuating 2D superconductivity regime survives in the spin order state, up to $T_{SO} = 40$ K in LBCO 12.5%, and 1D correlations persist up to the charge order transition, $T_{CO} = 54$ K. Scanning tunneling spectroscopy and angle-resolved photoemission also detect evidence of fluctuating superconductivity throughout the charge ordered regime [107].

Using mid-infrared (MIR) excitation, Fausti, *et al.* [33] showed that it was possible to generate c-axis interlayer coupling reminiscent of Josephson coupling in LESCO 12.5%. The transient THz response is characterized by the appearance of a plasma mode near the Josephson plasma resonance of related superconducting compounds. The MIR light targets a phonon mode associated with stretching of the Cu-O bonds in the CuO_2 planes, and they posited that the excitation was distorting the lattice structure of the compound, destabilizing the charge and spin stripes and restoring superconducting coupling. The effect was detected up to 10-20 K, near the spin order transition temperature.

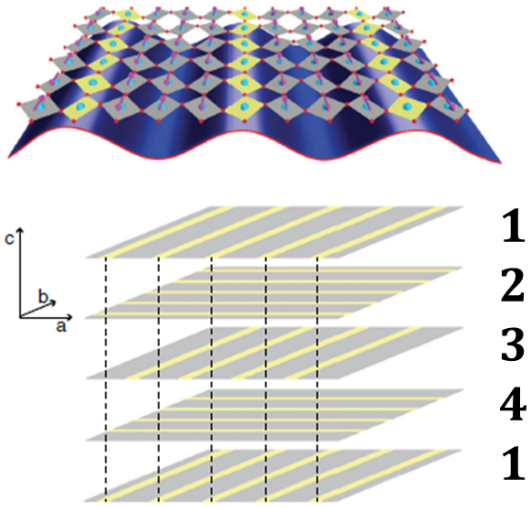

Figure 4.1: **Charge ordering along the c-axis of lanthanides. Top:** The CuO_2 planes of LESCO with the LTT distortion. Cu atoms are in blue and O in red. Arrows indicate the spin alignment between charge stripes, which are illustrated as yellow plaquettes. At $x = 1/8$ doping, the periodicity of the stripes syncs with every fourth CuO_2 plaquette. **Bottom:** The grey sheets represent a stack of CuO_2 planes and the yellow lines indicate the location of the charge stripes. The charges alternate alignment between the a and b axes, with the stripe location moving two lattice spacings in next-nearest planes to reduce Coulomb interaction between stripes. Figure adapted from Ref. [32].

The same MIR excitation was found to cause a suppression of charge stripe order in LBCO 12.5%. The magnitude of the charge ordering peak, measured with soft x-ray scattering (SXR) at the Linac Coherent Light Source (LCLS), was promptly reduced by ∼60% within the 300 fs resolution of the experiment [32]. The lattice structure, however, was only weakly modified and the distortion occurred much more slowly, over a 15 ps timescale, suggesting the *electronic* suppression of stripes, rather than the lattice distortion, is key to the formation of the transient coupling measured by Fausti *et al.*

In this project we examine in more detail this light-induced plasma mode, taking a careful look at the temperature and timescales of the transient state. Most of the results reported here have been published in Ref. [34]. We find that coherent interlayer coupling can in fact be generated up to the charge-order transition $T_{CO} \approx 80$ K, far above the equilibrium superconducting transition temperature of

any lanthanide cuprate. The relaxation kinetics of the interlayer coupling support the assignment of Josephson coupling as the origin of the transient plasmon.

Two key observations are extracted from the relaxation. First, the plasma mode relaxes through a collapse of the carrier coherence length and not the carrier density. Second, two distinct kinetic regimes are observed for this relaxation, above and below spin-order transition $T_{SO} \approx 25$ K. In particular, the temperature-independent relaxation rate observed below T_{SO} is anomalous and may indicate coexistence of superconductivity and stripes rather than competition. Both observations support arguments that a low temperature coherent stripe (or pair density wave) phase suppresses c-axis tunneling by disruptive interference rather than by depleting the condensate. Preliminary results extending this study to LESCO $x < 1/8$ will be presented that suggest the transient coupling is enhanced as $x \to 1/8$.

4.2 Experimental design and methods

4.2.1 The $La_{1.8-x}Eu_{0.2}Sr_xCuO_4$ phase diagram

$La_{1.8-x}Eu_{0.2}Sr_xCuO_4$ (LESCO x) has a tetragonal crystal structure consisting of stacks of CuO_6 octehedra, spaced by the La, Eu, and Sr atoms. The lattice undergoes a structural transition at ∼130 K [108], transitioning from the "high temperature tetragonal" phase, in which the octehedra are vertically aligned along the c-axis, and entering the "low temperature tetragonal" (LTT) phase, in which the octehedra become canted. The structural and electronic phase diagram of LESCO is shown in Figure 4.2. The black line tracks the LTT distortion temperature. The LTT phase crystal structure is illustrated in Figure 4.3.A and the canting is depicted in Figure 4.3.B.

In both LNSCO and LBCO, the transition to static charge stripe order occurs at the same temperature as the onset of the LTT phase [98], whereas in $La_{2-x}Sr_xCuO_4$ (LSCO x), the LTT phase is never realized and static charge stripes fail to develop. This might suggest that the LTT distortion drives static stripe formation. However, LESCO throws a wrench into that picture, with the LTT distortion occurring nearly 50 K above the charge ordering temperature (blue line in Figure 4.2). While the LTT distortion certainly plays a role in stabilizing stripes, the charge order transition appears to be ultimately determined by electronic factors.

Strong spin fluctuations are found throughout the charge ordered state [109, 110], and static spin stripes form at a lower temperature, about $T_{SO} = 25$ K for LE-

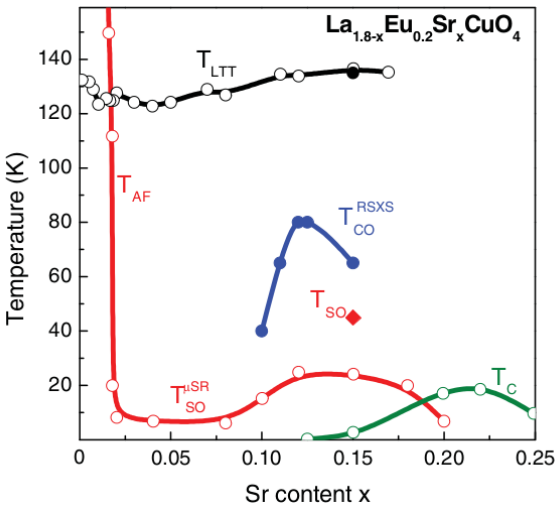

Figure 4.2: **Electronic and structural phase diagram of $\mathbf{La_{1.8-x}Eu_{0.2}Sr_xCuO_4}$.** Phase diagram from Ref. [108].

SCO 12.5% [100, 108] (see red line in Figure 4.2). Superconductivity is completely suppressed at 12.5% doping. The single crystals measured in this experiment were confirmed to be non-superconducting down to 5 K by resistivity and magnetization measurements. Hard X-ray diffraction and Hall coefficient measurements show the appearance of the static stripe ordering below 80 K [33].

4.2.2 Phonon pumping

The low temperature tetragonal (LTT) phase of LESCO has D_{4h}^{16}-$P4_2/ncm$ symmetry and four IR-active E_u modes associated with the motion of its CuO_6 octahedra [111]. We targeted the Cu-O stretching mode along the a-axis[1], which has a resonant frequency at 20.5 THz (14.5 μm wavelength). This mode is illustrated in Figure 4.3.C. The crystal was excited at normal incidence with ~300 fs mid-infrared (MIR) pulses with a central frequency at ~15 μm, polarized along the crystallographic a-axis. The MIR spectrum is plotted in Figure 4.4 along with the a-axis optical conductivity $\sigma_1(\omega)$, which peaks at the mode resonance frequency.

[1]Note that the a- and b-axes are equivalent in the LTT phase.

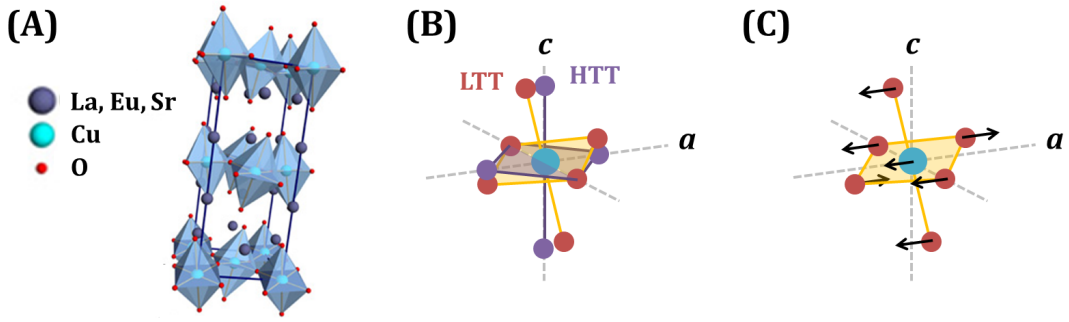

Figure 4.3: **Phonon pumping of the CuO_2 planes in LESCO.** **(A)** The crystal structure of LESCO in the LTT phase. Figure by Jörg Harms. **(B)** Illustration of the LTT distortion of the CuO_6 octehedra. **(C)** Illustration of the atomic motion of the CuO_6 octehedra due to the Cu-O stretching mode.

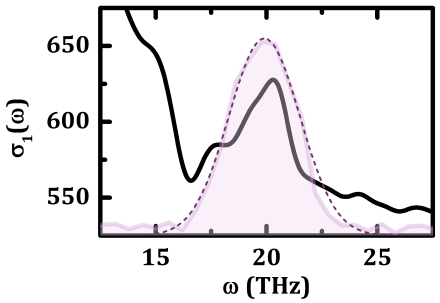

Figure 4.4: **The mid-infrared pump spectrum and the phonon resonance.** The pump spectrum (purple) fit by a Gaussian (dotted line) with a beam waist of $\sigma = 1.6$ THz. The Ohmic conductivity $\sigma_1(\omega)$ (black) is plotted in units of $1/\Omega$-cm. The conductivity peaks at the Cu-O stretching mode resonance.

4.2.3 Probing with time-domain THz spectroscopy

The optically excited sample was probed with time-domain THz spectroscopy as described in Chapter 2. Single cycle THz probe pulses were generated via 800 nm excitation of a photoconductive antenna. The time resolution of the experiment was limited by the THz bandwidth to about 300 fs. The experiment was performed with THz pulses *s*-polarized (TE) along the *c*-axis at 30° angle of incidence. The low frequency spectral cutoff was limited by the sample size and day-to-day alignment to between 0.2 and 0.4 THz.

4.2.4 Calculation of the transient optical response

The equilibrium optical reflectivity of LESCO 12.5% was measured by Fourier transform infrared spectroscopy (FTIR) up to 9000 cm^{-1} and by time-domain THz spectroscopy between 1 and 2.5 THz by Fausti, *et al.*. The reflectivity below 7 THz has been fit with a simple single Lorentzian oscillator model of the conductivity, which explicitly maintains Kramers-Kronig consistency.

The THz probe samples a crystal volume on order 100 times greater than the 15 μm pump. The full transient optical response of the photo-excited volume alone was calculated by modeling the system as an excited surface on an unperturbed bulk, following the procedure described in Chapter 2 (see Figure 4.6). Both the single layer model and multilayer model produce equivalent results (see Appendix B.1). The transient optical response calculated from the single layer model is reported in the following sections.

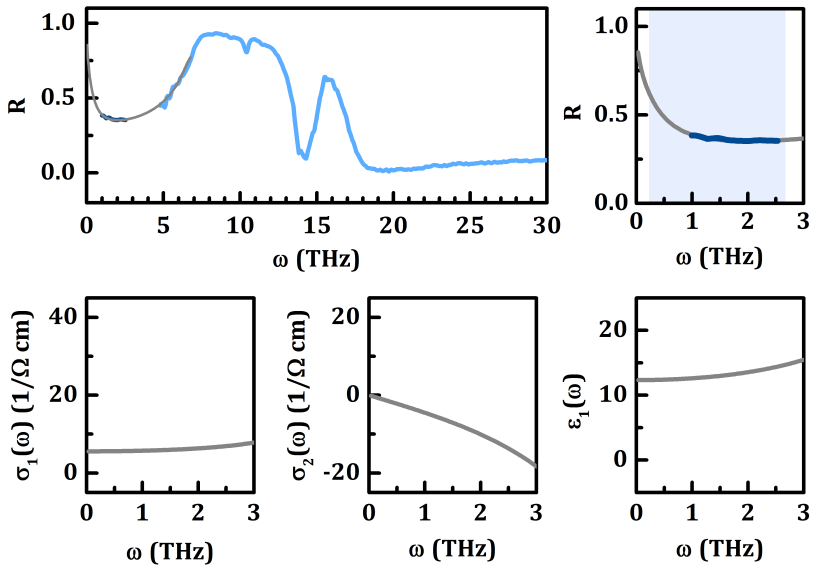

Figure 4.5: **The low frequency THz response in equilibrium. Top row:** The broadband (left) and low frequency (right) reflectivity of LESCO 12.5%. The broadband (light blue) and THz (dark blue) was measured by Fausti, *et al.* (See supplemental material of Ref. [33].) A fit to the low frequency spectrum (grey) models the conductivity with a single Lorentzian oscillator. The spectral range probed in the present study is indicated by the shaded region of the right-hand figure. **Bottom row:** Low frequency conductivity $\sigma_1(\omega) + i\sigma_2(\omega)$ and real part of the dielectric function $\varepsilon_1(\omega)$ modeled by the Lorentzian oscillator.

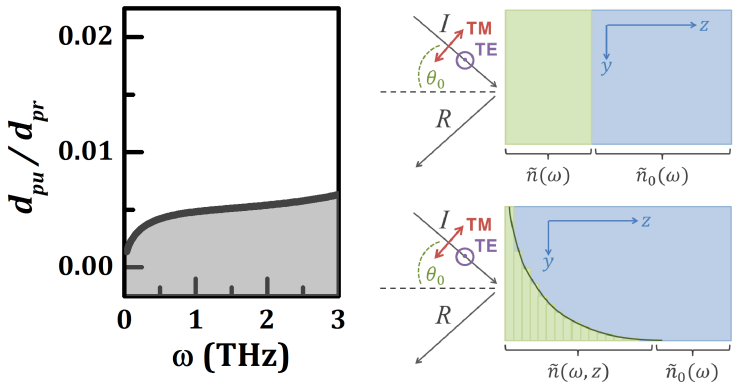

Figure 4.6: **Pump-probe penetration depth mismatch. Left:** The ratio between the pump penetration depth $d_{pu} = 85$ nm and the probe penetration depth d_{pr} of LESCO 12.5% in the range from 0 to 3 THz. **Right:** Illustrations depicting the two models used to calculate the full transient optical response at the surface of the crystal.

4.3 Restoration of c-axis coupling

4.3.1 Generation of a transient plasma mode

Figure 4.7 summarizes the primary results of Ref. [33]. Upon optical excitation, a transient plasma mode develops, as measured by the appearance of a reflectivity edge in the reflected THz field $\tilde{E}(\omega)$, $\Delta r/r \equiv |(\tilde{E}(\tau,\omega) - \tilde{E}(\omega))/\tilde{E}(\omega)|$. This mode is located near the frequency of the equilibrium Josephson plasma resonance (JPR) mode of superconducting lanthanides. Note that the small 0.1% change in the raw reflectivity can be ascribed to the high pump-probe penetration depth mismatch. The plasma mode is shown in Panel 4.7.A at 10 K. The mode could be detected up to between 10-20 K.

The JPR magnitude, ΔR, measured as the difference between the maximal and minimal reflectivity changes, scales with the log of the fluence, $\Delta R \propto \ln(F/F_{sat})$, where F_{sat} is the fluence above which the optical response would reach saturation. Panel 4.7.B shows the fluence dependence at three pump wavelengths. The amplitude of the raw ΔR response more than doubles between 1 mJ/cm^2 of 15 μm excitation (the fluence used in Panel 4.7.A and throughout the main text of Ref. [33]) and 4 mJ/cm^2, the highest fluence measured. A quantitative analysis of the full optical

response would be required to determine if the increase in the size of the signal can be accounted for by a stiffening of the plasma mode. However, this trend may also be a result of inhomogeneous excitation, due to inhomogeneity of the sample itself. Even the most pristine cuprate materials exhibit inherent spatial variation in their equilibrium properties, including the superconducting order parameter [112].

The magnitude of the plasma edge was also found to track the Cu-O stretching mode resonance. Panel 4.7.C plots $1/F_{sat}$ at several wavelengths, illustrating that the saturation fluence is optimal at resonance.

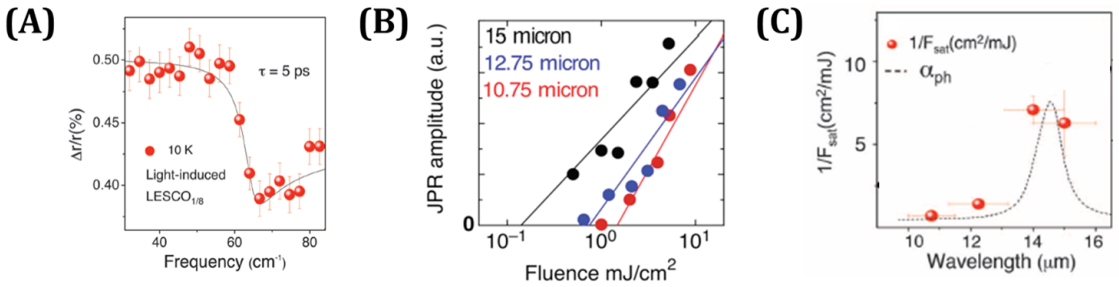

Figure 4.7: **Resonant behavior of the transient plasmon. (A)** A transient plasmon induced in LESCO 12.5% at 10 K after 15 μm excitation at a fluence of 1 mJ/cm^2. The raw reflectivity, $\Delta r/r \equiv |(\tilde{E}(\tau = 5 \text{ ps}) - \tilde{E})/\tilde{E}|$ is shown at 5 ps after excitation. **(B)** The fluence dependence of the JPR amplitude for three pump wavelengths. **(C)** The saturation fluence shows resonance behavior with the Cu-O stretching mode frequency, indicated as a Gaussian (dashed line). Figures adapted from Ref. [33].

4.3.2 Transient c-axis coupling throughout the charge order regime

The transient plasmon was reported in Ref. [33] to persist up to 10-20 K, near the spin ordering temperature $T_{SO} \approx 25$ K. We now report the observation of the same mode throughout the charge order (CO) regime [34]. Figure 4.8.A shows the phase diagram of LESCO, with the SO+CO region highlighted in red and the CO region in blue. The three dots on the phase diagram indicate the three temperatures at which the transient change in reflectivity $|\Delta\tilde{E}(\omega)/\tilde{E}| = |(\tilde{E}(\tau,\omega) - \tilde{E}(\omega))/\tilde{E}(\omega)|$ is plotted

in Panels 4.8.B. A transient plasma mode, like that reported in Figure 4.7.A, can be seen at 5 K (red, Figure 4.8.B.1) and 30 K (blue, B.2), above the spin ordering temperature. The spectrum above T_{CO}, which is featureless and increasing with frequency, is shown in Panel 4.8.B.3 at 100 K. Panel 4.8.C shows the temperature dependence of the edge height ΔR at the peak of the transient response. The edge was measured up to 65 K, near the charge order transition $T_{CO} \approx 80$ K.

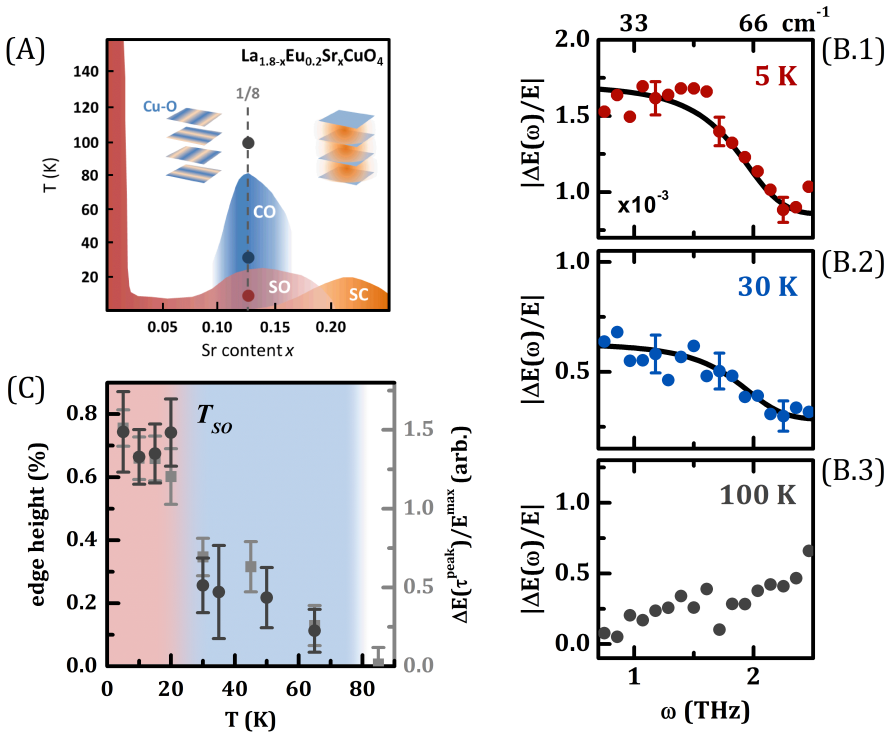

Figure 4.8: **The transient plasma mode throughout the charge order regime. (A)** Phase diagram of LESCO, based on Ref. [108], indicating regions of bulk superconductivity (SC) and static spin (SO) and charge (CO) order. The static stripes suppress c-axis coupling of the CuO_2 planes (inset cartoon, left), with bulk superconductivity restored at dopings in which the stripe order is reduced (inset cartoon, right). **(B)** The raw transient reflectivity changes measured 1.8 ps after MIR excitation. At 5 K **(B.1)** and 30 K **(B.2)**, an edge is apparent at 1.5-2 THz. The black lines indicate the reflectivity spectrum (rescaled) due to a longitudinal plasma mode, shown as a guide to the eye. Above the charge-ordered transition temperature T_{CO} no edge is observed [shown at 100 K; **(B.3)**]. **(C)** The size of the reflectivity edge (dark grey circles) and the change in the THz amplitude $E(\tau^{peak})/E^{max}$ (light grey squares) as a function of temperature. This figure adapted from Ref. [34].

Note that the size of the plasma edge is ∼0.7% at 10 K, much larger than that reported in Ref. [33]. We attribute the ability to detect the plasmon above T_{SO} to improvements in the experimental apparatus[2] and to an increase in pump fluence, which for all measurements reported here is ∼4 mJ/cm^2.

We define another quantity that is useful in characterizing the transient response, the normalized transient changes in reflectivity,

$$\frac{\Delta E(\tau)}{E^{max}} = \frac{E(\tau, t^{max}) - E_{\rm eq}(t^{max})}{E_{\rm eq}(t^{max})}, \tag{4.1}$$

measured at the maximum amplitude of the THz response, $E^{max} = E_{\rm eq}(t^{max})$. The peak change in reflectivity, at time delay τ^{peak}, is plotted in Panel 4.8.C (light grey). This quantity, $\Delta E(\tau^{peak})/E^{max}$, which represents a mix of frequencies, tracks the size of the reflectivity changes and completely disappears above T_{CO}.

We now address the full transient optical response. Figures 4.9 and 4.10 show the peak of the optical response of LESCO 12.5% at at five temperatures, below (red) and above (blue) the spin-order transition $T_{SO} \approx 25$ K. In both regimes, the transient response (dots) is characterized by the appearance of a longitudinal plasma mode at ∼1 THz. This mode is most clearly discerned in the real dielectric response $\varepsilon_1(\omega)$, shown in the top row of Figure 4.9, which exhibits a zero crossing near the mode resonance. The highest temperature at which the longitudinal mode could be seen in $\varepsilon_1(\omega)$ in the THz spectral window was 65 K. The Ohmic conductivity $\sigma_1(\omega)$ is only weakly affected by the pump, maintaining a gapped response (bottom row of Figure 4.9), suggesting the pump is not producing significant quasiparticle excitations.

The dashed black lines in Figures 4.9 and 4.10 represent a fit to a single longitudinal Josephson plasma mode, which we saw in Chapter 3 has the Drude form,

$$\tilde{\varepsilon}(\omega) = \tilde{\varepsilon}_c - \frac{\omega_p^2}{\omega^2 - i\omega\Gamma}. \tag{4.2}$$

where $\tilde{\varepsilon}_c = \tilde{\varepsilon}_{\rm eq}$, the equilibrium dielectric function[3].

[2] Particularly, improvements in the THz focusing and signal-to-noise can be attributed to moving the THz generation and detection to a vacuum environment. See Chapter 2 for a discussion of the experimental design.

[3] An additional small, flat increase in $\sigma_1(\omega)$ may be the result of either a slight quasiparticle heating or a phonon reshaping, either of which primarily modifies frequencies beyond our THz range. An additional constant term has been added to account for this effect, however it does not impact the best-fit values of ω_p or Γ. See Ref. [34], including supplementary material.

The advantage of the Drude formalism is that it includes just two free parameters, ω_p and Γ. Within this model, the scattering rate term Γ encompasses all transient processes that impact the mobility along the c-axis. Fluctuations in the superconducting correlation length and time scale, for instance, have been shown to give rise to an effective Γ term near T_c in superconducting LSCO x [80] and $Bi_2Sr_2CaCu_2O_{8+x}$ [81]. At resonance, transport occurs across the CuO_2 planes with a velocity $2\omega_p L$, where L is the CuO_2 plane separation. The rate can be related to the coherence length d of the c-axis plasma by $d = 2\omega_p L/\Gamma$.

The transient response is best fit by $\omega_p = 2.45$ THz (1.65 THz) at 5 K (30 K) with a scattering rate of $\Gamma \approx 0.25$ THz. Note that the reflectivity edge and the zero crossing of $\varepsilon_1(\omega)$ do not appear exactly at the plasma resonance, ω_p, but are shifted due to decoherence, as well as other higher frequency intra- and interband contributions to $\varepsilon_{1,\mathrm{eq}}$ which can be captured in the THz regime by a single parameter $\varepsilon_{\mathrm{FIR}}$. For long coherence (or scattering) lengths, $d \to \infty$, the zero crossing occurs

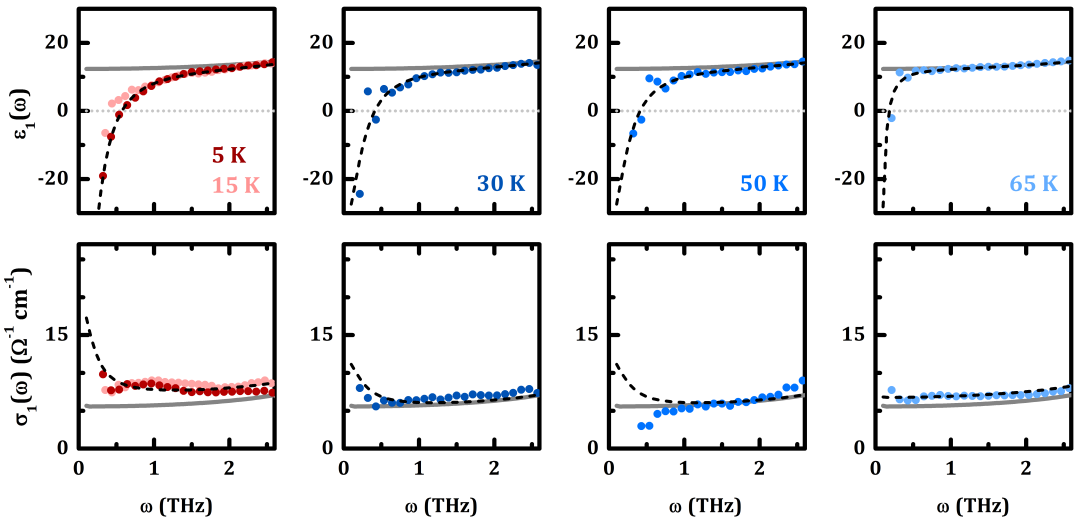

Figure 4.9: **The transient plasmon generated in LESCO 12.5% at 5 temperatures.** Upon MIR excitation, LESCO 12.5% develops a high-mobility state, shown here at the peak of the response (dots). The transient plasmon is characterized by a zero crossing in the real part of the dielectric function, $\varepsilon_1(\omega)$ **(top row)**. The real conductivity $\sigma_1(\omega)$ **(bottom row)** remains gapped, showing only minimal signs of quasiparticle heating at lowest temperatures. The dashed lines are a fit to Equation 4.2, as described in the text. The left-hand column shows a fit to the response at 5 K.

near the screened frequency $\tilde{\omega}_p = \omega_p/\sqrt{\varepsilon_{\rm FIR}}$ and shifts to the red as d decreases. If $\Gamma > \tilde{\omega}_p$, the zero crossing is entirely lifted. For the plasma mode $\tilde{\omega}_p$ reported here, we take $\varepsilon_{\rm FIR} = 30$, a standard value for cuprates [113].

The inductive conductivity, $\sigma_2(\omega)$, which is negative in equilibrium (grey line) and approaches zero as $\omega \to 0$, instead increases towards low frequency in the photoexcited state (bottom row of Figure 4.10). The response turns positive below 0.75 THz at 5 K, 0.5 THz at 30 K, and 0.3 THz at 65 K. At the peak of the response, the conductivity change, $\Delta\sigma_2(\omega) = \sigma_2(\omega) - \sigma_{2,\rm eq}(\omega)$, scales as $1/\omega$, as shown by the dotted line in Figures 4.10. This divergent behavior is the hallmark of a high mobility state.

The $1/\omega$ divergence of $\Delta\sigma_2(\omega)$ corresponds to Equation 4.2 in the limit $\Gamma = 0$ ($d \to \infty$). The London equations give a conductivity of the same form, with the superconducting component of the inductive conductivity $\omega\sigma_2 \propto n_S$. For the c-axis response of a cuprate, only the portion of the superfluid density n_S that contributes

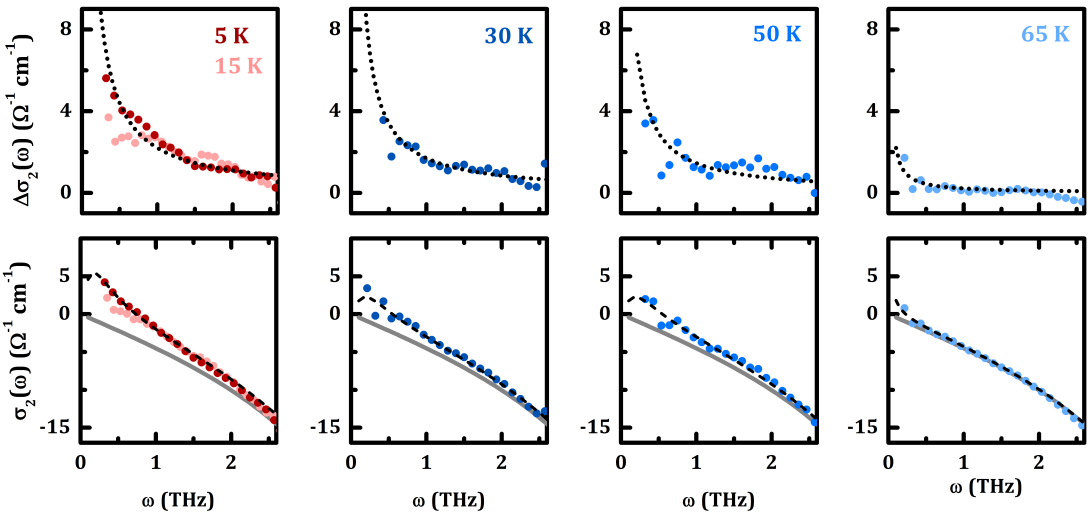

Figure 4.10: **The transient inductive conductivity of LESCO 12.5% at 5 temperatures.** The appearance of the transient plasmon is accompanied by a divergent behavior in the transient component of the inductive response, $\Delta\sigma_2(\omega) = \sigma_2(\omega) - \sigma_{2,\rm eq}(\omega)$ **(top row)**. A fit to $1/\omega$ is shown as a dotted line. The total inductive conductivity $\sigma_2(\omega)$ **(bottom row)** goes positive at lowest frequencies. The dashed lines are a fit to Equation 4.2 (the same fit shown in Figure 4.9).

to Josephson tunneling produces the divergent behavior, with $\omega\Delta\sigma_2(\omega) \propto \omega_p^2 \propto n_S$. See Chapter 5.3.1 of this thesis for a more detailed description of the equilibrium low frequency c-axis optical response of a cuprate superconductor.

Taking $\omega\Delta\sigma_2(\omega)$ as a rough measure for the magnitude of the transient response, we find that the plasmon seems to disappear somewhere around 70 K. The response was fit in two ways, shown in Figure 4.11. First a simple linear fit, which crosses $\omega\Delta\sigma_2(\omega) = 0$ at 67 $\pm$ 14 K. In the spirit of the parallel with superconductivity, mean field fits of the type $\sqrt{1 - T/T'}$ were also employed for the SO+CO and CO regions, with T' values of 26 K and 66 K respectively. While the first value corresponds well to T_{SO}, the second temperature scale is a bit lower than T_{CO}. It may be that this temperature scale is underestimated, reflecting the fact that the $1/\omega$ divergence at 65 K sets in primarily below the THz frequency window (< 0.2 THz).

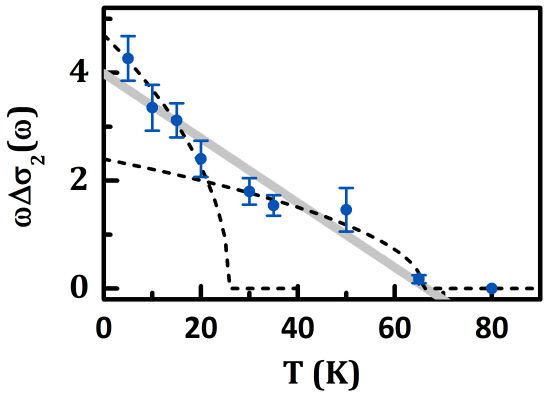

Figure 4.11: **The temperature dependence of the inductive response.** The inductive response at early times is characterized by a relatively flat $\omega\Delta\sigma_2(\omega)$. The maximum $\omega\Delta\sigma_2(\omega)$ at each temperature, averaged over the frequency regime in which the response remains flat, is shown here (blue dots) up to 80 K. The response is fit in two ways. A simple linear fit (grey line) of all values below 80 K suggests $\omega\Delta\sigma_2(\omega) \to 0$ at 67 $\pm$ 14 K. A second set of fits assumes mean field behavior $\omega\Delta\sigma_2(\omega) \propto \sqrt{1 - T/T'}$ (dashed lines). Below T_{SO}, the fit uses $T' = 26$ K and for $T_{SO} < T < T_{CO}$, $T' = 66$ K.

4.4 Mid-infrared excitation of $La_{1.8-x}Eu_{0.2}Sr_xCuO_4$, $x < 1/8$

While the same overall trends in the transient response are seen at lower dopings, the magnitude of the response, characterized by the plasma frequency ω_p^2, is greatly reduced. Figures 4.12 and 4.13 show the response of LESCO 8% and 10% respectively at 5 K. In both compounds, the Ohmic conductivity $\sigma_1(\omega)$ is virtually unchanged. The inductive conductivity $\sigma_2(\omega)$ shows a small diverging increase, corresponding to the generation of the plasmon and the drop in $\varepsilon_1(\omega)$. The dielectric function does not cross zero within the THz frequency window, which was limited by the sample size and THz focal area to 0.5 THz.

As a preliminary measure of the plasmon, we fit to Equation 4.2 in the limit that $\Gamma = 0$. The strength of the transient plasmon, $\omega\Delta\sigma_2(\omega) \propto \omega_p^2$, is plotted as a function of doping x in Figure 4.14. The plasmon is sharply dependent on doping, rising dramatically at $x = 1/8$. Future investigations at $x > 1/8$ would be required to conclude whether the transient effect peaks with the charge and spin order parameters, or perhaps tracks the "suppressed" superconducting dome that survives in LSCO and other cuprates.

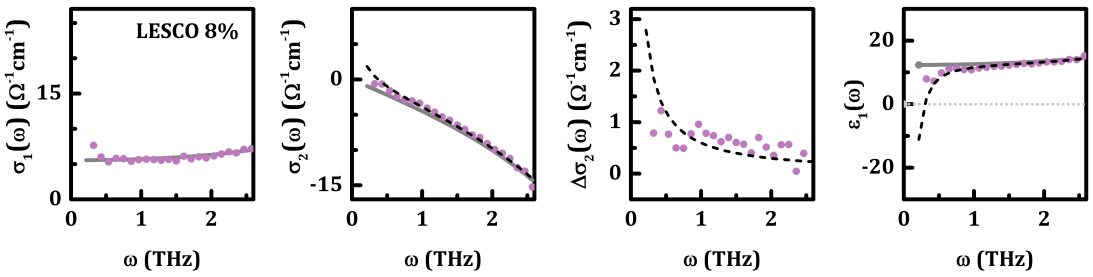

Figure 4.12: **Transient optical response of LESCO 8% at 5 K.** From left to right: The Ohmic conductivity $\sigma_1(\omega)$, the inductive conductivity $\sigma_2(\omega)$, the transient changes to the inductive conductivity $\Delta\sigma_2(\omega) = \sigma_2(\omega) - \sigma_{2,\mathrm{eq}}(\omega)$, and the real part of the dielectric response $\varepsilon_1(\omega)$. Dashed lines are fits to a single longitudinal mode, as described in the main text.

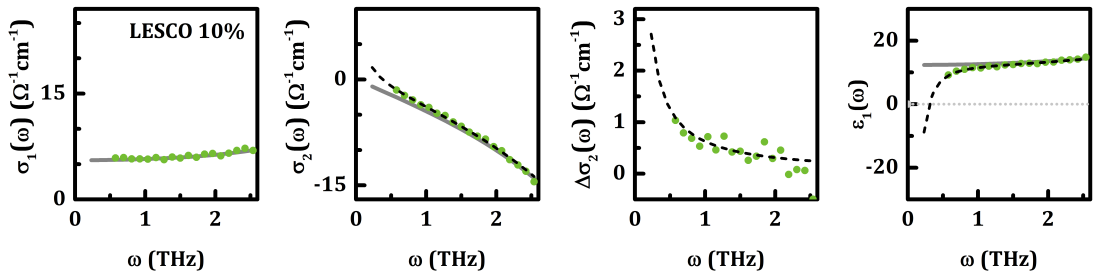

Figure 4.13: **Transient optical response of LESCO 10% at 5 K.** From left to right: The Ohmic conductivity $\sigma_1(\omega)$, the inductive conductivity $\sigma_2(\omega)$, the transient changes to the inductive conductivity $\Delta\sigma_2(\omega) = \sigma_2(\omega) - \sigma_{2,\mathrm{eq}}(\omega)$, and the real part of the dielectric response $\varepsilon_1(\omega)$. Dashed lines are fits to a single longitudinal mode, as described in the main text.

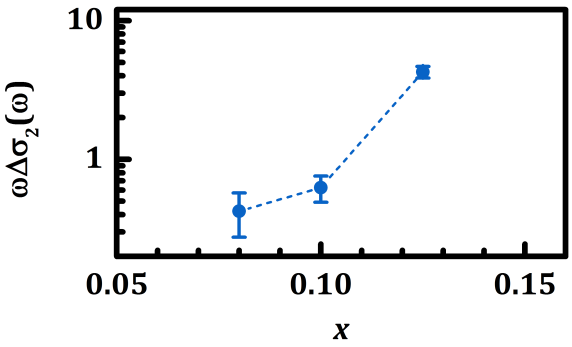

Figure 4.14: **Doping dependence of the inductive response at 5 K.** The inductive response $\omega\Delta\sigma_2(\omega)$, expressed in units of THz/Ω-cm, rises towards $x = 1/8$, the highest doping measured. This doping corresponds to the peak of the charge and spin ordering parameters.

4.5 Two temperature regimes for the relaxation of the transient plasmon

The relaxation pathway of the transient mode is determined in part by the equilibrium ground state it emerges from. Studying the evolution of the mode after excitation can therefore reveal something about how these states compete. Two ground states give rise to the plasma mode: spin and charge stripes below T_{SO}, and

charge stripes above. I will now present a quantitative analysis of the relaxation pathway of the transient state of LESCO 12.5% in both regimes.

Figure 4.15 shows the transient inductive conductivity and loss function at several delays after excitation. Figure 4.16 shows the corresponding time evolution of $\varepsilon_1(\omega)$ at 5 K (A.1), 35 K (A.2), and 65 K (A.3). Fits to the optical response using Equation 4.2 are used to extract the time evolution Γ, expressed as a coherence length d (Panel 4.16.B), and the screened plasma mode $\tilde{\omega}_p$ (C). After the transient state is formed, both quantities initially decay following a 2 ps (1 ps) time scale at 5 K (35 K). At longer time delays, the plasma frequency stabilizes to a finite value, indicating that the carrier density does not reduce significantly throughout the relaxation. Rather, the decay of the plasma mode is characterized by a dramatic decrease in the correlation length from ∼15 unit cells (10 nm) to zero.

The relaxation time scales are also captured by the changes in reflectivity measured at the peak of the THz field, $\Delta E(\tau)/E^{max}$, which could be measured with finer delay steps. Figure 4.17.A shows $\Delta E(\tau)/E^{max}$ as a function of pump-probe delay τ. Two lifetimes could be extracted, shown in blue in Figure 4.17.B. The lifetimes measured from the coherence length decay are shown in red for comparison. In both the spin-ordered and charge-ordered regimes, the time scales of the double exponential decay are commensurate with the decay of the coherence length. Both lifetimes exhibit two distinct regimes. Below T_{SO} , the lifetimes remain temperature independent. Above T_{SO}, where only static charge order remains, the lifetime drops exponentially with base temperature.

The exponential dependence of the relaxation between $T_{SO} < T < T_{CO}$ can be reconciled with the expected kinetic behavior for a transition between two distinct thermodynamic phases separated by a free energy barrier. This is quantitatively captured by the slope of the logarithmic plot in Figure 4.17.B, which reflects an activated relaxation of the type $\exp(-E_{\text{barrier}}/k_B T)$. From a double exponential relaxation with lifetimes τ_1 and τ_2, we extract an energy scale E_{barrier} ∼40 K (4 meV) and 9 K (0.8 meV), respectively. Interestingly, this energetic regime corresponds to the energy scale of strong spin fluctuations measured in LSCO 12.5% [114–116] and in LBCO 12.5% [117], suggesting that the transition between the two phases may be regulated by spin rearrangements. This would be consistent with the temperature regime of strong spin fluctuations, which develop abruptly below T_{CO} and persist to T_{SO} [109, 110]. The departure from activated behavior for $T < T_{SO}$ may therefore be related to the freezing out of spin fluctuations.

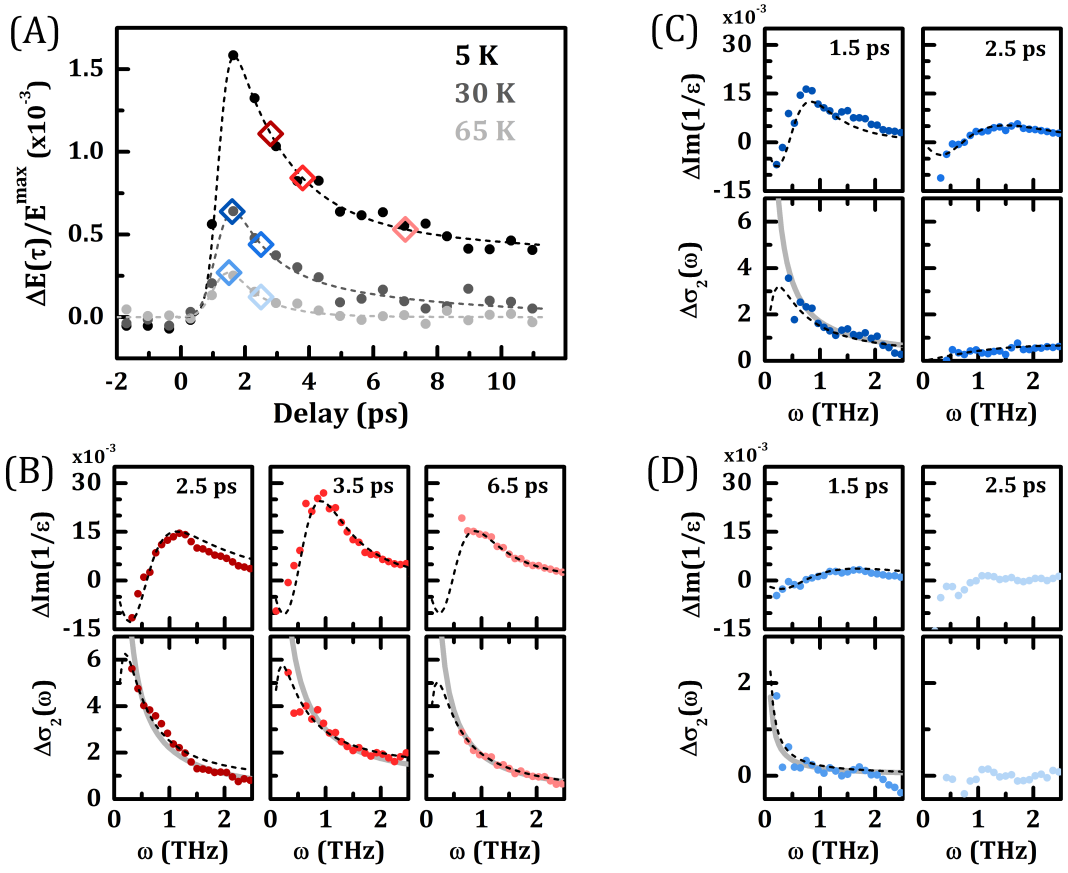

Figure 4.15: **The time evolution of the transient plasmon.** **(A)** One dimensional traces of $\Delta E(\tau)/E^{\mathbf{max}}$ as a function of delay time after excitation τ. Dashed lines indicate a double exponential fit, described in the main text. Diamonds indicate the time delays shown in Panels (B)-(D). The transient changes in the energy loss function $\Delta\Im(-1/\varepsilon)$ and inductive conductivity $\Delta\sigma_2(\omega)$ are shown at **(B)** 5 K, **(C)** 30 K, and **(D)** 65 K. Grey lines indicate a $1/\omega$ fit and black dashed lines show a fit to Equation 4.2.

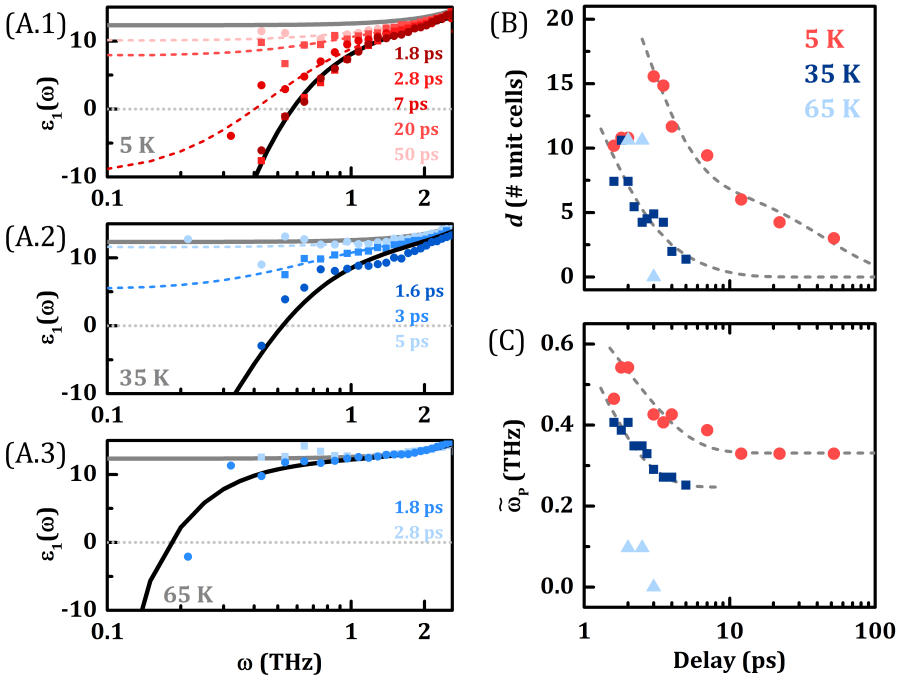

Figure 4.16: **The relaxation of the transient plasmon. (A)** The real dielectric function $\varepsilon_1(\omega)$ (alternating circle and square dots) as a function of pump-probe delay at 5 K **(A.1)**, 35 K **(A.2)**, and 65 K **(A.3)**. The response is fit with a single longitudinal mode, as described in the main text (solid black and dashed lines). The drop in coherence length causes a flattening in the low frequency $\varepsilon_1(\omega)$. **(B)** The c-axis coherence length of the transient plasma as a function of delay for three temperatures: 5 K (circles), 35 K (squares), and 65 K (triangles). The length is expressed in units of the CuO_2 plane spacing. The decay can be fit with a double exponential (dashed lines) with time constants 2 ps (1 ps) and 45 ps (4 ps) at 5 K (35 K). **(C)** The plasma frequency $\tilde{\omega}_p = \omega_p/\sqrt{\varepsilon_{\mathrm{FIR}}}$ redshifts at early times, decaying to a constant value following single exponential (dashed lines) of 2 ps (1 ps) at 5 K (35 K). Figure adapted from Ref. [34].

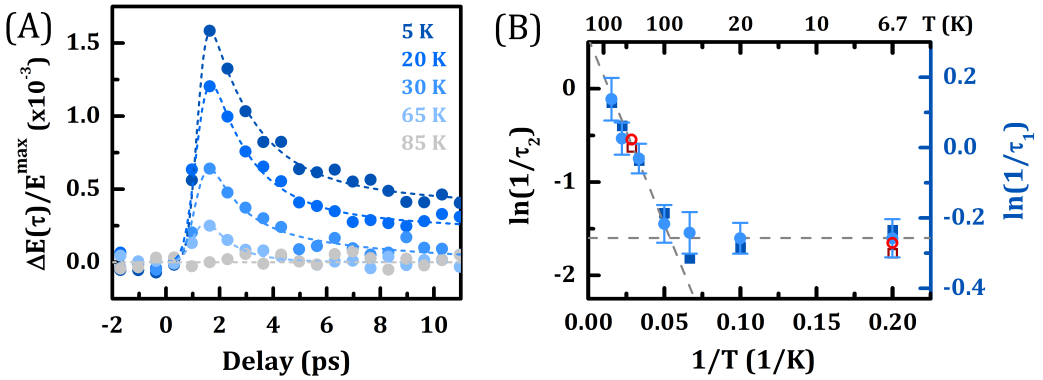

Figure 4.17: **Two kinetic regimes for the relaxation of the transient state.** **(A)** The time profile of the transient state as a function of pump-probe delay. The vertical axis indicates the transient change of the peak of the THz probe field. For clarity, each point shown represents an average of ten delay measurements. The lifetime of the transient state was extracted using a double exponential fit (dashed lines), with each exponential given roughly equal weight, 50% ± 10%. **(B)** An Arrhenius plot of the relaxation rate as a function of temperature. The short lifetime τ_1 (dark blue squares) and the long lifetime τ_2 (light blue circles) track the decay of the coherence length of the transient plasma. Lifetimes used in the fits shown in Figure 4.16 are plotted in red. The lifetime of the transient state remains temperature independent (horizontal grey dashed line) below the spin- order transition temperature, $T_{SO} \approx 25$ K. Above this transition, the lifetime exhibits an exponential temperature dependence, with an energy scale of 4 meV for τ_2 and 0.8 meV for τ_1 (grey dashed line). Figure adapted from Ref. [34].

4.6 Mid-infrared c-axis excitation of $La_{1.675}Eu_{0.2}Sr_{0.125}CuO_4$

The pump wavelength dependence of the transient plasmon indicates that it is resonant to the excitation of the planar Cu-O stretching mode. However, Nicoletti, *et al.* [15] have shown that a transient plasmon can be induced in charge- and spin-ordered LBCO with c-axis excitation at 800 nm, suggesting that resonant excitation is just one method of generating transient coupling. In Appendix B.2, I show preliminary results that the same excitation appears to generate a plasmon in LESCO 12.5% as well. With all this in mind, I attempted c-axis excitation at 15 μm pump wavelength. Along the c-axis, there is no resonant mode at 15 μm, as illustrated in Figure 4.18.

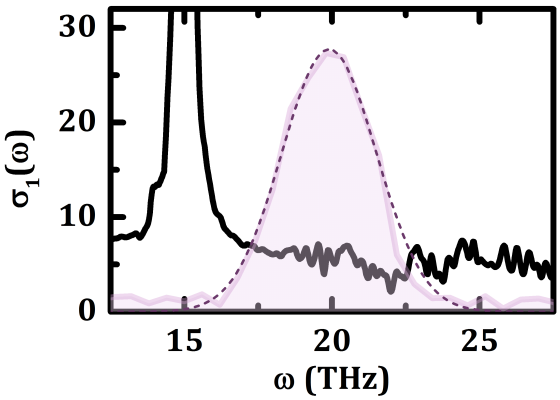

Figure 4.18: **The mid-infrared pump spectrum and the c-axis Ohmic conductivity.** The pump spectrum (purple) fit by a Gaussian (dotted line) with a beam waist of $\sigma = 1.6$ THz. The Ohmic conductivity $\sigma_1(\omega)$ (black) is plotted in units of $1/\Omega$-cm. The conductivity shows no resonant mode at 15 μm (20 THz).

Figure 4.19 shows the c-axis response after MIR excitation. We find that there is no pump-probe response in the THz range. The fluence of the pump, $\sim$4 mJ/cm^2, is higher than that used for 800 nm excitation; however, this energy is distributed over a volume 10 times as large since the penetration depth along the c-axis is 5 μm for 20 THz excitation. So the lack of response may perhaps be due to the excitation

being insufficient to completely suppress stripe order, as in the case of LBCO 12.5% after 800 nm excitation [15].

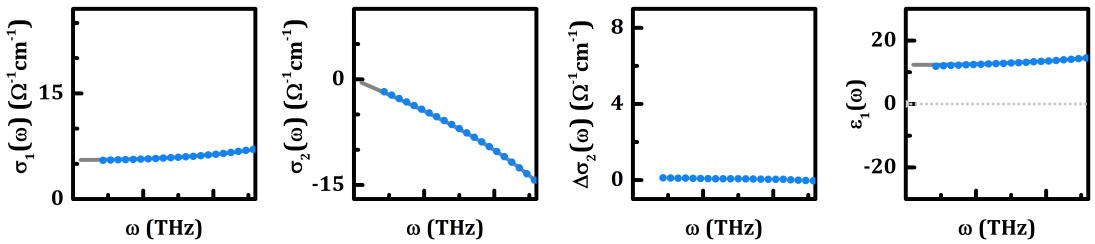

Figure 4.19: **Transient response of LESCO 12.5% after c-axis MIR excitation.** The transient response (dots) shows no change from the equilibrium response (grey) after c-axis MIR excitation.

4.7 Discussion of these results

The origin of a plasma mode at such low frequency with an anomalously high mobility, $\Gamma << \omega_p$, requires some careful consideration. The transient plasmon was initially identified by Fausti *et al.* [33] as a Josephson plasma mode. This is an exciting interpretation, because if true, it lends strong credence to the pair density wave picture of stripe competition. And these newest results would suggest that the lanthanides, long relegated to the lowest T_c's of the copper oxide materials, may in fact have "hidden" superconducting pairing that survives up to the ∼100 K regime of their cuprate brethren. Before considering this interpretation, I will examine some alternative ideas in the context of the data presented in the preceding sections.

The most intuitive picture would perhaps be that of quasi-particle excitation. We can immediately rule out any significant contribution to the transient state from incoherent quasi-particle heating, for example from excitations of the reststrahlen band, which for the optically gapped ground state of LESCO would result primarily in an increase in $\sigma_1(\omega)$ in the 0-3 THz range. While a small excitation of this kind might account for the slight increase in $\sigma_1(\omega)$ observed at low temperatures, such

incoherent excitation could not, in any event, account for the appearance of a narrow THz frequency plasmon and the accompanying divergent $\sigma_2(\omega)$.

A sharp Drude-like mode at THz frequencies is seen in some materials, notably in doped semiconductors. In principle, transient quasi-particle "doping" at similar levels as the condensate density of superconducting lanthanides could produce a plasma mode in this frequency range. The photoinduced state emerges out of a charge ordered ground state that gaps out the same regions of Fermi surface as the superconducting condensate [107], and one could envision that, absent superconducting pairing, the destruction of charge order might cause these carriers to become highly mobile quasi-particles.

However, the relaxation pathway of the mode we observe does not support this interpretation. The transient plasma mode relaxation is driven by a decrease in coherence, plotted in Figure 4.16.B as the decay of the coherence length d or, equivalently an *increase* in the effective scattering rate Γ of Equation 4.2. In contrast, the generalized Drude plasmon produced by excited quasi-particles in doped semiconductors has been found to relax through a depletion of the carrier density $\propto \omega_p^2$, at constant scattering [118, 119] or with a *decrease* in the scattering rate [120, 121].[4]

A sliding charge density wave (CDW) state [122–124] could be a more exotic explanation for the plasmon, where the pump acts to de-pin the charge stripes and the Γ term accounts a pinning rate that increases as the system relaxes. This would be corroborated by the observation that, at least on the underdoped side, the transient high mobility state is most enhanced at dopings where charge ordering is strongest. A sliding CDW was recently observed in the manganite compound $La_{0.5}Ca_{0.5}MnO_3$, where the sliding occurred along the a-axis, corresponding to the reciprocal lattice vector a^* of the CDW superstructure wavevector [124]. However, a c-axis sliding CDW, or an a-axis sliding state producing the c-axis mode, remains an intriguing but unlikely scenario. Equilibrium generation of a sliding CDW state in this compound, for example through electronic depinning of charge order in the vein of Ref. [124], would lend further support to such an interpretation.

The labeling of the plasmon as a Josephson mode was motivated by several observations. First and most apparent, the mode appears at a frequency commensurate with the Josephson plasmon in superconducting LESCO and other related lanthanides. There are no other equilibrium IR active excitations in this frequency regime. As a plasma mode generated by pair tunneling, the transient state reported

[4]The decrease in scattering rate may be attributed to the decrease in scattering pathways available as the excited quasiparticles lose energy.

here corresponds to a condensate density of roughly half that of near-optimal doped $La_{1.85}Sr_{0.15}CuO_4$ in equilibrium.

Second, recent theoretical models [104, 105, 125] support the idea that superconductivity and charge order competition is not a simple battle between instabilities, but in fact coexist together, even in the absence of bulk 3D superconductivity. The temperature-independent relaxation rate below T_{SO} would be compatible with quantum coherent tunneling between two states, for instance between superconducting and pair density wave phases at constant carrier density. In this picture, Cooper pairing would be superimposed or intertwined [126–128] with the stripe phase, where the dynamical destruction of stripes allows a finite Josephson current rather than driving pairing directly. Indeed, as discussed in Ref. [33], the prompt timescale of the appearance of the longitudinal mode renders it unlikely that the optical excitation is causing pair formation [8] but rather suggests that pairing in the planes persists in equilibrium.

Most recent discussion of the pair density wave has focused on intertwined order between charge stripes and superconductivity, neglecting the role of spin ordering [126]. Experimental evidence for two-dimensional superconductivity fluctuations in the stripe phase, however, has primarily been found below T_{SO} [102, 106]. The observation here of transient coupling between T_{SO} and T_{CO} lends support, then, to the pair density wave picture and the important role of charge order in suppressing T_c. The reduced strength of the coupling we find above T_{SO} may help explain why other probes are less sensitive to this order in this temperature regime.

Chapter 5

Manipulating superconductivity with phonon pumping in underdoped $YBa_2Cu_3O_x$

5.1 Introduction

Increasing the superconducting transition temperature T_c of cuprate materials has been a long-standing goal, ever since this family of compounds was discovered to have overcome the T_c limits imposed by BCS electron-phonon coupling. Tuning chemical doping, applied pressure or strain, and external magnetic field are some of the most common ways to manipulate T_c in an adiabatic (equilibrium) manner. Changing these parameters may promote superconductivity directly, for example by increasing the pair density with chemical doping. Or they may instead target a competing order, for example by favoring charge order over superconductivity under an applied field.

Superconductivity in underdoped $YBa_2Cu_3O_x$ (YBCO x) lies in close proximity to the so-called pseudogap phase, a partially gapped state that has long defied theoretical explanation—including whether or not this state is in fact a true *phase* with an accompanying order parameter. The problem is not a dearth of theory, but rather nearly 30 years of strong and compelling theoretical and experimental work that mainly falls into two competing categories of interpretation [129].

The first is that the pseudogap state is in fact a competing regime, with its own hidden order, that robs the condensate and suppresses T_c. Theoretical pictures have focused on how holes dope the parent Mott state [130, 131], with emergent behavior generally tied to the CuO_2 plane geometry [132, 133]. The earliest proposed model of the pseudogap is the resonating valence band (RVB) picture, first developed by P. W. Anderson in 1987, in which the CuO_2 planes host a frustrated lattice of antiferromagnetically coupled spin singlets [134–136]. This idea is the basis of a recently proposed "Amperean pairing" mechanism [128]. Another class of theories

propose the spontaneous generation of circulating currents [137–139], which break various combinations of time-reversal, rotational, and translational symmetries. A nematic phase which breaks rotational symmetry [140], electronic liquid crystal phases [141], and other forms of spatially segregated charge and spin order [142], have also been put forward.

Experimentally, distinguishing between these scenarios is difficult. Some of these proposed phases are found to only occupy a portion of the pseudogap. There is evidence of broken time reversal [143, 144] and rotational [133, 140, 145] symmetry developing at the onset temperature of the pseudogap. So far no theoretical approach has conclusively encapsulated the rich and complex phenomenology reported across the pseudogap regime.

The second interpretation is that the pseudogap is not in fact a distinct phase, but rather, arises in connection with phase fluctuations of the superconducting order parameter, which survive after the bulk condensate is depleted. A wide variety of experimental probes have detected signatures of superconductivity extending far above T_c [15, 85, 102, 106, 146–148], though generally not all the way to the pseudogap temperature T^*. Recent theoretical works suggests that the competition and coexistence pictures might not be opposed after all. Instead, the pseudogap and superconducting states may both represent different regimes of one many-faceted order parameter that includes charge ordering and superconducting components [149]. Similar schemes, as we saw in Chapter 4, have been invoked for the charge ordering state of the lanthanides [105, 125, 126]. Regardless of the nature of the pseudogap, there is compelling evidence that, unlike BCS materials, it is the loss of global phase coherence that drives the suppression of superconductivity and sets T_c [81, 85, 150–152].

As we've seen in Chapter 4 on light-induced Josephson coupling in the lanthanide cuprate $La_{1.675}Eu_{0.2}Sr_{0.125}CuO_4$, ultrafast light excitation can act in a manner counter to an applied magnetic field, promoting superconductivity indirectly by suppressing charge order. In the project presented in this chapter, rather than aim at destroying a competing order, the mid-infrared excitation was chosen to directly manipulate superconductivity in underdoped $YBa_2Cu_3O_x$ (YBCO x). We targeted the motion of the apical oxygen atom, whose relative position in the lattice has been shown to be closely tied with the superconducting transition temperature, both within a single family of compounds [4, 27] and across cuprate families [153, 154].

As in the LESCO experiment, we use the Josephson plasma resonance as a measure of superconducting coupling. This chapter lays out our primary findings, most

of which are published in Refs. [1, 2]. Below T_c, we find that c-axis superconducting coupling is enhanced by the excitation, as evidenced by a blue shift in the Josephson plasmon. More remarkably, we find that above T_c a transient plasma mode is generated at similar frequencies to the Josephson plasma mode. This mode has been seen in all of the four underdoped compounds investigated, including the non-superconducting doping YBCO 6.3 ($p = 0.05$). The transient mode frequency blue shifts as one approaches optimal doping, tracking the blue shift of the Josephson plasmon.

The light-induced plasma mode survives throughout the pseudogap state. Its behavior can be divided into two temperature regimes. Below a cusp temperature T'', the c-axis coupling is enhanced as base temperature increases. Above T'', this trend reverses and the mode diminishes following a mean field behavior, finally disappearing at a temperature T' that tracks the pseudogap transition temperature T^*. The T'' temperature coincides with the onset of spin fluctuations, suggesting they may play a role in suppressing the transient plasmon.

The light excitation appears to be inhomogeneous. I modeled the plasma mode as an effective medium, finding that the decrease in c-axis coupling with base temperature is actually related to a decrease in the fraction of the material volume that is photo-excited, rather than a drop in the carrier density. The maximum photo-excited volume remains below the percolation threshold for all dopings and temperatures measured. I discuss in what circumstances this threshold might be exceeded, generating a bulk high mobility response.

Finally I discuss the possible origins of the transient mode above T_c, which in Refs. [1, 2] we attribute to being a consequence of Cooper pair tunneling. If in fact the apical oxygen excitation is driving a stiffening of the superconducting order parameter phase, then the appearance of this plasmon would support the idea that some fluctuating superconductivity state survives in equilibrium throughout the pseudogap regime.

5.2 Experimental design and methods

5.2.1 Phonon pumping

$YBa_2Cu_3O_x$ (YBCO x) is a bilayer cuprate, consisting of pairs of CuO_2 planes oriented in the ab-plane with each pair of planes separated by a gap containing chains of Cu-O atoms aligned along the b-axis. Above and below these chains sit

the apical oxygen O(4) atoms. We resonantly drive a B_{1u} mode of the apical oxygen atom with 15 μm mid-infrared (MIR) pump pulses at field strengths of up to ~3 MV/cm. The excitation is illustrated in Figure 5.1.

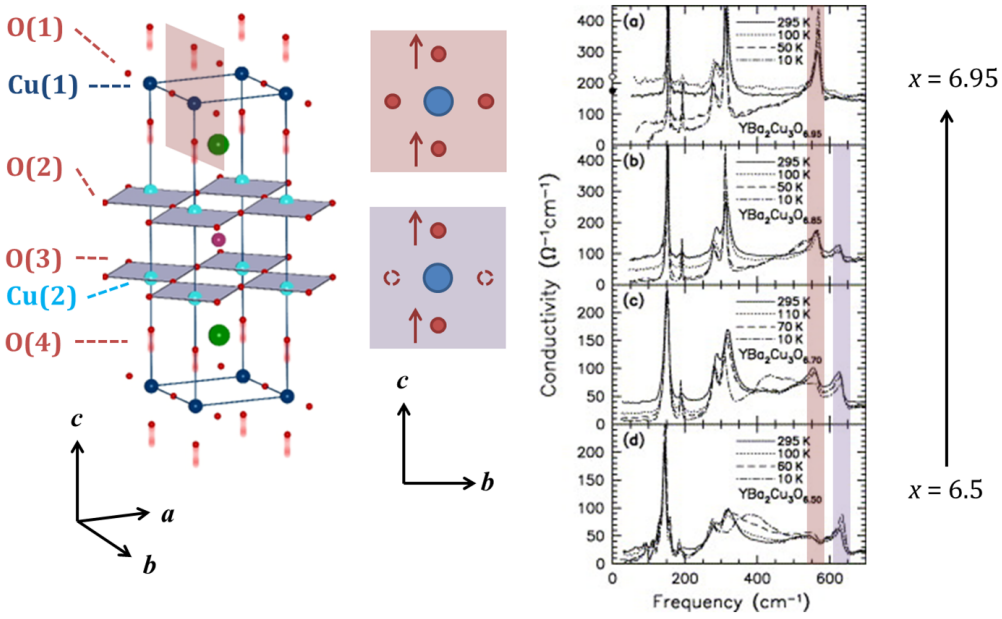

Figure 5.1: **The $YBa_2Cu_3O_x$ crystal structure and the apical oxygen modes.** The YBCO 7 crystal structure is illustrated (left) with copper atoms in blue and oxygen atoms in red. The pink square highlights the Cu-O chains (along the *b*-axis) and the apical oxygen atoms (above and below the Cu(1) atoms). The motion of the apical oxygen B_{1u} mode is illustrated (center) with the YBCO 7 structure in pink and the YBCO 6 structure in purple. These modes produce peaks in the Ohmic conductivity response (right) at around 670 cm^{-1} (YBCO 6 mode, purple) and 570 cm^{-1} (YBCO 7 mode, pink). Conductivity figure from Homes, *et al.* [84]

There are two B_{1u} modes of the apical oxygen atom, one associated with the YBCO 6 crystal structure, in which the chain oxygen O(1) atoms are depleted, and a second associated with YBCO 7, in which the chains are filled [155]. These modes are illustrated in the purple and red squares, respectively, in the center of Figure 5.1.

We excite the mode associated with the YBCO 6 crystal structure.[1] The 15 μm pulses are generated with a commercial TOPAS optical parametric amplifier (OPA) and difference frequency generator (DFG). The pump impinges on the single crystal samples at normal incidence with polarization aligned along the c-axis.

5.2.2 Probing with time-domain THz spectroscopy

The optically excited sample was probed via time-domain THz spectroscopy as described in Chapter 2. The optical response of YBCO below 2.5 THz was interrogated using single-cycle THz pulses generated via optical rectification of ∼100 fs, 800 nm pulses in a 1 mm thick ZnTe crystal. The spectral regime covered by the THz probe (blue) and the MIR pump (purple) are indicated as colored regions in Figure 5.2. The experiment was performed in reflection geometry, with the THz p-polarized (TM) along the c-axis (s-polarized along the a-axis) at a 30° angle of incidence.

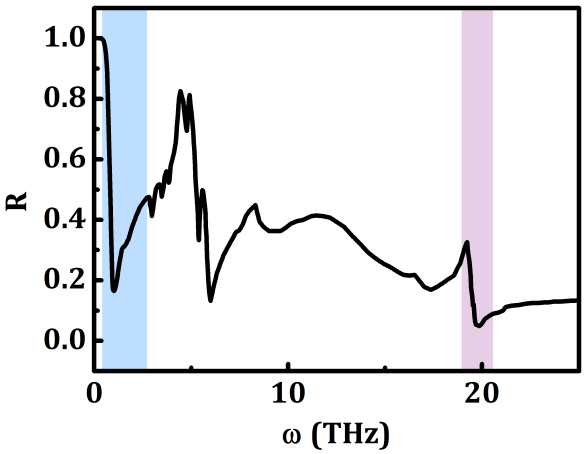

Figure 5.2: **Pump and probe spectral regimes.** The reflectivity of YBCO 6.5 at 5 K (black). Data from Ref. [84]. The width of the purple region indicates the full width half maximum of the spectrum of the mid-infrared pump pulse and the blue region indicates the spectral range of the THz probe.

[1]The YBCO 7 B_{1u} mode is outside the frequency range of most OPA + DFG systems (see Chapter 2).

5.2.3 Calculation of the transient optical response

The full transient optical response was found by measuring the pump-induced changes in the THz spectrum and referencing off the equilibrium spectrum, following the procedure described in Chapter 2. The method for determining the equilibrium spectrum is described in Appendix B.3.

Calculation of the transient response requires accounting for the mismatch in the MIR pump and THz probe penetration depths. Figure 5.3.A shows the pump penetration depth d of YBCO 6.5 near the pump wavelength. The Gaussian-shaped pump spectrum is illustrated in purple. We take the pump penetration depth as $d \approx 0.7$ μm, assuming resonant absorption of the light at the phonon frequency. The THz probe samples a crystal volume on order 10 times greater than the 15 μm pump, as illustrated in Figure 5.3.B. The full transient optical response was calculated by modeling the system as an excited surface on an unperturbed bulk. Both the single layer model and multilayer model, described in Chapter 2, produce equivalent results (see a model comparison in Section 2.6.3). The transient optical response calculated from the single layer model is reported in this chapter.

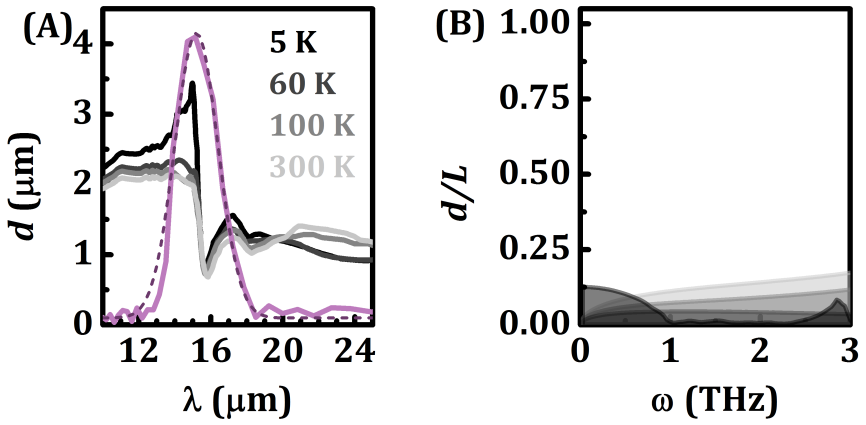

Figure 5.3: **Penetration depth mismatch between 15 μm pump and THz probe. (A)** The penetration depth of YBCO 6.5 at four temperatures (grey). The pump spectrum (purple) is centered around a B_{1u} phonon mode at 15 μm. A Gaussian fit to the spectrum (dashed line) indicates a width of ± 1.5 μm. **(B)** The penetration depth mismatch between the pump ($d \approx 0.7$ μm) and the THz probe.

5.2.4 Samples

In this study we considered four different underdoped compounds of $YBa_2Cu_3O_x$ (YBCO x), $x = 6.3$, 6.45, 6.5, 6.6 and optimally doped $x = 7$, which correspond to holed dopings of $p = 0.05$, 0.07, 0.09, 0.12, and 0.16 respectively. The lowest doping, $p = 0.05$, shows some diamagnetic response at low temperature, but the bulk remains non-superconducting down to 4.2 K. The other four compounds range in T_c from 35 K to 90 K. The crystals were grown in Y-stabilized zirconium crucibles and had typical dimensions of 2x2x1 mm^3 [2, 156]. The T_c values were determined by dc magnetization measurements in a SQUID, as shown in Figure 5.4 [157]. For all crystals, including YBCO 6.5, the YBCO 6 and YBCO 7 crystal structures are inhomogeneously mixed and not in the Ortho II phase.

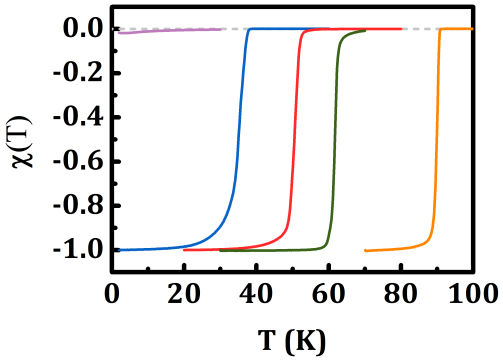

Figure 5.4: **SQUID measurements of $YBa_2Cu_3O_x$ (YBCO x)** with $x = 6.3$ (purple), 6.45 (blue), 6.5 (red), 6.6 (green), and 7 (orange). Throughout this chapter, each doping will be indicated following this color code, except where otherwise stated. Superconducting dopings have T_c values of 35 K (6.45), 51 K (6.5), 62 K (6.6), and 90 K (7).

5.3 Enhancement of Josephson coupling, $T < T_c$

5.3.1 Equilibrium c-axis optical response

The far-infrared response of a superconductor is characterized by two features associated with superconductivity, making time-domain THz spectroscopy an ideal ultrafast probe of the superconducting state. The first feature is unique to cuprates, the Josephson plasma resonance (JPR) [70, 71, 82, 84]. This longitudinal mode appears due to the resonant tunneling of Cooper pairs between CuO_2 planes. See Chapter 3 for a discussion of the Josephson plasmon. The bilayer structure of YBCO, with two closely spaced CuO_2 planes per unit cell (illustrated in Figure 5.5), gives rise to two longitudinal JPR modes [77]. The mode associated with tunneling across the inter-bilayer gap occurs in the 0-7 THz frequency range in underdoped compounds, and a resonance identified as the bilayer mode is seen at ∼17 THz. This study focuses primarily on the transient response of the inter-bilayer mode. In Section 3.2, I address in more detail the full landscape of modes that develop due to the bilayer structure and in Section 6.2 I present a study on how the mid-infrared excitation impacts higher frequency modes.

The inter-bilayer JPR can be measured in the optical response as a peak in the loss function, $\Im(-1/\tilde{\varepsilon})$, near the plasma resonance frequency ω_p. The left-hand panel of Figure 5.6 plots $\Im(-1/\tilde{\varepsilon})$ of YBCO 6.5 at four temperatures below $T_c = 51$ K. As the condensate is depleted, the mode frequency redshifts, following the "effective" condensate density $n_S \propto \omega_p^2$. The condensate density is effective in the sense that only those pairs that tunnel contribute to the density along the c-axis, making n_S also an indirect measure of the tunneling rate, which is $\propto \omega_p$ [158]. Above T_c, the loss function is featureless in this frequency regime. (See Appendix B.3 for a discussion of how the equilibrium response is measured.)

The second THz frequency feature of superconductivity is a divergent inductive conductivity, $\sigma_2(\omega)$. The divergent component scales as $1/\omega$ and is the Kramers-Kronig equivalent of the spectral weight of the Ohmic conductivity $\sigma_1(\omega) \propto n_s\delta(\omega = 0)$. It is this component which gives rise to the zero resistivity state of a superconductor, making $\sigma_2(\omega)$ an ac measure of the dc condensate.

The density can be extracted exactly from the quantity $n_S \propto \omega\sigma_2(\omega)|_{\omega\to 0}$. At $\omega = 0$, the normal state component of the inductive conductivity, shaped by higher frequency phonons, is zero and only the superfluid component remains. Within the THz range, the total inductive conductivity above T_c, $\sigma_2(\omega, T > T_c)$, is very close

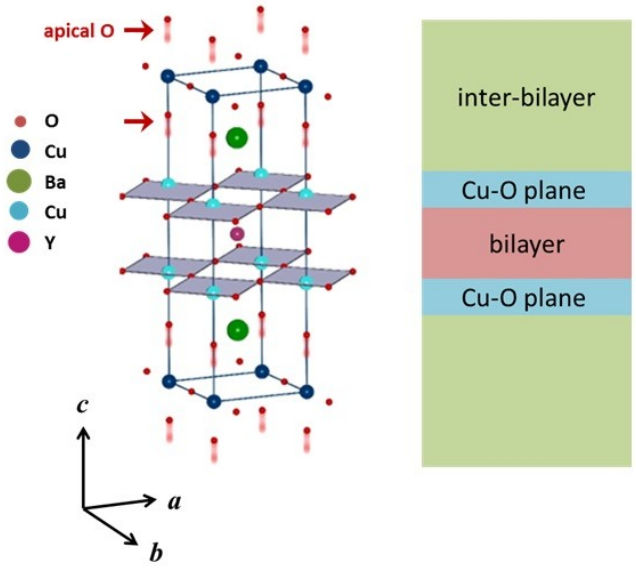

Figure 5.5: **Bilayer structure of YBCO. Left:** YBCO crystal structure, highlighting the CuO_2 planes in grey. The apical oxygen atoms sit in the inter-bilayer gap, between pairs of planes. **Right:** Illustration depicting the organization of the crystal structure into pairs CuO_2 planes (blue) spaced by a small bilayer gap (pink) and separated by a larger inter-bilayer gap (green).

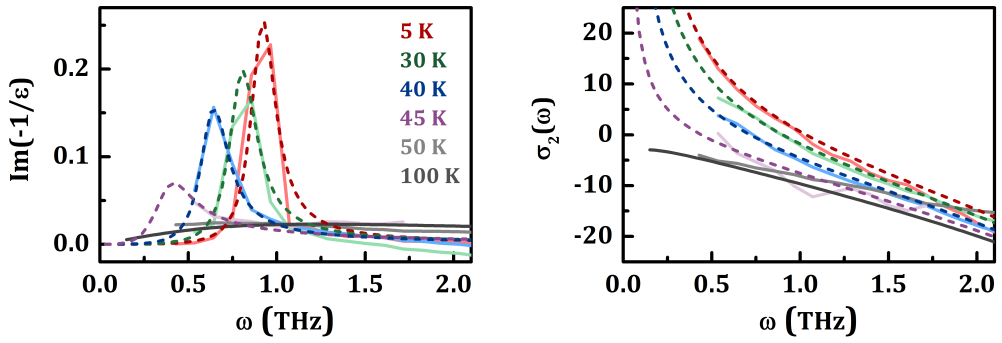

Figure 5.6: **Equilibrium response of YBCO 6.5 between 5 K and 100 K. Left:** The loss function, which peaks at the Josephson plasma frequency below $T_c = 51$ K. **Right:** The inductive conductivity, which diverges to low frequency. Conductivity expressed in units of $1/\Omega$-cm. Dashed lines indicate a $1/\omega$ fit, as described in the main text.

to the normal state component below T_c. Thus $\omega\sigma_2(\omega)|_{\omega\to 0} \approx \omega\Delta\sigma_2(\omega)$, where $\Delta\sigma_2(\omega) = \sigma_2(\omega) - \sigma_2(\omega, T > T_c)$.

The right-hand panel of Figure 5.6 shows the divergent behavior of $\sigma_2(\omega)$. The dashed lines indicate a fit to $\sigma_2(T < T_c) = \sigma_2(100\text{ K}) + \tilde{n}_S/\omega$. The fit to the loss function $\Im(-1/\tilde{\varepsilon})$ uses the dielectric response,

$$\tilde{\varepsilon} = \varepsilon_\infty - \frac{4\pi i}{\omega}\left[\sigma_{1,0} + i\sigma_2(T < T_c)\right], \tag{5.1}$$

where the constant $\sigma_{1,0}$ accounts for broadening of the plasma mode due to an increase in quasiparticles as $T \to T_c$.[2] Thus the appearance of the plasmon is a direct result of the $\tilde{n}_S/\omega$ term, illustrating that it is the same pairs that contribute to tunneling that generate the diverging inductive response along the c-axis. Indeed, the measured $\sigma_2(\omega)$ response along the ab-plane is typically 1000× that measured along the c-axis, as illustrated in Figure 5.7.

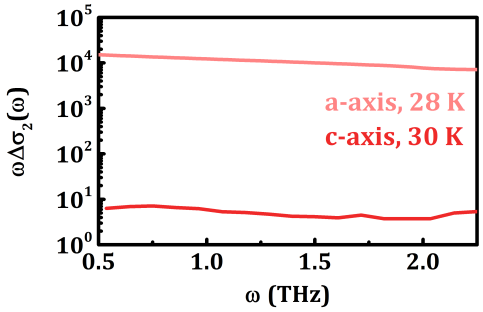

Figure 5.7: **Comparison of the a-axis and c axis inductive response.** The superfluid density at 30 K in terms of $n_S \propto \omega\Delta\sigma_2(\omega) = \omega(\sigma_2(30\text{ K}) - \sigma_2(60\text{ K}))$. Units are THz/Ω-cm. The c-axis response is in red, the a-axis in pink. The a-axis response is taken from Hwang, *et al.* [69].

The effective c-axis pair density follows the typical BCS mean field behavior with temperature, as shown in Figure 5.8. The left panel of Figure 5.8 illustrates the flat

[2]Inhomogeneities intrinsic to the sample also lead to a broadening of the plasmon in cuprates [82, 112], even in the highest quality samples [27]. In practice, the $\sigma_{1,0}$ term effectively takes into account all broadening contributions. In Equation 5.1 we take $\varepsilon_\infty = 4.5$ for the high-frequency dielectric constant, a standard value for cuprates [79]. Note that for a conductivity in units of 1/Ω-cm and frequency in THz, the cgs prefactor $4\pi \to 1.8$.

behavior of $\omega\Delta\sigma_2(\omega) \propto n_S$ at low frequency. We find that the temperature dependence of $\omega\Delta\sigma_2(\omega)$ can be well-fit with the mean field equation $n_S \propto \sqrt{1 - T/T_c}$.

For convenience, throughout this thesis the quantity $\tilde{n}_S = \omega\Delta\sigma_2(\omega)$ is expressed in units of THz/Ω-cm, which is close to unity for the densities found here. Using the conversion, $Z_0 = \sqrt{\mu_0/\varepsilon_0} \approx 377\ \Omega \rightarrow 4\pi/c \approx 419\ \text{cm}^{-1}/\text{THz}$, this quantity can be recast as $\tilde{n}_S$ [THz/Ω-cm] $\rightarrow \sim 1000\ \tilde{n}_S$ [cm^{-2}].

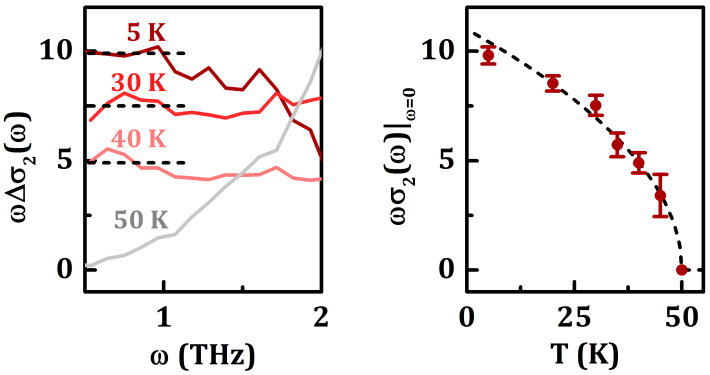

Figure 5.8: **Superfluid density of YBCO 6.5.** The vertical axes are in units of THz/Ω-cm. **Left:** The superconducting component of the inductive conductivity diverges as $1/\omega$. The quantity $\omega\Delta\sigma_2(\omega)$ is flat and proportional to the superfluid density, n_S. **Right:** The mean value of $\omega\Delta\sigma_2(\omega)$ follows a mean field temperature dependence, with $n_S \propto \sqrt{1 - T/T_c}$ (dashed line fit). Error bars indicate the standard deviation to the average low frequency $\omega\Delta\sigma_2(\omega)$.

The frequency of the Josephson plasma resonance depends upon several factors, including the crystal geometry, superfluid density, and compressibility [77]. However, within a single family of compounds, the relative position of the resonance can be related to the superfluid density. Therefore as one approaches optimal doping, the resonance blue shifts as more carriers are available to condense. In the doping region between YBCO 6.3 and 6.6, the hole content p scales roughly linearly with ω_p, as plotted in the top panel of Figure 5.9. The relationship between the superfluid density and plasma frequency, $n_S \propto \omega\Delta\sigma_2(\omega) \propto \omega_p^2$ is illustrated in the lower panel.

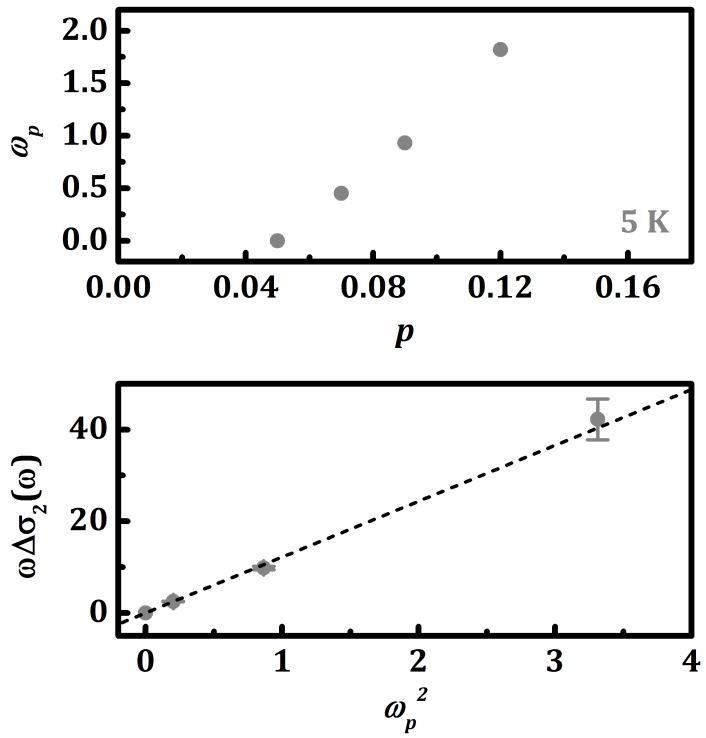

Figure 5.9: **Josephson plasma mode tracking hole doping. Top panel:** The plasma frequency ω_p tracks the doping level p of the material. In this hole doping range, the relationship is roughly linear. **Bottom panel:** Along the c-axis, the divergence in the inductive response $\omega\Delta\sigma_2(\omega)$ is proportional to the square of the plasma frequency, ω_p^2. The dashed line indicates a linear fit.

The Josephson plasma modes of three dopings, YBCO 6.45, 6.5, and 6.6[3], are shown at 5 K in Figure 5.10. The first row shows the THz reflectivity R. The edge in reflectivity tracks the plasma resonance, as can be seen by comparing with the peaks in the loss function plotted in the second row. The third row panels show the full inductive conductivity $\sigma_2(\omega)$, which goes positive at low frequency as the $1/\omega$ component starts to dominate the response. The fourth row panels show the Ohmic conductivity, which is partially gapped by the condensate.

[3]A small "wiggle" is seen in the conductivity and reflectivity of YBCO 6.6 below 1 THz in Figure 5.10. This is a result of diffraction effects due to the small sample size, which are amplified by the high reflectivity below ω_p.

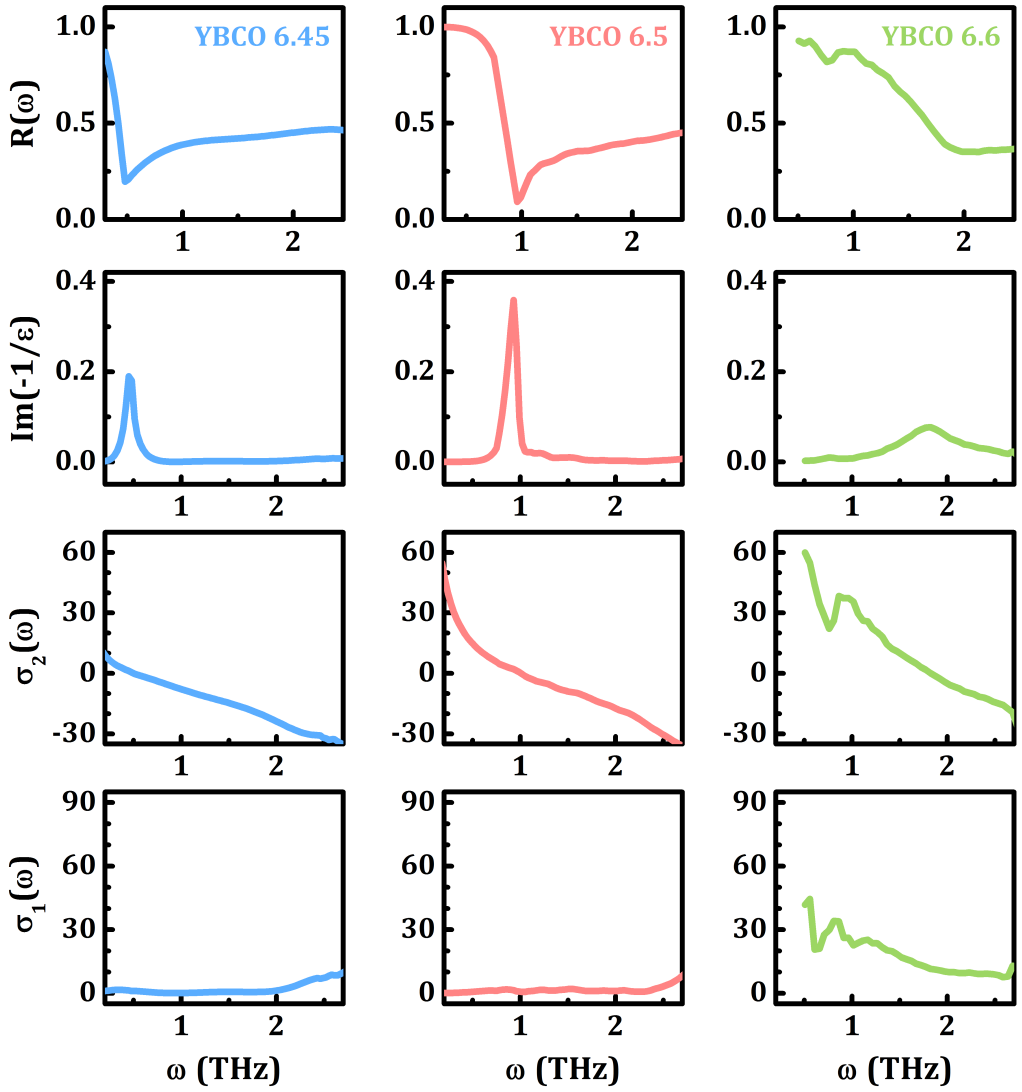

Figure 5.10: **Equilibrium response of underdoped YBCO below T_c at three dopings. Top row:** The reflectivity R show the appearance of a edge at ω_p. **Second row:** The loss function $\Im(-1/\varepsilon)$, which peaks near the resonance frequency ω_p. **Third row:** The inductive conductivity $\sigma_2(\omega)$ which goes positive as it diverges to low frequency. **Fourth row:** The real conductivity $\sigma_1(\omega)$ which is partially gapped.

5.3.2 Response after optical excitation

The transient response below T_c is characterized by an enhancement in the inductive conductivity and a blue shift of the loss function peak associated with the Josephson

plasma resonance. Figure 5.11 plots the transient optical response of YBCO 6.5 at 5 K, 0.6 ps after excitation. The loss function peak broadens, with its central frequency shifting to the blue. The net blue shift of the loss function corresponds to an increase in the low frequency $\sigma_2(\omega)$, just as expected for an increase in ω_p^2.

Part of the broadening of the loss function can be attributed to some transient quasiparticle excitation, which also produces a flat increase in $\sigma_1(\omega)$. However, as I will show in Chapter 7, some of the apparent broadening is actually due to a splitting of the Josephson mode which is more apparent at later delays, and is likely a consequence of inhomogeneous excitation. This splitting also leads to an the increase in $\sigma_1(\omega)$.

It is the enhancement of interbilayer tunneling, characterized by a blue shifted ω_p, that I will refer to as "enhanced" superconductivity. In principle, such a blue shift could either originate from an increase in the pair density or an increase in the tunneling rate. As I will discuss in Section 6.2, the latter seems to be the most likely scenario.

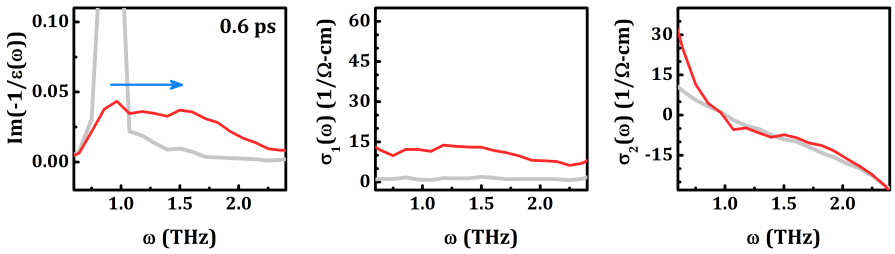

Figure 5.11: **Transient response of YBCO 6.5 at 5 K.** The loss function $\Im(-1/\varepsilon)$ **(left)**, Ohmic conductivity $\sigma_1(\omega)$ **(center)**, and inductive conductivity $\sigma_2(\omega)$ **(right)**, at 0.6 ps after excitation. The transient response is shown in red and the equilibrium response in grey.

The pump-induced increase in $\sigma_2(\omega)$ drops with increasing temperature, as illustrated in Figure 5.12. The magnitude of the transient inductive response $\omega\Delta\sigma_2(\omega) = \omega(\sigma_2(\omega,\tau) - \sigma_{2,eq}(\omega, T > T_c))$ appears to deviate from a mean field behavior, roughly scaling linearly with temperature to a critical value of $\sim$55 K ($T_c = 51$ K).

The same trends are seen in the superconducting state of all underdoped compounds. Figure 5.13 shows the transient response of YBCO 6.45, 6.5, and 6.6 at

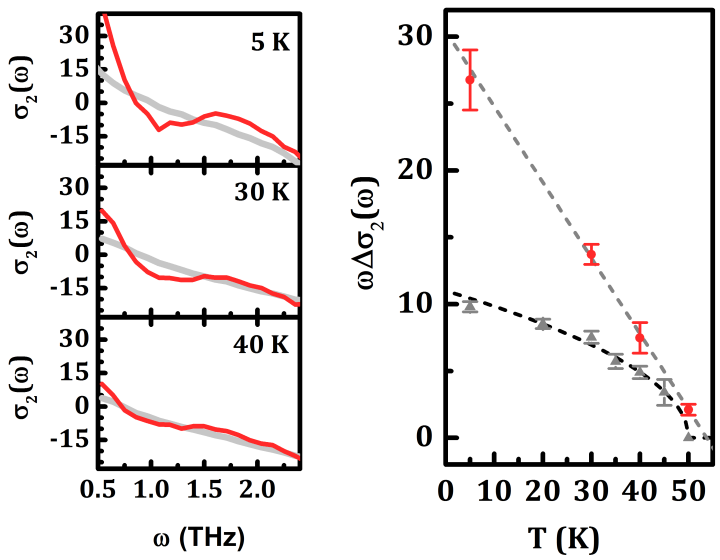

Figure 5.12: **Transient enhancement of superconductivity in YBCO 6.5, 5-40 K. Left:** The inductive conductivity $\sigma_2(\omega)$ at three temperatures 5 K, 30 K, and 40 K (top to bottom). The equilibrium response is in grey, the transient response 0.8 ps after excitation is in red. **Right:** The temperature evolution of the transient response (red) and the static response (grey, from Figure 5.8). Dashed grey line indicates a linear fit to the transient response.

5 K, 0.6 ps after excitation. All compounds show a similar broadening and blue shift of the Josephson plasmon loss function peak and corresponding increase in the inductive response.

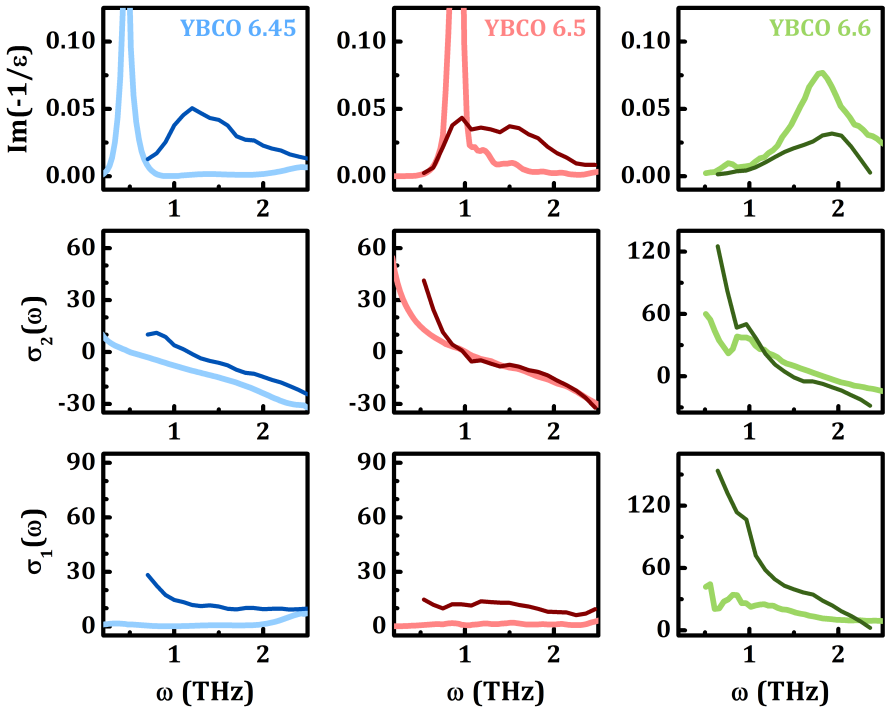

Figure 5.13: **Transient response of underdoped YBCO** $T < T_c$**.** The loss function $\Im(-1/\varepsilon)$ **(top row)**, inductive conductivity $\sigma_2(\omega)$ **(second row)**, and Ohmic conductivity $\sigma_1(\omega)$ **(bottom row)** for YBCO $x = 6.45$ (blue), 6.5 (red), and 6.6 (green) at 0.6 ps after excitation. The equilibrium response is in thick pale lines for comparison.

5.4 Generation of a transient plasmon, $T > T_c$

5.4.1 Equilibrium c-axis optical response

There are no IR active excitations above T_c in the 0-3 THz spectral range of underdoped YBCO and the conductivity in this regime is flat and featureless. Unlike below T_c, where the position and shape of the Josephson plasmon is highly sensitive to the temperature and doping of the individual sample, the response above T_c between 0-3 THz remains relatively unchanged even up to 300 K. The most significant feature is the slight increase in $\sigma_1(\omega)$ due to thermally populated carriers, as shown in Figure 5.14.

At higher frequencies, phonon reshaping leads to larger changes in the conductivity. These changes are most significant between T_c and 100 K. They do not impact the conductivity near the apical oxygen mode frequency.

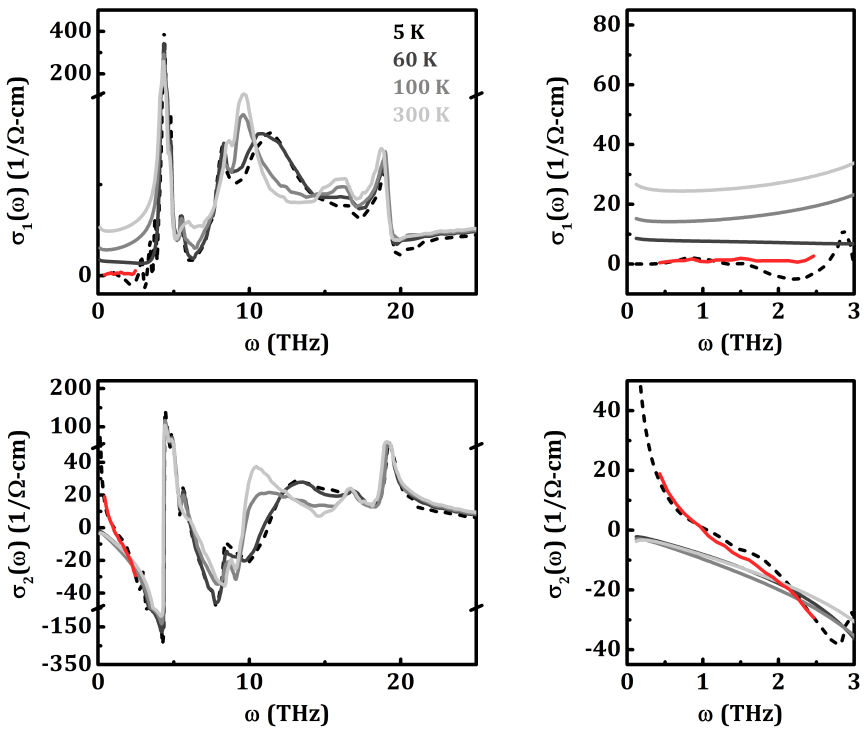

Figure 5.14: **Equilibrium conductivity of YBCO 6.5.** The normal state conductivity (grey) and the superconducting state at 5 K (black dashed line) are data from Ref. [84]. The superconducting response at 5 K measured with THz spectroscopy on the sample used in this work is shown in red. **Top row:** The Ohmic conductivity $\sigma_1(\omega)$ over a broadband range (left) and between 0-3 THz (right). **Bottom row:** The inductive conductivity $\sigma_2(\omega)$ in the same frequency regimes.

5.4.2 Response after optical excitation

The strengthening of superconductivity below T_c in the form of a blue-shifting Josephson plasma frequency ω_p suggests that we may hope to increase the superconducting transition temperature of the excited material. What we find in practice is that throughout the pseudogap regime, the pump excitation generates a plasma mode at roughly the same frequency as the equilibrium Josephson plasma mode below T_c.

The top row of Figure 5.15 shows the equilibrium change in reflectivity above and below T_c, $|\Delta\tilde{E}/\tilde{E}| \equiv \Delta R/R$ where

$$\frac{\Delta\tilde{E}}{\tilde{E}} = \frac{\tilde{E}(T < T_c) - \tilde{E}(T > T_c)}{\tilde{E}(T > T_c)}, \tag{5.2}$$

for three superconducting compounds, YBCO 6.45, 6.5, and 6.6. In non-superconducting YBCO 6.3, by comparison, there is no plasmon and the reflectivity is nearly unchanged between $\tilde{E}$(5 K) and $\tilde{E}$(100 K) (top left-most figure).

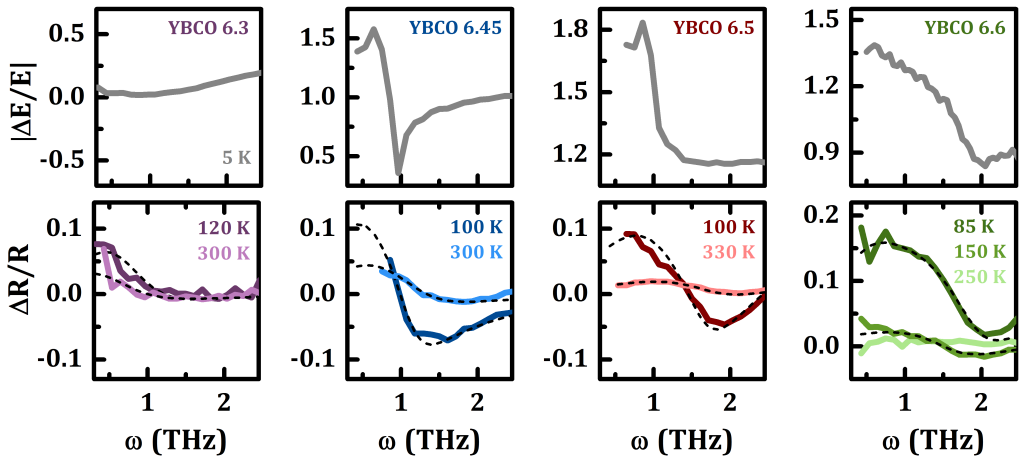

Figure 5.15: **Transient reflectivity of underdoped YBCO $T > T_c$. Top row:** The equilibrium change in reflectivity above and below T_c, $\Delta R/R \equiv |\Delta\tilde{E}/\tilde{E}|$. For non-superconducting YBCO 6.3, we take $\tilde{E}$(5 K) and $\tilde{E}$(100 K). **Bottom row:** The transient changes in reflectivity above T_c, at 0.6 ps after excitation. Evidence of an edge appears in YBCO 6.3 at the lower limit of our THz spectrum window. The frequency of the transient plasmon blue shifts with doping, tracking the equilibrium Josephson plasmon. Fits (dashed lines) described in Section 5.5.

Above T_c, the pump induces a transient plasma mode in all four underdoped compounds. The pump-induced changes to the equilibrium reflectivity, $\Delta R/R = [R(\omega,\tau) - R_{\rm eq}(\omega)]/R_{\rm eq}(\omega)$, are plotted in the bottom row of Figure 5.15. YBCO 6.3 (purple) develops an edge right at the low frequency cut-off of our THz spectrum. For higher doped samples, the transient mode blue shifts, tracking the equilibrium Josephson plasmon.

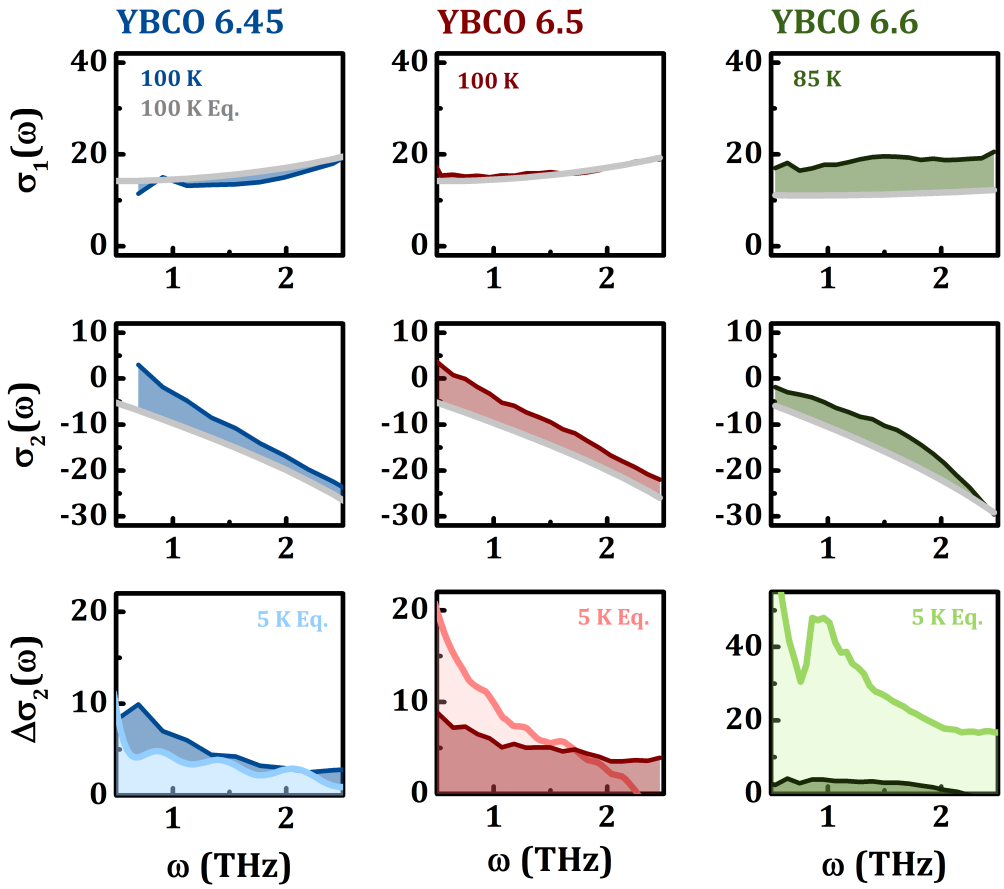

Figure 5.16: **Comparing the transient response above T_c and the equilibrium superconducting response.** The transient conductivity is shown for YBCO 6.45 (blue) and 6.5 (red) at 100 K, and 6.6 (green) at 85 K. The equilibrium conductivity at 100 K is shown in grey. **Top row:** The Ohmic conductivity $\sigma_1(\omega)$. **Middle row:** The inductive conductivity $\sigma_2(\omega)$. **Bottom row:** The transient changes to the inductive conductivity $\Delta\sigma_2(\omega) = \sigma_2(\omega) - \sigma_{2,\mathrm{eq}}(\omega)$. The equilibrium superconducting response (thick pale lines), $\Delta\sigma_{2,\mathrm{eq}}(\omega) = \sigma_{2,\mathrm{eq}}(\omega, 5\ \mathrm{K}) - \sigma_{2,\mathrm{eq}}(\omega, 100\ \mathrm{K})$, is shown for comparison.

The full optical conductivity of underdoped YBCO is shown in Figure 5.16 for the three underdoped superconducting compounds. The equilibrium conductivity in the normal state, well above T_c, is shown in grey. The transient response at the same temperature is shown in blue, red, and green for YBCO 6.45, 6.5, and 6.6 respectively. In all dopings, the appearance of the plasma mode corresponds with

an increase in the inductive conductivity $\sigma_2(\omega)$. The equilibrium superconducting response at 5 K is shown for comparison.

The transient changes in the optical response of *all* measured dopings, from YBCO 6.3 to 7, are shown in Figure 5.17. For the underdoped compounds, a common theme emerges: a positive and diverging $\Delta\sigma_2(\omega)$ accompanied by the appearance of a peak in the loss function. The dotted lines in the $\Delta\sigma_2(\omega)$ plots indicate a fit to $\tilde{n}/\omega$.

While YBCO 6.6 still exhibits a marked increase in $\sigma_2(\omega)$, the shape deviates from $1/\omega$. This can be accounted for by the influence of transient incoherent contributions to the conductivity, which are easiest to identify by the uniform increase in Ohmic conductivity, $\Delta\sigma_1(\omega)$ [159]. The changes in $\Delta\sigma_1(\omega)$ remain negligible at lower dopings, but in YBCO 6.6 they have a size scale on the same order as the total inductive changes. As a result, the inductive component of the incoherent part of the excitation reshapes $\Delta\sigma_2(\omega)$. The doping dependent increase in $\sigma_1(\omega)$ suggests that quasiparticle excitations increase with equilibrium hole concentration.

The magnitude of the loss function and inductive features are comparable across all underdoped materials, however in YBCO 6.3 the changes appear somewhat smaller. As of the writing of this thesis, I cannot be certain if the magnitude of the optical changes are accurate for this compound since the equilibrium response of YBCO 6.5 was used to extract the transient response. This was a practical constraint, since the equilibrium *c*-axis response has not yet been measured on this sample and could not be found in literature.[4] The *shape* of the transient changes should not be impacted by the choice of equilibrium response, since the compounds are so similar at these temperatures. However the *magnitude* of the changes may be slightly off due to differences in the pump-probe penetration depth mismatch of YBCO 6.3 and 6.5.

The transient response of YBCO 7 (orange in Figure 5.17) is qualitatively quite different from the underdoped compounds. If a transient mode were to appear following the trend at lower dopings, the loss function would peak near the Josephson plasma frequency, 7.5 THz at 5 K [84], which is outside our spectral range. Yet there should still be a divergent behavior in $\Delta\sigma_2(\omega)$ between 0-3 THz if a higher frequency plasmon were being generated. Instead the inductive conductivity decreases.

[4] Measurements of the equilibrium response on the same YBCO 6.3 crystal are underway.

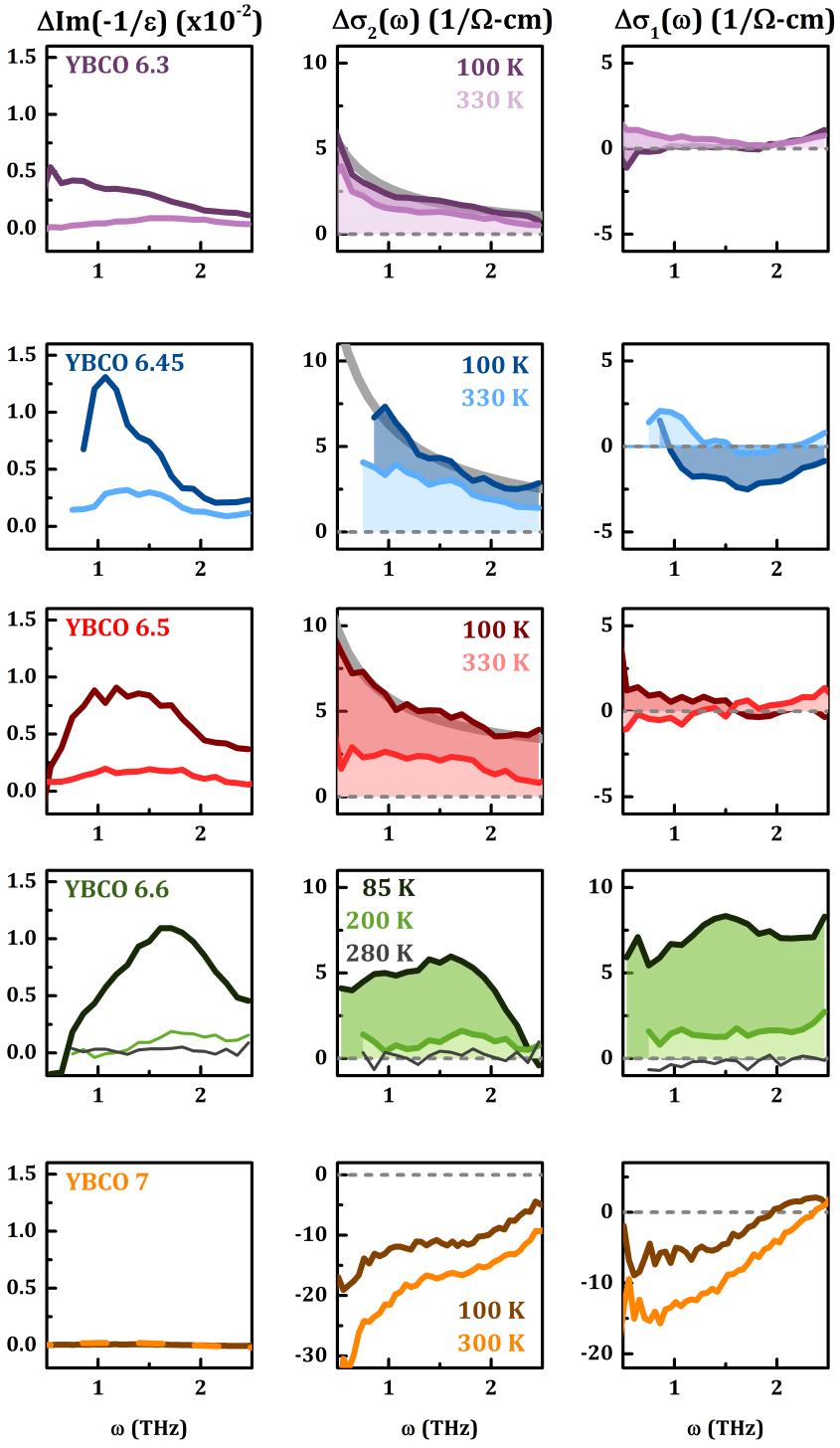

Figure 5.17: **Optical response of underdoped YBCO $T > T_c$.** The pump-induced changes in the loss function $\Delta\Im(-1/\varepsilon)$ (left column), inductive conductivity $\Delta\sigma_2(\omega)$ (middle), and Ohmic conductivity $\Delta\sigma_1(\omega)$ (right column), for YBCO $x = 6.3$ (purple), 6.45 (blue), 6.5 (red), 6.6 (green), and 7 (orange). Thick grey lines are fits to $\Delta\sigma_2(\omega) \propto 1/\omega$. Dashed lines on conductivity plots indicate the "zero changes" level.

The excitation targets a phonon mode of the YBCO 6 crystal structure, which is essentially absent at this doping, therefore the absence of a transient plasma mode may be due to the lack of resonant excitation of the apical oxygen.

As an analogy with superconductivity, we consider again the quantity $\omega\Delta\sigma_2(\omega)$, where $\Delta\sigma_2(\omega) = \sigma_2(\omega) - \sigma_{2,\mathrm{eq}}(\omega)$ captures the inductive response due to pumping. Figure 5.18.A shows $\omega\Delta\sigma_2(\omega)$ for YBCO 6.45 at four temperatures. The mean $\omega\Delta\sigma_2(\omega)$ was extracted by averaging the response in the range where it remains frequency-independent.

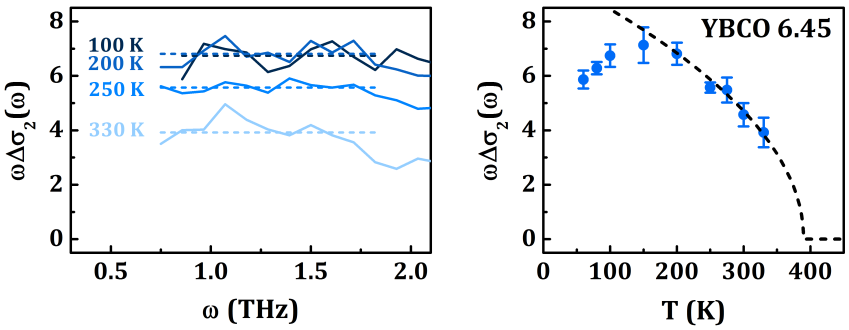

Figure 5.18: **Temperature dependence of the inductive response of YBCO 6.45. Left:** The inductive response $\omega\Delta\sigma_2(\omega)$ of YBCO 6.45 at four temperatures. The dashed line indicates the mean value of the response. **Right:** The mean $\omega\Delta\sigma_2(\omega)$ is plotted for several temperatures. The error bars indicate the standard deviation of the mean $\omega\Delta\sigma_2(\omega)$ over the averaged region. The temperature dependence is fit to a mean field response $\omega\Delta\sigma_2(\omega) \propto \sqrt{1 - T/T'}$ (dashed line), with $T' \approx 390$ K.

Interestingly, we find two temperature regimes emerge. Starting just above T_c, the inductive response increases somewhat linearly with increasing temperature until a crossover point T''. Above T'' the response follows the mean field behavior typical of a superfluid, dropping to zero at a temperature T'. Both regimes are illustrated for all dopings in Figure 5.19. The T'' crossover temperature is estimated by the intersection of a linear fit to the low temperature response (grey dashed line) and the mean field fit to the high temperature response (black dashed line).

The temperature scales T' and T'' are plotted on the phase diagram in Figure 5.20. Immediately striking is the similarity between the T' temperature scale and the T^*

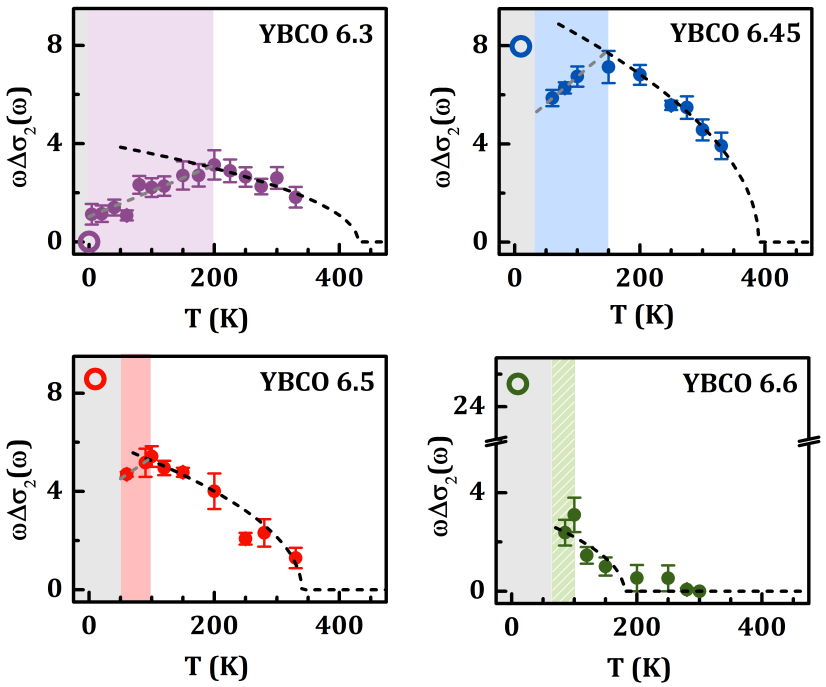

Figure 5.19: **Critical temperatures of the transient response.** For each $\omega\Delta\sigma_2(\omega)$ vs T plot, the superconducting regime below T_c is shaded grey and the regime below T'' is shaded in color. The equilibrium superfluid density for each doping is indicated by the empty circles. The solid circles represent the pump induced inductive response, $\omega\Delta\sigma_2(\omega) \equiv \omega\sigma_2(\omega)|_{\omega\to 0}$. A linear fit to the inductive response below T'' is indicated by the grey dashed lines. A mean field fit of the form $\propto \sqrt{1 - T/T'}$ is indicated by the black dashed lines. The crossover point T'' marks the peak $\omega\Delta\sigma_2(\omega)$. The temperature T' marks when $\omega\Delta\sigma_2(\omega) = 0$.

line associated with the transition to the pseudogap phase. The T'' crossover appears to track the T_{ELC} temperature scale identified by Haug, *et al.*[5] [160, 161] as the electronic liquid crystal (ELC) temperature, where there is an onset of nematic behavior due to collective excitations between spins (see Figure 5.21). The suppression of $\omega\Delta\sigma_2(\omega)$ below this temperature suggests that spin fluctuations may be competing with the transient plasmon.

[5]The YBCO 6.3 sample I studied is from the same batch as the YBCO 6.3 sample used in Ref. [160].

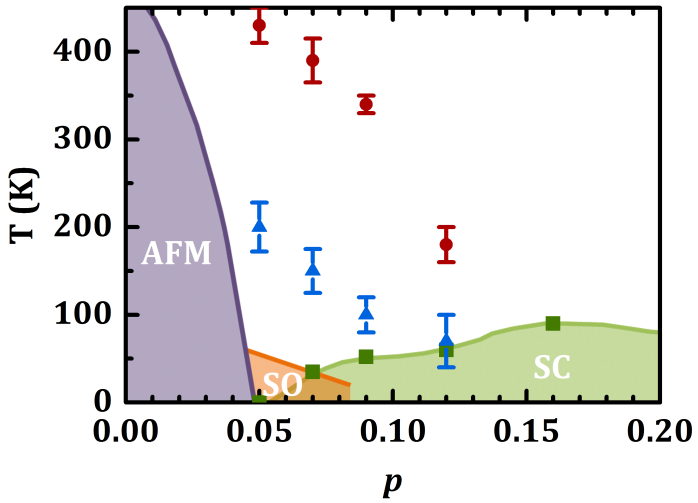

Figure 5.20: **Transient phase diagram of YBCO.** The crossover point T'' (blue triangles) indicates the temperature with the peak transient inductive response. The transient response disappears above T' (red circles). Green squares indicate the equilibrium superconducting transition temperatures.

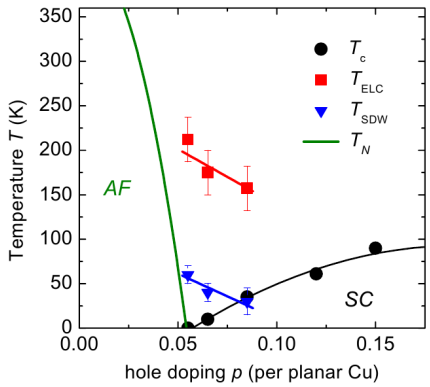

Figure 5.21: **The electronic liquid crystal regime.** Above the spin density wave transition there is a regime of nematic behavior due to collective excitations between spins. The scale T_{ELC} was defined by neutron resonant spin-echo measurements as the onset temperature for in-plane anisotropy of the incommensurate peaks of the spin excitation spectrum. Figure reproduced from Ref. [160].

5.5 Inhomogeneity of the transient state

The transient response has several features that indicate the response is inhomogeneous. The amplitude of the reflectivity does not reach $R = 1$ below the plasma frequency ω_p. Although the inductive response $\omega\Delta\sigma_2(\omega)$ drops with increasing temperature, the plasma frequency does not red shift a corresponding degree, marking a deviation from $\omega\Delta\sigma_2(\omega) \propto \omega_p^2$ behavior. As we will see in Section 7.2, the Josephson plasmon below T_c also shows obvious signs of inhomogeneity. The plasmon splits into two peaks after excitation, with one component remaining at the equilibrium plasma frequency.

The inhomogeneous behavior can be quantitatively captured with the Bruggeman effective medium model [162], which has the form,

$$f\frac{\tilde{\varepsilon}_a(\omega) - \tilde{\varepsilon}_E(\omega)}{\tilde{\varepsilon}_a(\omega) + \left(\frac{1-q}{q}\right)\tilde{\varepsilon}_E(\omega)} + (1-f)\frac{\tilde{\varepsilon}_b(\omega) - \tilde{\varepsilon}_E(\omega)}{\tilde{\varepsilon}_b(\omega) + \left(\frac{1-q}{q}\right)\tilde{\varepsilon}_E(\omega)} = 0, \tag{5.3}$$

where medium a with optical response $\tilde{\varepsilon}_a(\omega)$ occupies a volume fraction f and medium b occupies volume $1 - f$. The effective optical response is $\tilde{\varepsilon}_E(\omega)$. This model was developed for dc response, but is applicable whenever the size scale of the inclusions are small compared with the probing wavelength, in this case 120-600 μm. The depolarization factor q sets the shape of the inclusions of each material [163]. We assume simple spherical inclusions, $q = 1/3$. See Appendix B.4 for a discussion on how q shapes the response and influences the percolation threshold.

We model medium a with the optical response of a single longitudinal Josephson plasma mode, which we saw in Chapter 3 has the Drude form,

$$\tilde{\varepsilon}(\omega) = \tilde{\varepsilon}_c - \frac{\omega_p^2}{\omega^2 - i\omega\Gamma}. \tag{5.4}$$

The advantage of the Drude formalism is that it includes just two free parameters, ω_p and Γ. Within this model, the scattering rate term Γ encompasses all transient processes that impact the mobility along the c-axis. For incoherent carriers, this relates to their effective mean free path; for a superconductor, it is associated with the superconducting coherence length and time scales. For a "perfect" superconductor, $\Gamma \to 0$.

The $\tilde{\varepsilon}_c(\omega)$ term accounts for the other components of the response in the superconducting state besides the Josephson plasmon—the higher frequency phonon modes which add small contributions to the THz conductivity, but most dramati-

cally impact the shape of the response outside our spectral window. The influence of these modes can be described well using two Lorentzian oscillators, $\tilde{\varepsilon}_{\rm lor}(\omega)$, resulting in $\tilde{\varepsilon}_c(\omega) = \varepsilon_\infty + \tilde{\varepsilon}_{\rm lor}(\omega)$. Figure 5.22 plots the equilibrium conductivity $\tilde{\sigma}(\omega)$ and reflectivity $R(\omega)$ of YBCO 6.5 at 5 K (red) along with the response calculated from $\tilde{\varepsilon}_c(\omega)$ (grey). A fit to the equilibrium response using Equation 5.4 with $\Gamma = 0$ is also shown (dashed line). Note that even in the superconducting state, some broadening is needed to account for the inhomogeneity of the sample [82, 112] and incoherent contributions to the response [77].

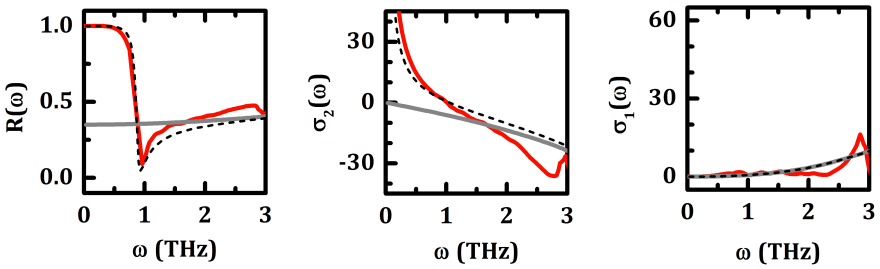

Figure 5.22: **Superconducting medium for effective medium fits.** Superconducting response of YBCO 6.5 at 5 K (red) and the response of two Lorentzian oscillators (grey). The oscillator response was combined with a single plasma mode to model the optically excited regions of YBCO. An example of this is shown (black dashed line).

The response for medium b was taken from the equilibrium material, $\tilde{\varepsilon}_b(\omega) = \tilde{\varepsilon}_{eq}(\omega)$. At higher temperatures and as we move towards optimal doping, a small quasiparticle contribution to the transient response must be accounted for. This can be done in one of two equivalent ways. First, to be fully Kramers-Kronig consistent, we add a small Drude component to $\tilde{\varepsilon}_b(\omega)$. In practice, since the major features of this contribution are far outside the THz spectral range, this is equivalent to simply adding a small frequency-independent contribution to the Ohmic conductivity instead, $\tilde{\varepsilon}_b(\omega) = \tilde{\varepsilon}_{eq}(\omega) + 4\pi i\sigma_{1,0}/\omega$.

Figure 5.23 plots the peak transient optical response of YBCO 6.45 at 250 K (dots). Effective medium fits are shown in black and red (top row). The first fit (black) uses a small constant $\sigma_{1,0} = 5$ 1/Ω-cm and the second (red) employs the

Drude model to account for the quasiparticle contribution. The fits are virtually identical in the 0-3 THz spectral range. The components of both effective medium fits are plotted in the second row. The two models of medium b are shown in black and red for the respective black and red fits in the top row. Each fit used the same superconducting response for medium a, plotted in blue.

For comparison, the equilibrium superconducting response of YBCO 6.45 at 5 K is plotted in light blue. The transient plasma mode of medium a is blue shifted with respect to the equilibrium plasmon, implying that the tunneling strength of the transient state is enhanced compared to the equilibrium superconductor.

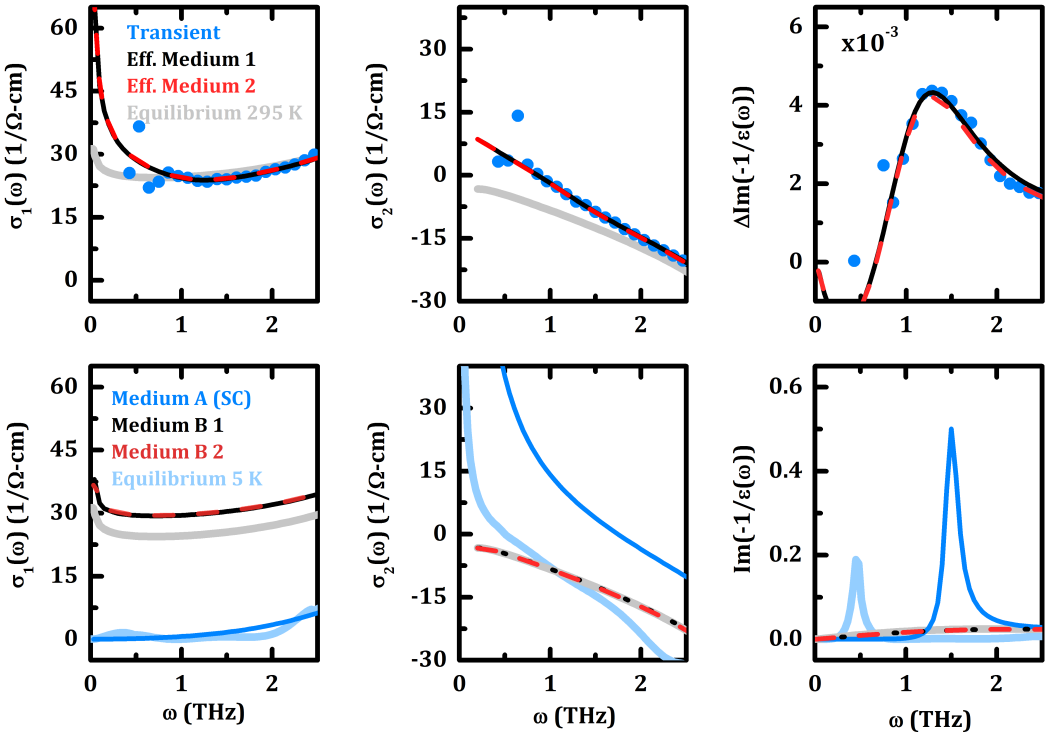

Figure 5.23: **Effective medium fit of YBCO 6.45 at 250 K. Top row:** The transient response (dots) fit with two effective medium models (black and red). Equilibrium data in grey. **Bottom row:** The two materials used in each effective medium model. Both utilize the same superconducting inclusions (blue lines). For comparison, the equilibrium response at 5 K is also shown (light blue). The medium b optical response is taken from the equilibrium spectrum (grey) with either a small Drude component added (red) or a constant addition to $\sigma_1(\omega)$ (black).

Effective medium fits at three temperatures calculated using the above method are shown in Figures 5.24 (YBCO 6.45), 5.25 (YBCO 6.5), and 5.26 (YBCO 6.6). The grey region indicates the lower limit of the trusted THz spectral range, where some spectral content remains but is noisy due to diffraction fringes at frequencies comparable to the sample size. The volume fraction values f extracted from the fits and $\omega\Delta\sigma_2(\omega)$ are plotted in Figure 5.27. The volume fraction tracks the inductive response, $\omega\Delta\sigma_2(\omega) \propto f$, suggesting that primary effect of increasing temperature is not a softening of the mode, but rather a reduction in the volume fraction of the material that is excited. For all dopings and temperatures, the maximum superconducting volume fraction f did not not exceed 20%, well below the percolation threshold $f_c \approx 33\%$.

The origin of the inhomogeneity of the transient response is probably tied to inhomogeneity of the samples. The inherent inhomogeneity of cuprate crystals has been shown to produce spatial variation in their equilibrium properties, including the superconducting order parameter [82, 112]. Inhomogeneous excitation is especially unsurprising here, given that the mid-infrared pump targets a mode associated with just the YBCO 6 sublattice. Resonant absorption would only occur in those regions of the lattice where the chain oxygen atoms are absent. The volume fraction of the crystal occupied by the YBCO 6 sublattice reduces as the doping increases to $x = 7$. Accordingly, we find that the volume fraction occupied by the transient plasmon decreases with increased doping, as shown in Figure 5.27[6].

[6]The YBCO 6.3 response has not yet been fit with the inhomogeneous model described here. It will be fit once the equilibrium spectrum has been measured.

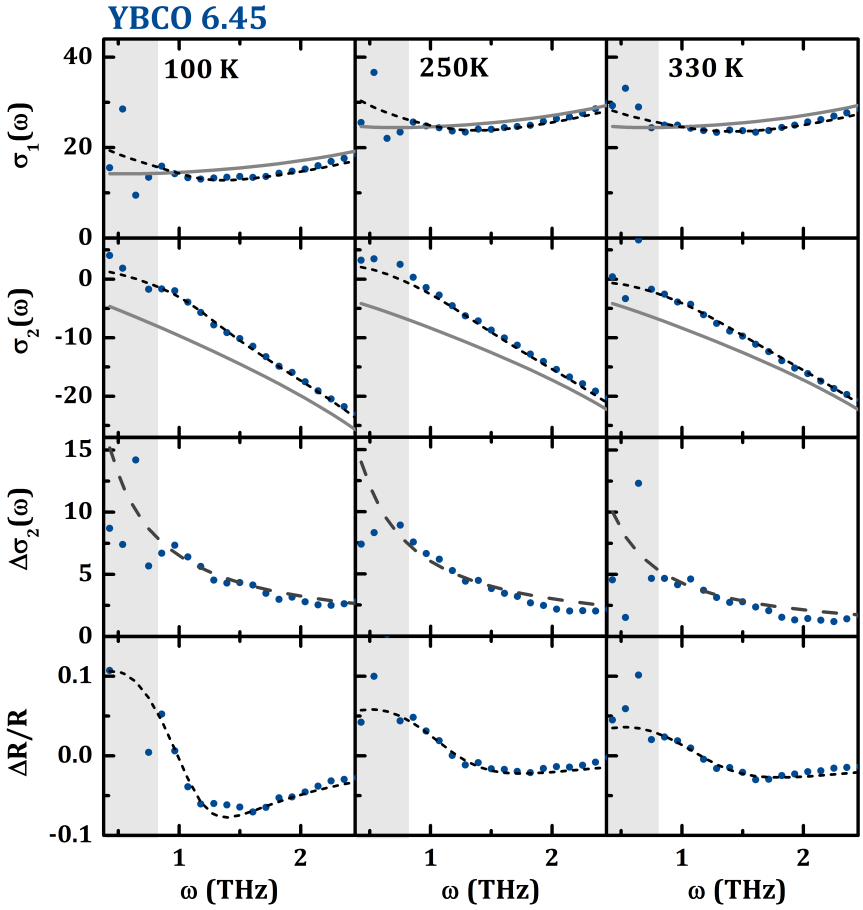

Figure 5.24: **Effective medium fits for YBCO 6.45 at three temperatures.** The transient (blue dots) and equilibrium (grey line) Ohmic conductivity $\sigma_1(\omega)$ is plotted in the first row and inductive conductivity $\sigma_2(\omega)$ in the second row. The changes in the inductive conductivity, $\Delta\sigma_2(\omega) = \sigma_2(\omega) - \sigma_{2,eq}(\omega)$ (third row) are fit to $\tilde{n}/\omega$ (grey dashed line). The change in reflectivity $\Delta R/R$ is plotted in the fourth row. Effective medium fits are indicated with black dashed lines. The grey shaded regions indicate the low frequency limit of the THz spectrum.

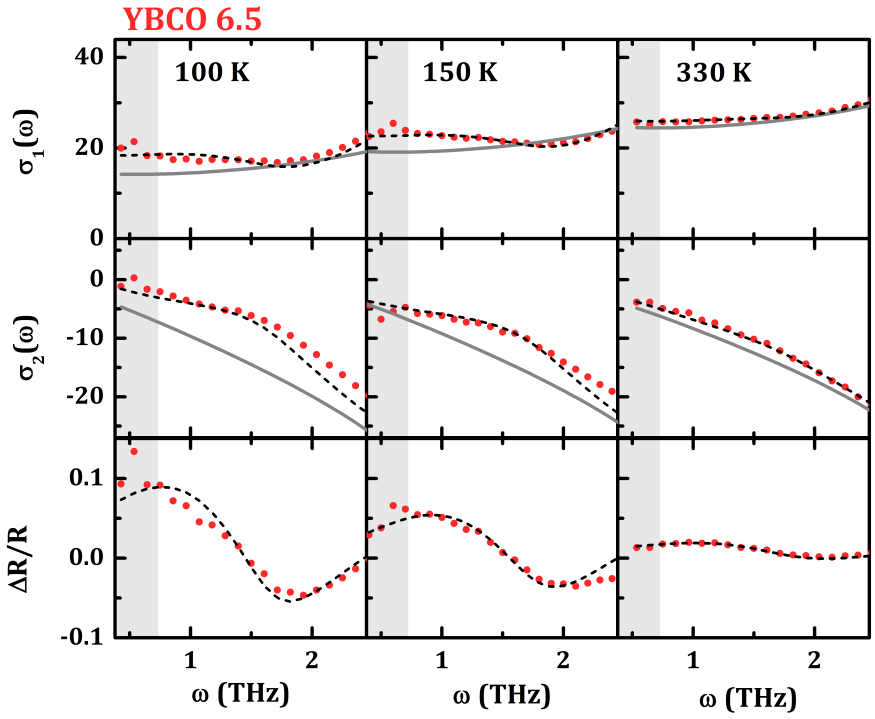

Figure 5.25: **Effective medium fits for YBCO 6.5 at three temperatures.** The transient (red dots) and equilibrium (grey line) Ohmic conductivity $\sigma_1(\omega)$ (first row), inductive conductivity $\sigma_2(\omega)$ (second row) and the change in reflectivity $\Delta R/R$ (third row). Effective medium fits are indicated with black dashed lines. The grey shaded regions indicate the low frequency limit of the THz spectrum.

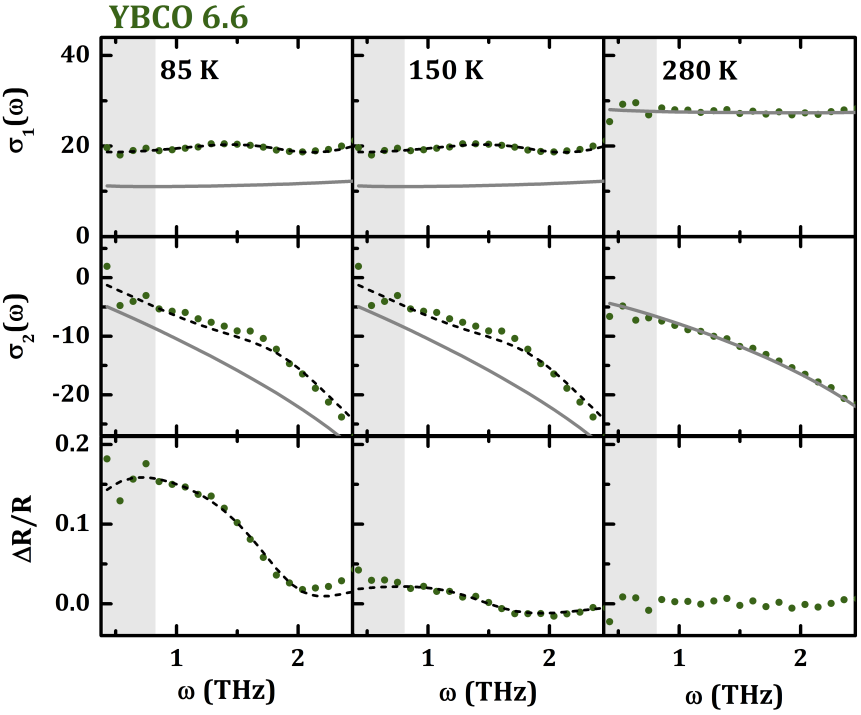

Figure 5.26: **Effective medium fits for YBCO 6.6 at three temperatures.** The transient (green dots) and equilibrium (grey line) Ohmic conductivity $\sigma_1(\omega)$ (first row), inductive conductivity $\sigma_2(\omega)$ (second row) and the change in reflectivity $\Delta R/R$ (third row). Effective medium fits are indicated with black dashed lines. The grey shaded regions indicate the low frequency limit of the THz spectrum.

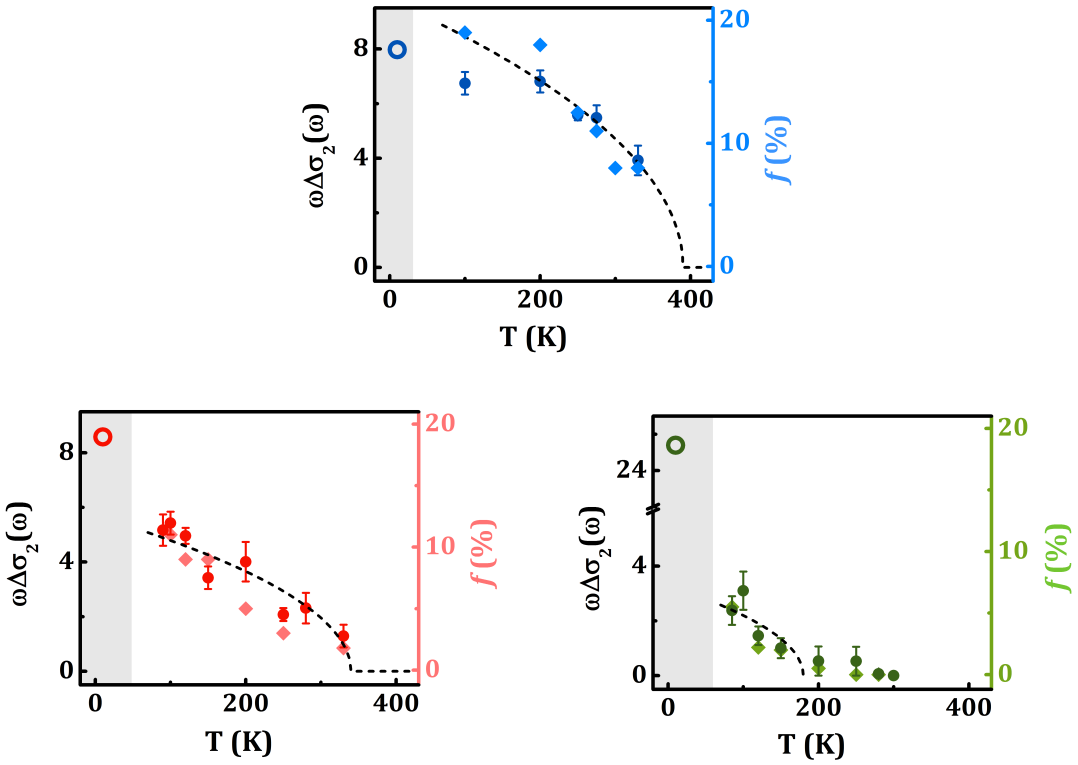

Figure 5.27: **Temperature dependence of the transformed volume fraction.** The temperature dependence of the volume fraction f (diamonds) tracks the inductive response $\omega\Delta\sigma_2(\omega)$ (circles). Dashed lines indicate a mean field fit, $\sqrt{1-T/T'}$. Equilibrium superfluid density at 5 K indicated by empty circles.

5.6 Transient a-axis optical response, $T > T_c$

So far we have only considered the optical response along the c-axis. The enhanced coupling of the planes may also indicate a change in the response within the CuO_2 planes as well. The a-axis inductive conductivity below T_c reflects the total condensate density, as we saw in Section 5.3.1, and one may suppose that a stiffening of the condensate phase between planes may also imply a stiffening within each plane as well. Unfortunately, the THz reflectivity in-plane is nearly 1.0 below T_c due to screening by Cooper pairs below the superconducting gap. Accurately measuring the full transient response with such high reflectivities is a challenge, because even relatively small amounts of noise in the THz source or in the phase of the reflected field are amplified to the point where they can qualitatively distort the response.

Even above T_c, the THz response is metal-like, with a reflectivity on order $\sim$0.98. However, in this regime we were able to accurately and repeatably measure the transient response. After excitation of the apical oxygen, the transient conductivity does not show evidence of an enhanced mobility. Rather, the changes in the response are quite small and consistent with quasiparticle heating. Figure 5.28 shows the transient response at 70 K along with the equilibrium response at 70, 100, and 150 K. Unlike the c-axis response, the in-plane Ohmic conductivity in the THz regime drops with increasing temperature, due to increased quasiparticle scattering.[7] There is a corresponding decrease in the inductive conductivity and reflectivity. The transient response exhibits the same trend. The magnitude of the transient response decreases with increasing base temperature, though the qualitative behavior remains the same, as shown in Figure 5.29.

[7] A gapped state, by contrast, exhibits an *increase* in the THz Ohmic conductivity with temperature, due to an increase in the number of thermally populated carriers.

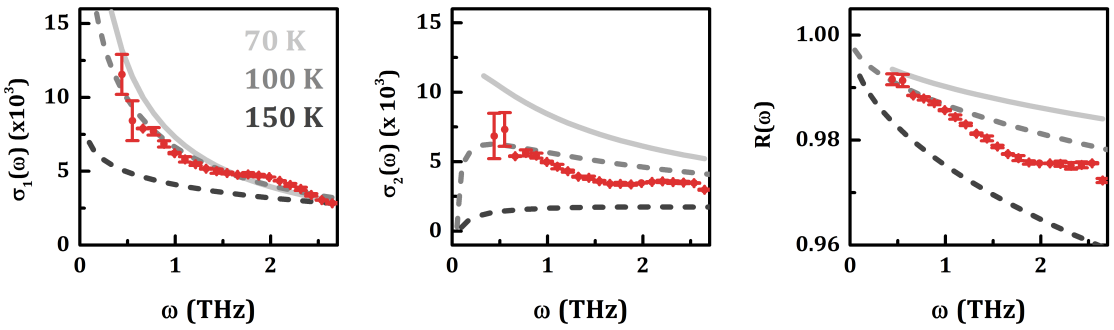

Figure 5.28: **Transient a-axis response of YBCO 6.5 at 70 K.** From left to right, the Ohmic conductivity $\sigma_1(\omega)$, inductive conductivity $\sigma_2(\omega)$, and the reflectivity, $R(\omega)$. The equilibrium response at 70, 100, and 150 K are in grey and the transient response is shown in red at the peak of the excitation. Error bars reflect the propagated standard deviation in the THz reflectivity, averaged over several scans.

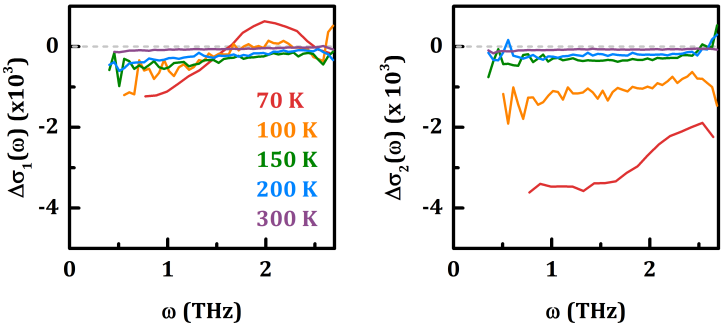

Figure 5.29: **Temperature evolution of the transient a-axis conductivity of YBCO 6.5.** Transient changes in the optical conductivity, $\Delta\tilde{\sigma}(\omega) = \tilde{\sigma}(\omega) - \tilde{\sigma}_{\mathrm{eq}}(\omega)$, at several temperatures between 70 and 300 K.

5.7 Role of the mid-infrared pump

5.7.1 Fluence dependence

The inductive response increases with increasing pump field, as shown in Figure 5.30, up to the highest fluences we could reach (3 MV/cm $\approx$ 4 mJ/cm^2). The fluence dependence of the inductive response at all temperatures can be fit with a saturation model, $\omega\Delta\sigma_2 = \tilde{n}_{\mathrm{max}}(1 - \exp(-\Phi/\Phi_0))$, with $\Phi_0 = 2.4$ MV/cm.

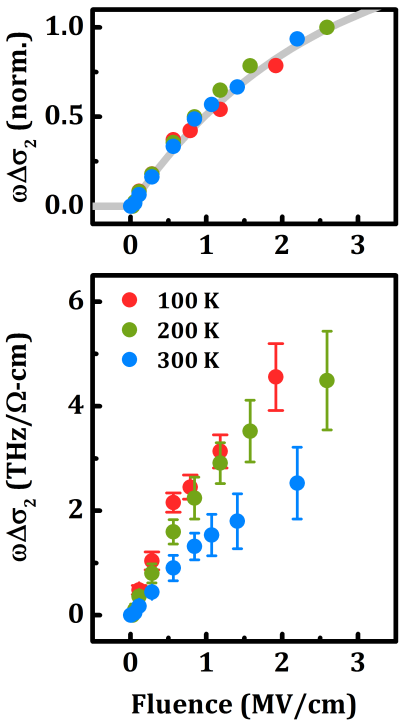

Figure 5.30: **The effect of pump fluence on the inductive response.** The inductive response, $\omega\Delta\sigma_2(\omega)$ of YBCO 6.45 at 100 K (red), 200 K (green) and 300 K (blue). While the inductive response decreases with temperature, the saturation scaling remains temperature independent. The response at all temperatures can be well-fit with the saturation relation $\omega\Delta\sigma_2 \propto (1 - \exp(-\Phi/\Phi_0))$ (grey line).

The pump-induced optical response of YBCO 6.45 at 300 K is shown in Figure 5.31 at three fluences, from 3 down to 0.3 MV/cm. One immediately noticeable feature of the response is that while the inductive conductivity drops with decreasing fluence, the plasma mode does not red shift by an equivalent degree. We quantify this relationship using an effective medium fit, indicated by the dashed lines in Figure 5.31. The inductive response $\omega\Delta\sigma_2(\omega)$, screened plasma frequency $\tilde{\omega}_p = \omega_p/\sqrt{\varepsilon_{FIR}}$[8], and volume fraction f are all plotted in the left-hand panel of Figure 5.32 for YBCO 6.45 at 300 K. While the plasma frequency changes by roughly 1/3 over the fluence range measured, the inductive response changes by a factor of 3. The breakdown of the

[8]The reflectivity edge due to the plasmon does not occur precisely at the plasma frequency, ω_p, but is shifted due to decoherence, as well as other higher frequency intra- and interband contributions to $\varepsilon_{1,\mathrm{eq}}$ which can be captured in the THz regime by a single parameter $\varepsilon_{\mathrm{FIR}}$. For the plasma mode $\tilde{\omega}_p$ reported here, we take $\varepsilon_{\mathrm{FIR}} = 30$, a standard value for cuprates [113].

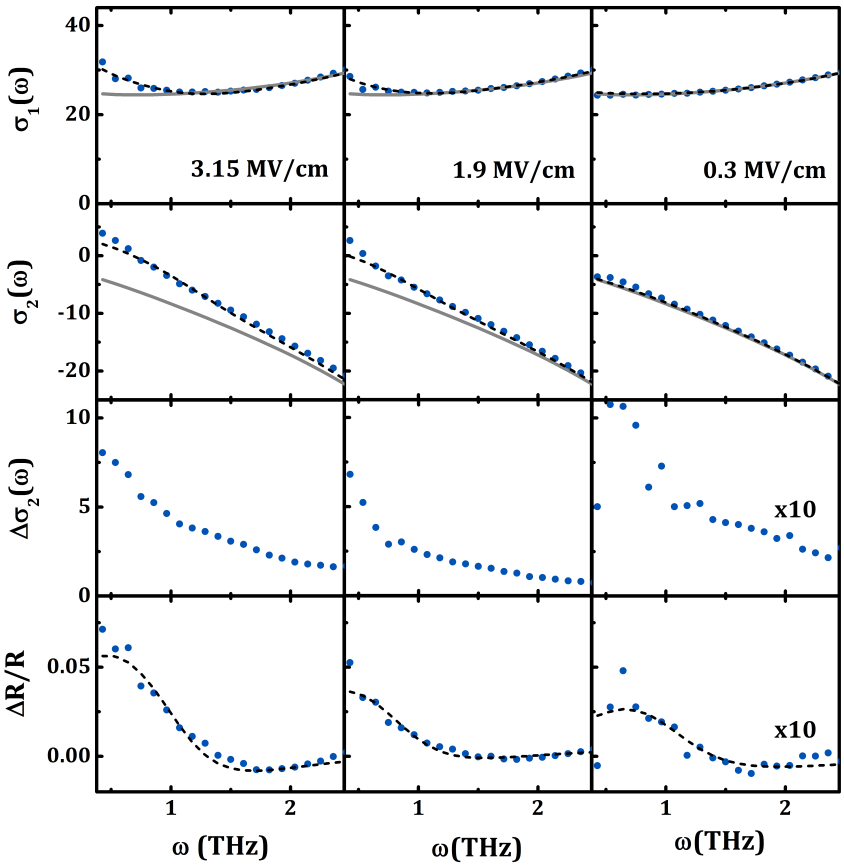

Figure 5.31: **Transient response of YBCO 6.45 at 300 K at three fluences.** The transient (blue dots) and equilibrium (grey line) Ohmic conductivity $\sigma_1(\omega)$ is plotted in the first row and inductive conductivity $\sigma_2(\omega)$ in the second row. The changes in the inductive conductivity, $\Delta\sigma_2(\omega) = \sigma_2(\omega) - \sigma_{2,eq}(\omega)$ are plotted in the third row and the changes in reflectivity $\Delta R/R$ in the fourth row. Effective medium fits are indicated with black dashed lines.

relationship $\omega\Delta\sigma_2 \propto \omega_p^2$, which holds for superconductors in equilibrium, can be understood as a consequence of the excitation being inhomogeneous: the effective carrier density (and tunneling rate) remaining only weakly fluence dependent while the total volume of the photo-excited inclusions decreases.

If there is a minimum cut off fluence necessary to induce the transient effect, it must be very low. The transient mode was detected down to 0.1 MV/cm. Below that fluence, detection of the mode may be limited by the THz noise. The inductive response also did not saturate up to the highest fluence we could achieve, about 3

MV/cm, leaving open the tantalizing possibility that a higher fluence may be able to drive the system past the percolation threshold, $f \approx 0.33$. From the saturation model, the highest volume fraction achievable would be $f \approx 0.24$ at 100 K and just $f \approx 0.12$ at 300 K, well below percolation. However, the fluence dependence of f can also be well-fit with a simple linear relationship, which is also in good agreement with the inductive conductivity within our resolution, as shown by the grey line in Figure 5.32. Assuming a linear trend with the pump field, percolation ($f = 0.33$) would be reached at a fluence of 9.9 MV/cm, a little over triple the field we can currently generate.

The right panel of Figure 5.32 shows the inductive response at six fluences (colored dots). The 200 K $\omega\Delta\sigma_2(\omega)$ values have been renormalized to the same level in order to emphasize the temperature evolution of the inductive response. At lower fluences, < 0.8 MV/cm, there appears to be some drop in critical temperature T' with pump fluence, however, within one standard deviation of $\omega\Delta\sigma_2(\omega)$, the temperature T' remains fluence independent.

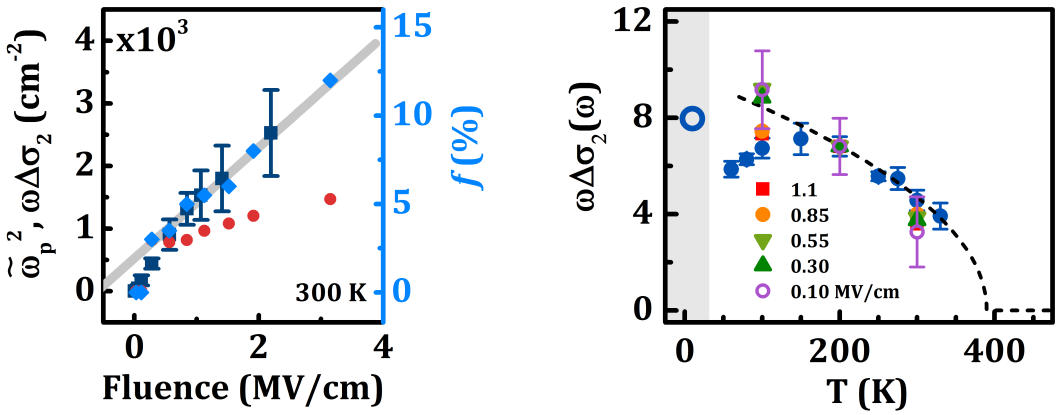

Figure 5.32: **The fluence dependence of the plasmon. Left:** The plasma mode (red dots) and inductive response (blue squares) are both plotted in units of cm^{-2}. The volume fraction f (blue diamonds) tracks the inductive response. Both f and $\omega\Delta\sigma_2$ can be well-fit using either a saturation relation (see Figure 5.30) or a linear fit with pump field (grey line). **Right:** The inductive response at 100 K, 200 K, and 300 K at several fluences between 1.1 and 0.1 MV/cm. They are vertically rescaled so that the 200 K values are equal in order to better visualize the temperature dependence. The highest fluence, 3 MV/cm, is also shown (blue).

5.7.2 Wavelength dependence

We have seen indirectly from the optical response of YBCO 7, and from the doping dependence of the excited volume fraction f, that the transient mode does appear to be dependent on the excitation of the apical oxygen phonon. By varying the pump wavelength, we find that the inductive response is enhanced as resonance is approached from higher frequency. Figure 5.33 plots the peak inductive response in YBCO 6.45 as a function of pump wavelength. The equilibrium $\sigma_1(\omega)$, which peaks at the resonant mode frequency, is also shown. The dashed line represents a Lorentzian fit to the phonon and the pink Gaussian represents the same mode convolved with the pump spectral width. At each wavelength, the average power was adjusted to maintain the same photon count. Frequencies lower than 19 THz (16 μm) cannot be readily reached with sufficient fluence using our optical parametric amplifier (see Section 2.2), so the regime below the resonance frequency cannot be accessed.

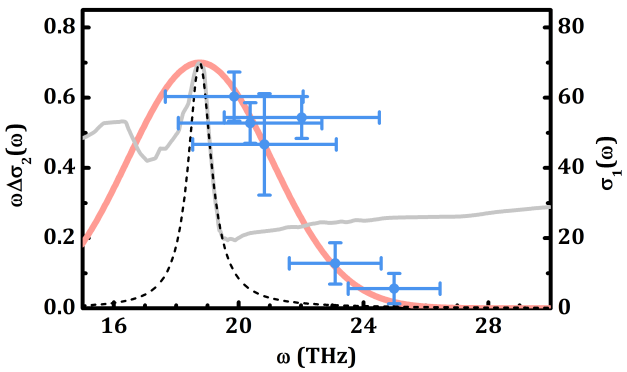

Figure 5.33: **Wavelength dependence of the transient inductive response.** The inductive response $\omega\Delta\sigma_2(\omega)$ at six pump wavelengths (blue dots). The real conductivity $\sigma_1(\omega)$ (grey line) peaks at the B_{1u} phonon frequency. The mode is modeled by a Lorentzian (dashed line). The Gaussian curve (pink) has a width indicating the spectral width of the pump.

5.7.3 Pumping other phonon modes

As a further test that the optical response is due to resonant excitation of the apical oxygen, we pumped at the same frequency along the a-axis. A B_{3u} Cu-O stretching mode of the CuO_2 planes exists along the a-axis at a frequency similar to the c-axis apical oxygen mode [155]. This mode is analogous to the E_u Cu-O stretching mode of $La_{1.8-x}Eu_{0.2}Sr_xCuO_4$ that is targeted in Chapter 4. The penetration depth along the a- and c-axes are plotted in the left panel of Figure 5.34 along with the spectrum of the MIR pump. A kink in the a-axis spectrum (grey) indicates the frequency of the phonon. The resonant motion of the O(3) oxygen atoms is illustrated in the right panel.

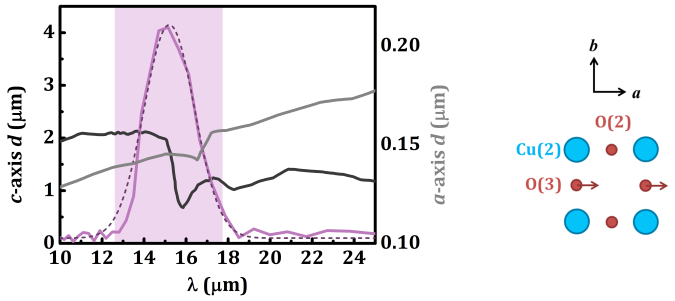

Figure 5.34: **In-plane phonon of YBCO at 15 μm. Left:** The penetration depth d of YBCO 6.5 along the c-axis (black) and a-axis (grey). The pump spectrum is also shown (purple) along with a Gaussian fit (dashed line). The pump width is $\sigma = 1.5$ μm. **Right:** The copper (blue) and oxygen (red) atoms in the CuO_2 planes. The motion of the Cu-O stretching mode is indicated by the arrows.

The c-axis THz response after a-axis pumping is qualitatively quite different than what is observed from c-axis pumping, as illustrated in Figure 5.35 for YBCO 6.5 at 300 K. The most dramatic change in the response is a drop in the inductive conductivity upon photo-excitation. The Ohmic conductivity remains unaffected by the pump in the THz spectral window.

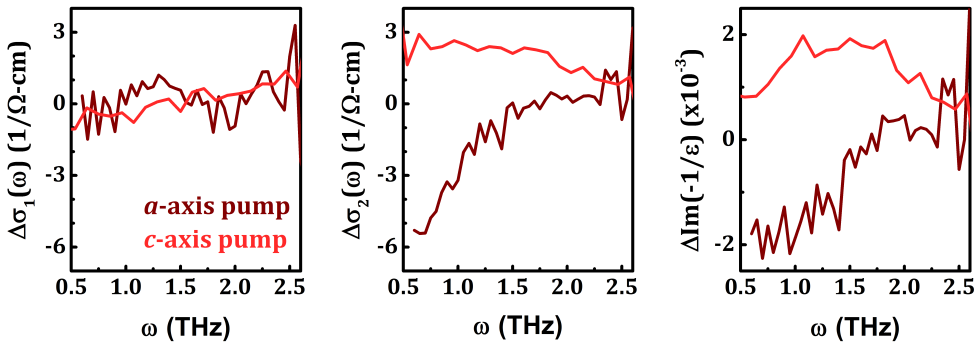

Figure 5.35: **In-plane phonon pumping of YBCO 6.5.** The photo-induced response along the c-axis 0.6 ps after excitation at 300 K. The response is shown with the 15 μm excitation is aligned along the a-axis (dark red) and c-axis (red).

5.8 Discussion of these results

The origin of the transient plasmon has been ascribed in Refs. [1, 2] to a Josephson plasmon produced by pair tunneling, even far above T_c. From a competing order perspective, this interpretation would imply that external driving can support the superconducting order in overcoming a competing pseudogap instability. From the perspective of a pseudogap in which superconducting fluctuations survive, these results support the notion that stiffening the superconducting phase is key to increasing T_c. Here I will first examine alternate ideas for the plasmon origin, then consider these results in the context of transient superconductivity.

Below T_c, the transient plasmon blue shifts continuously from the equilibrium Josephson plasmon, leaving little doubt as to the origin of the carriers. Here we see the least controversial proof that apical oxygen excitation promotes pair tunneling across the inter-bilayer gap. Some broadening of the plasmon accompanies the blue shift, which can be tied to two origins. One, the excitation also results in some quasiparticle excitation, and perhaps inhomogeneity [82], of the stiffened phase. And two, some of the apparent broadening is actually a splitting of the resonance due to the inhomogeneous excitation of the apical oxygen, which is discussed in some detail in Chapter 7.

Above T_c, the situation is less immediately clear. The frequency and the doping dependence of the transient plasma frequency offer strong evidence, at least, that the carriers generating the mode are the same carriers that condense below T_c and contribute to Josephson tunneling. Even in YBCO 6.3, which does not achieve bulk

superconductivity down to 5 K, the small diamagnetic response of the material at lowest temperatures suggests that some pairing does occur in equilibrium.

One straightforward interpretation would be that the transient carriers, un-paired in the pseudogap regime, are dynamically driven into a high mobility state, perhaps from the gapped out regions of the pseudogap. A high mobility state, with relatively few carriers, would generate a Drude response in this frequency range.

While such a high mobility state would be novel in itself, the fluence dependence of the transient plasmon does not support such an interpretation. The density of photo-excited carriers should increase with the number of absorbed photons, but we find that the plasma frequency remains roughly fixed for all pump fluences. Instead the *fraction* of the sample volume that develops the plasmon increases, at constant density. Moreover, the relaxation pathway of the plasmon, discussed in Chapter 7, suggests that decoherence effects govern the time evolution of the mode. For quasiparticle excitation, one would expect a relaxation governed by the depletion of excited carriers (see discussion in Section 4.7).

A more exotic high mobility state would be the sliding charge density wave (CDW) [122–124], where the pump acts to de-pin the CDW. Incommensurate charge density wave order was recently discovered in parts of the pseudogap regime [91]. However, the CDW regime does not track the doping or temperature scale of the transient state reported here.

Let us now consider what mechanisms could drive transient pair tunneling above T_c. Photo-induced redistribution of quasiparticles, leading to an effective doping of the condensate, has been shown to enhance superconductivity at microwave [164–166] and optical [11, 12] frequencies. However, this mechanism is unlikely to be the origin here. First, the frequency of the transient plasmon suggests a carrier density comparable to the equilibrium condensate. Second, the transient state tracks the phonon resonance, disappearing at higher frequency, whereas charge excitations should still be generated above the phonon resonance.

The process may be inherently non-equilibrium, where the dynamic motion of the apical oxygen is directly enhancing the tunneling of pairs. In response to our findings, this scenario was recently modeled by R. Höppner and collaborators in the group of Ludwig Mathey [167]. They found that driving a bilayer superconductor with an oscillating field gradient produced a net cooling of the phase fluctuations across the interbilayer junction, and an increase in fluctuations across the bilayer. This is compatible with both the observations above and below T_c. Cooling of the phase in the superconducting state would support Josephson tunneling, leading

to a blue shift of the interbilayer Josephson plasmon. Likewise, in a pseudogap state with surviving fluctuating superconductivity, cooling the fluctuations could permit a finite Josephson current that is suppressed in equilibrium. Along these lines, recent optical conductivity measurements [85] suggest that tunneling across the short bilayer junction does in fact persist into the pseudogap state, implying that local phase coherence between neighboring planes survives the destruction of bulk superconductivity. This scenario is explored more in Section 6.2.

Höppner, *et al.* [167] found that the oscillating field did not produce a homogeneous cooling of the interbilayer, but rather that phase fluctuations developed hot and cool spots on the planes. This may account for the *a*-axis response reported in Section 5.6. The in-plane conductivity may remain dominated by the "resistive" component—the normal regions of the planes—while the *c*-axis response is dominated by the Josephson channel. Only phase coherence between planes would be enhanced by the *c*-axis excitation. This scenario is illustrated in Figure 5.36.

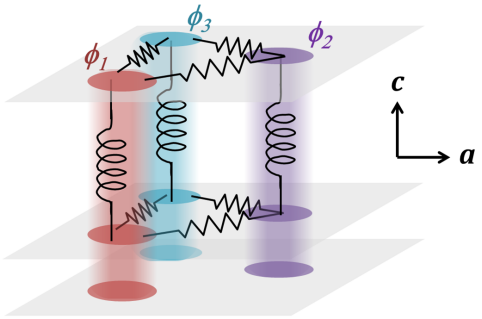

Figure 5.36: **In-plane and *c*-axis coupling of an inhomogeneous superconducting state.** The CuO_2 planes are illustrated as grey squares containing colored regions of superconducting pairing with order parameter phase ϕ. While phase coherence is enhanced along the *c*-axis, regions remain phase-incoherent in-plane.

Other mechanisms may also be at play. Non-linear coupling of the B_{1u} mode to Raman modes has been shown to lead to a deformation of the YBCO lattice [3]. This deformation forms and relaxes on the same timescale as the transient plasmon. If the transient lattice structure is responsible for enhanced superconductivity, then

perhaps one could entertain the prospect of engineering such a structure in equilibrium. The role of lattice deformation for the transient optical response is discussed further in Section 6.3. Finally, the underdoped regime has recently been shown to support a charge density wave state that may compete with superconductivity [91]. Using inelastic x-ray scattering, we have shown that the mid-infrared excitation we employ does reduce charge order [42]. This experiment is discussed in Section 6.4.

Chapter 6

The origin of the transient plasmon in underdoped $YBa_2Cu_3O_x$

6.1 Introduction

The discovery of the transient plasmon in YBCO discussed in Chapter 5 and continued in Chapter 7 has spawned several follow-up projects, which I will briefly discuss here. Each of these experiments targets a different possible mechanism for the generation of transient interbilayer coupling. All three have, as their motivation, the interpretation that the plasmon arises from Josephson tunneling, even above T_c in the pseudogap state.

First we consider whether the excitation is causing pair formation or rather promoting pair tunneling, for example by stiffening the phase of the condensate. This question inspired the development of a broadband THz set-up to investigate the high frequency response of the material, including the transverse mode and the bilayer Josephson plasmon. This project was led by Wanzheng Hu and Isabella Gierz.

The second project, led by Roman Mankowsky and Alaska Subedi [3], looked at lattice deformation as a possible origin of enhanced tunneling. The nonlinear coupling of the B_{1u} excitation to Raman modes was found to cause shifts in atomic positions within the lattice. Here I will briefly discuss their results and offer some of my own thoughts and analysis.

The third project investigated the role of the recently discovered charge density wave (CDW) order in underdoped YBCO [91]. In this project [42], led by Sarnjeet Dhesi and Michael Först, we sought to address whether suppressing a competing charge order could promote superconductivity and account for the observed enhanced tunneling, perhaps in a similar manner to what is observed in $LaEu_xSr_{2-x}CuO_4$ [33, 34]. Using time-resolved soft x-ray diffraction, we could measure the effect of apical oxygen excitation on the charge density wave order. We

found that although the excitation suppresses the CDW ordering by roughly 50%, charge order destruction is likely not the primary cause for the transient effect we see.

6.2 Redistribution of coupling strengths

So far I have presented only the pump-induced behavior of the interbilayer plasmon and the low frequency conductivity. This regime, below 3 THz, is critical for measuring the superconducting response, as this is where the condensate shapes the inductive conductivity most dramatically. However, this is not the whole story. Because YBCO has a bilayer structure, with two CuO_2 planes per unit cell, the tunneling across each gap–the smaller *bilayer* and larger *interbilayer*–both determine the effective c-axis effective carrier density and thus the macroscopic superconducting behavior.

We have already seen in Section 3.2 that the intrinsic bilayer and interbilayer Josephson junctions of YBCO gives rise to a transverse plasma mode, which appears as a broad peak at about 400 cm^{-1} (12 THz) in YBCO 6.5. This mode shares spectral weight with the condensate at $\omega \approx 0$ [83]. The transient increase in spectral weight of $\sigma_1(0)$, as observed by the low frequency increase in $\omega\Delta\sigma_2(\omega)$, is therefore only part of the picture. The combined spectral weight of both modes is necessary to determine how the pair density shifts in time.

A plasma source was developed for generating broadband THz in order to probe the transient response of YBCO 6.5 up to 500 cm^{-1} (15 THz). Below T_c, pumping the apical oxygen mode leads to a red shift in the bilayer plasmon, as illustrated in Figure 6.1.B. The shifts of the interbilayer plasmon ω_{IB} and bilayer plasmon ω_B were found to conserve the loss function spectral weight, $\int_0^\infty \Im(-1/\epsilon)d\omega \equiv \omega_p^2$, such that before and after excitation, $\omega_{IB}^2 + \omega_B^2 =$ constant. The bilayer mode red shifts and relaxes on the same timescale as the blue shift of the interbilayer plasmon.

The red shift of the plasmon is accompanied by a red shift of the transverse mode, shown in Figure 6.1.C. Within the van der Marel and Tsvetkov picture (Equation 3.5) the frequency of the transverse mode is given by a weighted sum of the two Josephson plasma frequencies, $\omega_T^2 = z_{IB}\omega_B^2 + z_B\omega_{IB}^2$. At constant spectral weight, we can describe the shift in frequencies as $\bar{\omega}_{IB}^2 = \omega_{IB}^2 + \delta$ and $\bar{\omega}_B^2 = \omega_B^2 - \delta$, and therefore the shift in the transverse mode frequency is $\bar{\omega}_T^2 = \omega_T^2 + \delta(z_B - z_{IB})$. The

weights z_{IB} and z_B are largely determined by the relative volumes of each junction [77] and thus the redshift in ω_T can be seen as a consequence of $z_{IB} > z_B$.

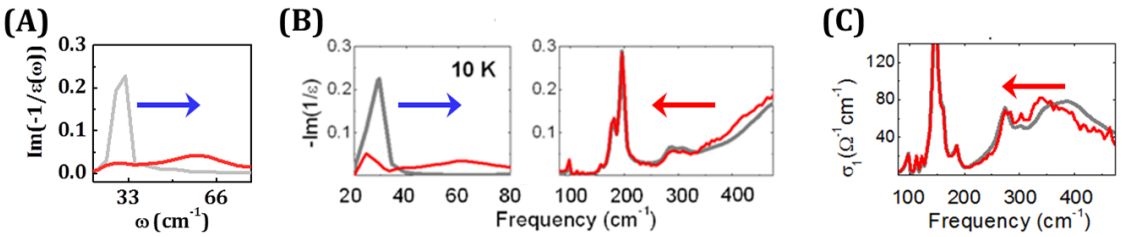

Figure 6.1: **Broadband transient response of YBCO 6.5 at 5 K. (A)** The transient (red) and equilibrium (grey) loss function $\Im(-1/\epsilon)$ measured with ZnTe THz generation. **(B)** The loss function measured with plasma generated THz, showing the blue shift of the interbilayer mode and the red shift of the bilayer mode. **(C)** The broadband Ohmic conductivity, showing a red shift of the transverse mode. Panels (B) and (C) adapted from Hu, *et al.* [1]

The shift in spectral weight from the bilayer mode to the interbilayer mode can be understood as a redistribution of coupling strength, favoring tunneling across the larger interbilayer gap at the expense of tunneling within the bilayer. The conservation of spectral weight suggests that the pair density itself is not altered by the excitation. Indeed, Hu found that the loss in spectral weight from the transverse mode,

$$\left(\frac{120}{\pi}\right)\int_{20\ \mathrm{cm}^{-1}}^{500\ \mathrm{cm}^{-1}}(\sigma_1(\omega)-\sigma_{1,eq}(\omega))d\omega = -1.0\times10^5\ \mathrm{cm}^{-2}, \tag{6.1}$$

is approximately that gained by the interbilayer plasmon, $\Delta SW = \bar{\omega}_{IB}^2 - \omega_{IB}^2 = 8.4\times10^4\ \mathrm{cm}^{-2}$. It is also approximately the gain in spectral weight of $\sigma_1(0)$, as measured by $\omega\Delta\sigma_2(\omega) \approx 1.7\times10^5\ \mathrm{cm}^{-2}$ (see Section 5.3.2 for a discussion of the transient low frequency response). The gain in the apparent condensate density can therefore be attributed to a transfer of spectral weight from the transverse mode to $\sigma_1(0)$. That is, the redistribution of coupling strengths drives more pairs to contribute to the condensate rather than be "wasted" on the finite frequency mode. A cartoon depicting the transfer of spectral weight is shown in Figure 6.2.

The dynamic motion of the apical oxygen may account for the enhancement of interbilayer coupling. This scenario was modeled by the group of Ludwig Mathey

[167]. They found that driving a bilayer superconductor with an oscillating field gradient produced a cooling of the phase fluctuations across the long junction, and an increase in fluctuations across the short.

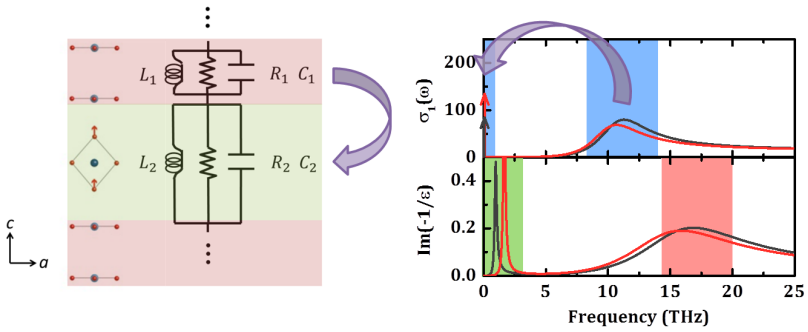

Figure 6.2: **Redistribution of coupling strengths. Left:** The Cu (blue) and O (red) atoms of the YBCO lattice with the intra-bilayer (red) and interbilayer (green) regions highlighted. **Right:** Calculations of the two plasmons using Equation 3.5 at equilibrium (grey) and after excitation (red). The redistribution of coupling strengths is depicted in this figure with exaggerated shifts in the intra- and interbilayer plasmon positions to highlight the red shift in the transverse mode peak position and loss of spectral weight. Purple arrows indicate the redistribution of coupling strength to the interbilayer leading to an increase in the spectral weight at $\sigma_1(0)$.

Above T_c, a similar mechanism seems to be at work. The response at 60 K (T_c = 51 K) is shown in Figure 6.3. In equilibrium, the broad peak in the loss function associated with the bilayer plasmon and the peak in $\sigma_1(\omega)$ associated with the transverse mode both appear to survive above T_c (see Figure 3.5). Again we see a red shift in the positions of the transverse mode and the bilayer plasmon after optical excitation. This is accompanied by the appearance of the peak in the loss function near the equilibrium interbilayer Josephson resonance frequency. The shifts of the higher frequency modes occur on the same timescale as the appearance and relaxation of the lower frequency plasmon.

These results support recent analysis of YBCO and related compounds that found that bilayer coupling extends deep into the pseudogap state [85]. Moreover, the ap-

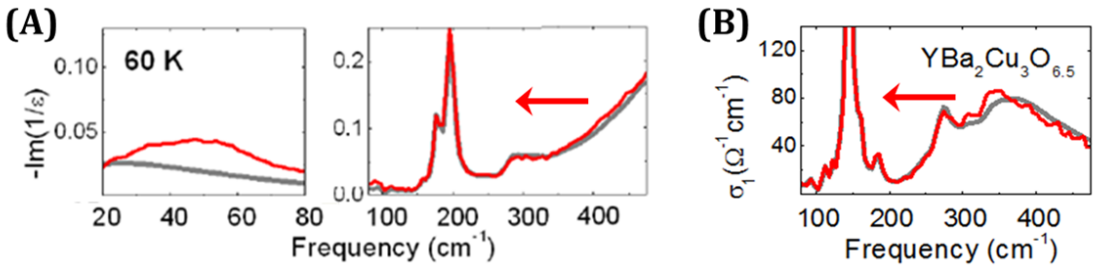

Figure 6.3: **Broadband transient response of YBCO 6.5 at 60 K (A)** The transient (red) and equilibrium (grey) loss function $\Im(-1/\epsilon)$, showing the appearance of a low frequency mode and the red shift of the bilayer mode. **(B)** The broadband Ohmic conductivity, showing a red shift of the transverse mode.

pearance of the transient interbilayer mode up to T^* suggests that this region of local bilayer coupling extends even higher in temperature than it could be detected in Ref. [85]. Distinguishing the onset temperature for the transverse mode is complicated by the presence of phonons near the transverse plasmon frequency. In underdoped YBCO, one phonon mode in particular (at 320 cm^{-1} in YBCO 6.5) couples strongly to the transverse mode, distorting its shape. The persistence of locally coherent superconducting pairing throughout the pseudogap would lend strong credence to theoretical ideas that associate the pseudogap phase with fluctuating superconductivity.

6.3 Distortion of the lattice

Infrared active lattice modes are dipole excitations that do not produce a net distortion in the lattice. However, nonlinear coupling to Raman active modes can generate transient, net shifts in atomic positions. The lowest order coupling to Raman modes are the $Q_1^2 Q_2$ couplings, which can be expressed in the Hamiltonian for a Raman mode R as

$$H_R = \frac{\omega_R^2}{2} Q_R^2 - a_{12} Q_{IR} Q_R^2 - a_{21} Q_{IR}^2 Q_R, \tag{6.2}$$

where Q_R is the normal coordinate of the Raman mode and Q_{IR} is the coordinate of the infrared driving mode. For centrosymmetric crystals like YBCO, the product $Q_{IR} Q_R^2$ vanishes since Q_{IR} and Q_R^2 have odd and even symmetries respectively. However, the $Pmmm(D_{2h}^1)$ space group symmetry of YBCO allows Q_{IR}^2 coupling of

B_{1u} modes to Raman modes of A_g symmetry. Along the Raman Q_R coordinate, the minimum energy position for the mode R shifts by $a_{21}Q_{IR}^2/\omega_R^2$.

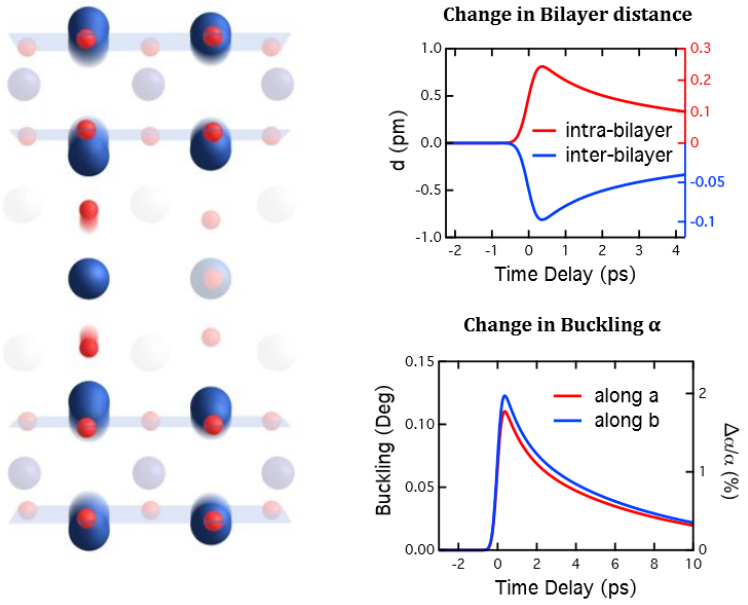

Figure 6.4: **Optically induced lattice distortion of YBCO 6.5. Left:** The copper (blue) and oxygen (red) atoms of the transient lattice structure of Ortho II YBCO 6.5 shown in the ac-plane, with the YBCO 6 structure (left column of atoms) and YBCO 7 (right) distinguished by the absence and presence, respectively, of the chain oxygen atom (center row of atoms). **Right:** The change in bilayer distance (top) and Cu(2)-O(2,3)-Cu(2) buckling along the a,b-axes (bottom). Figures from Mankowsky, *et al.* [3]

In order to determine the net distortions of the lattice, Mankowsky *et al.* [3] combined frozen phonon density functional theory (DFT) calculations of Ortho II YBCO 6.5 with measurements of the change in certain atomic positions using X-ray diffraction at the Linac Coherent Light Source (LCLS) free-electron laser. They could reconstruct a transient crystal structure that was found to form and relax on the same timescale as the transient optical response. The authors posit that this transient structure may be responsible for generating the transient plasmon, and that such a lattice, in equilibrium conditions, may support a superconducting state that survives up to room temperature. Since their work has received some public

attention[1], it is worthwhile to present their findings in brief and to discuss whether the transient structure could account for the formation of Josephson coupling far above T_c.

They looked at the change in intensity of a total of 8 Bragg peaks, four that should be affected by $Q_{IR}^2 Q_R$ coupling and another four by higher order $Q_{IR}^2 Q_R^2$ coupling. DFT calculations were made based on a frozen phonon distortion of the B_{1u} mode to predict the shifts in the Bragg peaks due to $Q_{IR}^2 Q_R$ coupling. While no $Q_{IR}^2 Q_R^2$ coupling was found, the the four peaks associated with $Q_{IR}^2 Q_R$ showed transient shifts that matched the relative intensity and direction of the frozen phonon calculations.

Using the measured magnitude of the intensity change in the Bragg peaks to determine the effective magnitude of the apical oxygen distortion (+2.2 pm), the authors could determine the full transient structure of the crystal.

Their primary findings are illustrated in Figure 6.4. The Ortho II crystal structure consists of alternating empty and filled Cu-O chains, corresponding to the YBCO 6 and YBCO 7 substructures respectively. The left column of atoms in Figure 6.4 shows the Cu (blue) and O (red) atoms of the YBCO 6 structure and the right column has the YBCO 7 structure. They are distinguished by the center row of atoms (extending into the page) which represent the Cu-O chains. The YBCO 6 substructure experiences the greatest shifts in atomic position, since only the YBCO 6 apical oxygen atoms are being excited.

The O(4) apical oxygen atoms move towards the CuO_2 planes. The Cu(2) planar copper atoms buckle after photoexcitation, increasing their angle with with the planar O(2) and O(3) oxygen atoms. We define the separation of the CuO_2 planes by the Cu(2) atomic positions. The increased buckling thus leads to an increase in the bilayer spacing and an equal decrease in the interbilayer spacing. Note that the Raman distortions conserve the net dimensions of the unit cell, meaning the overall c-axis unit cell length L is unchanged after optical excitation. This is an important contrast with other methods of distorting atomic positions in the unit cell—for example through pressure, strain, or doping–which do not conserve the cell volume.

[1]For example, in online articles on Science Daily, Science Alert, Business Standard, and EE Times amongst many others.

6.3.1 Comparison of the transient lattice structure with equilibrium distortions

To assess whether or not the transient lattice structure may support bulk superconductivity at temperatures comparable to the pseudogap line, I will briefly compare the transient structure with equilibrium studies of cuprate lattice structure. There are several studies that compare the superconducting response to the relative atomic positions within the lattice, across families of cuprates [153, 154] and under strain [24, 26, 27] and pressure [168]. These studies have primarily focused on the role of the apical oxygen and the buckling of the CuO_2 plane, which occurs concomitantly.

The relationship between these atomic distortions and superconductivity is still not entirely clear. A positive correlation between T_c and *increasing* apical oxygen distance from the CuO_2 planes is found when comparing between different families of cuprates [153]. However, this finding runs counter to the trend measured by studying the naturally occurring local variations in the apical oxygen position in $Bi_2Sr_2CaCu_2O_x$ with scanning tunneling microscopy [27]. Across underdoped and overdoped compounds, it was found that *decreasing* apical oxygen distance from the CuO_2 planes corresponded with a larger local gap energy.

A systematic study of $YBa_2Cu_3O_x$ was performed by Jin, *et al.* [4] using dopants to tune the atomic positions. In order to dope holes into the system, they substituted Ca^+ for Y and to dope electrons, they substituted La^- for Ba. In this way, they could tune atomic positions while keeping the overall doping level fixed. The left panel of Figure 6.5 plots the distance between the planar Cu(2) and apical O(4) atoms of $(Y_{1-x}Ca_x)(Ba_{2-y}La_y)Cu_3O_z$. In the underdoped regime ($y > x$), T_c increases with the apical oxygen distance. I plot for comparison the difference in atomic spacing between the equilibrium (grey) and optically excited (red) lattice for the YBCO 6 (dashed) and YBCO 7 (solid line) substructures, from Ref. [3]. Even assuming that the excited material follows the overdoped trend, in which T_c correlates positively with an *decrease* in Cu(2)-O(4) distance, the magnitude of this deformation alone does not appear to justify a transient T' as high as ∼300 K. Neither can the increase in buckling, plotted in the right panels of Figure 6.5.

We now consider the reported change in the interbilayer spacing d, which is considered by Mankowsky *et al.* to be the central finding in support of a structural distortion driving the increase in interbilayer coupling. The Josephson tunneling current drops exponentially with the spacing between superconducting planes [169].

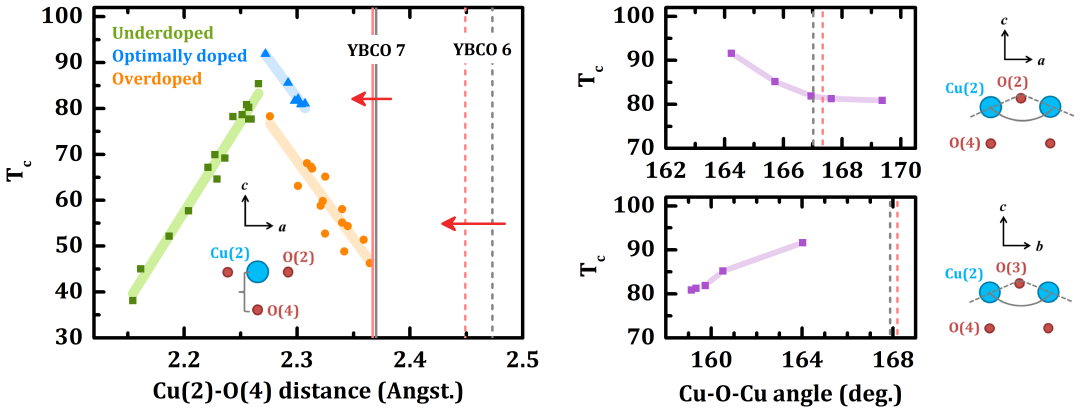

Figure 6.5: **Relationship between atomic positions and T_c.** The superconducting transition temperature T_c as a function of atomic positions in $(Y_{1-x}Ca_x)(Ba_{2-y}La_y)Cu_3O_z$. Data adapted from Jin, *et al.* [4]. The equilibrium atomic positions (grey lines) and maximum transient displacement (red) for YBCO 6.5 (Ortho II), measured by Mankowsky, *et al.* [3], is also shown for comparison. The YBCO 6 substructure is indicated with dashed lines and the YBCO 7 substructure with solid lines. **Left:** The superconducting transition temperature T_c as a function of apical oxygen distance from the CuO_2 planes (Cu(2)-O(4) bond length). **Right:** T_c as a function of Cu(2)-O(2)-Cu(2) (top) and Cu(2)-O(3)-Cu(2) (bottom) bond angles (purple squares).

Thus a 0.63% increase in the intrabilayer distance, as reported by Mankowsky *et al.*, would imply a 2% increase in interbilayer tunneling current.

The dependence of T_c on the interbilayer distance is not so well reported. In Figure 6.6 I present the results of my own meta-analysis of the $(Y_{1-x}Ca_x)(Ba_{2-y}La_y)$-$Cu_3O_z$ system, plotting the relative size of the interbilayer gap d (defined as the spacing between planar Cu(2) atoms) with the total unit cell size L. The left and center panels of Figure 6.6 plots the relationship between the interbilayer spacing d/L and T_c for nominal hole concentrations $h = x - y$. At constant nominal doping, there is, at best, a weak *positive* correlation between d/L and T_c. However, as h approaches optimal doping, the d/L distance appears to decrease slightly on average as T_c increases dramatically.[2] The equilibrium (grey) and transient (red) d/L for

[2]In contrast, the trends for Cu(2)-O(4) distance vs T_c hold even at constant doping, remaining positively correlated for underdoped compounds and negatively correlated for optimal and overdoped compounds.

the YBCO 6 sublattice of the YBCO 6.5 Ortho II sample measured by Mankowsky, *et al.* are shown for comparison.

The effect of equilibrium lattice distortions can offer at best an incomplete basis of comparison to the transient lattice structure. The relationship between the atomic positions and T_c, while often quite sensitive, is complicated to disentangle when the motion of many atoms work in concert to tune effective doping, spatial charge and spin behavior, and global phase coherence. However, from the trends investigated here, I conclude that while the motion of the planar Cu atoms may help to promote tunneling, the atomic shifts alone do not appear to account for a transient superconducting state with such a dramatic increase in critical temperature.

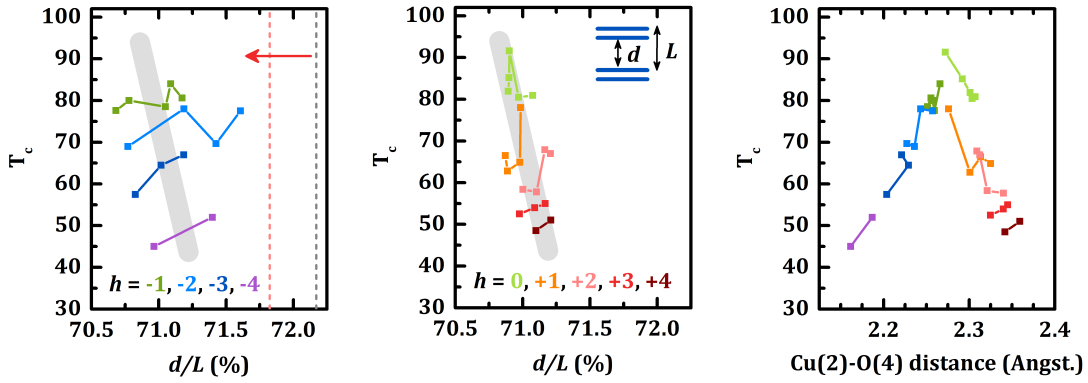

Figure 6.6: **Relationship between interbilayer spacing and T_c.** Data (squares) from Jin, *et al.* [4]. **Left, center:** The superconducting transition temperature T_c as a function of the interbilayer gap d, expressed as a percentage of the c-axis unit cell length L. The slight decrease in d/L approaching optimal doping is indicated with a thick grey line, shown as a guide to the eye. The equilibrium (grey) and transient (red) values of d/L for YBCO 6.5 (Ortho II) are shown as dashed lines (values from Ref. [3]). **Right:** The apical oxygen distance from the CuO_2 planes, by contrast, exhibits the same trends in h vs T_c at constant doping as the trends for underdoped and overdoped compounds generally.

6.4 Role of the charge density wave

In several lanthanide superconductors [88, 98, 100], the complete suppression of superconductivity near $p = 1/8$ doping is accompanied by the formation of charge stripes. The charges organize in the CuO_2 planes, with uniaxial stripes alternating alignment along the a and b crystalline axes in neighboring planes, with a stripe periodicity that locks with every fourth unit cell at 1/8 doping. The onset of charge stripe order is accompanied by strong spin fluctuations with small gapping on the order of meV [117]. In other families of cuprates, a similar apparent suppression of superconductivity near $p = 1/8$ occurs, yet no stripe ordering has been found. Spin excitations also appear to be gapped out, with gapping an order of magnitude larger than in lanthanides [170].

Recently, two groups have reported that this doping range actually plays host to charge density wave (CDW) order in $YBa_2Cu_3O_x$ and the related compound $Nd_{1+x}Ba_{2-x}Cu_3O_7$ [91, 171]. The signature of this state was first measured by resonant x-ray scattering of the planar Cu L_3 edge, corresponding to the $2p_{3/2} \rightarrow 3d$ orbital transitions. Thus the measured energy loss spectrum was very sensitive to the valence electrons in the CuO_2 planes. They found a resonance in the loss spectrum arising from low energy fluctuations in the valence-electron charge density. The regime of CDW order is indicated in the phase diagram in Figure 6.7. A scan of the planar momentum transfer $q_\parallel$ is also shown, with a peak at $q_\parallel = (0.31, 0)$ due to the CDW order. The CDW peaks are found both at $q_\parallel = (\pm 0.31, 0)$ and $q_\parallel = (0, \pm 0.31)$. However it is still unclear whether this signifies domains of each orientation or a single biaxial charge modulation [91, 172].

The peak was found to form inside the pseudogap phase, enhancing with decreasing temperature to T_c, and then reducing below the superconducting dome, apparently via competition with the condensate [91]. An applied magnetic field counteracts the reduction below T_c, favoring the charge density wave order [171].

Mid-infrared excitation has been shown to cause a reduction in static stripe order in $La_{1.875}Ba_{0.125}CuO_4$ [32] and, as discussed in Chapter 4, the destruction of charge order is implicated as the mechanism driving transient interlayer coupling in $La_{2-x}Ba_xCuO_4$ [15] and $La_{1.675}Eu_{0.2}Sr_{0.125}CuO_4$ [33, 34]. To explore whether the destruction of charge density wave order is related to the transient coupling observed in underdoped YBCO, we looked at the effect of the mid-infrared apical oxygen excitation on the charge density wave order peak.

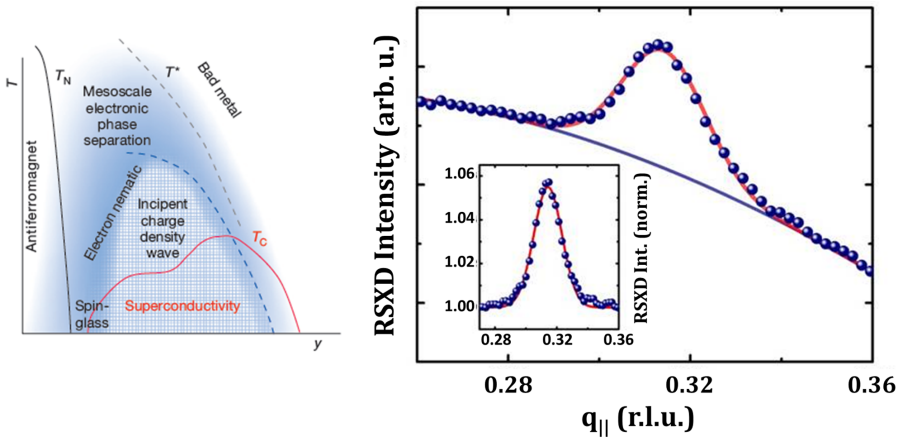

Figure 6.7: **Charge density wave order in $YBa_2Cu_3O_x$. Left:** A generic phase diagram indicating the region of charge density wave (CDW) order measured in $YBa_2Cu_3O_x$ and related compounds. Figure from Ref. [173]. **Right:** The CDW energy loss peak of $YBa_2Cu_3O_{6.6}$ as a function of $q_{||}$ just above $T_c = 62$ K. Figure adapted from Ref. [42].

The soft x-ray beamline at the Stanford Linac Coherent Light Source (LCLS) free electron laser is equipped with the capability to pump with 300 fs long mid-infrared pulses centered at 15 μm, with a pump fluence of 4 mJ/cm^2, the same as the THz measurements. The x-ray probe only penetrates $\sim$0.2 μm into the sample, over three times less than the pump penetration depth, so pump-induced effects reflect the bulk response of the material.

Sitting on the maximum of the CDW peak at $q_{||} = (0.31, 0)$, the changes in the peak intensity were measured as a function of delay after excitation. The profile of the transient changes is shown in Figure 6.8. A reduction of $\sim$50% is seen in the charge density wave peak, developing over 1-2 ps and surviving for a longer timescale, >10 ps.

The partial destruction of CDW order occurs on a different timescale than the development of the plasma mode. The THz mode establishes promptly on a 0.5-1 ps timescale and, at 61 K, it survives for a maximum of between 5-7 ps. The majority of the dynamics occur within the first 2 ps. The mismatch of timescales suggest that while CDW destruction may play a role in supporting the transient plasmon, it is unlikely to be the origin of the transient state.

This conclusion is further supported by measurements of the CDW transition regime T_{CDW}. For the $p = 0.12$ doping measured here, the onset temperature of

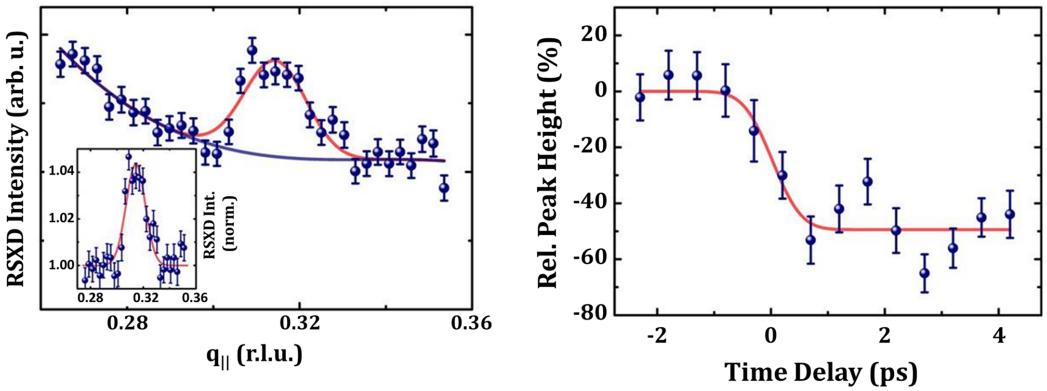

Figure 6.8: **Transient response of the charge density wave order in $YBa_2Cu_3O_{6.6}$. Left:** The CDW peak measured at LCLS. **Right:** The transient changes of the CDW peak amplitude ($q_{\|} = 0.31$). Measured at a base temperature just above $T_c = 62$ K. Figure adapted from Ref. [42].

the CDW, $T_{CDW} \approx 150$ K, agrees well with the onset of the transient plasmon T'. However, at lower dopings, where the CDW ordering begins to lose intensity (see Figure 6.9), the transient plasmon is still strengthening[3], even persisting down to $p = 0.05$, where no CDW signal has been found.

[3]As measured by the inductive response $\omega\Delta\sigma_2(\omega)$ and the volume fraction occupied by the transient state. See discussions in Sections 5.4.2 and 5.5.

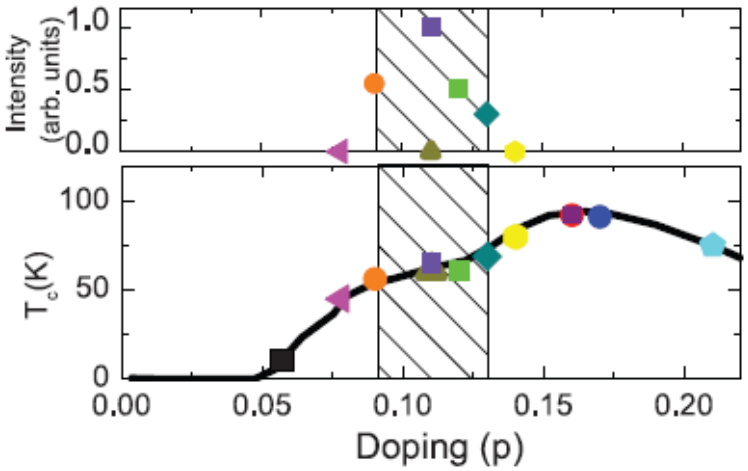

Figure 6.9: **Doping dependence of the charge density wave intensity.** The charge density wave peak intensity is shown for several dopings of $Nd_{1+x}Ba_{2-x}Cu_3O_7$ (purple squares and orange circles) and $YBa_2Cu_3O_x$. The Ortho II symmetry of $YBa_2Cu_3O_{6.5}$ is indicated with a gold triangle. Figure from Ref. [91].

Chapter 7

Decoherence driven relaxation of the transient plasma mode in underdoped $YBa_2Cu_3O_x$

7.1 Introduction

Chapter 5 showed how resonant mid-infrared excitation was able to drive a blue shift of the interbilayer Josephson plasmon in underdoped $YBa_2Cu_3O_x$ (YBCO x). The blue shift of the plasmon indicates an enhancement in c-axis tunneling. This could be caused by either an increase in the superconducting pair density or an increase in the tunneling rate, for example by a stiffening of the superconducting phase. More remarkably, above T_c, the same excitation produces a transient plasma mode at a frequency comparable to the Josephson plasma frequency and which shows the same frequency scaling with doping as the Josephson plasmon. Moreover, this plasmon can be generated throughout the pseudogap regime, even for YBCO 6.3 ($p = 0.05$), which is non-superconducting at equilibrium.

The MIR pump was shown to be resonant to a c-axis excitation of the apical oxygen atom which lies in the interbilayer gap. The position of this atom within the lattice is known to be related to T_c, supporting the idea that the excitation may be driving non-equilibrium superconducting transport throughout the pseudogap. At least, the frequency of the transient plasma mode strongly suggests that the same carriers that participate in the condensate are responsible for the transient plasmon.

There are two apical oxygen excitation modes, associated with the YBCO 6 and YBCO 7 sublattices, and only the YBCO 6 mode is being driven. The excited mode seems to reflect this inhomogeneity and can be quantitatively fit by assuming an effective medium, where some volume fraction of the crystal is excited and the rest remains in equilibrium.

This chapter will analyze the formation and relaxation dynamics of the Josephson plasmon below T_c and the transient plasmon that develops above T_c. Below T_c,

the blue shift of the Josephson plasmon is seen to also be inhomogeneous, with one component remaining near the equilibrium plasma frequency. Above T_c, the principle finding is that the relaxation of the transient plasmon is driven by a loss of coherence, characterized by a decrease in carrier mobility, rather than a drop in carrier density as one might expect from quasiparticle excitation. Furthermore, during the relaxation, the transient plasmon splits, with one component centered near the equilibrium Josephson frequency and one component shifted to the blue.

A splitting in the equilibrium Josephson plasmon of cuprates occurs whenever the intrinsic Josephson junctions—the CuO_2 planes and the gaps between them—become differentiated. In YBCO, there is a natural splitting due to the bilayer structure of the lattice. A splitting in the interbilayer plasmon has been shown to occur when the superconducting phase between planes is made inhomogeneous, such as when vortices form under an applied field. The splitting of the transient plasmon may therefore indicate that the relaxation is governed by a drop in transient superconducting phase coherence.

7.2 Inhomogeneous enhancement of Josephson tunneling, $T < T_c$

In Section 5.3.2, the transient response of YBCO below T_c was introduced. The Josephson plasma resonance, characterized optically as a peak in the energy loss function $\Im(-1/\varepsilon)$, was shown to blue shift after mid-infrared excitation. The pump-induced changes to the material appear to be inhomogeneous, however, with some spectral weight remaining near the equilibrium plasma frequency. Figure 7.1 shows the transient response at 0.8 ps after excitation, where the blue shifted mode can be clearly distinguished from a component that remains at the equilibrium plasma frequency. This splitting of the plasmon gives rise to a transverse mode which produces a peak in $\sigma_1(\omega)$. This peak appears at about $\omega_T \approx 1.5$ THz (center panel of Figure 7.1), between the frequencies of each plasmon.

The response is fit to Equation 3.5, indicated by the dashed line in Figure 7.1. This fit is in excellent agreement considering it includes only the plasmons and no contributions from higher frequency phonon modes.[1]

[1] As the fit takes $z_{IB} + z_B < 1$, the full response should have an additional contribution, added in series.

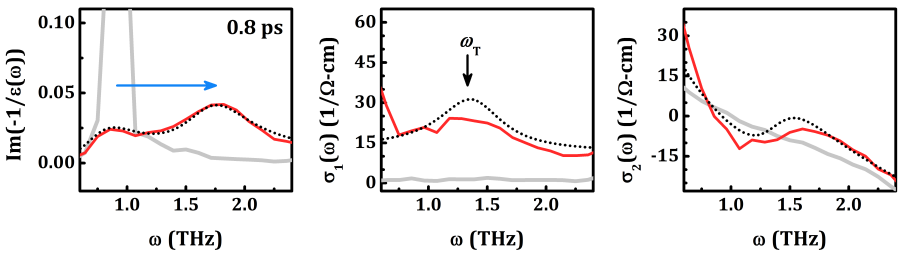

Figure 7.1: **Splitting of the transient Josephson plasmon.** The loss function $\Im(-1/\epsilon)$ (left), Ohmic conductivity $\sigma_1(\omega)$ (center), and inductive conductivity $\sigma_2(\omega)$ (right) of YBCO 6.5 at 5 K, 0.8 ps after excitation (red) and in equilibrium (grey). A split plasmon calculated from Equation 3.5 is shown for comparison (dashed line).

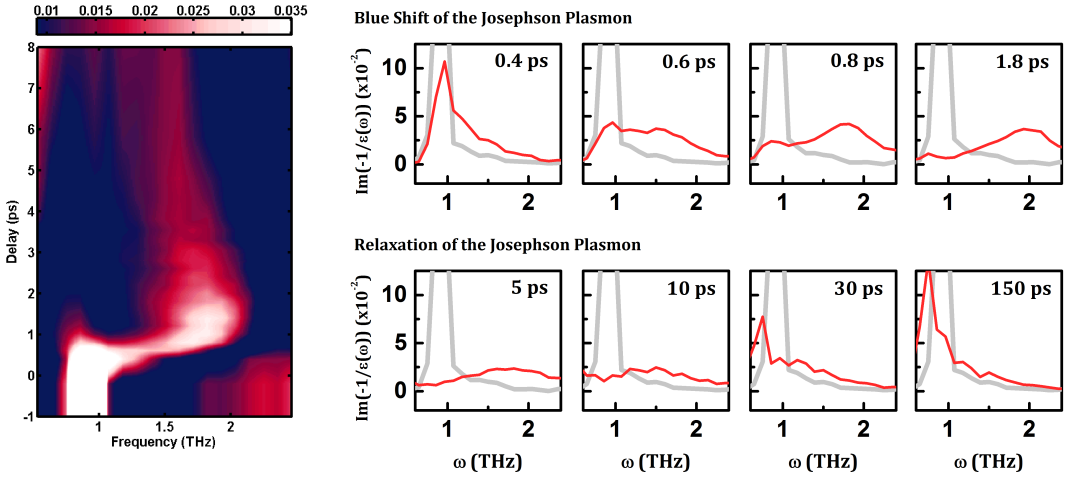

Figure 7.2: **Time evolution of the Josephson plasmon for YBCO 6.5 at 5 K.** The loss function $\Im(-1/\varepsilon)$ peaks near the Josephson plasma frequency in equilibrium (grey). After excitation (red), the mode appears to split, with one mode blue shifting from 1 THz to about 2 THz. The relaxation occurs over the scale of >150 ps.

The initial pump-induced blue shift of the plasmon occurs within the first 2 ps of excitation. The blue shifted plasmon then broadens and redshifts back to the equilibrium plasmon position. This relaxation is much slower, occurring over >150 ps, as illustrated in Figure 7.2. Two plasma frequencies were extracted from the peak positions of the $\Im(-1/\varepsilon)$ response and are plotted in Figure 7.3. The figure indicates

that the lower frequency plasmon red-shifts; however, due to the low frequency limit of the THz spectrum, it is difficult to ascertain if this represents a true red shift, or if the plasmon simply loses spectral weight and then recovers. The blue shifted plasmon is easier to track, remaining well within our spectral window for the entire duration of the dynamics. The relaxation of the plasma frequency can be well-fit by a single exponential decay, with a time constant $\tau = 10.5$ ps.

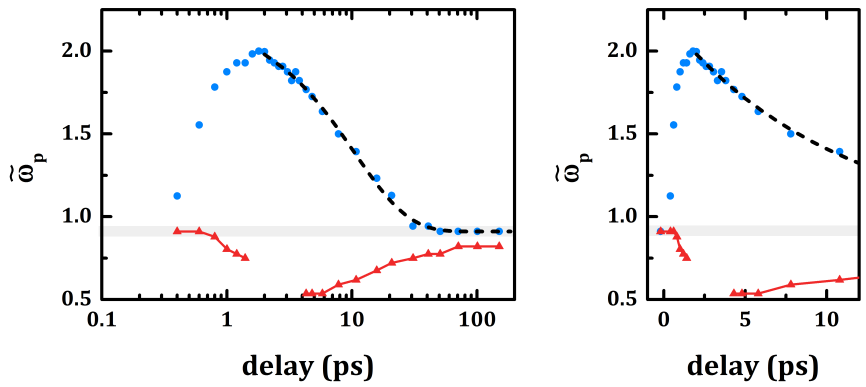

Figure 7.3: **Relaxation timescale of the Josephson plasma frequency.** The two plasma mode frequencies $\tilde{\omega}_p = \omega_p/\sqrt{\varepsilon_{\mathrm{FIR}}}$ are plotted as a function of delay time for YBCO 6.5 at 5 K. The blue shifted plasmon (blue dots) is fit with a single exponential decay with a lifetime of $\tau = 10.5$ ps. The grey region indicates the equilibrium plasma frequency.

7.3 Relaxation of the transient state, $T > T_c$

7.3.1 Decoherence-driven relaxation

The relaxation dynamics of the transient coupling above T_c do not follow a simple thermalization behavior but instead appear to be driven by decoherence effects. This is most clearly seen in the relaxation of the transient component of the inductive conductivity, $\Delta\sigma_2(\omega) = \sigma_2(\omega) - \sigma_{2,\mathrm{eq}}(\omega)$. For a plasma mode with no decoherence contributions ($\Gamma = 0$ in Equation 3.2), the transient inductive conductivity should diverge as $1/\omega$ and therefore $\omega\Delta\sigma_2(\omega)$ is a constant. The quantity $\omega\Delta\sigma_2(\omega)$ is

proportional to the spectral weight of $\sigma_1(\omega = 0)$, and therefore indicates the density of carriers moving along the c-axis (see Section 5.3.1).

A flat $\omega\Delta\sigma_2(\omega)$ in the THz regime is characteristic of a superconductor, where the tunneling of pairs dominates the c-axis transport. The depletion of the condensate with increasing temperature appears as a constant reduction in $\omega\Delta\sigma_2(\omega)$ (see Figure 5.8 in Section 5.3.1). Fluctuations in the superconducting correlation length and time scale have been shown to give rise to an effective Γ term near T_c in superconducting $La_{2-x}Sr_xCuO_4$ [80] and $Bi_2Sr_2CaCu_2O_{8+x}$ [81]. In the inductive conductivity $\omega\Delta\sigma_2(\omega)$, this appears as a deviation from constant behavior in the form of a suppression of the low frequency response.[2]

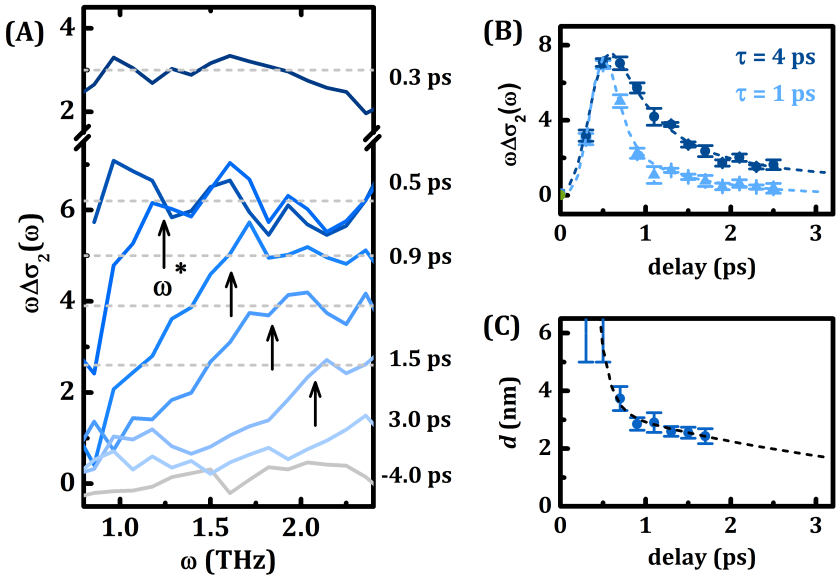

Figure 7.4: **Decoherence driven relaxation of the inductive response. (A)** The transient changes to the inductive conductivity $\omega\Delta\sigma_2(\omega)$ remain flat at early time delays, indicating a high mobility response. Later times are characterized from a low frequency drop in the response, below a frequency ω^* (arrows). **(B)** The average $\omega\Delta\sigma_2(\omega)$ above ω^* (blue) and at 1 THz (light blue). The response decays following a double exponential (dashed lines) with a long time constant of 4 ps (blue) and 1 ps (light blue). **(C)** The coherence length, defined as $d = 2\omega_p L_{IB}/\omega^*$, as a function of delay after excitation. The coherence length decays following a time scale of 4 ps (dashed line).

[2] In equilibrium, the inductive component due to the superconducting condensate is defined as $\Delta\sigma_2(\omega) = \sigma_2(\omega) - \sigma_2(\omega, T > T_c)$.

The same phenomenon appears to dominate the relaxation of the transient response. At early time delays, $\omega\Delta\sigma_2(\omega)$ remains constant. As the transient plasma mode relaxes, a deviation from flat $\omega\Delta\sigma_2(\omega)$ behavior appears below a characteristic frequency ω^*, with the conductivity dropping towards zero. This same relaxation pathway was seen in the optically induced plasma mode of LESCO 12.5% presented in Chapter 4. Following the analysis performed in that case, we define a coherence length of the transient plasmon $d = 2\omega_p L_{IB}/\omega^*$ where L_{IB} represents the size of the interbilayer gap[3].

Figure 7.4 shows the relaxation of $\omega\Delta\sigma_2(\omega)$ for YBCO 6.45 at 100 K. The frequency ω^* is indicated with an arrow at several delays in Panel 7.4.A. The value of $\omega\Delta\sigma_2(\omega)$ averaged above ω^* (blue) and at 1 THz (light blue) is plotted as a function of delay after excitation in Panel 7.4.B. The inductive response decays following a double exponential, with a long lifetime of 4 ps for the "stiff" response above ω^*. For the low frequency conductivity we find a faster decay, of just 1 ps, reflecting the decoherence at long length and time scales. The drop in coherence length d can also be fit with a double exponential, with the same long lifetime of 4 ps setting the relaxation rate, as shown in Panel 7.4.C. The total size of a single YBCO unit cell is ∼1.1 nm.

The average inductive conductivity $\omega\Delta\sigma_2(\omega)$ was measured as a function of delay after excitation over the flat range of the response (above ω^*) at all temperatures. The analysis is focused on the $x = 6.45$ doping because quasiparticle contributions to the optical response are minimal. At higher dopings, these contributions begin to influence the shape of the inductive response and a similar analysis would require subtracting this incoherent component of the conductivity.[4] For this analysis, we simply consider the bare $\omega\Delta\sigma_2(\omega)$ response. Within the effective medium picture, this quantity was found to be proportional to the volume fraction of the high mobility state (see Section 5.5).

Figure 7.5 plots the inductive response at 10 temperatures, each fit with a single exponential decay (grey) and a double exponential decay (red). At temperatures up to ∼100 K ($T_c = 35$ K), the single exponential fit adequately captures the relaxation. At higher temperatures, a second timescale appears, though it is difficult to fit as

[3] As discussed in the next section, the interbilayer plasmon splits at later frequency delays. We take the higher frequency mode for ω_p.

[4] This is complicated by the inhomogeneous nature of the response (see Section 5.5). Accounting for the incoherent contributions requires making assumptions about the excitation in order to model it. For example, determining which fluid experiences quasiparticle excitations—the high mobility regions or the bulk.

it only begins to dominate at the longest delays measured. The delay range that can be considered is limited by ω^* remaining within the spectral window of the THz probe, below 2.7 THz.

The timescales extracted from these fits are plotted in Figure 7.6. The lifetime of the single exponential fit τ appears to decrease somewhat linearly with temperature. A linear fit to the lifetime (dashed line in Figure 7.6) projects to $\tau = 0$ at $\sim$470 K, a little higher than the T' temperature for YBCO 6.45. The double exponential decay has the form $\omega\Delta\sigma_2(\omega) \propto (1 - w_2)\exp(-\tau/\tau_1) + w_2\exp(-\tau/\tau_2)$. The single lifetime τ seems to reflect an average of the double exponential timescales, $\tau \approx \tau_{ave} = (1 - w_2)\tau_1 + w_2\tau_2$. This is illustrated in the bottom left panel of Figure 7.6, which plots the τ (grey dots) and τ_{ave} (light grey squares) along with τ_1 and τ_2 of the double exponential fit.

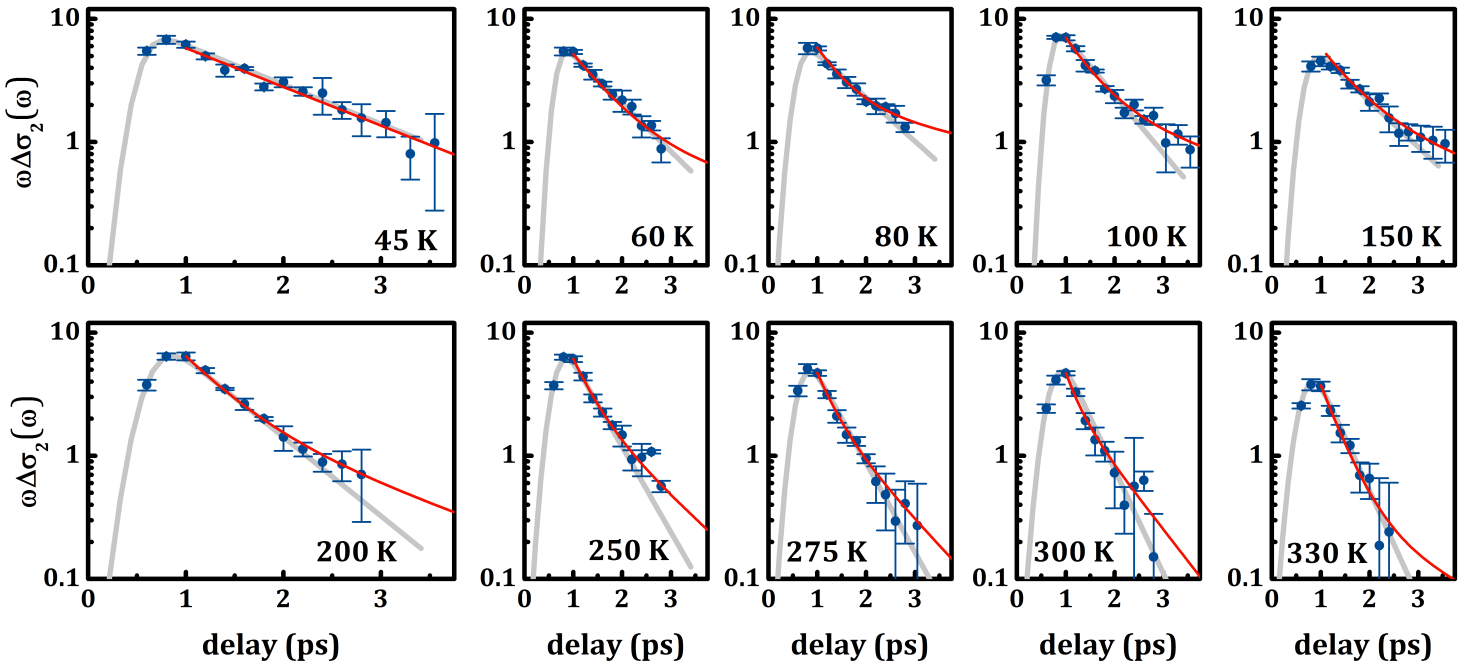

Figure 7.5: **Relaxation of the transient inductive response.** The inductive conductivity $\omega\Delta\sigma_2(\omega)$ of YBCO 6.45 averaged over the flat region of the response (above ω^*) as a function of delay at several temperatures. The relaxation is fit with a single exponential (grey) and a double exponential (red). The single exponential fit is plotted with an error function fit to early time delays, however this component was not included when optimizing the relaxation rate.

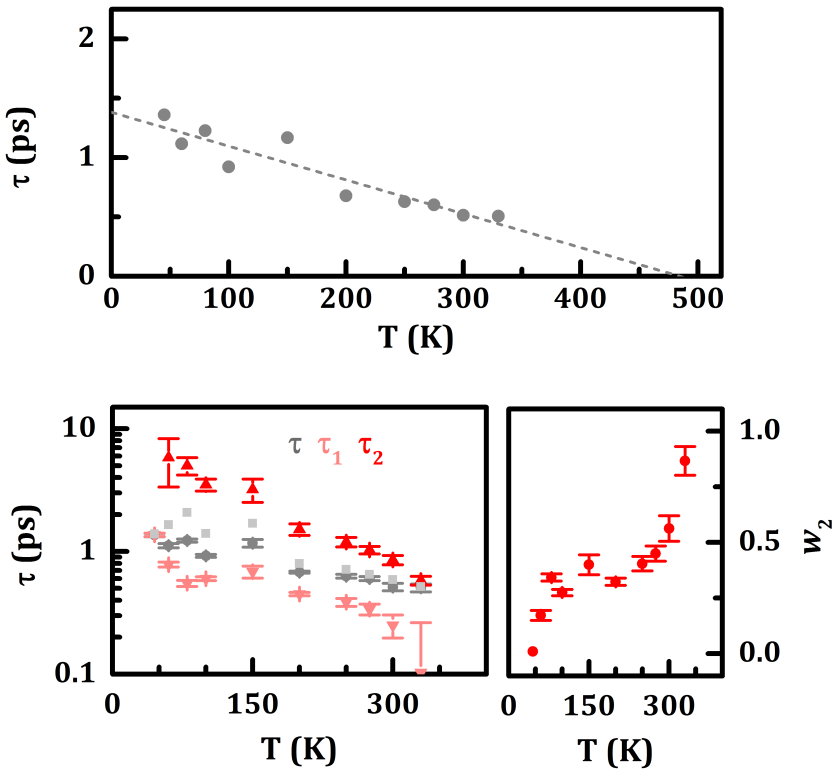

Figure 7.6: **Timescales governing the relaxation of the transient state. Top:** Plot of the relaxation timescale of the transient inductive response vs temperature. The lifetime τ was determined by a single exponential fit. **Bottom, left:** The time constants from single (dark grey) and double (pink, red) exponential fits. The weighted average of the double exponential timescales, $(1-w_2)\tau_1 + w_2\tau_2$ is shown in light grey squares. **Bottom, right:** The relative weight of the long lifetime of the double exponential, $\omega\Delta\sigma_2(\omega) \propto (1-w_2)\exp(-\tau/\tau_1) + w_2\exp(-\tau/\tau_2)$.

7.3.2 Splitting of the transient plasmon

A second feature of the relaxation is a splitting of the transient plasmon that develops about 1.2 ps after excitation. The transient changes in the loss function $\Delta\Im(-1/\varepsilon)$ and Ohmic conductivity $\Delta\sigma_1(\omega)$ are plotted in Figure 7.7 for YBCO 6.45 at 0.5 ps and 1.5 ps after excitation. At early times, the response is characterized by the appearance of a single mode near the equilibrium Josephson plasma frequency. The Ohmic conductivity is partially reduced. At 1.5 ps, a second mode at lower frequency has formed and a peak in $\Delta\sigma_1(\omega)$ develops at a frequency between the two plasma modes.

The response in Figure 7.7 is fit as an effective medium (dashed lines), following the method presented in Section 5.5. The bulk of the sample remains in equilibrium (Medium B for both delays, with volume $1-f$), while a volume fraction f is modeled as a high mobility state. At 0.5 ps, this volume fraction (Medium A) can be described by a single longitudinal plasma mode, following Equation 3.2.[5] At 1.5 ps, the volume f is modeled with two resonances, following Equation 3.5. The two mediums used in each fit are plotted in Figure 7.7.C. The single plasma mode is in pink, the split plasmon in red. The equilibrium response is in grey. The single peak in the Ohmic conductivity at 1.5 ps corresponds to the transverse mode ω_T described in Section 3.2.

The splitting of the plasmon is a universal feature across all underdoped compounds. The loss function is plotted at two delays, 0.7 ps after excitation and 1.5 ps after excitation for YBCO 6.3, 6.45, 6.5, and 6.6 in Figure 7.8. The position of the single plasmon (at early delays) blue shifts with doping, as does the position of the higher frequency plasmon (at later delays).

Two snapshots alone cannot tell us how this splitting develops [174]. Figure 7.9 shows the time evolution of the plasma mode in 200 fs steps for YBCO 6.5 at 100 K. The loss function develops a single peak after excitation that blue shifts with delay time. Then, a second lower frequency peak rises up near the equilibrium Josephson plasma frequency.

[5] A small constant component has been added to $\sigma_1(\omega)$ to account for quasiparticle contributions to the transient state (see Section 5.5). This can be seen in Figure 7.7.C.2 by comparing the baseline value of $\sigma_1(\omega)$ at 0.5 ps with 1.5 ps, which has no quasiparticle contribution added.

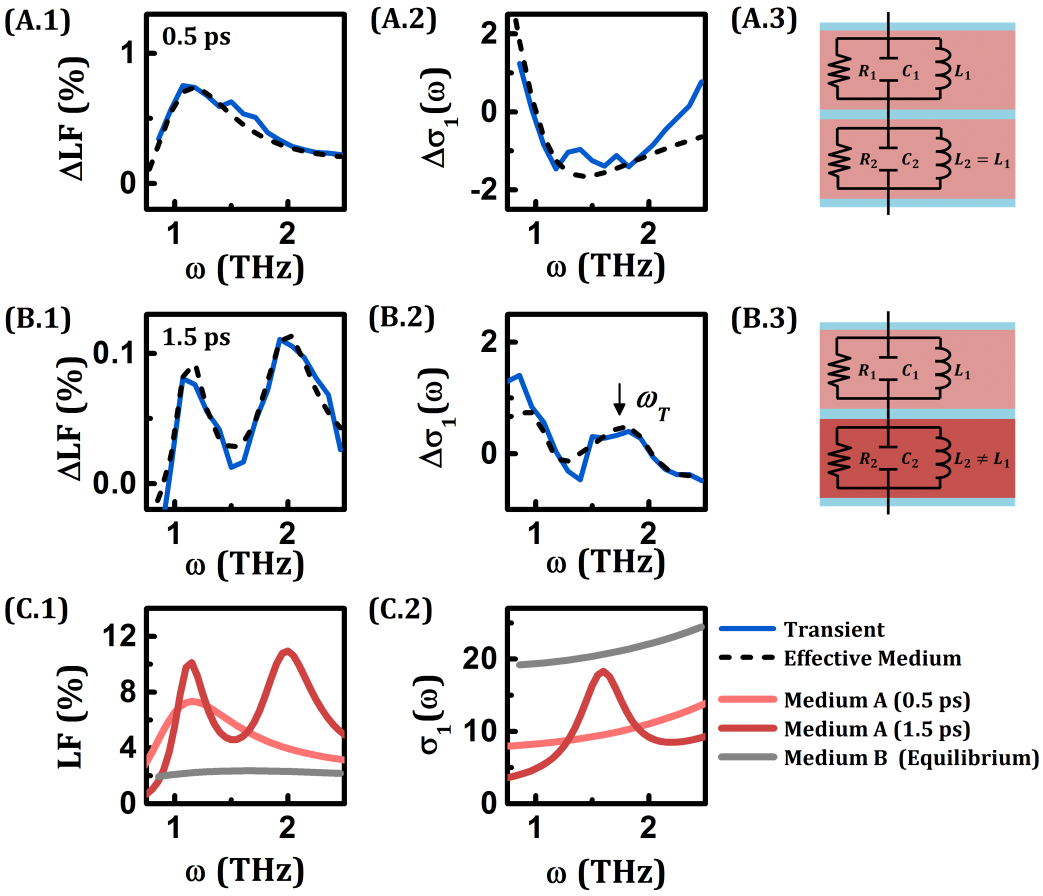

Figure 7.7: **Splitting of the transient plasmon.** The optical response of YBCO 6.45 at 200 K shown at two delays (blue). The response is fit by an effective medium of the equilibrium response and one (0.5 ps) and two (1.5 ps) transient plasma modes (dashed line). **(A)** The transient changes in the loss function (A.1) and Ohmic conductivity (A.2) at 0.5 ps after excitation. **(B)** Same, at 1.5 ps after excitation. **(C)** The two material responses used in the effective medium fits. In both fits, Material 2 is the equilibrium response.

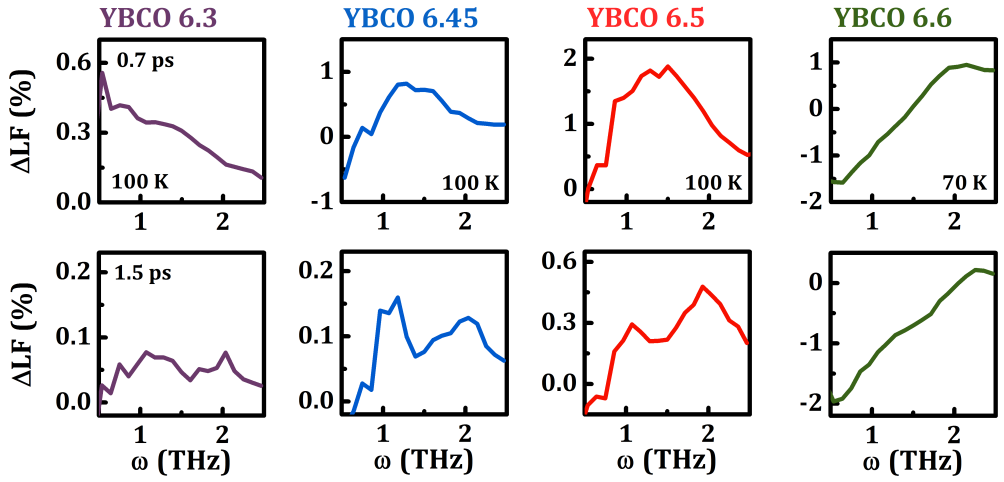

Figure 7.8: **Splitting of the transient plasmon at four dopings.** The transient changes in the loss function at 0.7 ps after excitation **(top row)** and 1.5 ps **(bottom row)**.

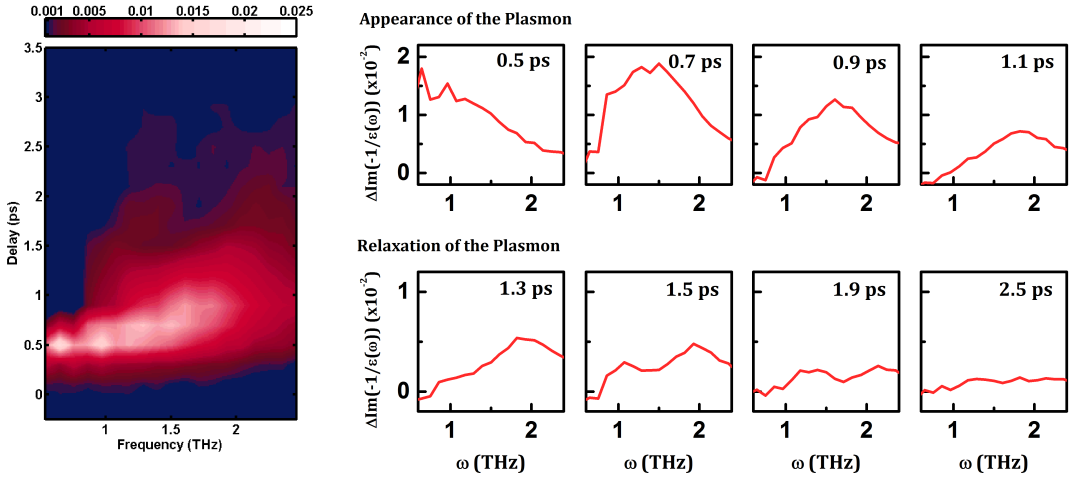

Figure 7.9: **Time evolution of the transient plasmon,** $T > T_c$**.** The loss function is plotted at 200 fs time delay steps, starting 0.5 ps after excitation. A single peak develops at early time delays, which blue shifts. A lower frequency peak develops after 1.2 ps, near the position of the equilibrium Josephson plasma resonance.

7.4 Discussion of these results

The apparent splitting of the plasmon below T_c appears to be the product of inhomogeneous excitation. The phonon excitation targets a mode that is spatially inhomogeneously distributed in the sample. The transient mode above T_c must also be modeled as an effective medium mix of excited regions in an unperturbed bulk. The below T_c response may therefore reflect a mix of regions where the plasmon remains at its equilibrium position (or is slightly red-shifted) and excited regions in which the plasmon blue-shifts.

The relaxation pathway of the transient plasmon above T_c further supports that the transient plasmon is due to Josephson coupling across the interbilayer gap. In Chapter 5, I discussed how the fluence dependences of the transient plasmon does not support quasiparticle excitation as the origin of the mode. The relaxation pathway provides further evidence against such a scenario. The transient plasma mode relaxation is driven by a decrease in coherence, plotted in Figure 7.4 as the decay of the coherence length d or, equivalently an *increase* in the effective scattering rate Γ of Equation 3.2. As discussed in Chapter 4, a plasmon produced by quasiparticle excitation instead relaxes through a depletion of the carrier density $\propto \omega_p^2$, at constant scattering [118, 119] or with a *decrease* in the scattering rate [120, 121].

Furthermore, a splitting of the plasmon is a strong indication of decoherence driven relaxation. A spatially varying plasma resonance frequency, for example due to inhomogeneity in the sample, would simply result in a broadening of the plasmon [82], but the appearance of two distinct modes suggests the development of *two* inequivalent interbilayer gaps. This may be related to the generation of (zero field) vortices, in a manner similar to the thermal vortex regime that forms an extended dome above T_c in the equilibrium phase diagram of cuprates [81, 147, 150, 175].

In YBCO, an applied magnetic field along the CuO_2 planes has been shown to cause a splitting of the interbilayer plasmon due to the generation of vortices [83, 176, 177]. The spatial distribution of the phase variation determines the degree and shape of the splitting [178]. Figure 7.10. shows the interbilayer Josephson plasmon of YBCO 6.75 split by a field of 8 T applied along the *ab*-plane. A transverse mode is generated between the split frequencies of the longitudinal modes, as seen by the peak in $\sigma_1(\omega)$. The split plasmon is fit with a model developed by Koshelev [177] (purple) that accounts explicitly for the phase inhomogeneity due to the applied field. In certain limits, the form of this expression is very similar to the van der

Marel and Tsvetkov expression (Equation 3.5), as illustrated by the dashed black line fit.

The position of the second plasmon near the equilibrium Josephson plasma frequency suggests another possible explanation for the split plasmon. Perhaps as the system relaxes, the energetic landscape favors the equilibrium Josephson plasma mode, resulting in a short-lived bi-stability point with the blue-shifted transient mode.[6]

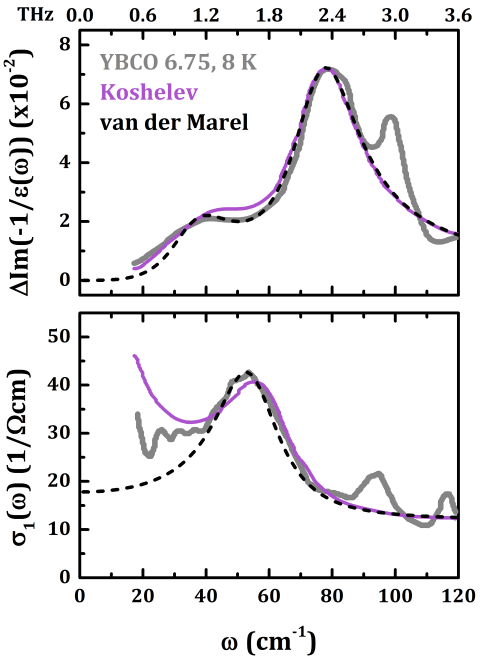

Figure 7.10: **Plasmon splitting due to condensate phase inhomogeneity.** Splitting of the Josephson plasmon of YBCO 6.75 at 8 K in the presence of an 8 T applied field along the a-axis. The upper panel shows the loss function. The peak due to the Josephson plasmon is split into two major peaks at 38 and 70 cm^{-1}. The lower panel shows the Ohmic conductivity, which peaks at the transverse plasma mode at 55 cm^{-1}. (Additional higher frequency features in both responses are also present in the absence of a field.) The data (grey) is fit with a model from Koshelev [178] (purple) that accounts for the inhomogeneous phase of the superconducting order parameter. A fit using the van der Marel and Tsvetkov model (Equation 3.5) is also shown (black dashed line). Data and Koshelev fit from [177].

[6]The presence of a second mode in the YBCO 6.3 system would suggest the former scenario; however further conclusions await analysis of this data with the equilibrium response of the same doping.

Chapter 8

Point contact spectroscopy investigation of the iron-based high-temperature superconductors

8.1 Introduction

This chapter represents a departure from the subject area of the rest of this manuscript. In some sense, I am completing my thesis by returning to the beginning, to present work I began at the start of my graduate school career. I joined the superconductor research community at an exciting time, in mid-2009 when the iron-based high-temperature superconductors were first blazing onto the community's collective radar. As a result, my perspective is shaped by the unusual background of having first explored unconventional superconductivity by studying the iron pnictides, before learning about cuprates.

There are many striking parallels between these classes of materials. Both have as their foundation an antiferromagnetic parent state, and play host to spatial charge (nematic) ordering and structural transitions that support the electronic order. It is believed that antiferromagnetic spin fluctuations serve an important role in pairing in both classes of superconductors [179–181]. The iron-pnictogen, Fe-Pn, (or iron-chalcogenide, Fe-Ch) tetrahedron appears to be critical to these fluctuations, with the electronic state proving highly sensitive to distortion or doping of this layer [182].

Unlike the cuprates, the presence of multiple Fermi sheets and multiple gaps with $s_{\pm}$-wave order parameter symmetry is believed to be important to superconductivity in the iron-based compounds [179, 183, 184]. To this end, point contact spectroscopy (PCS) and scanning tunneling microscopy (STM) studies have focused on detecting evidence of multiple gaps and elucidating the order parameter (OP) [185–189]. PCS has proven an excellent tool for both detecting OP symmetry and probing multiband behavior in the superconducting state [190, 191]. Point contact measurements of

MgB_2, for example, played an important role exposing its multi-gap behavior and order parameter coupling strength [191–195].

I will begin with a brief introduction to iron-based superconductors, describing the multi-gap behavior that makes them unique. Then I will present an introduction to point contact spectroscopy. This technique has historically been used to study bosonic excitations (*e.g.* phonons, magnons) and superconducting gap behavior via Andreev reflection, but as I will show, PCS is sensitive to a wide range of correlated electron behavior. Discovering the range of order that point contact spectroscopy can detect is still an active area of research. Finally, I will present some PCS results on the $Sr(Fe_{1-x}Co_x)_2As_2$ system, which is part of the "122" family of compounds.

8.2 Iron-based superconductors

The discovery of the first pnictide superconductor, LaOFeAs with a T_c of 26 K, was announced in early 2008 [196], and soon sprouted a firestorm of activity. The Bardeen-Cooper-Schrieffer (BCS) electron-phonon mechanism was found to be an unlikely candidate for pairing, with electron-phonon coupling about 5 times too small to account for measured T_c values [197]. Experimental techniques that had been honed the previous 20 years to understand the cuprate superconductors were quickly turned to this new class of high-temperature superconductors.

Certain parallels with cuprate superconductivity were found. As with cuprate materials, superconductivity in the Fe-based compounds resides near an antiferromagnetic phase, with electron or hole doping giving rise to a superconducting dome in the temperature vs. doping phase diagram. The Neel transition is stabilized by a structural transition from tetragonal to orthorhombic or monoclinic symmetry [180, 198, 199]. A nematic regime, associated with electronic, spin, and orbital anisotropy but not linked to the underlying structural phase, has been found to extend far above T_c in underdoped materials [200–202]. Whether or not the pnictides host a pseudogap phase like that found in cuprates remains an open question [203, 204].

To date, six families of pnictide crystal structures have been identified, each given an abbreviated name representing the number of each type of atom they contain; *e.g.* LaOFeAs belongs to the 1111 family, and $SrFe_2As_2$ belongs to the 122 family. The highest T_c realized so far is 57 K, in the 1111 family [205]. The crystal structures for the four most well-studied families are shown in Figure 8.1.

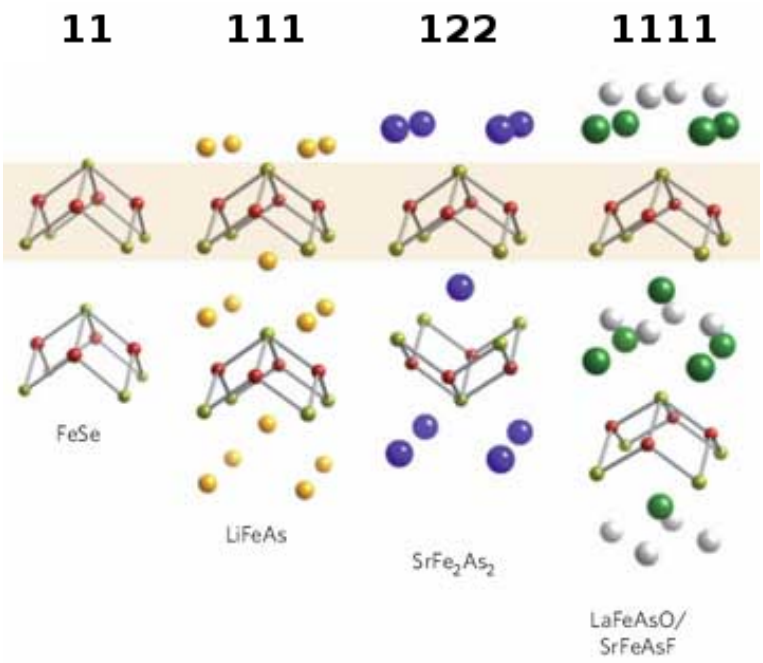

Figure 8.1: **Lattice structure of four pnictide families.** The FeAs layers are highlighted in beige. Iron atoms are in red, pnictide and chalcogenide atoms in are in yellow. Figure modified from Ref. [206].

They have in common the FePn tetrahedron structure, containing an Fe atom surrounded by four pnictide (generally As) atoms. The 11 chalcogenides have a similar tetrahedral FeCh structure with Ch =Te, Se, S. (The 122 crystal structure is shown in Figure 8.9 with the tetrahedron structure highlighted.) As in the case of the cuprate octehedra (the CuO_2 planes and neighboring apical oxygen(s)), the superconducting transition temperature is found to be closely linked to the relative positions of atoms within the tetrahedra [25, 207, 208].

The pairing mechanism is thought to deviate from simple s-wave symmetry [179], with a form of s-wave pairing in which the order parameter phase takes on a different sign depending on the Fermi sheet hosting the pairs. Up to five bands cross the Fermi surface, corresponding to the five $3d$ orbitals of the Fe atoms. In momentum space, the two electron-like orbitals form quasi-cylindrical sheets around the M-point. The three hole-like Fermi surfaces form cylinders around the Γ point. The leading proposal [179, 209–211] for the pairing mechanism involves antiferromagnetic spin fluctuation-mediated hopping of pairs between hole-like and electron-like Fermi

surfaces. The exchange interaction itself is repulsive, but the phase reversal of the superconducting order parameter creates a net attractive interaction, acting as the pairing "glue". Nesting of the Fermi surfaces may enhance this exchange, but the absence of nesting in some superconducting compounds suggests this cannot be the whole story [212]. The pnictides may sit at the precipice of a transition to a Mott or charge-transfer insulator, with local moments as well as itinerant electrons shaping the magnetic behavior [212–214].

8.3 Point contact spectroscopy

Point contact spectroscopy (PCS) is an electronic probe that measures transport between materials connected by a microconstriction. This technique has been shown to be a good probe of bosonic excitations, and in superconductors PCS is sensitive to the superconducting order parameter via Andreev reflection. More recently, we have shown PCS to be sensitive to the density of states arising from correlated electron states. The technique was a serendipitous discovery. I. K. Yanson was studying the phonon spectrum of Pb by measuring the differential conductance of planar tunnel junctions and found that even after superconductivity in the Pb had been completely suppressed by an applied field, he could still measure nonlinearities in the tunneling current that corresponded to the Pb phonon spectrum [215]. A planar tunnel junction should only show spectral content in the superconducting state, because without the phonon coupling to the condensate, spectral information is not preserved crossing the tunnel barrier.

The source of the phonon spectral features turned out to be micro-shorts through the tunnel barrier. Point contact spectroscopy utilizes small microconstrictions, smaller than the elastic mean free path of the carriers, to measure spectroscopic information about materials [216] and has been used to measure phonon spectra of an array of metals [217].

As I will show in this section, the current across a microconstriction is also sensitive to spectroscopic information whenever there are correlated electron effects in the material of study. Understanding how the PCS conductivity relates to these correlations is an area of active research. Until recently, point contact spectroscopy has been primarily utilized to probe superconducting order parameter symmetry because this was one of the few applications for which excellent theoretical models [5, 218] exist to interpret conductance spectra. In recent years, a concert of theoretical de-

velopments [214, 219–222] and experimental effort [223–227] have shown PCS to be sensitive to a variety of orders in correlated systems.

8.3.1 Point contact junction configurations

The key element of a point contact junction is that the probing current passes through a microconstriction which has a contact radius a on the order of the elastic mean free path ℓ_{el} or smaller. The junction can be characterized by the Knudsen ratio, $K = \ell_{el}/a$. The Wexler formula [228] for the resistance at a point contact junction is

$$R_0 = \frac{\rho}{2a}\left[\frac{8K}{3\pi} + \gamma(K)\right], \tag{8.1}$$

where ρ is the sample resistivity and the function $\gamma(K)$ was determined by a Green's function analysis of the point contact geometry.

In the Sharvin, or ballistic, limit the elastic mean free path is larger than the contact size, $K >> 1$, and $\gamma(K) \to 0.694$. The Wexler formular reduces to $R_0 \approx 4\rho\ell_{el}/3\pi a^2$. In this regime, carriers do not scatter in the microconstriction volume and can be accelerated by the bias energy eV_B as they traverse the junction, where V_B is the bias voltage across the junction.

In the Maxwell, or thermal, regime the contact size is larger than the inelastic scattering length ℓ_{in}, and inelastic scattering events occur in the junction area. The injected carriers may therefore cross the microconstriction at a different final energy difference than the applied eV_B bias. In this case $K \to 0$ and $\gamma(K) \to 1$, reducing Wexler's formula to the equation for bulk resistance, $R_0 = \rho/2a$. One test for a clean contact in the Sharvin limit is that the temperature dependence of the zero bias resistance $(dI(0)/dV)^{-1}$ of the junction is distinct from that of the bulk resistivity $\rho(T)$.

Between these two extremes is the so-called "diffusive" limit, where the contact size lies somewhere between the elastic and inelastic mean free path lengths, $\ell_{el} < a < \sqrt{\ell_{el}\ell_{in}}$. In this regime, elastic scattering can occur in the junction volume, however, some spectral information may be obtained.

Point contact junctions can be made in several ways. A point contact junction can be patterned with nano-lithography. This method allows for systematic control of the contact size and system geometry, but its application is limited to clean films that make good candidates for lithography. The real advantage to point contact spectroscopy is that it can be applied to a wide variety of systems and requires

minimal sample preparation. The technique is less sensitive to surface quality than scanning tunneling spectroscopy. One more robust method is a break junction, which consist of using strain to physically break a material. Pressure applied to the broken sample is used to put the pieces into physical contact. The junction itself consists of many nanoscale contacts in parallel.

For a more controlled junction interface, the needle-anvil technique is both robust and reproducible. It is the most popular PCS technique. A needle anvil junction is made by bringing a sharp probe tip into contact with the material of interest. The tip is often made of a highly conducting metal, such as gold. The Au tips made in the Greene group's lab [229], such as that shown in Figure 8.2, are curled at the tip in order to give them a bit of spring in their response to applied pressure. In this way, even with thermal contraction and expansion effects, a stable contact can be maintained.

The tip material may be chosen to tune the junction response. For example, ferromagnetic tips are employed to produce spin-polarized currents. Superconductors also make excellent tip materials for studying superconducting gap energies since the Andreev features produced by superconductor-superconductor junction appear sharper in conductance spectra than normal metal-superconductor junctions.

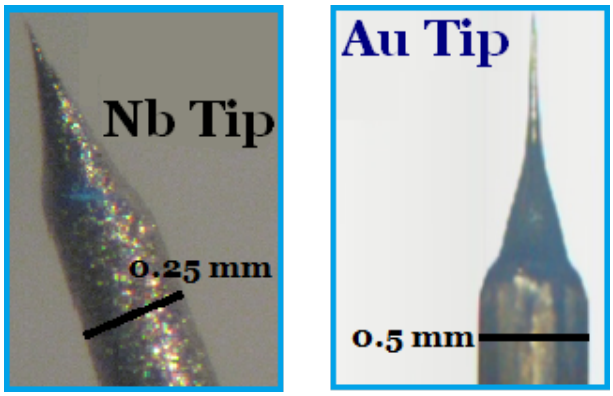

Figure 8.2: **Photos of Nb and Au tips for needle-anvil PCS. Left:** A Niobium tip made by electro-chemical etching in HF acid. **Right:** A gold tip made by electro-chemical etching in HCl acid. The long, soft tip is pre-bent into a curl (not shown) to give it a spring-like behavior that helps the tip maintain mechanical contact with a sample even under thermal contraction and expansion.

Even with tips designed to withstand some thermal effects, maintaining stable contact between a tip and sample becomes difficult at temperatures above the liquid nitrogen regime. "Soft" point contact junctions are more robust. Fellow graduate student Hamood Arham and I developed a technique to produce soft point contacts on pnictides by thermally evaporating a thin insulating AlO_x layer onto the sample under study, and then using Ag paint to affix μm-scale wire to the surface. Using a current source to "frit" across the junction produced multiple nanoscale bridges through the AlO_x layer [191, 230]. Illustrations of a needle-anvil junction and the soft point contact junction geometry are shown in Figure 8.3. Soft PCS junctions have proven far more mechanically stable than needle anvil junctions [225], though at the sacrifice of sometimes having larger effective junction sizes.

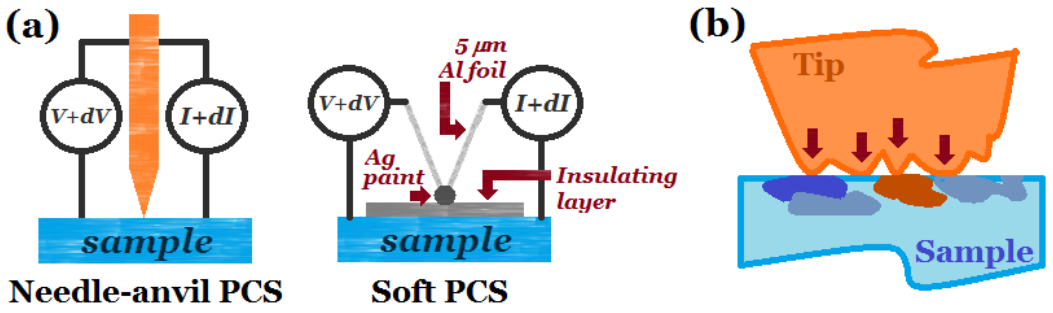

Figure 8.3: **Needle anvil and soft point-contact configurations. (A)** Needle anvil and soft point contact configurations. **(B)** Each contact represents many parallel nanoscale junctions between probe and sample.

The junction size is influenced by the size of the contact, and in the case of needle anvil configuration the applied pressure as well. However, the effective junction size is not the total area in contact. The needle, on a nanoscopic level, actually forms many parallel junctions with the sample. The same is true in the soft point contact geometry, where many parallel shorts determine the total dI/dV characteristic. This is illustrated in Figure 8.3.B.

8.3.2 Andreev reflection

Andreev reflection [231] dominates the point contact conductivity of a metal-superconductor (M-SC) or SC-SC interface at bias energies below the superconducting gap. In this section I will introduce the Andreev process, and in Section 8.3.3 I show how it can be used to extract the density of states and order parameter symmetry of a superconductor.

Material mismatch at an interface breaks translational symmetry and acts as a potential barrier for electrons to scatter from. At the junction interface in the Sharvin limit, electrons may either be reflected or transmit into the material with an energy eV_B with respect to the chemical potential. In a superconductor, a single electron cannot be transmitted below the gap energy, $eV_B < \Delta$.

Although the single particle density of states of a superconductor is gapped at low energy, electrons can still cross the point contact junction and enter into the condensate via Andreev reflection. In the Andreev reflection process, an electron picks up a second electron and forms a Cooper pair. To preserve particle number, the second electron is retro-reflected as a hole, with a spin and wavevector opposite to the incident electron (for s-wave pairing). The Andreev reflection process is illustrated in Figure 8.4, along with a cartoon of normal quasiparticle reflection for comparison.

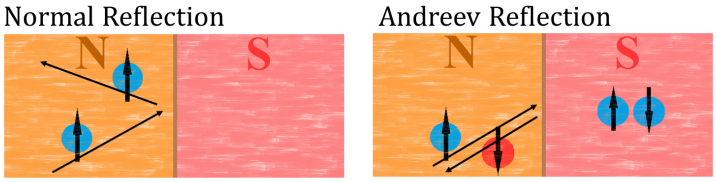

Figure 8.4: **Normal reflection and Andreev reflection at a superconductor interface.**

8.3.3 Modeling a point contact junction with a superconductor

In this section I will consider a one-dimensional point contact junction in which only the transport normal to the junction interface, k_z, is of interest. While this captures the essential physics, in practice, the PCS tunneling current is sensitive to some in-plane scattering $\vec{k}_{\parallel}$.

Harrison [232] worked out the general case of the tunneling current of independent quasiparticles.

$$J_{ab} = \frac{4\pi e}{\hbar} \int_{-\infty}^{\infty} |M_{ab}|^2 \rho_a \rho_b (f_a - f_b) dE, \tag{8.2}$$

where ρ_a is the density of states of material a and f_a is the probability of state a being occupied (generally, the Fermi function). The matrix element M_{ab} is proportional to the Fermi velocity of each material,

$$M_{ab} \propto \left(\frac{m}{\hbar^2}\right)^2 \left(\frac{\partial E}{\partial k_z}\right)_a \left(\frac{\partial E}{\partial k_z}\right)_b. \tag{8.3}$$

But the Fermi velocity is inversely proportional to the density of states for independent quasiparticles,

$$\rho_a \propto \left(\frac{\partial E}{\partial k_z}\right)_a^{-1}. \tag{8.4}$$

Thus the final tunneling current contains no density of states information.

A point contact junction with a superconducting material retains spectroscopic information about the superconducting gap due to the many body interactions of the electrons, which condense into a paired state. The point contact conductance of a normal metal-superconductor interface is well described with the Blonder-Tinkham-Klapwijk (BTK) model [5]. The BTK model is a one-dimensional approximation of an N-S junction, where the interface is treated as a delta function potential barrier. The original formulation was developed for s-wave symmetry. Starting with the Bogoliubov equations,

$$\begin{aligned} i\hbar \frac{\partial f}{\partial t} &= \left(-\frac{\hbar^2}{2m}\nabla^2 - \mu(z) - V(z)\right) f(z,t) + \Delta(z) g(z,t), \\ i\hbar \frac{\partial g}{\partial t} &= -\left(-\frac{\hbar^2}{2m}\nabla^2 - \mu(z) - V(z)\right) g(z,t) + \Delta(z) f(z,t), \end{aligned} \tag{8.5}$$

the model assumes the chemical potential, μ, and the superconducting gap, Δ, to be constant. The only potential is at the N-S barrier, $V(z) = H\delta(z)$. The barrier strength is defined as the unitless parameter $Z = H/\hbar v_F$. A low Z corresponds to a highly transparent, Andreev-dominated junction and a high Z corresponds to a low transparency tunneling junction. By tuning this single parameter, therefore, this model can be applied to both tunneling and point contact spectroscopy geometries.

Assuming a plane wave description of the charge carriers, the incident wavefunction for an electron is,

$$\psi_{\text{inc}} = \begin{pmatrix} 1 \\ 0 \end{pmatrix} e^{iq^+ z}. \tag{8.6}$$

We've adopted the notation $\psi = \binom{f(z,t)}{g(z,t)}$. Two reflection processes and two transmission processes may occur at the N-S interface. The first is Andreev reflection, which we denote as having probability $A = a^*a$. The second is regular reflection, with probability $B = b^*b$. The electron can be transmitted without crossing the Fermi surface with probability $C = c^*cN_S(E)$, where $N_S(E)$ denotes the superconducting density of states. It can also transmit by crossing the Fermi surface with probability $D = d^*dN_S(E)$. See Figure 8.5 to visualize the four processes.

The reflection and transmission wavefunctions are,

$$\begin{aligned} \psi_{\text{ref}} &= a \begin{pmatrix} 0 \\ 1 \end{pmatrix} e^{iq^- z} + b \begin{pmatrix} 1 \\ 0 \end{pmatrix} e^{-iq^+ z}, \\ \psi_{\text{trans}} &= c \begin{pmatrix} u_0 \\ v_0 \end{pmatrix} e^{ik^+ z} + d \begin{pmatrix} v_0 \\ u_0 \end{pmatrix} e^{-ik^- z}, \end{aligned} \tag{8.7}$$

where $u_0^2 = 1 - v_0^2 = 0.5(1 + \sqrt{E^2 - \Delta^2}/E)$. Solving Equations 8.5 yields the probability amplitudes a, b, c, and d, which can be used to calculate the current across the junction. If we define the distribution of quasiparticles moving in each direction as $f_{\rightarrow}(E, V)$ and $f_{\leftarrow}(E, V)$, then the total current density across a junction with bias voltage V is,

$$J(V) = 2N(0)v_F e \int_{\infty}^{\infty} \left(f_{\rightarrow}(E, V) - f_{\leftarrow}(E, V)\right) dE, \tag{8.8}$$

where $N(0)$ is the one-spin density of states at the Fermi level and v_F is the Fermi velocity at the interface. The quasiparticle distributions can be defined in terms of

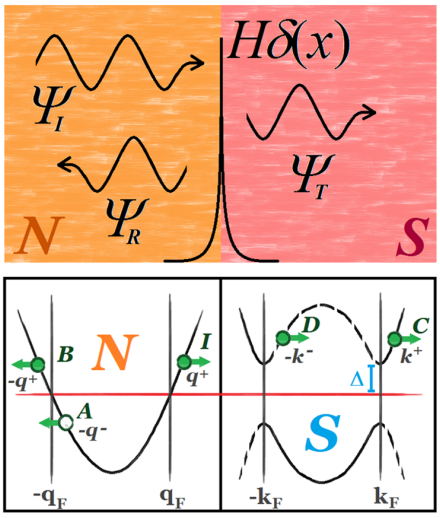

Figure 8.5: **One-dimensional model of a point contact junction. Top:** The point contact interface is modeled as a delta function potential. **Bottom:** A simplified energy vs. momentum diagram of a normal metal (N) and superconductor (S). The momenta of incident (I) carriers and normally reflected (B) and Andreev reflected (A) carriers are illustrated on the normal metal side. The two transmission processes, without band crossing (C) and with band crossing (D) are illustrated on the superconductor side.

the reflection and transmission probabilities,

$$\begin{aligned} f_{\rightarrow}(E,V) &= f_0(E-eV), \\ f_{\leftarrow}(E,V) &= A(E)(1-f_{\rightarrow}(E,V)) + B(E)f_{\rightarrow}(E,V) + \\ &\quad (C(E)+D(E))\, f_0(E), \end{aligned} \tag{8.9}$$

where $f_0(E)$ is the Fermi distribution. Equation 8.8 can be simplified to,

$$J(V) = 2N(0)v_F e \int_{-\infty}^{\infty} (f_0(E-eV) - f_0(E))\,(1 + A(E) - B(E))\, dE. \tag{8.10}$$

Figure 8.6 shows the BTK model applied in the low Z (Andreev) and high Z (tunneling) limit. Figure 8.6.A plots a normalized point contact conductance spectrum $G(V)/G_0$ measured with a superconducting Nb tip on an Au substrate. G_0 is the normal state conductivity of Nb. Below the superconducting gap, transport across the point contact junction is enhanced due to Andreev reflection. The maximum enhancement is $G(V)/G_0 = 2$, corresponding to a perfectly transparent barrier $Z \rightarrow 0$.

In this limit, for every injected electron, two electrons cross the microconstriction and enter the condensate as a Cooper pair.

Figure 8.6.B plots the tunneling spectrum from a Pb-AlO_x-Al planar tunnel junction at 4.3 K, where the Al is normal metallic and the Pb is superconducting. The drop in conductance is due to the Pb superconducting gap, with spectral weight pushed to the gap edge as seen by an enhanced $G(V)/G_0 > 1$ around the gap energy. Andreev reflection is suppressed by the AlO_x tunnel barrier. Above the gap edge, additional features in the conductance are the result of phonons. Both spectra have been fit with the BTK formula, Equation 8.10 (red lines).

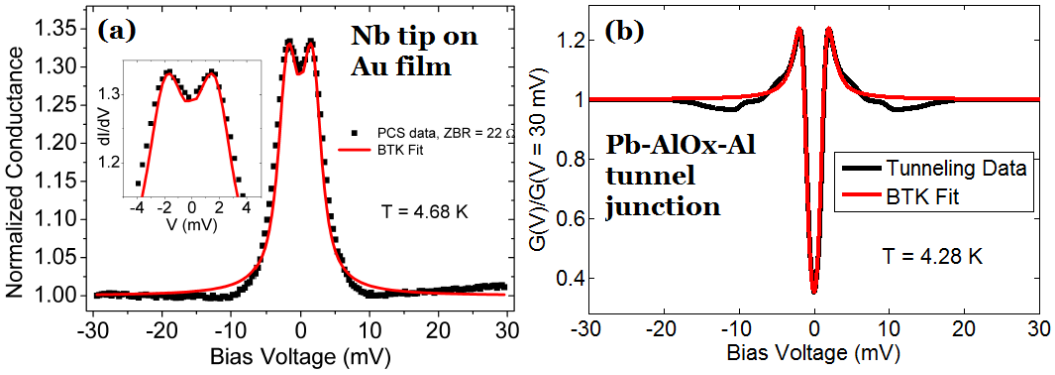

Figure 8.6: **A comparison of the Andreev and tunneling limits. Left:** Spectra produced by a Nb point contact tip in mechanical contact with an Au film in the needle anvil configuration. **Right:** Spectra produced by a planar Pb-AlO_x-Al tunnel junction. Red lines in both figures are fits using the s-wave BTK model described in the text.

Given the simplicity of the BTK model, it has been remarkably accurate at describing s-wave N-S junctions. Since its publication in 1982, the BTK model has been successfully extended to describe quasiparticle lifetime effects [233] and other OP symmetries including d-wave [218, 234], p-wave [235], and anisotropic s-wave [236]. The discovery of the iron-based compounds has generated new interest on the role of multiple bands and several attempt to extend the BTK picture to $s_{\pm}$- and s_{++}-wave symmetries have emerged [6, 7].

8.3.4 Multiband models of superconductivity

In practice, it is sufficient for most systems to restrict the multiband description to two bands. In MgB_2, although four bands participate in the superconducting state, they can be divided into quasi-2D σ bands and 3D π bands, reducing the problem to effectively two bands [237]. Likewise in the pnictides, the hole-like bands all have a similar gap energy, as do the electron-like bands.

Proposed multiband models incorporate interference effects between the bands in different ways. The simplest multiband description is to treat the bands as independent, each described by the BTK model (Equation 8.10), and the net conductance as a weighted sum between bands 1 and 2,

$$\frac{dI}{dV} = w_1 \frac{dI_1}{dV} + (1 - w_1)\frac{dI_2}{dV}. \tag{8.11}$$

In the model by Golubov, *et al.* [6], the modified BTK transmission wavefunction looks like,

$$\begin{aligned} \psi_{\text{trans}} &= c\left\{\Phi_{k_1^+}(z)\begin{pmatrix} u_1 \\ v_1 e^{-i\phi_1}\end{pmatrix} + \alpha\Phi_{k_2^+}(z)\begin{pmatrix} u_2 \\ v_2 e^{-i\phi_2}\end{pmatrix}\right\} \\ &\quad + d\left\{\Phi_{-k_1^-}(z)\begin{pmatrix} v_1 \\ u_1 e^{-i\phi_1}\end{pmatrix} + \alpha\Phi_{-k_2^-}(z)\begin{pmatrix} v_2 \\ u_2 e^{-i\phi_2}\end{pmatrix}\right\}. \end{aligned} \tag{8.12}$$

where Bloch waves, $\Phi_q(z) = \sum_G A_{G,q}\exp\{i(q+G)z\}$, have replaced the plane waves of the BTK model. The parameter α governs the strength of the interference between the bands. The phase difference $\Delta\phi = \phi_2 - \phi_1$ differentiates between $s_\pm$-wave ($\Delta\phi = \pi$) or s_{++}-wave ($\Delta\phi = 0$).

As a test of the model, I applied it to the case of MgB_2. The results are plotted in Figure 8.7. To agree with experiment, I needed to introduce an interface velocity mismatch for each band. The interface velocity is defined as,

$$v_k = -\frac{i}{m}\frac{1}{\Phi_k}\frac{d\Phi_k(z)}{dz}\bigg|_{z=0}. \tag{8.13}$$

The mismatch falls between $v_2/v_1 = 4.0$ in the Andreev limit and $v_2/v_1 = 6.4$ in the tunneling limit. These values fall in line with calculations of the Fermi velocity mismatch between the π and σ bands [238]. The calculated Fermi velocity ratio was found to be $v_\pi/v_\sigma = 1.22$ in the ab-plane and $v_\pi/v_\sigma = 8.65$ along the c-axis. Since PCS has a wide momentum resolution, the values we measure should fall somewhere

between these limits, though closer to the c-axis ratio as the point contact junction approaches the tunneling limit. Indeed this is what we find.

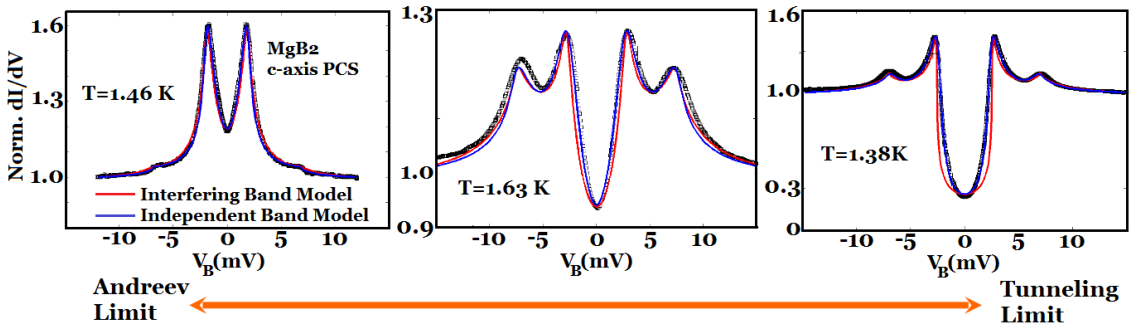

Figure 8.7: **Two band models applied to MgB_2.** Three c-axis oriented thin films of MgB_2 measured with an Au tip via needle-anvil PCS. In the Andreev limit, both the interfering band model proposed by Golubov, *et al.* [6] and the independent BTK band model accurately reproduce the measured spectra. As we move into the tunneling regime, the interfering band model begins to deviate from the independent band model at low bias. The lower-most spectra was taken on a film with a hard surface oxide layer, allowing a planar tunneling measurement using PCS techniques. The interfering band model predicts a steeper gap edge than what we find experimentally.

The interfering band model appears deficient in the tunneling limit, however. The model yields a steeper gap edge than what we find experimentally, as can be seen in Figure 8.7. The red line indicates the interfering band model fit. Compare this with a fit to two independent BTK bands (blue line), calculated with Equation 8.11. The fundamental problem with the Golubov, *et al.* picture is that the interference between the bands cannot be tuned; turning down the interference (reducing α) turns off the second band as well. In the weak coupling limit, such as with MgB_2, we expect minimal interference. However for the iron-based superconductors, where coupling between bands is believed to be strong, the model may find a more appropriate home.

Another promising modified BTK model, developed by Sperstad, *et al.* [7], treats the particle and hole components of each band as a separate channel, and the Hamiltonian becomes a 4x4 tensor. The coupling is controlled by a tunable hopping pa-

rameter. When this parameter goes to zero, the model reduces to the independent band model (Equation 8.11).

8.3.5 Beyond superconductivity: a probe of correlated states

Although point contact spectroscopy was first utilized as a probe of phonon spectra, it found its home as a probe of superconductivity. PCS has become almost synonymous with the Andreev process, often referred to in the literature as PCARS (point contact Andreev reflection spectroscopy). However, in the past few years, the scope of correlated systems that have shown sensitivity to point contact techniques has proven that PCS is a general probe of correlated effects.

The heavy fermion material URu_2Si_2 is known to have a second order phase transition at 17.5 K, however the nature of that transition remains unclear [239, 240]. This so-called hidden order transition was proposed to be linked to the opening of a hybridization gap [222, 241], which neutron scattering [242] and scanning tunneling spectroscopy [243] indicated appeared near 17.5 K.

W. K. Park *et al.* [223] used point contact spectroscopy to show that the hybridization gap in URu_2Si_2 was not related to the hidden order transition in this material, setting in almost 20 K higher in temperature [226]. They also found that the spectral response was sensitive to the underlying Kondo lattice, producing a Fano lineshape in the conductance response [244]. Some trends in the spectra did appear to change when crossing 17.5 K, showing that PCS is at least indirectly sensitive to the hidden order as well.

Point contact spectroscopy has also been shown to be sensitive to orbital fluctuations. In a broad study of iron-based materials, H. Arham and collaborators found that enhanced conductance features could be tied to orbital fluctuations and the onset of electronic nematic order [225, 245]. We looked at the AFe_2As_2 system with A = Ca,Sr,Ba, the 111 compound NaFeAs, and the chalcogenide $Fe_{1+y}Te$. The Ba-122 system was investigated with both hole doping with K on the Ba sites and electron doping with Co on the Fe sites.

The enhanced zero bias conductance (ZBC) sets in at a temperature T_{onset} above the structural transition T_S in those compounds that exhibit electronic nematicity, as measured by other methods such as in-plane resistive anisotropy [225]. Using a five-orbital tight-binding model, Lee *et al.* [214] showed an enhanced point contact conductance would be a consequence of orbital fluctuations above T_S. An enhanced

ZBC was found in Co-doped (electron-doped) $BaFe_2As_2$, $SrFe_2As_2$, and NaFeAs; P-doped (isovalent-doped) $BaFe_2As_2$; and $Fe_{1+y}Te$. The doping trend for Co-doped Ba-122 is shown in Figure 8.8. The temperature scale of T_{onset} tracks the orbital ordering temperature measured for $Ba(Fe_{1-x}Co_x)_2As_2$ with angle resolved photoemission spectroscopy (ARPES) [246].

In $CaFe_2As_2$ and K-doped (hole-doped) $BaFe_2As_2$, on the other hand, the enhanced ZBC conductance is suppressed. The compound $CaFe_2As_2$ shows no evidence of nematic order while K-doped $BaFe_2As_2$ shows some evidence of a fluctuating nematic regime [247], smaller than that of electron-doped compounds.

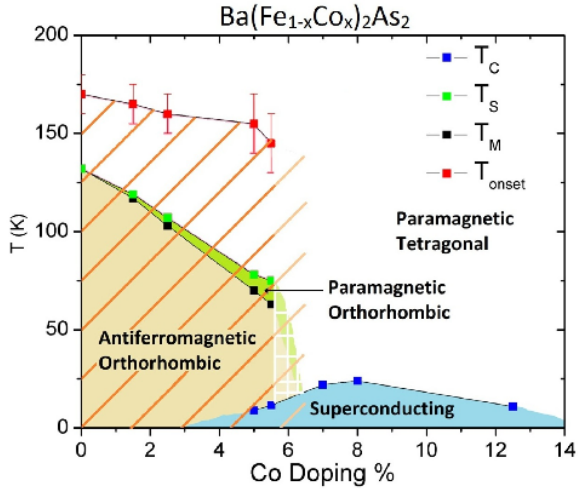

Figure 8.8: **Phase diagram of $Ba(Fe_{1-x}Co_x)_2As_2$.** The temperature scale T_{onset} represents the onset of orbital fluctuations. Figure from Ref. [225].

Interestingly, the dI/dV conductance curves show the formation of a finite bias peak and ZBC dip structure at lower temperatures. This may be related to a simple competition between scattering processes [245]. However, the energy scale seems to correspond to the spin density wave gap [188], suggesting the possibility that the drop in conductance may be related to this gapping. PCS has been shown to be sensitive to SDW order in chromium [248] and, recently, the CDW gap in Nb_3Sn [249].

8.4 Point contact spectra of $Sr(Fe_{1-x}Co_x)_2As_2$

8.4.1 Samples

$Sr(Fe_{1-x}Co_x)_2As_2$ is a 122 compound doped with Co atoms. The 122 crystal structure is shown in Figure 8.9, with the FeAs tetrahedron highlighted. Single crystals of Co-doped $SrFe_2As_2$ were prepared using flux-growth techniques with Sn flux and elemental Sr, Fe, and As with purities greater than 99.99%, as described in [250]. Substituting Co atoms at the Fe sites acts as an electron dopant. At $x = 0.125$, we are near optimal doping, far from the antiferromagnetic and nematic regimes. The superconducting transition temperature for this compound is $T_c = 14.5$ K.

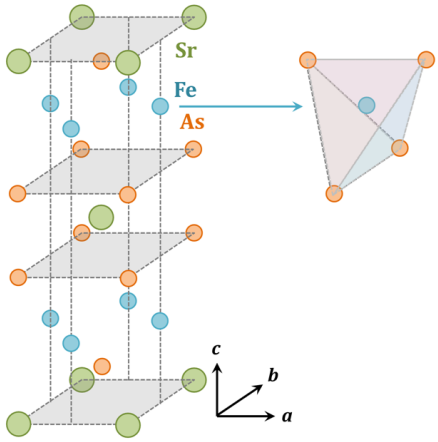

Figure 8.9: **Crystal structure of AFe$_2$As$_2$ (A = Sr,Ba,Ca).** The typical unit cell is shown at left, with green circles representing the the A sites, Fe atoms in blue, and As in orange. Co dopes the Fe sites. The $FeAs_2$ tetrahedron is illustrated at right.

8.4.2 Features of the point contact spectrum

The sensitivity of c-axis spectra to each gap varies contact-to-contact, with the balance sometimes favoring just one gap energy. These are probably the hole-like bands, which exhibit more three-dimensional character than the electron-like bands [251]. Figure 8.10.A plots a characteristic spectrum measured along the c-axis at sev-

eral temperatures up to 16 K, above the superconducting transition temperature $T_c = 14.5$ K. This spectrum shows evidence of only one gap, with higher frequency features between 10 and 30 mV due to phonons (see Section 8.4.4).

The spectra were fit with the single band BTK model (blue lines in Figure 8.10.A). Three fit parameters were employed; the barrier energy Z and the gap energy Δ are described in Section 8.3.3. The Γ term takes into account quasiparticle lifetime effects [233] by mapping the energy E in Equation 8.11 to $E \to E - i\Gamma$.

The superconducting gap (blue dots in Figure 8.10.C) is well-fit by an approximate form of the BCS mean field gap function in the strong coupling regime (dashed line),

$$\Delta = \Delta_0 \tanh\left(\beta\sqrt{T_c/T - 1}\right). \tag{8.14}$$

For a BCS superconductor, $\beta = 1.74$ and $2\Delta_0/k_BT \approx 3.53$ [252]. The BCS case is plotted in Figure 8.10.C by a thick grey line. For Sr-122, we find $\beta = 1.27$ and $2\Delta_0/k_BT_c \approx 6.5$. The large value for $2\Delta_0/k_BT_c$ puts this superconductor firmly in the strong coupling regime.

The apparent shift in the phonon spectrum with the gap energy may be tied to the changing value of Z, which becomes more transparent as $T \to T_c$. In the transparent limit, $Z \to 0$, the phonon features are shifted from the phonon frequency ω_{ph} to an energy $E_{ph} = \hbar\omega_{ph} - \Delta$ [253]. The energy of one of these features, at $E_{ph}(0) = 24$ meV, is plotted with green squares in Figure 8.10.C.

A similar spectral feature, seen in optimally doped $Ba(Fe_{1-x}Co_x)_2As_2$, has been attributed by Tortello *et al.* [254] as due to spin-resonance excitations. A spin excitation feature has been reported in inelastic neutron scattering measurements at $\hbar\omega_{sp} = (1.58 \pm 0.3)\Delta \approx 9$ meV which tracks $\Delta(T)$ [204]. Evidence for this mode has also been seen in specific heat measurements [255]. However, the feature at 20 meV in Ref. [254] is too high in frequency to be directly related to this mode[1]. And the shift in energy is observed for *all* modes above the gap. I will show in Section 8.4.4, the 20 meV mode can be attributed to the A_{1g} phonon excitation of the As atoms.

Near T_c where the gapping is small, and extending several Kelvin above T_c, the phonon spectrum continues to show some small temperature dependent shift. This is plotted for the $E_{ph}(0) = 24$ meV feature in Figure 8.10.C. A zero bias peak also

[1] In Ref. [254], they claim the actual mode frequency is at $\hbar\omega_{sp}(T) = E_{sp}(T) - \Delta(0)$, however this does not seem to be justified in the $Z \to 0$ range. And, at any rate, the shift should track $\Delta(T)$ at all temperatures and not just $\Delta(0)$.

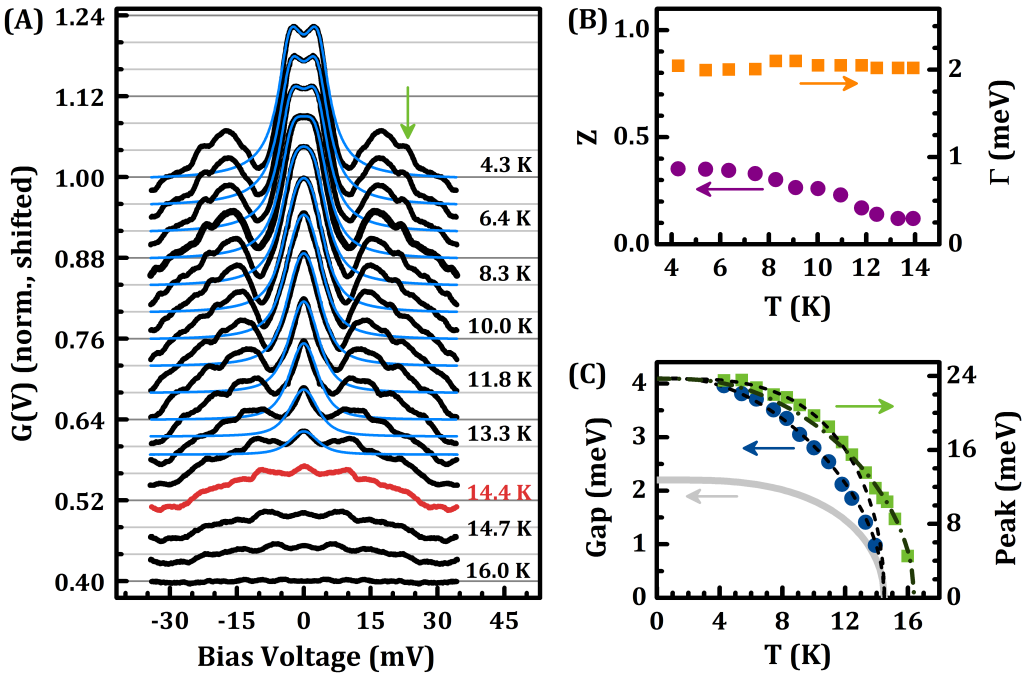

Figure 8.10: **Gap evolution of Sr-122. (A)** The symmeterized spectrum of 12.5% Co-doped Sr-122 (black), normalized by the spectrum at $T = X$ K. The spectrum is fit to Equation 8.11 from Ref. [5] (blue). **(B)** The fit parameters Z and Γ, as described in the text. **(C)** The superconducting gap (blue dots) as a function of temperature, fit to the mean field Equation 8.14 (black dashed line). The BCS behavior for a gap with $T_c = 14.5$ K is plotted for comparison (grey line). The mean phonon frequency (green squares) is also fit to the same equation, by enforcing $T_c = 14.5$ K (black dashed line) and by the best-fit transition temperature, 16.5 K.

appears to persist above T_c, as seen in Figure 8.10.A. This is a continuous feature above and below T_c and directly attributable to Andreev reflection. (The gap values for the Andreev peak above T_c are not shown in Figure 8.10.C). A gap that shows a "tail" extending above T_c can be accounted for by inhomogeneous doping, with the point contact probing several regions, in parallel, with spatially varying T_c values. Such a scenario is modeled in Figure 8.11.

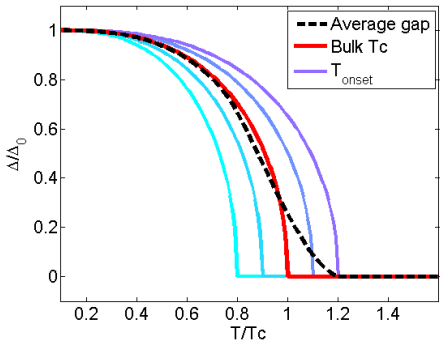

Figure 8.11: **Average gap energy due to inhomogeneity of the gap distribution.** A weighted distribution of gaps centered at $T/T_c = 1$ (red line) gives rise to a divergence from mean field behavior and a "tail" in the Δ vs T behavior (dashed line). The range of T_c values is illustrated with colored lines.

8.4.3 Detection of multiple gaps

For spectra that exhibit single gaps, the Andreev peaks are centered at 4 meV at 4.3 K and can be equally well-fit with a single band BTK model (Equation 8.10) as with the $s_{\pm}$-wave description by Golubov, *et al.* [6]. The slightly better fit of the Golubov model at higher bias (∼10 mV) may well be a coincidence due to the distortions caused by the higher energy phonon modes.

Spectra that exhibit multiple bands generally have features at 2 and 5 meV at 4.3 K. One of the clearest examples of two bands in the c-axis spectrum is shown in Figure 8.13[2]. The spectrum is fit with a two independent band s-wave BTK model, in the form of Equation 8.11 (blue lines). The quality of this fit suggests that efforts to distinguish $s_{\pm}$-wave order from s_{++}-wave will be challenging. Note that the independent band model gives the same solution as the $s_{\pm}$-wave model by Sperstad, *et al.* [7] in the limit of no interference between the bands.

The temperature evolution of the two bands is fit with the strong-coupling mean field form (Equation 8.14). We find gap energies of $2\Delta_1(0)/k_BT_c = 3.5$, at the BCS value, and $2\Delta_2(0)/k_BT_c = 11.3$, well in the strong coupling regime. The shape of the temperature evolution $\Delta(T)$ also shows evidence of strong coupling. The "flattening" of the temperature dependence compared with the BCS behavior (grey line in Figure 8.13.C) is a signature of strong coupling [191]. The fit captures the

[2]The data does not extend past T_c because unfortunately the contact was lost during heating.

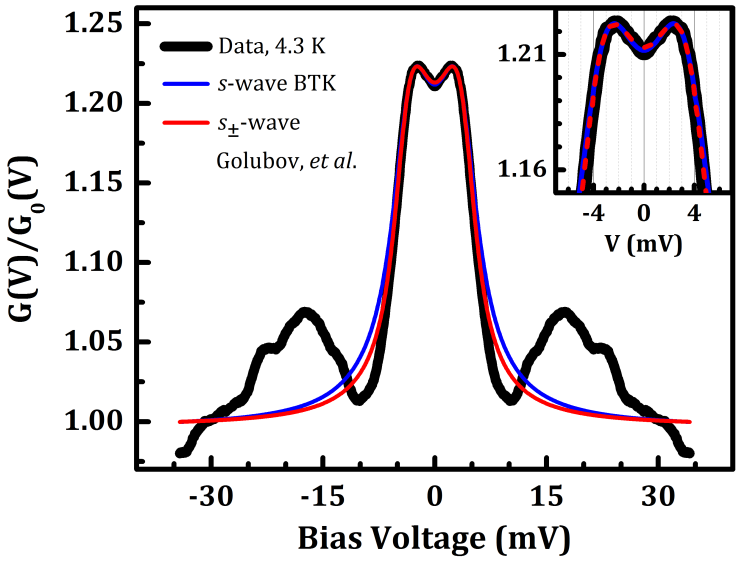

Figure 8.12: **Applying s-wave and $s_{\pm}$-wave models.** The point contact spectrum of 12.5% Co-doped Sr-122 at 4.3 K (black line). The spectrum has been symmeterized and normalized by the spectrum above $T_c = 14.5$ K. Two fits have been employed to model the conductance. A single band s-wave model from Ref. [5] (blue) and an $s_{\pm}$-wave model from Ref. [6] (red).

flattening by the decrease in the parameter β from the BCS value of 1.74, down to 1.05 and 0.95 for $\Delta_1(T)$ and $\Delta_2(T)$, respectively.

Spectra measured in-plane generally show evidence of both gaps. An example spectrum is shown in Figure 8.14. A histogram showing the gap energies of several contacts, measured at 4.3 K, is shown in Figure 8.15. The gap values were estimated by the position of the spectral peaks.

Fitting the gap energies is complicated by an additional spectral contribution at ∼10 meV. The mode can be seen as a small peak in Figure 8.13.A (purple arrow). However for most contacts, the ∼10 meV feature is detected with higher spectral weight. In Figure 8.14 it appears as a broad shoulder on the Andreev peaks. *This* feature, which is universally seen across in-plane contacts (see purple bars in Figure 8.16), may well be related to the reported spin excitation mode [204, 255][3]. The energy of the mode follows the expected scaling, $\hbar\omega_{sp} \approx 1.58\Delta_2 = 11$ meV.

[3]The reproducibility of this 10 meV peak and the higher energy modes—junction-to-junction and at different junction resistances—is a strong indication that the point contacts are in the ballistic regime and detecting intrinsic spectroscopic features.

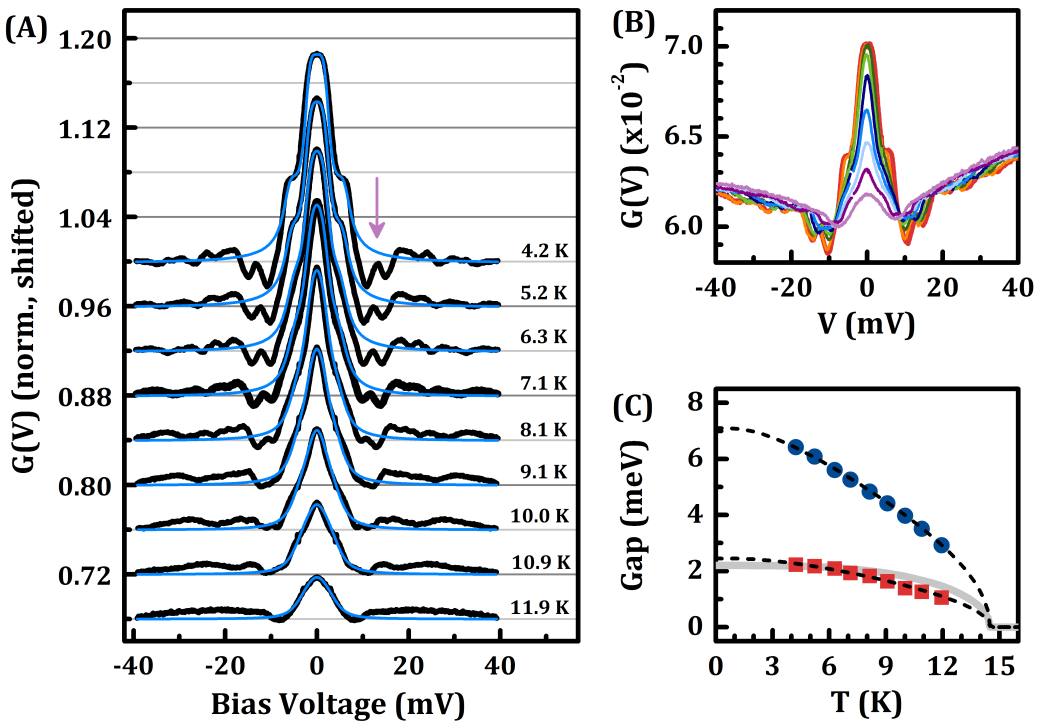

Figure 8.13: **Temperature evolution of two gaps.** **(A)** Symmeterized spectra (black lines) of 12.5% Co-doped Sr-122 at several temperatures up to near $T_c = 14.5$ K. Data has been normalized to a functional form approximating the normal state spectrum. Blue lines represent fits to Equation 8.11. **(B)** The raw spectrum at several temperatures. The background bias can be ascribed to electron-hole asymmetry. **(C)** The temperature evolution of the two gaps used in the fits. The dashed lines are mean field fits in the strong coupling regime (Equation 8.14). The grey line indicates the expected mean field behavior of a BCS superconductor.

A similar feature with the same $\hbar\omega_{sp}/\Delta$ scaling has also been reported in the 111 family [256].

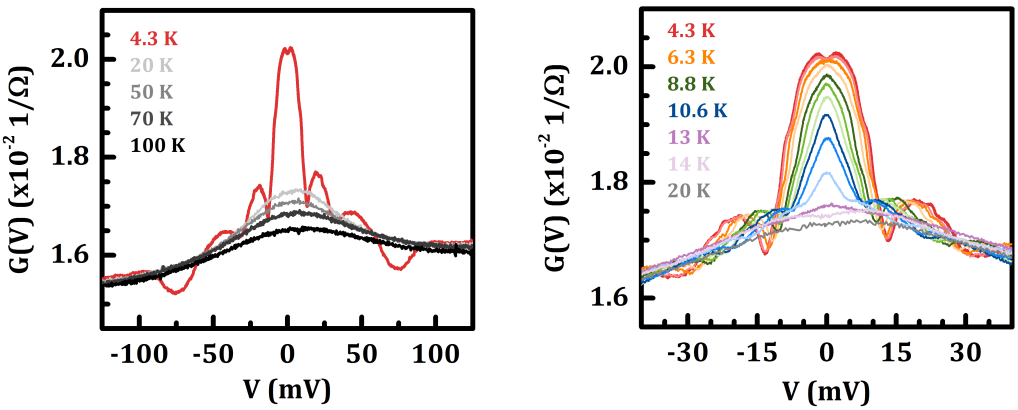

Figure 8.14: **Raw conductance spectra along the *ab*-plane. Left:** Spectrum over a broad energy range, showing the Andreev reflection peaks and accompanying phonon modes at 4.3 K. **Right:** Raw spectrum at several temperatures up to 20 K, above $T_c = 14.5$ K.

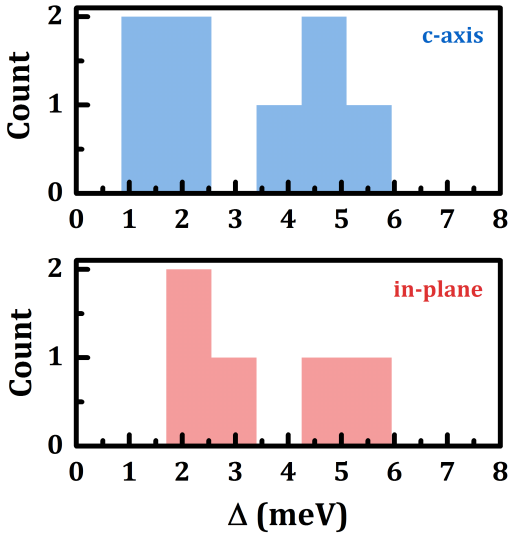

Figure 8.15: **Histogram of gap energies of $Sr(Fe_{0.875}Co_{0.125})_2As_2$.**

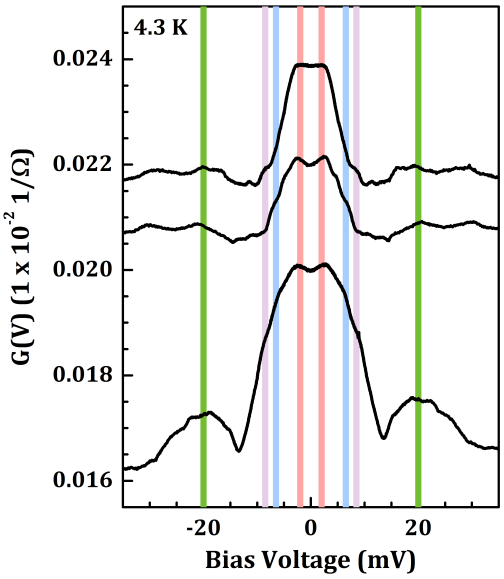

Figure 8.16: **Reproducibility of *ab*-plane contacts.** Spectra of three contacts (black), with vertical bars highlighting low energy features. The smaller gap is in pink and larger in blue. The two green lines indicate additional features at 9 meV and 20 meV. The 20 meV feature can be identified as the A_{1g} mode. The origin of the 9 meV feature is less clear, though it may be tied to spin excitations (see discussion in text).

8.4.4 Phonon spectrum

The Eliashberg function, $\alpha^2F(\omega)$, describes the density of phonon modes $F(\omega)$, weighted by the electron-phonon coupling of the modes α^2. Point contact spectra are sensitive to $\alpha^2F(\omega)$, where the second derivative of the conductivity $d^2I/dV^2 \propto -\alpha^2_{pcs}F(\omega)$. The term α^2_{pcs} reflects that the electron-phonon coupling for a point contact differs slightly from the Eliashberg term α^2 [191]. The exact shape of the spectrum depends on the transparency of the junction [191], but generally in the small Z limit, the modes appear as peaks in $-d^2I/dV^2$. In this section I will report the excitation spectrum of Co-doped Sr-122. Certain mode excitations around 20 meV have been characterized as arising from magnetic excitations [254]. In fact, the modes above 10 meV correspond exactly to the Raman phonon spectrum.

The tetragonal structure has a space group D^{17}_{4h}-$I4/mmm$, with Raman active modes along the c-axis of A_{1g} and B_{1g} symmetry and planar E_g symmetry modes [257]. These modes are depicted in Figure 8.17. Similar mode energies have been measured for $BaFe_2As_2$ and $SrFe_2As_2$. The E_g modes have resonances at 16 meV and 32 meV [258, 259]. The A_{1g} mode has an energy of about 22 meV and the B_{1g} mode is centered around 25 meV [257, 259].

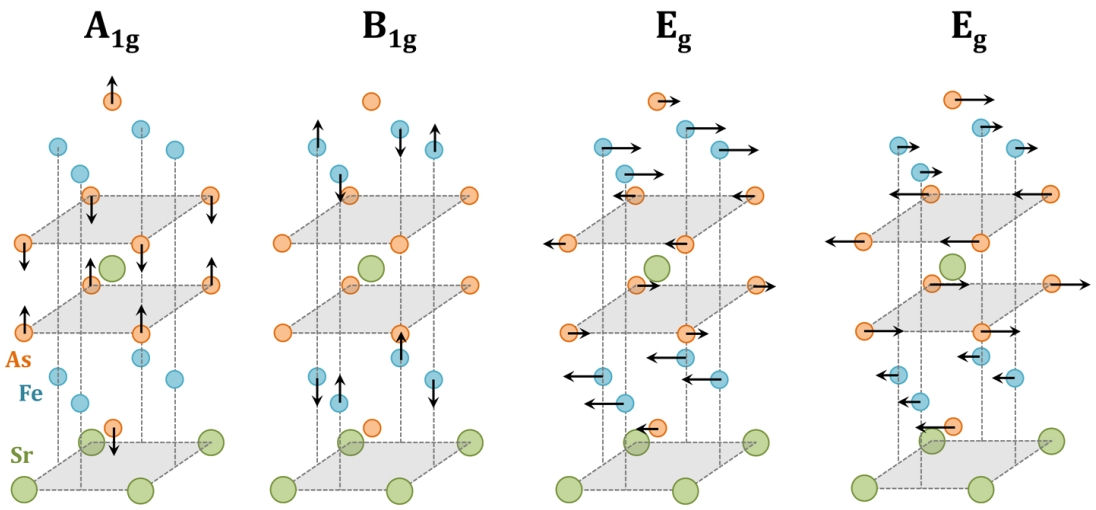

Figure 8.17: **Raman-active phonon modes of 122 pnictides.** Four lowest frequency excitations of the Fe and As atoms. In the tetragonal phase, the E_g modes are doubly degenerate along the a and b crystallographic axes.

The quantity $-d^2I/dV^2$, proportional to the phonon spectrum, is plotted in Figure 8.18 for spectra measured along the c-axis (top panel) and in-plane (bottom panel). For each orientation, spectra from two contacts are shown (plotted in different colors). While the contact orientation determines which axis dominates the response, the some spectral component is acquired along all directions. The c-axis spectra show four distinct peaks, centered at approximately 13 meV, 21 meV, 25 meV, and 32 meV. These energies correspond directly to the four Raman modes. In-plane, the phonons appear at similar frequencies, but the c-axis B_{1g} mode is notably absent. While this is not surprising in itself, it is interesting that the A_{1g} mode is detected while the B_{1g} is not. The increased sensitivity to the A_{1g} mode compared to the B_{1g} may be due to the stronger electron-phonon coupling of the A_{1g} mode [19], which is enhanced further upon Co-doping in Ba-122 [259].

As mentioned in Section 8.4.2, phonon modes detected by a point contact junction with a superconductor can appear at energies shifted with respect to their central frequency ω_{ph}, with a shift depending on the barrier Z across the junction [253]. In the tunneling regime, $Z \to \infty$, the phonon features shift to $E_{ph} = \hbar\omega_{ph} + \Delta$ while in the point contact limit $Z \to 0$, $E_{ph} = \hbar\omega_{ph} - \Delta$. At low temperatures, we calculate intermediate Z values $\sim$0.35-0.4. In this regime, the phonon spectrum should appear near its true frequency values [260]. Indeed we find that the phonon frequencies are at most 1-2 meV below the Raman-measured values.

The phonon spectrum measured by inelastic neutron scattering [258] is shown in the top panel of Figure 8.19 for the parent compound $SrFe_2As_2$ at 180 K. This is in the orthorhombic phase, however, the spectrum does not change significantly through the transition from tetragonal symmetry [257], and is indeed nearly temperature independent between 2 K and 300 K [258]. The bottom panel shows two *ab initio* calculations of the phonon spectrum, as described in Ref. [258]. The spectra measured by point contact agree remarkably well with the neutron scattering results and the calculated spectrum.

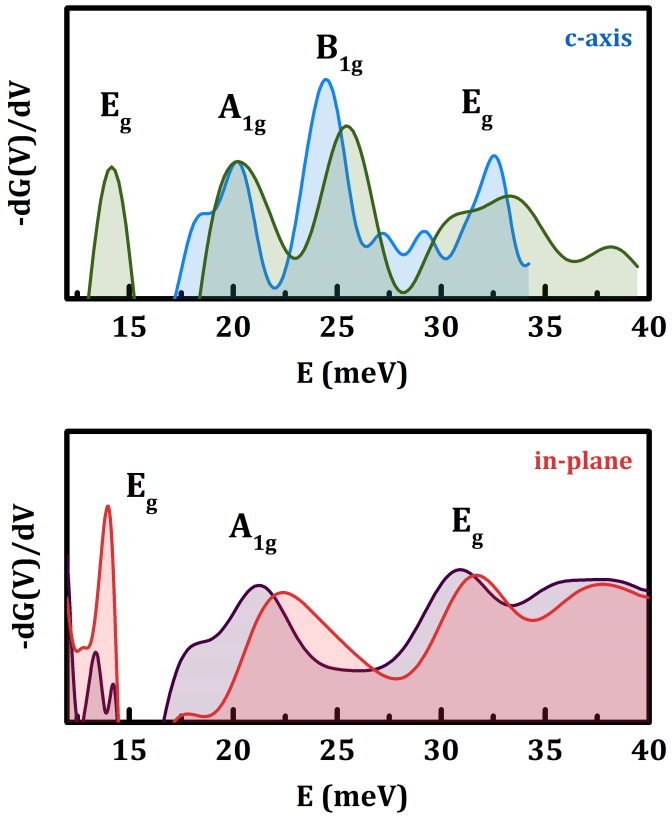

Figure 8.18: **Phonon spectrum measured along the c-axis and in-plane.** Spectra of $Sr(Fe_{0.875}Co_{0.125})_2As_2$, all measured at $T \leq 4.3$ K ($T_c = 14.5$ K). Spectrum has been smoothed for clarity.

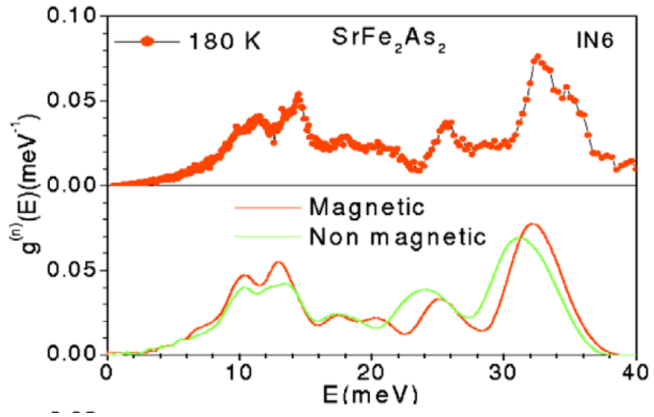

Figure 8.19: **$SrFe_2As_2$ phonon spectrum measured by neutron scattering.** **Top:** Inelastic neutron scattering measurement of the phonon spectrum of $SrFe_2As_2$. **Bottom:** *Ab initio* calculations of the spectrum. The non-magnetic measurement neglects the role of spin polarization, which shifts the modes above 20 meV. Figure from Ref. [258].

8.4.5 Quality of point contact junctions

Finally, I will end with a note on junction quality. Several thorough reviews have been written addressing how to characterize whether a junction is in the Sharvin limit [191, 225] and the topic is discussed in some detail in Naidyuk and Yanson's *Point Contact Spectroscopy* [216].

This issue is especially relevant for the Fe-based high temperature superconductors, which exhibit a very short elastic mean free path, on order 10 nm [261]. For these materials, a contact in the intermediate diffusive regime, approaching the thermal limit, has a few immediately identifying characteristics. First, the Andreev response does not clearly show peaks at the lower gap energy. These gaps have energies on the BCS scale, $2\Delta/k_bT_c \approx 3.5$ and are generally smeared out. Contacts may show some features characteristic of the higher gap energy, but the Andreev enhancement tends to be low. Even ballistic contacts tend to show enhancements of only 10-20% [4]. In the thermal regime, they may be only on order 1%. The Andreev peaks are accompanied by broad shoulders, with frequencies related to the phonon spectrum but which appear almost as a second set of Andreev peaks. In fact, they have been interpreted as such in literature [186].

A few examples of "clean", ballistic limit contacts and some that are more diffusive-to-thermal regime contacts are plotted in Figure 8.20. The superconducting gap values are highlighted as vertical bars.

[4] The 11 chalcogenides are a noted exception to this. We have reported anomalous enhancements of *greater* than 100% [262].

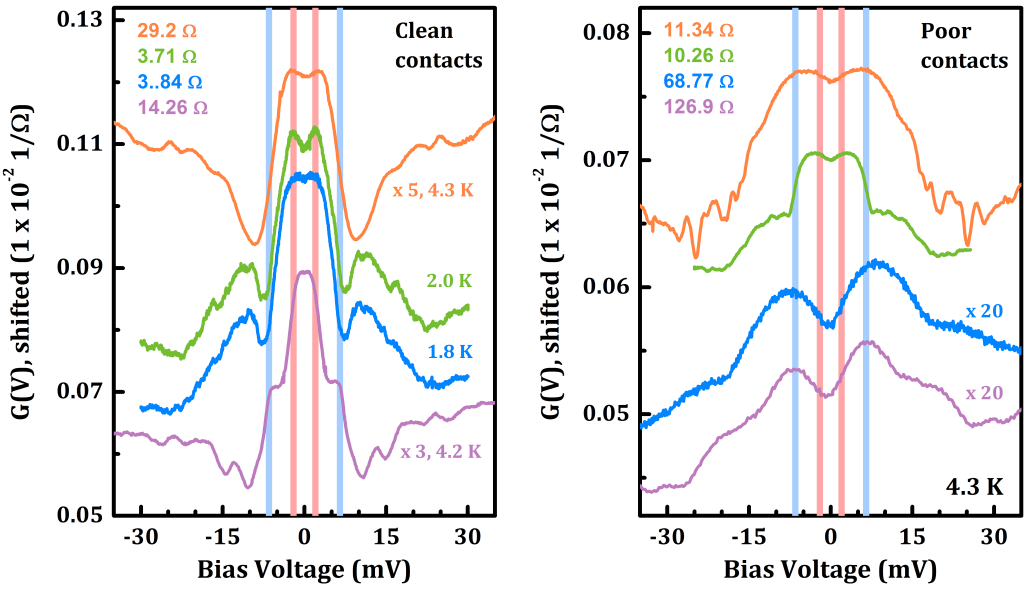

Figure 8.20: **Reproducibility of c-axis contacts. Left:** Contacts in or near the ballistic limit. Each contact shows clear features at both gap energies. Higher frequency phonon modes are also clearly distinguishable. **Right:** Contacts in or near the thermal regime. These contacts show little or no Andreev enhancement of the low frequency gap. They exhibit a broad shoulder, extending out to 20 meV or higher in frequency.

Chapter 9

Concluding remarks

9.1 Using selective light excitation to modify and enhance superconductivity

In this thesis I have explored two distinct scenarios in which selective light excitation of a cuprate can be used to transition from a non-superconducting ground state to a high mobility state that bears a striking resemblance to superconductivity. For both cases, $La_{1.8-x}Eu_{0.2}Sr_xCuO_4$ and $YBa_2Cu_3O_x$, the light-induced state is characterized by the appearance of a plasma mode at a frequency similar to the Josephson plasma frequency. This is a frequency regime which features no other equilibrium collective mode in any of the compounds considered.

While the fundamental observation is similar, each experiment is quite different in detail (see the discussion sections of Chapters 4, 5, and 7). In the case of $La_{1.8-x}Eu_{0.2}Sr_xCuO_4$, the excitation is chosen to target a competing order and thus indirectly supports the superconducting state. In the case of $YBa_2Cu_3O_x$, on the other hand, the apical oxygen phonon mode resonance was targeted to directly manipulate superconductivity. The relative position of the apical oxygen atoms in the lattice has been shown to correlate with T_c in equilibrium.

The transient plasma mode, attributed to Josephson coupling, was measured via its effect on the optical conductivity. Here I will discuss some other potential ultrafast probes of the superconducting state, and share a few thoughts on targeted excitation.

9.1.1 Detecting transient superconductivity

As I have shown in this work, the optical conductivity of a superconductor exhibits unique characteristics that can be used to identify the superconducting state. However the optical response alone cannot determine the existence of pairing. The Meissner effect is the only *direct* bulk probe of a paired state. A time-resolved measure of the Meissner effect would provide unequivocal support that the two light-induced states discussed in this thesis, in $La_{1.8-x}Eu_{0.2}Sr_xCuO_4$ and $YBa_2Cu_3O_x$, are in fact transient superconductivity.

The realization of such a measurement would require a highly sensitive magnetic field probe with a time resolution of 1 ps or better. The sensitivity requirements are especially problematic due to the inhomogeneous nature of the transient state, particularly in the case of $YBa_2Cu_3O_x$. One possible method of detection might be realized if the expelled field produces a measurable THz field. This could perhaps be enhanced by fabrication of the sample in the shape of an antenna structure.

The suppression of the light-induced plasma mode by a static magnetic field would be another form of confirmation that the transient state measured above T_c is related to superconductivity. I predict that a moderate (several Tesla) applied field would cause either a red shift or even a splitting of the transient plasmon. Neither of these effects would be expected for a plasma mode generated by excited quasiparticles. In the case of $La_{1.8-x}Eu_{0.2}Sr_xCuO_4$, perhaps, the suppression of the transient plasmon would be the most pronounced, as an applied field has been shown to support the charge and spin ordered ground state against superconductivity in equilibrium.

Besides the Meissner effect, an equilibrium superconductor is characterized by the onset of zero dc resistivity due to pair conductance. A transient superconducting state should in principle be accompanied by a large, low frequency enhancement in Ohmic conductivity. This enhancement may be detectable with GHz frequency pulses generated and detected along a stripline or perhaps by a microwave frequency probe. A conventional four-point resistivity measurement with a pulsed voltage probe may be possible for a transient superconducting state with a lifetime on order 100 ps or longer. The time resolution in this case is limited by the electronics. Even the fastest commercial pulse generators produce voltage profiles with $\sim$30 ps durations. This timescale is too slow for the effect seen in $La_{1.8-x}Eu_{0.2}Sr_xCuO_4$ and $YBa_2Cu_3O_x$ above T_c.

Time-resolved, angle-resolved photo-emission spectroscopy (tr-ARPES) offers another probe that could potentially strongly support or refute the transient super-

conducting state. The band structure and Fermi surface behavior of cuprate superconductors has been well-characterized by ARPES. The challenge here is that the strict surface preparation requirements imposed by ARPES largely limit this probe to c-axis oriented Bi-based cuprates. Excitation of a similar apical oxygen mode in the Bi-based materials [263], in the vein of the $YBa_2Cu_3O_x$ experiment introduced in Chapter 5, may produce a transient plasmon. However excitation along the c-axis would require a grazing-incidence pump configuration. Confirmation of the transient plasmon with THz probe measurements is not feasible with most Bi-based cuprates because the Josephson plasma mode fall in the GHz range[1]. Pb-doped $Bi_2Sr_2CaCu_2O_{8-x}$, however, has a Josephson plasma mode that reaches $\sim$1 THz [264] and may be an appropriate candidate for such a study.

9.1.2 Targeted excitation

Sources appropriate for optical pumping depend on the desired excitation pathway, but generally, the important tuning parameters are the pulse frequency, polarization, duration, and intensity. Depending on the application, pulses may also need to be phase stabilized. The bandwidth must be narrow enough to selectively target a single excitation channel and the pump fluence must be high enough to overcome any threshold behavior. The bandwidth of the pulse may also be limited by pulse duration requirements.

Enhancing pump fluence can often be achieved by conventional optical parametric amplification (OPA) and difference frequency generation (DFG) techniques. To a point, the maximum pump intensity is a practical limitation imposed by the power output of the laser and the number of amplification stages in the OPA. Both $YBa_2Cu_3O_x$ and $La_{1.8-x}Eu_{0.2}Sr_xCuO_4$ were pumped with 15 μm (20 THz) light produced by an OPA with a single amplification stage. The light-induced superconducting-like state generated in $YBa_2Cu_3O_x$ is inhomogeneously distributed in the sample, as discussed in Chapter 5. The state may reach percolation at pump field strengths on order $\sim$10 MV/cm, roughly three times the maximum pump field generated by the OPA + DFG. At percolation, the bulk response of the system should behave like a superconductor. Such enhancement of the pump intensity could be achievable, but it would require a higher power 800 nm input beam and a multi-stage amplification system.

[1] In the case of most bilayer compounds, the interbilayer plasmon also falls below 100 GHz.

A more difficult challenge is extending the pump frequency range. The efficiency of OPA + DFG systems drops off dramatically above ∼20 μm (15 THz). There is a dearth of high-fluence, narrowband sources in the 3-15 THz range. This window encompasses the majority of phonon modes, limiting the scope of materials for which phonon pumping is feasible. The 15 μm $YBa_2Cu_3O_x$ apical oxygen atom that is excited is only one of two similar modes, each associated with the $YBa_2Cu_3O_6$ and $YBa_2Cu_3O_7$ lattice structure. As I have shown in Chapter 5, exciting the $YBa_2Cu_3O_6$ apical oxygen mode produces a light-induced plasmon throughout the pseudogap state, with the effect vanishing for $YBa_2Cu_3O_7$. The $YBa_2Cu_3O_7$ apical oxygen mode frequency is beyond the reach of our pump set-up. Exciting both modes would firmly establish whether this transient phase diagram, presented in Chapter 5, is shaped by the fact that only the $YBa_2Cu_3O_6$ apical oxygen mode is pumped, or whether the onset temperature T' is intrinsic to the transient phase.

Finally, the low threshold fluence for inducing the transient phase opens up the possibility of exciting the system with high-repetition or even continuous wave pumping. Continuous wave sources have lower field strengths than the peak field of a pulsed system with similar total power. However, assuming additional heating effects are minimal, they offer the potential to bring the system into a driven, dynamic equilibrium phase that can be probed with more conventional methods, such as susceptibility and resistivity. Most continuous wave sources have been developed for wavelengths of 1 μm (300 THz) or less. Solid state devices, such as quantum cascade lasers, have been developed for the MIR range up to ∼12 μm (25 THz) [265] and longer wavelength sources are in development. The p-Ge lasers, first developed in the 1980's and 90's [266–268], have tunable ranges that can extend over 80-500 μm (0.6-4 THz).

9.2 Point contact spectroscopy and the iron-based superconductors

Point contact spectroscopy (PCS) has traditionally been used as a probe of phonon modes and Andreev reflection. The Andreev reflection process is sensitive to the phase of the superconducting order parameter, thus point contact spectroscopy can be used to determine the order parameter symmetry. The iron-based superconductors are multiband materials predicted to have a novel $s_{\pm}$-wave order parameter

symmetry. Several models have been developed to predict how interference between different bands due to this order would be detectable in point contact spectra.

In Chapter 8, I show that the Co-doped $SrFe_2As_2$ system produces PCS spectra consistent with two non-interfering bands and can be fit with the same type of model that has been successfully applied to the multiband BCS superconductor MgB_2. These spectra were measured in the Andreev limit, where the effective tunneling barrier at the junction between probe and sample is small. However, the largest differences between $s_{\pm}$-wave order and the s_{++}-wave order of MgB_2 are predicted to occur for larger tunneling barriers. A systematic study varying the tunneling barrier, perhaps using soft point contact spectroscopy to control the barrier size, may confirm or finally refute the accuracy of these models.

In the last few years, PCS has truly broken its traditional mold and been shown to be a sensitive probe of many types of correlated states, of which I give a few examples in Chapter 8. Along this line, above-gap features in the point contact spectrum of 122 pnictides have been attributed to electronic coupling to a spin-excitation mode. I have found that while at least one feature (at 10 meV in $Sr(Fe_{0.875}Co_{0.125})_2As_2$) may be related to spin excitations, most features of the point contact spectrum can be directly linked to phonon modes of the 122 lattice. A thorough study, including a variety of compounds and dopings, will clarify whether spin excitations can in fact be detected with point contact spectroscopy.

Appendix A

Modeling the transient optical response

A.1 Error propagation in the bulk limit

Because many important effects are measured with small signal-to-noise ratios, it is worthwhile to look at how the measurement uncertainty propagates to our calculated optical properties. We will consider only the standard deviation due to noise in the measured THz field, $\sigma_{\tilde{r}'}$. It is convenient to define the quantity,

$$f(\tilde{r}') = \frac{1-\tilde{r}'}{1+\tilde{r}'} = f_1 + if_2 \tag{A.1}$$

The variance of this quantity must be calculated in terms of $\tilde{r}' = r_1 + ir_2$, σ_{r_1}, and σ_{r_2}. The variance is

$$\sigma_{f_j}^2 = \left|\frac{\partial f_j}{\partial r_1}\right|^2 \sigma_{r_1}^2 + \left|\frac{\partial f_j}{\partial r_2}\right|^2 \sigma_{r_2}^2 \tag{A.2}$$

Solving explicitly for the first derivative of $f(\tilde{r}')$,

$$f(r_1, r_2) = \frac{(1-r_1^2-r_2^2) - 2ir_2^2}{(1+r_1)^2 + r_2^2} \tag{A.3}$$

we find,

$$\begin{aligned} \frac{\partial f_1}{\partial r_1} &= -2\frac{r_1 + f_1(1+r_1)}{(1+r_1)^2 + r_2^2}, & \frac{\partial f_1}{\partial r_2} &= -2\frac{r_2 + f_1 r_2}{(1+r_1)^2 + r_2^2} \\ \frac{\partial f_2}{\partial r_1} &= 4\frac{(1+r_1)\, r_2^2}{\left((1+r_1)^2 + r_2^2\right)^2}, & \frac{\partial f_2}{\partial r_2} &= -4\frac{(1+r_1)^2\, r_2}{\left((1+r_1)^2 + r_2^2\right)^2} \end{aligned} \tag{A.4}$$

The final step is to calculate the variance of the refractive index, $\tilde{n}$, in terms of σ_{f_1} and σ_{f_2}.

$$\sigma_{n,k}^2 = \left|\frac{\partial(n,k)}{\partial f_1}\right|^2 \sigma_{f_1}^2 + \left|\frac{\partial(n,k)}{\partial f_2}\right|^2 \sigma_{f_2}^2, \tag{A.5}$$

where $\tilde{n} = n + ik$. Equation 2.11 can be decomposed directly for the TE case,

$$\begin{aligned} n(f_1,f_2) &= \frac{1}{\sqrt{2}}\left[\left(\sin^2\theta_0 + f_1\cos^2\theta_0\right) + \sqrt{\left(\sin^2\theta_0 + f_1\cos^2\theta_0\right)^2 + \left(f_2\cos^2\theta_0\right)^2}\right]^{1/2}, \\ k(f_1,f_2) &= \frac{sgn(f_2)}{\sqrt{2}}\left[-\left(\sin^2\theta_0 + f_1\cos^2\theta_0\right) + \sqrt{\left(\sin^2\theta_0 + f_1\cos^2\theta_0\right)^2 + \left(f_2\cos^2\theta_0\right)^2}\right]^{1/2}. \end{aligned} \tag{A.6}$$

The decomposition makes use of the relation $\sqrt{a+ib} = \pm(p+iq)$, where

$$\begin{aligned} p &= \sqrt{\frac{a+\sqrt{a^2+b^2}}{2}}, \\ q &= sgn(b)\sqrt{\frac{-a+\sqrt{a^2+b^2}}{2}}. \end{aligned} \tag{A.7}$$

The TM case is more complex to solve. Making iterative use of the above relation, we define $a = 1 - 4\sin^2\theta_0\cos^2\theta_0\left(f_1^2 - f_2^2\right)$ and $b = 8\sin^2\theta_0\cos^2\theta_0 f_1 f_2$. Then $\sqrt{a+ib} = p+iq$ and $\sqrt{1+p+iq} = g+ih$. We end up with an expression for the TM case,

$$\begin{aligned} n(f_1,f_2) &= \frac{1}{\sqrt{2}\,|f^2|}\left[f_1 g + f_2 h\right] \\ k(f_1,f_2) &= \frac{1}{\sqrt{2}\,|f^2|}\left[f_1 h - f_2 g\right] \end{aligned} \tag{A.8}$$

and the derivatives,

$$\begin{aligned} \frac{\partial n}{\partial f_{1,2}} &= \frac{1}{\sqrt{2}\,|f^2|}\left[(g,h) + f_1\frac{\partial g}{\partial f_{1,2}} + f_2\frac{\partial h}{\partial f_{1,2}} - (f_1 g + f_2 h)\,\frac{1}{|f^2|^2}\frac{\partial\,|f^2|}{\partial f_{1,2}}\right], \\ \frac{\partial k}{\partial f_{1,2}} &= \frac{1}{\sqrt{2}\,|f^2|}\left[(h,-g) + f_1\frac{\partial h}{\partial f_{1,2}} - f_2\frac{\partial g}{\partial f_{1,2}} - (f_1 h - f_2 g)\,\frac{1}{|f^2|^2}\frac{\partial\,|f^2|}{\partial f_{1,2}}\right], \end{aligned} \tag{A.9}$$

where

$$\frac{\partial\,|f^2|}{\partial f_{1,2}} = \frac{4}{|f^2|}\left[\left(f_1^2 - f_2^2\right) f_{1,2} + f_{2,1}\right]. \tag{A.10}$$

A Matlab algorithm was developed to calculate the standard deviation for both TE and TM cases; it can be found in Appendix C.

A.2 Fit goodness for non-analytical models

The non-analytical models treat $\Delta\tilde{n}$ as a fit parameter to obtain the measured $\tilde{r}'$ at each frequency ω. This section will discuss the calculation of fit goodness for $\Delta\tilde{n}$. First I define the weighted error of a fit f to data y,

$$\chi^2(f) = \sum_i^N \frac{(y_i - f_i)^2}{\sigma_{y_i}^2}. \tag{A.11}$$

This quantity is called the chi-squared of the fit. A "good" fit is defined as when $\chi^2 \approx N$. At every frequency ω we have two fit parameters $\Re(\Delta\tilde{n}) = \Delta n$ and $\Im(\Delta\tilde{n}) = \Delta k$, used to fit two experimentally determined reflectivity components r_1 and r_2, where $\tilde{r}' = r_1 + ir_2$. Assuming fitting functions $f_1(\Delta n, \Delta k)$ and $f_2(\Delta n, \Delta k)$, we can define our chi-squared as

$$\chi^2(\Delta n, \Delta k) = \sum_{i=1}^{2} \frac{(r_i - f_i(\Delta n, \Delta k))^2}{\sigma_{r_i}^2}. \tag{A.12}$$

We now introduce the following assumption. Along the coordinate of each fit parameter a, the variation in $\chi^2(a)$ near the optimal value of a is parabolic, such that the best fit a^* represents a minimum in $\chi^2(a)$. The error in a^* can thus be estimated by defining σ_{a^*} as the variation in a that increases $\chi^2(a^*)$ by 1. If we vary a^* by some small amount δa, then

$$\sigma_{a^*}^2 = \frac{2\delta a}{\chi^2(a^* + \delta a) - 2\chi^2(a^*) + \chi^2(a^* - \delta a)}. \tag{A.13}$$

The derivation of the relation above can be found in Bevington and Robinson, chapter 8 [269].

A.3 An approximate multilayer model

If we assume very thin layers δz, then the characteristic matrix for a layer m simplifies to

$$M_m = \begin{bmatrix} 1 & -\dfrac{i}{p_m} k_0 \tilde{n}_m \delta z \cos\theta_m \\ -i p_m k_0 \tilde{n}_m \delta z \cos\theta_m & 1 \end{bmatrix}. \tag{A.14}$$

Retaining only terms linear in δz, the total characteristic matrix for the medium, M, is then,

$$M = \begin{bmatrix} 1 & G \\ F & 1 \end{bmatrix}, \tag{A.15}$$

where in the TE case

$$\begin{aligned} F &= -ik_0 \sum_{m=1}^{N} p_m \tilde{n}_m \delta z \cos\theta_m = -ik_0 \sum_{m=1}^{N} \tilde{n}_m^2 \delta z \cos^2\theta_m, \\ G &= -ik_0 \sum_{m=1}^{N} \frac{\tilde{n}_m}{p_m} \delta z \cos\theta_m = -ik_0 \sum_{m=1}^{N} \delta z. \end{aligned} \tag{A.16}$$

Our goal is to explicitly solve the sums in F and G to develop an analytical expression for $\tilde{r}'(\Delta\tilde{n})$. The expression for G can be trivially rewritten as an integral and solved,

$$G = -ik_0 \sum_{m=1}^{N} \delta z = -ik_0 \int_0^L dz = -ik_0 L. \tag{A.17}$$

where $L = N\delta z$ is the probe penetration depth. Next we note that $\sin\theta_m = \sin\theta_0/\tilde{n}_m$ and therefore we may rewrite F as

$$\begin{aligned} F &= -ik_0 \delta z \sum_{m=1}^{N} \tilde{n}_m^2 \left[1 - \left(\frac{\sin\theta_0}{\tilde{n}_m} \right)^2 \right] \\ &= -ik_0 \delta z \left[\sum_{m=1}^{N} \tilde{n}_m^2 - \sum_{m=1}^{N} \sin^2\theta_0 \right]. \end{aligned} \tag{A.18}$$

Using the form of the refractive index given in Equation (2.30), the first term in Equation (A.18) may be rewritten as

$$\sum_{m=1}^{N} \tilde{n}_m^2 = \sum_{m=0}^{N-1} \tilde{n}_0^2 + 2\tilde{n}_0 \Delta\tilde{n} \mathrm{e}^{-\alpha m \delta z} + \Delta\tilde{n}^2 \mathrm{e}^{-2\alpha m \delta z}. \tag{A.19}$$

Taking the limit of small δz,

$$\sum_{m=0}^{N-1} \mathrm{e}^{-\alpha \delta z m} \delta z \equiv \int_0^L \mathrm{e}^{-\alpha z} dz = \frac{1}{\alpha}\left(1 - \mathrm{e}^{-\alpha L}\right), \tag{A.20}$$

we find,

$$F(\Delta\tilde{n}) = -ik_0 L \left[\frac{1}{2\alpha L}\left(1 - \mathrm{e}^{-2\alpha L}\right)\Delta\tilde{n}^2 + \frac{2\tilde{n}_0}{\alpha L}\left(1 - \mathrm{e}^{-\alpha L}\right)\Delta\tilde{n} + \left(\tilde{n}_0^2 - \sin^2\theta_0\right)\right]. \tag{A.21}$$

After plugging the expressions for F and G into Equation (2.28), the final form for $\tilde{r}'(\Delta\tilde{n})$ can be expressed as,

$$\tilde{r}'(\Delta\tilde{n}) = \frac{\left(i/k_0 L + p_L\right) p_1 - \left(F(\Delta\tilde{n}) + p_L\right) i/k_0 L}{\left(i/k_0 L + p_L\right) p_1 + \left(F(\Delta\tilde{n}) + p_L\right) i/k_0 L}. \qquad \text{(TE wave)} \tag{A.22}$$

Unfortunately, because p_L is a function of $\Delta\tilde{n}$, we cannot explicitly invert this equation. As with the most general thin film stack described in Section 2.6.3, the fit can be performed using fsolve in Matlab. The code for the model is reproduced in the Appendix C.

Following a similar approach as before, we can apply Equation (2.28) to the TM wave case by substituting $p = \cos\theta/\tilde{n}$. The final expression for the reflectivity is,

$$r'(\Delta\tilde{n}) = \frac{\left(1 + g(\Delta\tilde{n})p_L\right) p_1 - \left(f(\Delta\tilde{n}) + p_L\right)}{\left(1 + g(\Delta\tilde{n})p_L\right) p_1 + \left(f(\Delta\tilde{n}) + p_L\right)}. \qquad \text{(TM wave)} \tag{A.23}$$

where

$$\begin{aligned} f(\Delta\tilde{n}) &= -ik_0 L \left[1 - \frac{\sin^2\theta_0}{\tilde{n}_0^2}\left[1 + \frac{1}{\alpha L}\ln\left(\frac{\tilde{n}(L)}{\tilde{n}_0}\right) + \frac{1}{\alpha L}\left(\frac{\Delta\tilde{n}\mathrm{e}^{-\alpha L}}{\tilde{n}(L)} - \frac{\Delta\tilde{n}}{\tilde{n}_0}\right)\right]\right], \\ g(\Delta\tilde{n}) &= -ik_0 L \left[\frac{1}{2\alpha L}\left(1 - \mathrm{e}^{-2\alpha L}\right)\Delta\tilde{n}^2 + \frac{2\tilde{n}_0}{\alpha L}\left(1 - \mathrm{e}^{-\alpha L}\right)\Delta\tilde{n} + \left(\tilde{n}_0^2 - \sin^2\theta_0\right)\right]. \end{aligned} \tag{A.24}$$

A.4 An analytic solution in the thin multifilm limit (TE case)

Calculating the solution using the method described in the previous sections can be time-consuming. The process is highly parallelizable, fortunately, as the calculation at each frequency is independent. But it would be nice to have an analytical solution that captures the same behavior. This section will discuss the derivation of an analytical version of the multilayer model for an incident TE wave.

Our goal is to derive an explicit form for $\Delta\tilde{n}(r')$. We begin by rewriting Equation (2.28) as,

$$F - (1 + Gp_L)\, p_1 \left(\frac{1 - r'}{1 + r'}\right) + p_L = 0. \tag{A.25}$$

Note that only F and p_L are dependent on $\Delta\tilde{n}$. If we assume that the refractive index at the probe penetration depth, L, is approximately the bulk value, we set $p_L = \tilde{n}_0\sqrt{1 - (\sin\theta_0/\tilde{n}_0)^2}$, which is independent of $\Delta\tilde{n}$. Plugging Equation (A.21) into Equation (A.25), we end up with a quadratic expression in $\Delta\tilde{n}$.

Solving this quadratic equation gives us an analytic expression for the change in the pump-induced refractive index, $\Delta\tilde{n}(r')$,

$$\Delta\tilde{n}(r') = \frac{-B \pm \sqrt{B^2 - 4AC}}{2A}, \tag{A.26}$$

where

$$\begin{aligned} A &= \frac{ik_0}{2\alpha}\left(1 - \mathrm{e}^{-2\alpha L}\right), \\ B &= \frac{2ik_0\tilde{n}_0}{\alpha}\left(1 - \mathrm{e}^{-\alpha L}\right), \\ C &= ik_0 L\left(\tilde{n}_0^2 - \sin^2\theta_0\right) + (1 - ik_0 L p_L)\, p_1 \left(\frac{1 - r'}{1 + r'}\right) - p_L. \end{aligned} \tag{A.27}$$

It's important to take a moment to consider when this analytical solution is appropriate. In the above derivation, we have implicitly assumed that p_L is $\Delta\tilde{n}$-independent. That is, after the multilayer we enter the bulk, un-pumped material. This is a reasonable approximation for situations in which we are in the "tail" of the pumped region, $L > 1/\alpha$, but can over-estimate the reflectivity in cases where they

are on the same order. As L decreases with respect to $1/\alpha$, we move into the bulk limit. The code for the analytic thin film model can be found in the Appendix C.

Appendix B

Experimental Details

B.1 Modeling the transient response of $La_{1.675}Eu_{0.2}Sr_{0.125}CuO_4$

Because the THz probe penetrates far deeper than the 15 μm pump, the reflected THz field includes contributions from both the photo-excited volume and the equilibrium bulk material. To isolate the optical response of the photo-excited volume alone, we model the system as a single excited layer on an unperturbed bulk, as described in Chapter 2. This model generates the same optical response as a more elaborate multilayer model that treats the refractive index as maximum at the sample surface, decaying exponentially with distance z as $\exp(-z/d)$ from the surface toward its unperturbed bulk value. The optical properties calculated from the single layer, multilayer, and a simple analytical thin film models are all plotted in Figure B.1.

The overall magnitude of the transient changes is sensitive to the penetration depth mismatch used by the models. However the variation in the recalculated properties when the pump penetration depth is changed by $\pm 10\%$, shown in Figure B.2, are well within the variation given by the three models above. Importantly, the qualitative behavior of the transient changes in the optical response, $\Delta\tilde{\sigma}(\omega)$, are the same regardless of the penetration depth mismatch. Figure B.3 shows the same LESCO 1/8 data (blue) alongside a recalculated optical response assuming a pump penetration depth 10x larger (light blue). The data has been rescaled by a factor of 10, such that $\tilde{\sigma}(\omega) = \tilde{\sigma}_{\mathrm{eq}} + 10\Delta\tilde{\sigma}(\omega)$, to illustrate that the transient changes retain the same qualitative behavior, namely, the diverging $\Delta\sigma_2(\omega)$ which is characteristic of a high mobility state and a London-like superconducting response.

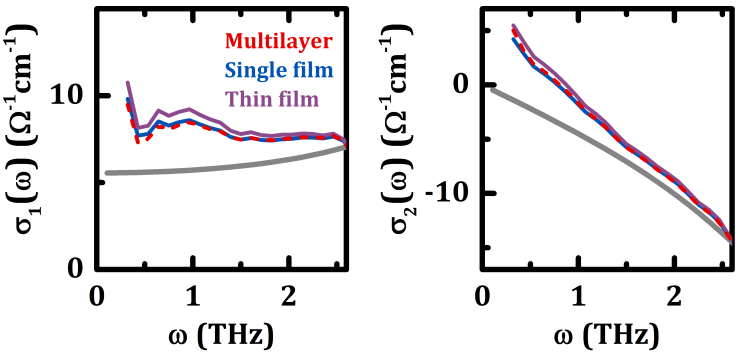

Figure B.1: **Comparison of the transient optical response calculated with three models.** The optically excited material can be well-modeled assuming a single excited layer on an unperturbed bulk (blue). A more extensive model was developed that treats the extinction of the pump into the material as an exponential decay of the transient refractive index (red). A third model, an analytic approximation assuming a large pump-probe penetration depth mismatch, is also shown for comparison (purple).

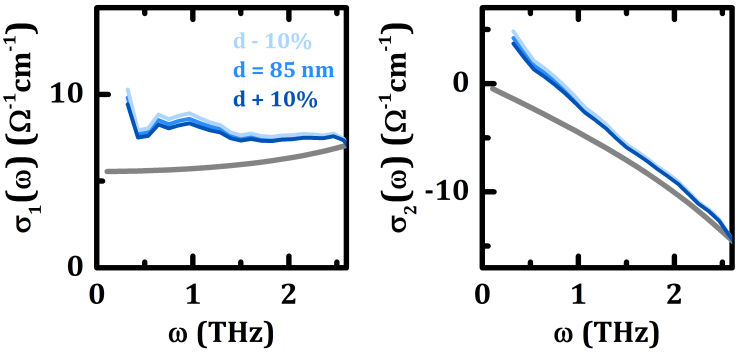

Figure B.2: **Effect of varying the penetration depth.** The penetration depth is determined experimentally by the in-plane optical response at 15 μm. However varying the penetration depth by some fraction does not significantly change the transient response. Here, the penetration depth d is varied by $\pm 10\%$, such that $d' = d \pm 0.1d$.

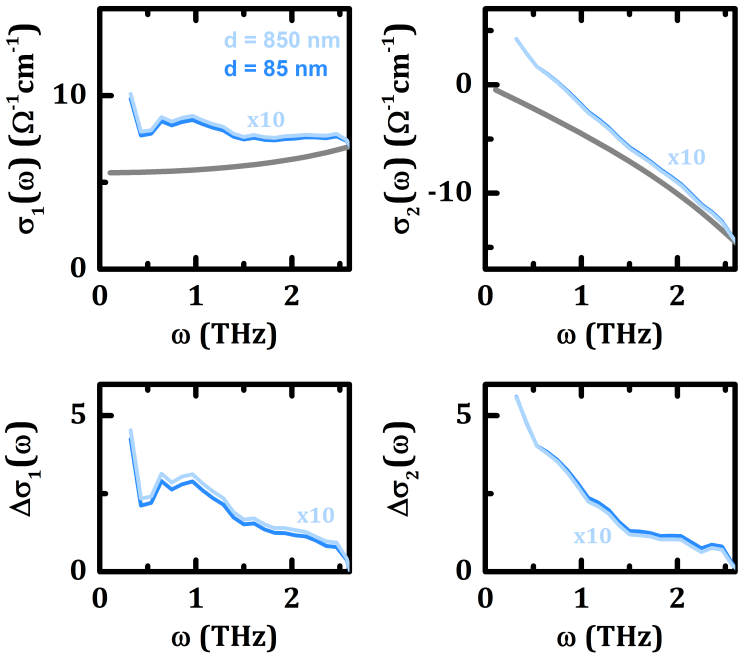

Figure B.3: **Scaling of the transient response with penetration depth.** The magnitude of the pump-induced changes in the transient response scale with the penetration depth mismatch. However, the qualitative behavior of the changes which mark the generation of a high mobility state, including a diverging $\Delta\sigma_2$, are present regardless of the magnitude of the mismatch.

B.2 800 nm excitation of $La_{1.675}Eu_{0.2}Sr_{0.125}CuO_4$

While the main thrust of this work on LESCO, and this thesis in general, is the use of targeted, resonant excitation to manipulate superconductivity, it is worth considering whether there are other avenues for generating transient c-axis coupling. Even in the case of phonon pumping, the apparent source of the transient coupling is the electronic destruction of stripe order. Other mechanisms that target the charge ordered state could in principle give rise to the same coupling, provided the excitation does not simultaneously act destructively towards the transient mode, for example through the generation of quasiparticle excitations.

Along this line, non-resonant excitation at 800 nm has recently been shown to generate transient coupling in LBCO for dopings $x < 1/8$ (12.5%) [15]. As with MIR excitation of LESCO, the effect is strongest in the spin order (SO) regime but appears to survive up to the charge order transition.

Here, I will present some preliminary results applying the same 800 nm excitation to LESCO 12.5%. The 800 nm pump beam was oriented at normal incidence along the c-axis in the same experimental conditions as those reported in Ref. [15], and with the same THz vacuum box, discussed in Chapter 2, used in the MIR excitation experiment and in Ref. [15]. Care was taken to prevent 800 nm light from entering the electro-optic sampling detection set-up through the erection of plastic barriers, permeable only to THz radiation.

The transient response[1] is plotted in Figure B.4 for two time delays after excitation. The response peaks about 1.5 ps after excitation, with the formation of a plasma mode that is comparable to the plasmon generated by MIR excitation (see Figure B.5).

I will now compare these results with the LBCO case reported in Ref. [15]. The range of dopings in which the plasmon could be induced in LBCO is shown in Figure B.6. Interestingly, the transient mode appears robust in LESCO 12.5%, comparable to LBCO 11.5% in the CO regime. The lefthand panel of Figure B.7, reproduced from Ref. [15], plots the transient reflectivity of the mode in LBCO 11.5% at four temperatures, extending from the superconducting state, through the stripe ordered regime, and to the normal state above T_{CO}. The righthand panel shows the transient reflectivity of LESCO 12.5% at 5 K, in the charge and spin ordered regime.

[1] The response is calculated using the same single layer model employed for the MIR excitation response, with a pump penetration depth of 400 nm.

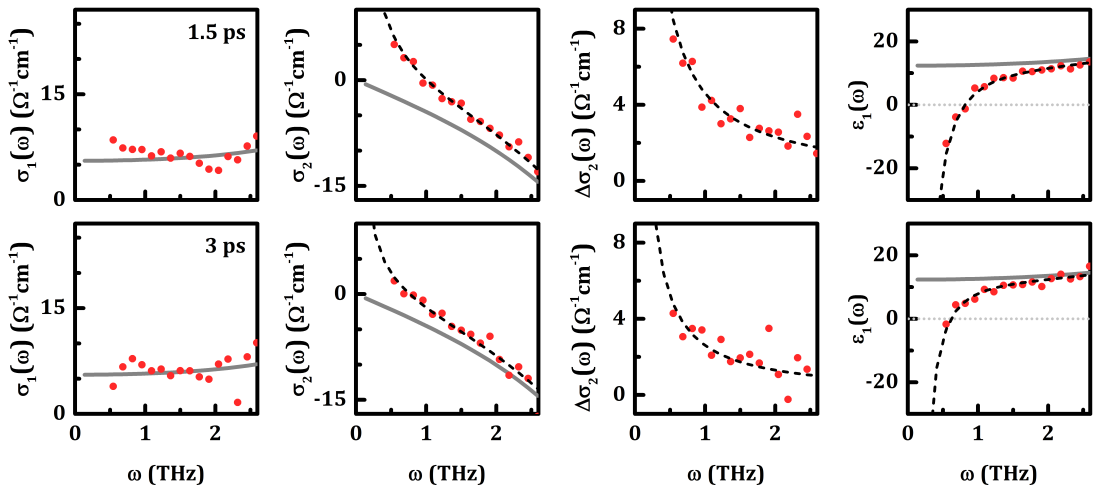

Figure B.4: **Transient optical response of LESCO 12.5% at 5 K after 800 nm excitation.** The optical response at 1.5 ps after excitation **(top row)** and 3.5 ps **(bottom row)**. From left to right: The Ohmic conductivity $\sigma_1(\omega)$, the inductive conductivity $\sigma_2(\omega)$, the transient changes to the inductive conductivity $\Delta\sigma_2(\omega) = \sigma_2(\omega) - \sigma_{2,\mathrm{eq}}(\omega)$, and the real part of the dielectric response $\varepsilon_1(\omega)$. Dashed lines are fits to a single longitudinal mode, as described in the main text.

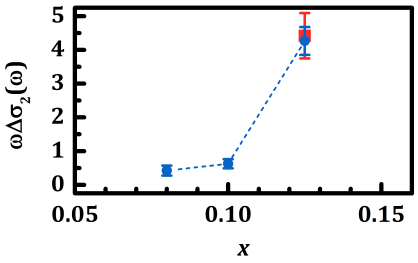

Figure B.5: **Comparison of the inductive response of LESCO after MIR and 800 nm excitation.** The average low frequency inductive response $\omega\Delta\sigma_2(\omega)$ after 15 μm mid-infrared excitation polarized in-plane (blue) and 800 nm excitation polarized along the c-axis (red). All measurements made at 5 K, taken at the peak of the transient response.

Meanwhile, there is no evidence of the transient coupling for LBCO 12.5%, even up to pump fluences of 3 mJ/cm^2, three times the saturation fluence found for LBCO 11.5%. Similarly, we found no plasmon could be generated by the a-axis MIR excitation of LBCO 12.5% up to 4 mJ/cm^2. This despite, as mentioned in

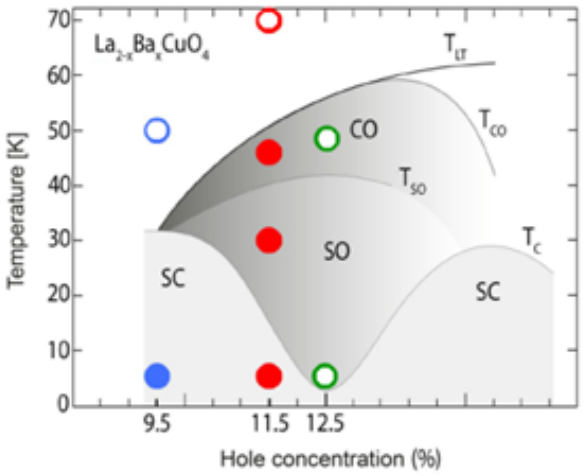

Figure B.6: **Phase diagram of the LBCO transient plasmon generated by 800 nm excitation.** Phase diagram of LBCO with filled dots indicating temperatures and dopings at which the 800 nm excitation produced a transient mode. Empty dots indicate where the excitation was made and no transient mode was found. Figure modified from Ref. [15].

earlier, the same MIR excitation (at 1 mJ/cm^2) reducing the charge ordering peak by 60% [32]. We cannot rule out the generation of a plasmon below our frequency window (< 0.2 THz); however even so, we can safely conclude that if c-axis coupling is being generated in this compound at all, it is very weak.

We conjecture this may be due to the stripe order parameter being much stronger in LBCO 12.5% compared to both LESCO 12.5% and LBCO at lower dopings. The c-axis charge order correlation length is about 200 Å for LBCO 12.5% and falls by half to 100 Å for LBCO 11.5% [102]. The correlation lengths of LESCO are about a factor of three smaller than for LBCO [108].[2] If the 800 nm excitation is driving the destruction of charge stripe order, as in the MIR excitation case, then the effectiveness of the light in overcoming the charge ordering energy scale determines whether a plasmon will form. The excitation may simply be insufficient to destroy charge ordering in LBCO 12.5%.

It may at first appear counter-intuitive that near infrared (NIR) excitation can support a condensate against charge ordering competition, as NIR light has been

[2]This is primarily attributed to the increased crystalline disorder produced by the Eu atom dopants.

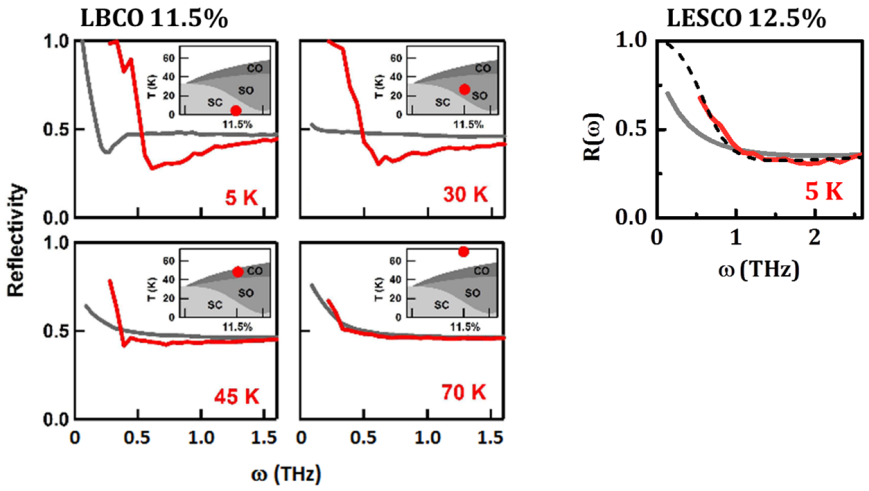

Figure B.7: **Comparing the 800 nm excitation of LBCO and LESCO. Left:** The transient (red) and equilibrium (grey) reflectivity of LBCO 11.5% after 800 nm *c*-axis excitation. Panels show the response for ground states that are (clockwise from top left) superconducting, spin and charge ordered, charge ordered, above T_{CO}. Figure adapted from Ref. [15]. **Right:** The transient (red) and equilibrium (grey) reflectivity of LESCO 12.5% after the same excitation. The ground state, at 5 K, is spin and charge ordered. Dashed line indicates a fit to the equilibrium spectrum plus a single excited mode (Equation 4.2) with $\Gamma = 0$.

shown to be destructive to cuprate superconductivity in certain circumstances. But there is good reason to support such a scenario. First, most 800 nm excitation measurements have focused on *in*-plane excitation, for the purpose of coupling to the superconducting condensate more directly and facilitating pair breaking [270–274]. In a perfectly 2D superconductor, no dipole coupling to the condensate is possible for excitation perpendicular to the plane, and in cuprates, the *c*-axis coupling is very weak [275].

Second, NIR excitation has been shown to be effective at melting charge order in a variety of systems [276–278] and couples more efficiently to charge order than to superconductivity for polarization along the *c*-axis. This destruction is generally fast, on the 100 fs timescale, compared to the destruction of superconductivity (for in-plane excitation) which is found to occur over a picosecond timescale in cuprates [279]. The longer timescale can be described by the Rothwarf-Taylor quasi-particle recombination mechanism [280, 281], in which electron-phonon coupling acts as a bottleneck in the transfer of energy to the condesate. This coupling to

phonons also makes pair-breaking with NIR excitation highly inefficient, requiring much higher fluences than would be expected from the condensation energy density [272, 274]. Charge order destruction, on the other hand, is highly efficient since the process is more direct, with the order highly sensitive to any electronic process that disturbs the Fermi surface nesting. This is fully consistent with the observations of Ref. [15], in which the plasmon appears stiff up to ∼2 ps after excitation, then shows incoherent contributions during the relaxation.

B.3 Measuring the equilibrium optical response of $YBa_2Cu_3O_x$

Determining the complex equilibrium conductivity is necessary to calculate the absolute optical conductivity of the *transient* (pump-induced) state that is presented in this chapter and Chapter 7. Fortunately, the low frequency THz response of YBCO is flat and featureless above T_c, as shown in Figure 5.14. As a result, we could calculate the absolute transient response using high quality measurements of the equilibrium reflectivity taken from literature for both the c-axis [84, 282] and a-axis [69]. The complex response was determined by Kramers-Kronig transformation.

Below T_c, the c-axis response is characterized by the appearance of a longitudinal plasma mode which gives rise to a sharp change in reflectivity at the plasma frequency, as illustrated in Figure 5.10. The position of this feature is highly sensitive to temperature and the precise carrier concentration of the sample, which can vary even for the same nominal doping. In order to accurately determine the transient response, it is therefore crucial to measure the absolute equilibrium response *in situ*.

The equilibrium THz reflectivity of the sample, $\tilde{E}(\omega)$, must be *referenced* in order to determine the absolute amplitude and phase of the equilibrium response. One way to reference the THz spectra is by using another time-domain THz measurement of a standard reflector placed at the same position as the sample. The placement of the reference reflector is crucial in order to ensure that the time of arrival of the THz (and accordingly the absolute phase of the spectrum) is the same for the sample and the reference. The most reliable way to do this is to sputter the sample with Au *in situ*, as is standard in Fourier Transform Infrared Spectroscopy (FTIR). Our THz reflectivity set-up is not equipped to perform this type of absolute calibration.

Instead, I developed a method of "relative" referencing of the reflected THz response below T_c, $\tilde{E}(\omega, T < T_c)$, with the response just above T_c, $\tilde{E}(\omega, T > T_c)$. The static reflectance below T_c, $\tilde{r}(\omega, T < T_c)$ can then be extracted from the two THz measurements plus the flat equilibrium response from literature above T_c, $\tilde{r}(\omega, T > T_c)$, by taking the ratio,

$$\tilde{r}(\omega, T < T_c) = \frac{\tilde{E}(\omega, T < T_c)}{\tilde{E}(\omega, T > T_c)} \tilde{r}(\omega, T > T_c). \tag{B.1}$$

The complex optical response, $\tilde{n}(\omega)$, is related to the reflectance $\tilde{r}(\omega)$ via an inversion of the Fresnel equations,

$$\begin{aligned} \tilde{n}(\tilde{r}) &= \sqrt{\sin^2\theta_0 + \cos^2\theta_0 \left(\frac{1-\tilde{r}}{1+\tilde{r}}\right)}, && \text{(TE wave)} \\ \tilde{n}(\tilde{r}) &= \frac{1}{\sqrt{2}} \left(\frac{1+\tilde{r}}{1-\tilde{r}}\right) \sqrt{1 + \sqrt{1 - 4\sin^2\theta_0 \cos^2\theta_0 \left(\frac{1-\tilde{r}}{1+\tilde{r}}\right)^2}}, && \text{(TM wave)} \end{aligned} \tag{B.2}$$

where θ_0 is the angle of incidence on the sample.

This approach needs to be undertaken with caution, as it requires the sample holder assembly to remain mechanically stable on heating/cooling, and is potentially vulnerable to phase noise due to thermal expansion/contraction of the cold finger. Because thermal contraction is a systematic effect, it can be accounted for by relative referencing a known sample. Thermal contraction of our cold finger and sample holder between 5 K and $T_c \sim 60$ K is minimal and can be corrected for, allowing this procedure to be applied.

Figure B.8 shows the transient optical response of YBCO 6.5 at 5 K, 0.8 ps after excitation (red). The same transient THz field has been referenced to two equilibrium responses (grey). The dotted line shows data taken from Ref. [84] and the solid line was measured *in situ* using a THz spectrum taken at 5 K, $\tilde{E}(\omega, 5\text{ K})$, referenced by a spectrum just above T_c, $\tilde{E}(\omega, 60\text{ K})$. The 60 K equilibrium response $\tilde{n}(\omega)$ was also taken from Ref. [84]. Notice that the transient conductivity referenced by literature data has a sharp peak right at the equilibrium plasma resonance (indicated by an arrow in Figure B.8). This is due to to the slight mismatch in response of our sample vs. Ref. [84]. However, this artifact is completely removed with the relative

referencing method, revealing a small, single peak remaining in the loss function near the equilibrium Josephson plasma frequency.[3]

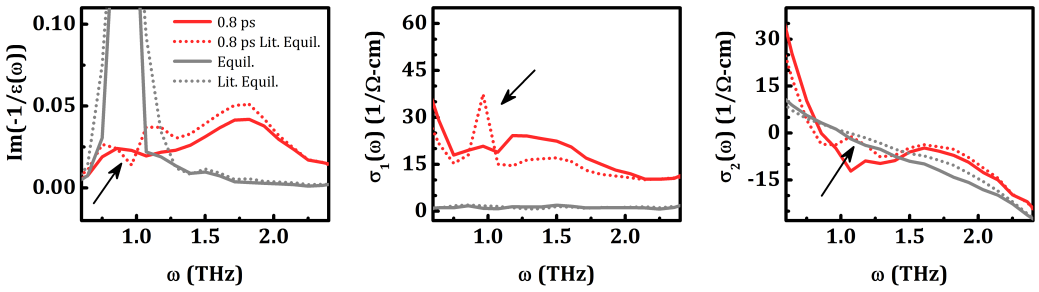

Figure B.8: **Artifacts due to improper referencing.** Calculation of the photo-induced reflectivity of YBCO 6.5 at 5 K. Referencing using the equilibrium optical response taken from Ref. [84] (dashed line) vs. referencing *in situ* as described in the text (solid line). Near the plasma edge, artifacts appear due to a mismatch in the literature JPR frequency and the true JPR position (indicated by arrows).

B.4 Percolation and the Bruggeman effective medium model

The Bruggeman effective medium model was used to describe the transient response of YBCO above T_c, as described in Section 5.5. For all dopings and temperatures, the maximum superconducting volume fraction f did not not exceed 20%, well below the percolation threshold $f_c \approx 33\%$. However, the percolation threshold tracks the polarization factor $f_c = q$ [283]. A low q describes rod-like inclusions with the inclusions becoming more pancake-like up to $q = 0.5$.

Figure B.9 shows the effect of varying q. The black line indicates the same fit as the black line in Figure 5.23. The top row shows fits just varying q and f. For $q = 0.5$, 0.33, and 0.1 the best fit volume fractions are $f = 0.12$, 0.15, and 0.21 respectively. The bottom row shows fits in which the plasma frequency ω_p is also

[3]The apparent splitting of the Josephson plasmon, with one component remaining near equilibrium and another blue shifting, is discussed in Chapter 7.

optimized. While all values of q reproduce the essential features of the transient state, the choice of $q = 1/3$ appears to offer the closest fit.

Importantly, for $q = 0.1$ (pink) we cross the critical volume fraction. Above this threshold, the bulk response should appear superconducting. This can be seen in the inductive conductivity $\sigma_2(\omega)$ of the effective medium in Figure B.9 (pink line in both top and bottom rows), which diverges even to zero frequency. Based on the relative fit quality, however, we can safely claim that the transient state remains below percolation.

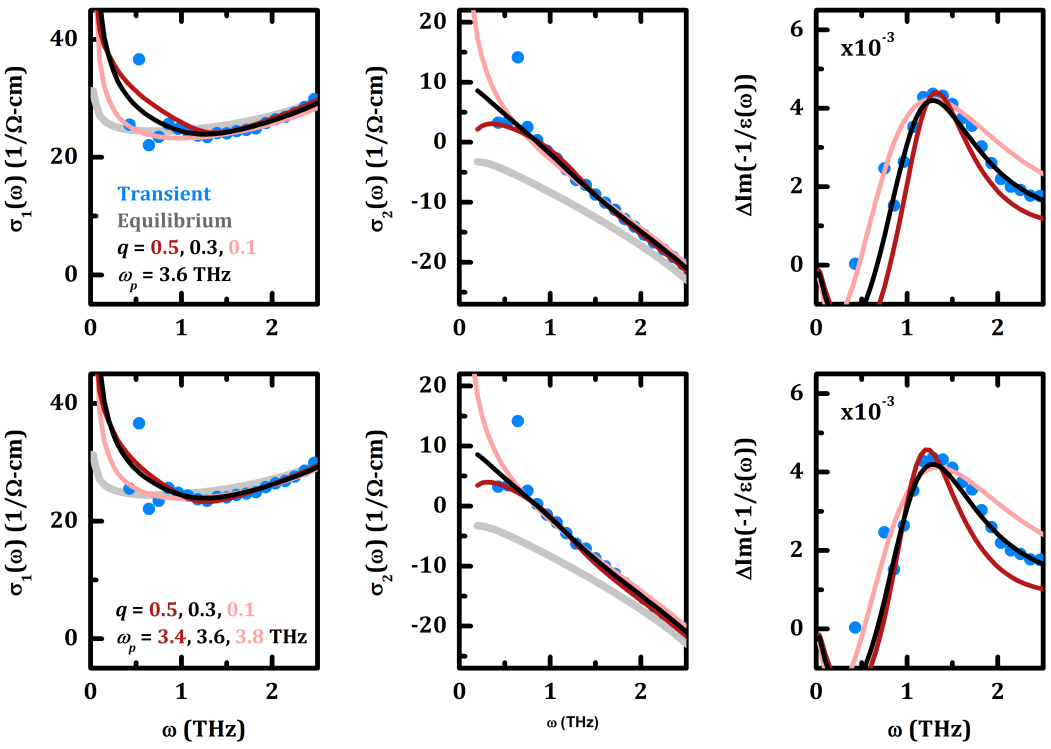

Figure B.9: **Varying inclusion shape in the effective medium fit.** The black lines represent the same fit as in Figure 5.23, with $q = 1/3$ and $f = 0.15$. The best-fit value for the plasma frequency is $\omega_p = 3.6$ THz. **Top row:** Dashed lines indicate fits to $q = 0.5$ (dark red) and $q = 0.1$ (pink). Equilibrium data in grey. The plasma frequency in all fits is fixed at 3.6 THz. **Bottom row:** Same q parameters, but with the plasma frequency optimized.

Appendix C

Matlab code for calculating the transient optical response

C.1 The bulk refractive index

```
function [trn,sigtrn] = bulkmodel(cn,delEE,sigdelEE,theta0,TE)

%-------------------------------------------------------------------------------
% Input parameters:
% cn        = static complex refractive index, cn = n + 1i*k
% delEE     = complex deltaE/E
% sigdelEE  = sigma(real(deltaE/E)) + i*sigma(imag(deltaE/E))
% theta0    = angle of incidence
% TE        = 1 for TE mode, 0 for TM mode
%
% Output parameters:
% trn       = transient complex refractive index, trn = n + 1i*k
%-------------------------------------------------------------------------------

sint = sin(theta0*pi/180); cost = cos(theta0*pi/180);

% The inverted Fresnel equations
if TE == 1,
    % TE incident light (s-polarized)
    statr = ( cost - cn.*sqrt(1-(sint./cn).^2) )./ ...
            ( cost + cn.*sqrt(1-(sint./cn).^2) );
    trr = (delEE+1).*statr;
    f = cost.*(1-trr)./(1+trr);

    trn1 = sqrt(sint.^2 + f.^2);
    trn2 = -sqrt(sint.^2 + f.^2);
    trn = choosesign(trn1,trn2);
```

```
    % Standard deviation propagation
    sigtrn = sigforTE(sigdelEE,statr,trr,theta0);
else
    % TM incident light (p-polarized)
    statr = -( sqrt(1-(sint./cn).^2) - cn.*cost )./ ...
            ( sqrt(1-(sint./cn).^2) + cn.*cost );
    trr = (delEE+1).*statr;
    f = cost.*(1-trr)./(1+trr);
    invf = 1./f;

    A = sqrt(1-4.*sint.^2./invf.^2);
    trn1 = invf./sqrt(2).*sqrt(1 + A);
    trn2 = -invf./sqrt(2).*sqrt(1 + A);
    trn = choosesign(trn1,trn2);

    % Standard deviation propagation
    sigtrn = sigforTM(sigdelEE,statr,trr,theta0);
end

end

function trn = choosesign(trn1,trn2)

%-------------------------------------------------------------------------
% The sign of the real part of the refractive index
% must be positive.
%-------------------------------------------------------------------------

% Choose first solution
trn = trn1;
% Keep track of how many times trn flips sign.
flip = 0; flipcount = 0;

for n = 1:length(trn1),
    if real(trn1(n)) < 0,
        trn(n) = trn2(n);
        if flip == 0,
            flipcount = flipcount+1;
            flip = 1;
        end
    else
        if flip == 1,
            flipcount = flipcount+1;
```

```
            flip = 0;
        end
    end
end
disp(['Bulk model flipped signs ' num2str(flipcount) ' times.'])

end

function sigtrn = sigforTE(sigdelEE,statr,trr,theta0)

%-------------------------------------------------------------------------------
% Propagate standard deviation of DeltaE/E.
%
% sigdelEE = sigma(real(DeltaE/E)) + 1i*sigma(imag(DeltaE/E))
% statr    = static complex reflectivity
% trr      = transient complex reflectivity
% theta0   = angle of incidence
%-------------------------------------------------------------------------------

sint = sin(theta0*pi/180); cost = cos(theta0*pi/180);
f = cost.*(1-trr)./(1+trr);

% Standard deviation of trr
sigRtrr2 = abs(real(statr)).^2.*real(sigdelEE).^2 + ...
       abs(imag(statr)).^2.*imag(sigdelEE).^2;
sigItrr2 = abs(real(statr)).^2.*imag(sigdelEE).^2 + ...
       abs(imag(statr)).^2.*real(sigdelEE).^2;

% Standard deviation of real(f)
trr1 = real(trr); trr2 = imag(trr);
A = (1+trr1).^2 + trr2.^2;
DRf_DRtrr = -(2.*cost./A).*(trr1 + (1+trr1).*(1-trr1.^2-trr2.^2)./A);
DRf_DItrr = -(2.*trr2.*cost./A).*(1 + (1-trr1.^2-trr2.^2)./A);
sigRf2 = abs(DRf_DRtrr).^2.*sigRtrr2 + ...
            abs(DRf_DItrr).^2.*sigItrr2;

% Standard deviation of imag(f)
DIf_DRtrr = 4.*cost.*trr2.*(1+trr1)./A.^2;
DIf_DItrr = 4.*cost.*trr2.^2./A.^2 - 2.*cost./A;
sigIf2 = abs(DIf_DRtrr).^2.*sigRtrr2 + ...
            abs(DIf_DItrr).^2.*sigItrr2;

% Standard deviation of trn
f1 = real(f); f2 = imag(f);
```

```
aa = sint.^2 + f1.^2 - f2.^2;
bb = 2.*f1.*f2; sgnb = bb./abs(bb);
cc = sqrt(aa.^2+bb.^2);
Daa_DRf = 2.*f1; Daa_DIf = -2.*f2;
Dbb_DRf = 2.*f2; Dbb_DIf = 2.*f1;
% Standard deviation of real(trn)
Dn_Daa = (1+aa./cc)./2./sqrt(2.*(cc+aa));
Dn_Dbb = bb./cc./2./sqrt(2.*(cc+aa));
Dn_DRf = Dn_Daa.*Daa_DRf + Dn_Dbb.*Dbb_DRf;
Dn_DIf = Dn_Daa.*Daa_DIf + Dn_Dbb.*Dbb_DIf;
sigRtrn = sqrt( abs(Dn_DRf).^2.*sigRf2 + ...
                abs(Dn_DIf).^2.*sigIf2 );
% Standard deviation of imag(trn)
Dk_Daa = sgnb.*(-1+aa./cc)./2./sqrt(2.*(cc-aa));
Dk_Dbb = sgnb.*bb./cc./2./sqrt(2.*(cc-aa));
Dk_DRf = Dk_Daa.*Daa_DRf + Dk_Dbb.*Dbb_DRf;
Dk_DIf = Dk_Daa.*Daa_DIf + Dk_Dbb.*Dbb_DIf;
sigItrn = sqrt( abs(Dk_DRf).^2.*sigRf2 + ...
                abs(Dk_DIf).^2.*sigIf2 );

sigtrn = sigRtrn + 1i.*sigItrn;
end

function sigtrn = sigforTM(sigdelEE,statr,trr,theta0)

%-------------------------------------------------------------------------
% Propagate standard deviation of DeltaE/E.
%
% sigdelEE = sigma(real(DeltaE/E)) + 1i*sigma(imag(DeltaE/E))
% statr    = static complex reflectivity
% trr      = transient complex reflectivity
% theta0   = angle of incidence
%-------------------------------------------------------------------------

[f1,f2,varf1,varf2] = getvarf(trr,statr,sigdelEE);
f = f1 + 1i.*f2;

a = 1 - 4.*sin(theta0).^2.*cos(theta0).^2.*(f1.^2-f2.^2);
b = 8.*sin(theta0).^2.*cos(theta0).^2.*f1.*f2;
dadf1 = -8.*sin(theta0).^2.*cos(theta0).^2.*f1;
dadf2 = 8.*sin(theta0).^2.*cos(theta0).^2.*f2;
dbdf1 = 8.*sin(theta0).^2.*cos(theta0).^2.*f2;
dbdf2 = 8.*sin(theta0).^2.*cos(theta0).^2.*f1;
```

```
[p,q,dpda,dpdb,dqda,dqdb] = getpq(a,b);
[g,h,dgdpp,dgdq,dhdpp,dhdq] = getpq(1+p,q);
dgdf1 = dgdpp.*(dpda.*dadf1 + dpdb.*dbdf1) + ...
        dgdq.*(dqda.*dadf1 + dqdb.*dbdf1);
dgdf2 = dgdpp.*(dpda.*dadf2 + dpdb.*dbdf2) + ...
        dgdq.*(dqda.*dadf2 + dqdb.*dbdf2);
dhdf1 = dhdpp.*(dpda.*dadf1 + dpdb.*dbdf1) + ...
        dhdq.*(dqda.*dadf1 + dqdb.*dbdf1);
dhdf2 = dhdpp.*(dpda.*dadf2 + dpdb.*dbdf2) + ...
        dhdq.*(dqda.*dadf2 + dqdb.*dbdf2);
abfsq = abs(f.^2);
dfsqdf1 = 4.*( (f1.^2-f2.^2).*f1 + f2 )./abfsq;
dfsqdf2 = 4.*( (f1.^2-f2.^2).*f2 + f1 )./abfsq;

dndf1 = ( g + f1.*dgdf1 + f2.*dhdf1 - ...
          (f1.*g + f2.*h).*dfsqdf1./abfsq.^2 )./(sqrt(2).*abfsq);
dndf2 = ( h + f1.*dgdf2 + f2.*dhdf2 - ...
          (f1.*g + f2.*h).*dfsqdf2./abfsq.^2 )./(sqrt(2).*abfsq);
dkdf1 = ( h + f1.*dhdf1 - f2.*dgdf1 - ...
          (f1.*h - f2.*g).*dfsqdf1./abfsq.^2 )./(sqrt(2).*abfsq);
dkdf2 = ( -g + f1.*dhdf2 - f2.*dgdf2 - ...
          (f1.*h - f2.*g).*dfsqdf2./abfsq.^2 )./(sqrt(2).*abfsq);

varn = abs(dndf1).^2.*varf1 + abs(dndf2).^2.*varf2;
vark = abs(dkdf1).^2.*varf1 + abs(dkdf2).^2.*varf2;

sigtrn = sqrt(varn) + 1i.*sqrt(vark);

end

function [p,q,dpda,dpdb,dqda,dqdb] = getpq(a,b)

% sqrt(a + ib) = p + iq

absq = sqrt(a.^2 + b.^2);
p = sqrt( (a + absq)./2 );
sgnb = (b./abs(b)); qq = sqrt( (-a + absq)./2 );
q = sgnb.*qq;

dpda = (1 + a./absq)./(4.*p);
dpdb = (b./absq)./(4.*p);
dqda = sgnb.*(-1 + a./absq)./(4.*qq);
dqdb = sgnb.*(b./absq)./(4.*qq);
```

```
end

function [f1,f2,varf1,varf2] = getvarf(trr,statr,sigdelEE)

% trr = (delEE+1).*statr;
% trr = (RdE + 1 + 1i.*IdE).*(Rsr + 1i.*Isr)
% Rtrr = (RdE + 1).*Rsr - IdE.*Isr
% Itrr = (RdE + 1).*Isr + IdE.*Rsr
sigr1 = real(statr).*real(sigdelEE) + imag(statr).*imag(sigdelEE);
sigr2 = real(statr).*imag(sigdelEE) + imag(statr).*real(sigdelEE);

r1 = real(trr); r2 = imag(trr);
f = (1-trr)./(1+trr); f1 = real(f); f2 = imag(f);
den = (1+r1).^2 + r2.^2;
df1dr1 = -2.*( r1 + f1.*(1+r1) )./den;
df1dr2 = -2.*( r2 + f1.*r2 )./den;
df2dr1 = 4.*(1+r1).*r2.^2./den.^2;
df2dr2 = -4.*(1+r1).^2.*r2./den.^2;

varf1 = df1dr1.^2.*sigr1.^2 + df1dr2.^2.*sigr2.^2;
varf2 = df2dr1.^2.*sigr1.^2 + df2dr2.^2.*sigr2.^2;

end
```

C.2 The analytic thin film model

```
function [cdeln,sig_cdeln] = thinfilmmodel(cn,delEE,sigdelEE,w,d,einf)

%-------------------------------------------------------------------------------
% Calculate deltaS (change in conductivity)
% Model assumes normal incidence
%
% Input parameters:
% delEE     = complex deltaE/E
% sigdelEE  = sigma(real(deltaE/E)) + i*sigma(imag(deltaE/E))
% w         = frequency
% d         = pump penetration depth
% einf      = epsilon infinity
%
% Output parameters:
% cn        = static complex refractive index, cn = n + 1i*k
% cdeln     = transient complex changes in the refractive index,
```

```
%             trn = cn + cdeln
%-------------------------------------------------------------------------

%-------------------------------------------------------------------------
% Constants
Z0 = 377; % Ohms
d = d.*1e-4; % um --> cm
%-------------------------------------------------------------------------

%-------------------------------------------------------------------------
% Calculate deltaS
pre = 1./(Z0*d); % 1/Ohm-cm
[deltaS,var_deltaS] = stdev_deltaS(pre,delEE,sigdelEE,cn);
%-------------------------------------------------------------------------

%-------------------------------------------------------------------------
% Calculate excited sample refractive index
S0 = w.*(cn.^2-einf)./(1.8.*1i); % Equilibrium conductivity (1/Ohm-cm)
trn = sqrt(1.8.*1i.*(S0+deltaS)./w + einf); % Transient refractive index

% Propagate standard deviation
sig_cdeln = stdev_N(w,trn,var_deltaS);
cdeln = trn-cn;
%-------------------------------------------------------------------------

end

function [deltaS,var_deltaS] = stdev_deltaS(pre,delEE,sigdelEE,cn)

%-------------------------------------------------------------------------
% Numerator
%   num = pre.*delEE.*(cn.^2.*(1-1./(2.*cn.^2)) - 0.5);
%   num = pre.*(cn.^2 - 1);
% Denomenator
%   den = delEE.*(1/sqrt(2) - cn.*sqrt(1-1./(2.*cn.^2))) + sqrt(2);
%   den = (1/sqrt(2) - sqrt(cn.^2-0.5)) + sqrt(2)./delEE;
% deltaS = num./den;
%-------------------------------------------------------------------------

% deltaS = A/(B + C/delEE)
A = pre.*(cn.^2 - 1); B = (1/sqrt(2) - sqrt(cn.^2-0.5)); C = sqrt(2);
deltaS = A./(B + C./delEE); Sr = real(deltaS); Si = imag(deltaS);

% Variance of deltaS...
```

```
% Define convenient terms
f2 = delEE.^2; frf2 = real(delEE)./f2; fif2 = imag(delEE)./f2;
D = (B + C.*frf2).^2 + (C.*fif2).^2;

% Define derivatives of D
dD_dfr = 2.*(B + C.*frf2).*(C./f2 - 2.*C.*frf2.^2);
dD_dfi = 2.*(C.*fif2).*(C./f2 - 2.*C.*fif2.^2);

% Define derivatives of deltaS
dSr_dfr = A.*C./(D.*f2) - 2.*A.*C.*frf2.^2./D - Sr.*dD_dfr./D;
dSi_dfi = A.*C./(D.*f2) - 2.*A.*C.*fif2.^2./D - Si.*dD_dfi./D;
dSr_dfi = -2.*A.*C.*frf2.*fif2./D - Sr.*dD_dfi./D;
dSi_dfr = -2.*A.*C.*frf2.*fif2./D - Si.*dD_dfr./D;

% Define standard deviation
var_fr = real(sigdelEE).^2; var_fi = imag(sigdelEE).^2;
var_Sr = abs(dSr_dfr).^2.*var_fr + abs(dSr_dfi).^2.*var_fi;
var_Si = abs(dSi_dfr).^2.*var_fr + abs(dSi_dfi).^2.*var_fi;

var_deltaS = var_Sr + 1i.*var_Si;

end

function sig_N = stdev_N(w,N,var_S)

%-------------------------------------------------------------------------
% Propagate the standard deviation from conductivity to refractive index
%-------------------------------------------------------------------------

% First get dielectric function
eps = N.^2; eps1 = real(eps); eps2 = imag(eps);
var_eps1 = abs(-1.8./w).^2.*imag(var_S);
var_eps2 = abs(1.8./w).^2.*real(var_S);

% Get N and derivatives
[~,~,dn_de1,dn_de2,dk_de1,dk_de2] = complex_sqrt(eps1,eps2);

% Get variance
var_n = abs(dn_de1).^2.*var_eps1 + abs(dn_de2).^2.*var_eps2;
var_k = abs(dk_de1).^2.*var_eps1 + abs(dk_de2).^2.*var_eps2;

%N = n + 1i.*k;
sig_N = sqrt(var_n) + 1i.*sqrt(var_k);
```

```
end

function [p,q,dp_da,dp_db,dq_da,dq_db] = complex_sqrt(a,b)

% +/-(p + i*q) = sqrt(a + i*b)

% Get p and q
abs_ab = sqrt(a.^2+b.^2); sgnb = sign(b);
p = sqrt((a + abs_ab)./2); q = sgnb.*sqrt((-b + abs_ab)./2);
%[p,q] = picksolution(p,q);

norm_a = a./abs_ab; norm_b = b./abs_ab;
dp_da = (1 + norm_a)./(4.*p);
dq_db = sgnb.*(-1 + norm_b)./(4.*q);
dp_db = (norm_b)./(4.*p);
dq_da = sgnb.*(norm_a)./(4.*q);

end
```

C.3 The single layer model

```
function trr = singlelayer(cn,cdeln,vars)

%-------------------------------------------------------------------------
% Input parameters:
% cn        = static complex refractive index, cn = n + 1i*k
% cdeln     = transient complex changes in the refractive index,
%             trn = cn + cdeln
% vars      = variables used in the fit:
% vars(1)   = inverse of the pump penetration depth, alpha = 1/d
% vars(3)   = angle of incidence theta
% vars(4)   = k0 = 2.*pi./lambda0;
%             lambda0 = c_light./w; % micron (w in THz)
% vars(6)   = 1 for TE polarization, 0 for TM polarization
%
% Output parameters:
% trr       = transient complex reflectivity
%-------------------------------------------------------------------------

alpha = vars(1); d = 1./alpha;
theta = vars(3); asq = (sin(theta*pi/180))^2;
```

```
k0 = vars(4); TE = vars(6); mu = 1; mu2 = 1;

trcn = cn + cdeln;

nn1 = sqrt(k0.^2.*(1-asq)); nnf = sqrt(k0.^2.*(cn.^2-asq));
nn = sqrt(k0.^2.*(trcn.^2-asq));

if TE == 1,
    % TE (s) polarization
    p1 = nn1./(k0); pf = nnf./(k0.*mu2);
    p = nn./(k0.*mu);

else
    % TM (p) polarization
    p1 = nn1./(k0); pf = nnf.*mu2./(cn.^2*k0);
    p = nn.*mu./(trcn.^2*k0);

end

m11 = cos(nn.*d); m12 = -(1i./p).*sin(nn.*d); m21 = -(1i.*p).*sin(nn.*d);

rnum = (m11+m12.*pf).*p1 - (m21+m11.*pf);
rden = (m11+m12.*pf).*p1 + (m21+m11.*pf);
trr = rnum./rden;

end
```

C.4 The full multilayer model

```
function trr = multilayer(cn,cdeln,vars)

%-------------------------------------------------------------------------
% Input parameters:
% cn        = static complex refractive index, cn = n + 1i*k
% cdeln     = transient complex changes in the refractive index,
%             trn = cn + cdeln
% vars      = variables used in the fit:
% vars(1)   = inverse of the pump penetration depth, alpha = 1/d
% vars(2)   = distance increment dz
% vars(3)   = angle of incidence theta
% vars(4)   = k0 = 2.*pi./lambda0;
%             lambda0 = c_light./w; % micron (w in THz)
```

```
% vars(5)   = The probe penetration depth L
% vars(6)   = 1 for TE polarization, 0 for TM polarization
% vars(7)   = cdelnTol, the tolerance value for the change in cdeln:
%             if cdeln(z+dz)-cdeln(z) < cdelnTol, then stop calculation of M
%
% Output parameters:
% trr       = transient complex reflectivity
%-------------------------------------------------------------------------

% Get all constants, vars = [alpha,dz,theta0,k0,probed,TE];
alpha = vars(1); dz = vars(2); theta = vars(3);
k0 = vars(4); probed = vars(5); TE = vars(6);
cdelnTol = vars(7);

% Set depth range
z = 0:dz:(probed);

% Get initial parameters
cost = cos(theta*pi/180); sint0 = sin(theta*pi/180);
if TE == 1,
    getp = @(n,c)(n.*c);
    p1 = cost;
else
    getp = @(n,c)(c./n);
    p1 = cost;
end

% Get initial characteristic matrix
M = ones(2,2);
M(1,2) = 0; M(2,1) = 0;

% Get refractive index at the surface
trcn2 = cn + cdeln;

n = 1; tolbool = 0; lenz = length(z);
while n < lenz && tolbool == 0,
    % Get the value of trcn for z_n
    trcn = trcn2;

    Mn = ones(2,2);
    p = getp(trcn,cost);

    % Get the new matrix for layer dz
    Mn(1,1) = cos(trcn.*k0.*dz.*cost);
```

```
    Mn(1,2) = -1i./p.*sin(trcn.*k0.*dz.*cost);
    Mn(2,1) = -1i.*p.*sin(trcn.*k0.*dz.*cost);
    Mn(2,2) = cos(trcn.*k0.*dz.*cost);
    % Get the total matrix
    M = M*Mn;

    % Get new theta
    cdeln_n = cdeln*exp(-alpha*(z(n) + dz));
    trcn2 = cn + cdeln_n;
    trcn2 = abs(real(trcn2)) + 1i.*abs(imag(trcn2));
    cost = getsnell(1,trcn2,sint0); %sint = sint0./trcn2;

    % Check for cdeln_n ~ 0
    if abs(cdeln_n) < cdelnTol,
        tolbool = 1;
        disp(['Note: Tolerance for abs(DeltaN) reached after ' ...
               num2str(n) ' of ' num2str(lenz) ' iterations.'])
    end

    n = n+1;
end
if tolbool == 1,
    dz2 = probed-n*dz;
    trcn = trcn2; Mn = ones(2,2);
    p = getp(trcn,cost);

    % Get the new matrix
    Mn(1,1) = cos(trcn.*k0.*dz2.*cost);
    Mn(1,2) = -1i./p.*sin(trcn.*k0.*dz2.*cost);
    Mn(2,1) = -1i.*p.*sin(trcn.*k0.*dz2.*cost);
    Mn(2,2) = cos(trcn.*k0.*dz2.*cost);
    % Get the total matrix
    M = M*Mn;

    cdeln_n = cdeln*exp(-alpha*(probed+dz));
    trcn2 = cn + cdeln_n;
    %trcn2 = abs(real(trcn2)) + 1i.*abs(imag(trcn2));
    cost = getsnell(1,trcn2,sint0); %sint = sint0./trcn2;

end

% Calculate the material reflectivity coefficient, trr
trcn = trcn2;
pbulk = getp(trcn,cost);
```

```
trRn = (M(1,1)+M(1,2).*pbulk).*p1 - (M(2,1)+M(2,2).*pbulk);
trRd = (M(1,1)+M(1,2).*pbulk).*p1 + (M(2,1)+M(2,2).*pbulk);
trr = trRn./trRd;

end

function cost2 = getsnell(n1,n2,sint1)
sint2 = (n1./n2).*sint1;
cost2 = sqrt(1-sint2.^2);
end
```

C.5 The approximate multilayer model

```
function trr = approx_multilayer(cn,cdeln,vars)

%-------------------------------------------------------------------------
% Input parameters:
% cn        = static complex refractive index, cn = n + 1i*k
% cdeln     = transient complex changes in the refractive index,
%             trn = cn + cdeln
% vars      = variables used in the fit:
% vars(1)   = inverse of the pump penetration depth, alpha = 1/d
% vars(3)   = angle of incidence theta
% vars(4)   = k0 = 2.*pi./lambda0;
%             lambda0 = c_light./w; % micron (w in THz)
% vars(5)   = The probe penetration depth L
% vars(6)   = 1 for TE polarization, 0 for TM polarization
%
% Output parameters:
% trr       = transient complex reflectivity
%-------------------------------------------------------------------------

% Get all constants, vars = [alpha,dz,theta0,k0,probed,TE];
alpha = vars(1); theta = vars(3); sint = sin(theta*pi/180);
k0 = vars(4); L = vars(5); TE = vars(6);

aL = alpha.*L;
cnf = cn+cdeln.*exp(-aL); % refractive index at depth L into sample

if TE == 1,
    % TE (s) polarization
```

```
    p1 = cn0.*cos(theta*pi/180);
    G = -1i.*k0.*L;
    FG = ( (1-exp(-2*aL))*cdeln^2/(2*aL) + ...
                   (2*cn/aL)*(1-exp(-aL))*cdeln + ...
                   (cn^2-sint^2) );
    pbulk = sqrt(cnf.^2-sint.^2);

    rnum = (1/G + pbulk)*p1 - (FG + pbulk/G);
    rden = (1/G + pbulk)*p1 + (FG + pbulk/G);
    trr = rnum/rden;
else
    % TM (p) polarization
    p1 = cos(theta*pi/180)./cn0;
    G = cdeln.^2.*(1-exp(-2*aL))./(2.*aL) + ...
          2.*cdeln.*cn.*(1-exp(-aL))./aL + cn.^2;
    FL = 1 + log(cnf./cn0)./aL + (cdeln./(aL.*cnf)).*exp(-aL);
    F0 = cdeln./(aL.*cn0);
    F = (1 - sint.^2.*(FL - F0)./cn.^2);
    pbulk = sqrt(1-(sint./cnf).^2)./cnf;
    ik0L = -1i.*k0.*L;

    rnum = (1/ik0L + pbulk*G)*p1 - (F + pbulk/ik0L);
    rden = (1/ik0L + pbulk*G)*p1 + (F + pbulk/ik0L);
    trr = rnum/rden;
end

end
```

C.6 The analytic approximate multilayer model (TE case)

```
function [cdeln,sigcdeln] = analytic(cn,r,sigr,L,k0,vars)

%-------------------------------------------------------------------------------
% Input parameters:
% cn        = static complex refractive index, cn = n + 1i*k
% r         = transient complex reflectivity
% sigr      = standard deviation of the transient complex reflectivity
% L         = probe penetration depth
% k0        = k0 = 2.*pi./lambda0;
%             lambda0 = c_light./w; % micron (w in THz)
```

```
% vars(1)   = inverse of the pump penetration depth, alpha = 1/d
% vars(2)   = angle of incidence theta0
%
% Output parameters:
% cdeln     = transient changes in the complex refractive index, trn = n + 1i*k
% sigcdeln  = sigma(real(cdeln)) + i*sigma(imag(cdeln))
%--------------------------------------------------------------------------

% Get experimental parameters
alpha = vars(1); theta0 = vars(2);

% Calculate initial and final conditions
sint = sin(theta0*pi/180); cost = cos(theta0*pi/180);
costf = sqrt(1-(sint./cn).^2);
pf = cn.*costf;

% Get the change in refractive index
A = 1i.*k0.*(1-exp(-2.*alpha.*L))./(2.*alpha);
B = 2.*1i.*k0.*cn.*(1-exp(-alpha.*L))./alpha;
C = 1i.*k0.*L.*(cn.^2-sint.^2) + ...
    (1-1i.*k0.*L.*pf).*cost.*(1-r)./(1+r) - pf;
cdeln1 = (-B - sqrt(B.^2 - 4.*A.*C))./(2.*A);
cdeln2 = (-B + sqrt(B.^2 - 4.*A.*C))./(2.*A);
cdeln = picksolution(cdeln1,cdeln2,cn);

% Get the error
dndC = 1./sqrt(B.^2-4.*A.*C);
dfrdr = -2./(1+r).^2;
dCdr = (1-1i.*k0.*L.*pf).*cost.*dfrdr;
sigcdeln = abs(dndC.*dCdr).*sigr;

end

function cdeln = picksolution(cdeln1,cdeln2,cn)

% Pick one solution and count the number of changes
% Real part of transient refractive index must be
% greater than zero.
cdeln = cdeln1; chg = 0;
trn1 = cn+cdeln1; trn2 = cn+cdeln2;
for n = 1:length(cdeln1),
    if real(trn1(n)) < 0,
        if real(trn2(n)) >= 0,
            cdeln(n) = cdeln2(n);
```

```
            chg = chg + 1;
        end
    end
end
if chg > 0,
    disp(['Number of points changed in Analytic Model: ' num2str(chg)])
end
end
```

References

[1] C. R. Hunt*, W. Hu*, S. Kaiser*, D. Nicoletti*, *et al.*, "Optically enhanced coherent transport in $YBa_2Cu_3O_{6.5}$ by ultrafast redistribution of interlayer coupling," Nature Mat. **13**, 705 (2014).

[2] S. Kaiser, C. R. Hunt, D. Nicoletti, W. Hu, *et al.*, "Optically induced coherent transport far above T_c in underdoped $YBa_2Cu_3O_{6+\delta}$," Phys. Rev. B **89**, 184516 (2014).

[3] R. Mankowsky, A. Subedi, M. Först, S. O. Mariager, *et al.*, "Nonlinear lattice dynamics as a basis for enhanced superconductivity in $YBa_2Cu_3O_{6.5}$," Nature **516**, 71 (2014).

[4] W. Jin, S. Hao, and H. Zhang, "The fixed triangle chemical bond and its effect in the $Y_{1-x}Ca_xBa_{2-y}La_yCu_3O_z$ system from underdoped to overdoped," New J. Phys. **11**, 113036 (2009).

[5] G. E. Blonder, M. Tinkham, and T. M. Klapwijk, "Transition from metallic to tunneling regimes in superconducting microconstrictions: Excess current, charge imbalance, and supercurrent conversion," Phys. Rev. B **25**, 4515 (1982).

[6] A. A. Golubov, A. Brinkman, Y. Tanaka, I. I. Mazin, and O. V. Dolgov, "Andreev spectra and subgap bound states in multiband superconductors," Phys. Rev. Lett. **103**, 077003 (2009).

[7] I. B. Sperstad, J. Linder, and A. Sudbø, "Quantum transport in ballistic $s_{\pm}$-wave superconductors with interband coupling: Conductance spectra, crossed Andreev reflection, and Josephson current," Phys. Rev. B **80**, 144507 (2009).

[8] R. A. Kaindl, M. A. Carnahan, D. S. Chemla, S. Oh, and J. N. Eckstein, "Dynamics of cooper pair formation in $Bi_2Sr_2CaCu_2O_{8+x}$," Phys. Rev. B **72**, 060510(R) (2005).

[9] Y. H. Wang, D. Hsieh, D. Pilon, L. Fu, D. R. Gardner, Y. S. Lee, and N. Gedik, "Observation of a warped helical spin texture in Bi_2Se_3 from circular

dichroism angle-resolved photoemission spectroscopy," Phys. Rev. Lett. **107**, 207602 (2011).

[10] C. L. Smallwood, J. P. Hinton, C. Jozwiak, W. Zhang, *et al.*, "Tracking Cooper pairs in a cuprate superconductor by ultrafast angle-resolved photoemission," Science **336**, 1137 (2012).

[11] G. Yu, C. H. Lee, A. J. Heeger, N. Herron, and E. M. McCarron, "Transient photoinduced conductivity in single crystals of $YBa_2Cu_30_{7-\delta}$: "photodoping" to the metallic state," Phys. Rev. Lett. **67**, 2581 (1991).

[12] G. Nieva, E. Osquiguil, J. Guimpel, M. Maenhoudt, *et al.*, "Photoinduced enhancement of superconductivity," Appl. Phys. Lett. **60**, 2159 (1992).

[13] K. W. Kim, A. Pashkin, H. Schäfer, M. Beyer, *et al.*, "Ultrafast transient generation of spin-density-wave order in the normal state of $BaFe_2As_2$ driven by coherent lattice vibrations," Nat. Mat. **11**, 497 (2012).

[14] G. Coslovich, C. Giannetti, F. Cilento, S. D. Conte, *et al.*, "Tracking Cooper pairs in a cuprate superconductor by ultrafast angle-resolved photoemission," Phys. Rev. Lett. **110**, 107003 (2013).

[15] D. Nicoletti, E. Casandruc, Y. Laplace, V. Khanna, *et al.*, "Optically induced superconductivity in striped $La_{2-x}Ba_xCuO_4$ by polarization-selective excitation in the near infrared," Phys. Rev. B **90**, 100503(R) (2014).

[16] M. Mitrano, G. Cotugno, S. Clark, R. Singla, *et al.*, "Pressure-dependent relaxation in the photoexcited Mott insulator ETF_2TCNQ: Influence of hopping and correlations on quasiparticle recombination rates," Phys. Rev. Lett. **112**, 117801 (2014).

[17] R. Singla, A. Simoncig, M. Frst, D. Prabhakaran, A. L. Cavalieri, and A. Cavalleri, "Photoinduced melting of the orbital order in $La_{0.5}Sr_{1.5}MnO_4$ measured with 4-fs laser pulses," Phys. Rev. B **88**, 075107 (2013).

[18] B. Mansart, D. Boschetto, A. Savoia, F. Rullier-Albenque, *et al.*, "Observation of a coherent optical phonon in the iron pnictide superconductor $Ba(Fe_{1-x}Co_x)_2As_2$ ($x = 0.06$ and 0.08)," Phys. Rev. B **80**, 172504 (2009).

[19] L. Rettig, S. Mariager, A. Ferrer, S. Grbel, *et al.*, "Ultrafast structural dynamics of the Fe-pnictide parent compound $BaFe_2As_2$," Phys. Rev. Lett. **114**, 067402 (2015).

[20] M. Först, R. Mankowsky, H. Bromberger, D. Fritz, *et al.*, "Displacive lattice excitation through nonlinear phononics viewed by femtosecond X-ray diffraction," Sol. State Comm. **169**, 24 (2013).

[21] H. Y. Hwang, T. T. M. Palstra, S.-W. Cheong, and B. Batlogg, "Pressure effects on the magnetoresistance in doped manganese perovskites," Phys. Rev. B **52**, 15046 (1995).

[22] M. Itoh, K. Nishi, J. D. Yu, and Y. Inaguma, "Annealing and pressure effects on structural and ferromagnetic transitions of $La_{0.85}Sr_{0.15}MnO_3$ single crystals," Phys. Rev. B **55**, 14408 (1997).

[23] M. Hücker, G. D. Gu, J. M. Tranquada, M. von Zimmermann, *et al.*, "Coupling of stripes to lattice distortions in cuprates and nickelates," Physica C **460-462**, 170 (2007).

[24] J.-P. Locquet, J. Perret, J. Fompeyrine, E. Mächler, J. W. Seo, and G. V. Tendeloo, "Doubling the critical temperature of $La_{1.9}Sr_{0.1}CuO_4$ using epitaxial strain," Nature **394**, 453 (1998).

[25] C.-H. Lee, A. Iyo, H. Eisaki, H. Kito, *et al.*, "Effect of structural parameters on superconductivity in fluorine-free $LnFeAsO_{1-y}$ (Ln = La, Nd)," J. Phys. Soc. Jpn. **77**, 083704 (2008).

[26] M. Mori, G. Khaliullin, T. Tohyama, and S. Maekawa, "Imaging the impact on cuprate superconductivity of varying the interatomic distances within individual crystal unit cells," Phys. Rev. Lett. **101**, 247003 (2008).

[27] J. A. Slezak, J. Lee, M. Wang, K. McElroy, *et al.*, "Imaging the impact on cuprate superconductivity of varying the interatomic distances within individual crystal unit cells," Proc. Nat. Acad. Sci. **105**, 3203 (2008).

[28] M. Först, R. Mankowsky, and A. Cavalleri, "Mode-selective control of the crystal lattice," Acc. Chem. Res. **48**, 380 (2015).

[29] M. Rini, Y. Zhu, S. Wall, R. I. Tobey, *et al.*, "Transient electronic structure of the photoinduced phase of $Pr_{0.7}Ca_{0.3}MnO_3$ probed with soft x-ray pulses," Phys. Rev. B **80**, 155113 (2009).

[30] R. I. Tobey, D. Prabhakaran, A. T. Boothroyd, and A. Cavalleri, "Ultrafast electronic phase transition in $La_{1/2}Sr_{3/2}MnO_4$ by coherent vibrational excitation: evidence for nonthermal melting of orbital order," Phys. Rev. Lett. **101**, 197404 (2008).

[31] H. Ehrke, R. I. Tobey, S. Wall, S. A. Cavill, *et al.*, "Photoinduced melting of antiferromagnetic order in $La_{0.5}Sr_{1.5}MnO_4$ measured using ultrafast resonant soft X-ray diffraction," Phys. Rev. Lett. **106**, 217401 (2011).

[32] M. Först, R. I. Tobey, H. Bromberger, S. B. Wilkins, *et al.*, "Melting of charge stripes in vibrationally driven $La_{1.875}Ba_{0.125}CuO_4$: Assessing the respective roles of electronic and lattice order in frustrated superconductors," Phys. Rev. Lett. **112**, 157002 (2014).

[33] D. Fausti, R. I. Tobey, N. Dean, S. Kaiser, *et al.*, "Light-induced superconductivity in a stripe-ordered cuprate," Science **331**, 189 (2011).

[34] C. R. Hunt, D. Nicoletti, S. Kaiser, T. Takayama, H. Takagi, and A. Cavalleri, "Two distinct kinetic regimes for the relaxation of light-induced superconductivity in $La_{1.675}Eu_{0.2}Sr_{0.125}CuO_4$," Phys. Rev. B **91**, 020505(R) (2015).

[35] S. Savelev, A. L. Rakhmanov, V. A. Yampolskii, and F. Nori, "Analogues of nonlinear optics using terahertz Josephson plasma waves in layered superconductors," Nat. Phys. **2**, 521 (2006).

[36] S. Savelev, V. A. Yampolskii, A. L. Rakhmanov, and F. Nori, "Analogues of nonlinear optics using terahertz Josephson plasma waves in layered superconductors," Rep. Prog. Phys. **73**, 026501 (2010).

[37] A. Dienst, E. Casandruc, D. Fausti, L. Zhang, *et al.*, "Optical excitation of Josephson plasma solitons in a cuprate superconductor," Nat. Mat. **12**, 535 (2013).

[38] P. W. Higgs, "Broken symmetries, massless particles and gauge fields," Phys. Lett. **12**, 132 (1964).

[39] Y. Nambu, "Energy gap, mass gap, and spontaneous symmetry breaking," Int. J. Mod. Phys. A **25**, 4141 (2010).

[40] T. Papenkort, V. M. Axt, and T. Kuhn, "Coherent dynamics and pump-probe spectra of BCS superconductors," Phys. Rev. B **76**, 224522 (2007).

[41] R. Matsunaga, Y. I. Hamada, K. Makise, Y. Uzawa, *et al.*, "Higgs amplitude mode in the BCS superconductors $Nb_{1x}Ti_xN$ induced by terahertz pulse excitation," Phys. Rev. Lett. **111**, 057002 (2013).

[42] M. Först, A. Frano, S. Kaiser, R. Mankowsky, *et al.*, "Femtosecond x rays link melting of charge-density wave correlations and light-enhanced coherent transport in $YBa_2Cu_3O_{6.6}$," Phys. Rev. B **90**, 184514 (2014).

[43] I. Gierz, M. Mitrano, H. Bromberger, C. Cacho, *et al.*, "Phonon-pump XUV-photoemission-probe in graphene: evidence for non-adiabatic heating of Dirac carriers by lattice deformation," (2014), arXiv:1411.3888 .

[44] R. W. Boyd, *Nonlinear Optics* (Academic Press, 2003).

[45] A. L. Gaeta, "Catastrophic collapse of ultrashort pulses," Phys. Rev. Lett. **84**, 3582 (2000).

[46] R. L. Fork, C. V. Shank, C. Hirlimann, R. Yen, and W. J. Tomlinson, "Femtosecond white-light continuum pulses," Optics Lett. **8**, 1 (1983).

[47] "TOPAS-800-fs: Ultrafast optical parametric amplifier," Coherent Data Sheet (2012).

[48] S. L. Dexheimer, ed., *THz Spectroscopy* (CRC Press, 2007).

[49] Q. Wu and X. C. Zhang, "7 terahertz broadband GaP electro-optic sensor," Appl. Phys. Lett. **70**, 1784 (1997).

[50] K. Liu, J. Xu, and X. C. Zhang, "GaSe crystals for broadband terahertz wave detection," Appl. Phys. Lett. **85**, 863 (2004).

[51] C. Kübler, R. Huber, S. Tübel, and A. Leitenstorfer, "Ultrabroadband detection of multi-terahertz field transients with gas electro-optic sensors: Approaching the near infrared," Appl. Phys. Lett. **85**, 3360 (2004).

[52] K. H. Yang, P. L. Richards, and Y. R. Shen, "Generation of far-infrared radiation by picosecond light pulses in $LiNbO_3$," App. Phys. Lett. **19**, 320 (1971).

[53] B. B. Hu, X. Zhang, D. H. Auston, and P. R. Smith, "Freespace radiation from electrooptic crystals," App. Phys. Lett. **56**, 506 (1990).

[54] P. Y. Han, M. Tani, F. Pan., and X.-C. Zhang, "Use of the organic crystal DAST for terahertz beam applications," Opt. Lett. **25**, 675 (2000).

[55] C. Vicario, B. Monoszlai, and C. Ruchert, in *FEL Technology III: Undulators, Beamlines, Beam Diagnostics* (New York, 2013).

[56] D. H. Auston, "Subpicosecond electro-optic shock waves," Appl. Phys. Lett. **43**, 713 (1983).

[57] D. H. Auston, K. P. Cheung, J. A. Valdmanis, and D. A. Kleinman, "Cherenkov Radiation from Femtosecond Optical Pulses in Electro- Optic Media," Phys. Rev. Lett. **53**, 1555 (1984).

[58] D. H. Auston, K. P. Cheung, and P. R. Smith, "Picosecond photoconducting Hertzian dipoles," Appl. Phys. Lett. **45**, 284 (1984).

[59] P. Smith, D. H. Auston, and M. C. Nuss, "Subpicosecond photoconducting dipole antennas," IEEE Journal of Quantum Electronics **24**, 255 (1988).

[60] S. Gupta, J. Whitaker, and G. Mourou, "Ultrafast carrier dynamics in III-V semiconductors grown by molecular-beam epitaxy at very low substrate temperatures," IEEE Journal of Quantum Electronics **28**, 2464 (1992).

[61] J. Maysonnave, S. Huppert, F. Wang, S. Maero, *et al.*, "Terahertz generation by dynamical photon drag effect in graphene excited by femtosecond optical pulses," Nano Lett. **14**, 5797 (2014).

[62] M. van Exter, C. Fattinger, and D. Grischkowsky, "Terahertz time-domain spectroscopy of water vapor," Opt. Lett. **14**, 1128 (1989).

[63] "Tera-SED: Large area THz emitter," Laser Quantum Data Sheet (Accessed: 2015).

[64] K. Y. Kim, A. J. Taylor, J. H. Glownia, and G. Rodriguez, "Coherent control of terahertz supercontinuum generation in ultrafast lasergas interactions," Nat. Phot. **2**, 605 (2008).

[65] M. D. Thomson, V. Blank, and H. G. Roskos, "Terahertz white-light pulses from an air plasma photo-induced by incommensurate two-color optical fields," Opt. Express **18**, 23173 (2010).

[66] P. B. Petersen and A. Tokmakoff, "Source for ultrafast continuum infrared and terahertz radiation," Opt. Lett. **35**, 1962 (2010).

[67] M. C. Beard, G. M. Turner, and C. A. Schmuttenmaer, "Subpicosecond carrier dynamics in low-temperature grown GaAs as measured by time-resolved terahertz spectroscopy," J. Appl. Phys. **90**, 5915 (2001).

[68] M. Born and E. Wolf, *Principles of Optics: Electromagnetic Theory of Propagation, Interference and Diffraction of Light* (Cambridge University Press (7th Ed.), 1999).

[69] J. Hwang, J. Yang, T. Timusk, J. P. Carbotte, D. A. Bonn, R. Liang, and W. N. Hardy, "a-axis optical conductivity of detwinned ortho-II $YBa_2Cu_3O_{6.50}$," Phys. Rev. B **73**, 014508 (2006).

[70] D. Bonn, J. Greedan, C. Stager, T. Timusk, *et al.*, "Far-infrared measurement of the gap of the high-T_c superconductor $La_{1.85}Sr_{0.15}CuO_{4-x}$," Phys. Rev. B **35**, 8843(R) (1987).

[71] P. Anderson, "Interlayer tunneling mechanism for high-T_c superconductivity: comparison with c axis infrared experiments," Science **268**, 1154 (1995).

[72] J. Fink, N. Nücker, E. Pellegrin, H. R. M. Alexander, and M. Knupfer, "Electron energy-loss and X-ray absorption spectroscopy of cuprate superconductors and related compounds," J. El. Spect. Rel. Phenom. **66**, 395 (1994).

[73] N. Gauquelin, D. G. Hawthorn, G. A. Sawatzky, R. X. Liang, D. A. Bonn, W. N. Hardy, and G. A. Botton, "Atomic scale real-space mapping of holes in $YBa_2Cu_3O_{6+\delta}$," Nat. Comm. **5**, 4275 (2014).

[74] W. E. Lawrence and S. Doniach, in *Proc. 12th International Conference on Low Temperature Physics, Kyoto (1970)*, edited by E. Kanda (Keigaku, Tokyo, 1971).

[75] S. Doniach and M. Inui, "Long-range Coulomb interactions and the onset of superconductivity in the high-T_c materials," Phys. Rev. B **41**, 6668 (1990).

[76] M. Tachiki, T. Koyama, and S. Takahashi, "Electromagnetic phenomena related to a low-frequency plasma in cuprate superconductors," Phys. Rev. B **50**, 7065 (1994).

[77] D. van der Marel and A. Tsvetkov, "Transverse-optical Josephson plasmons: Equations of motion," Phys. Rev. B. **64**, 024530 (2001).

[78] L. N. Bulaevskii, M. Zamora, D. Baeriswyl, H. Beck, and J. R. Clem, "Time-dependent equations for the phase differences and a collective mode in Josephson-coupled layered superconductors," Phys. Rev. B **50**, 12831 (1994).

[79] D. van der Marel, H. J. A. Molegraaf, J. Zaanen, Z. Nussinov, *et al.*, "Quantum critical behaviour in a high-T_c superconductor," Nature **425**, 271 (2003).

[80] L. S. Bilbro, R. V. Aguilar, G. Logvenov, O. Pelleg, I. Božović, and N. P. Armitage, "Temporal correlations of superconductivity above the transition temperature in $La_{2-x}Sr_xCuO_4$ probed by terahertz spectroscopy," Nat. Phys. **7**, 298 (2011).

[81] J. Corson, R. Mallozzi, J. Orenstein, J. N. Eckstein, and I. Božović, "Vanishing of phase coherence in underdoped $Bi_2Sr_2CaCu_2O_{8+\delta}$," Nature **398**, 221 (1999).

[82] D. van der Marel and A. Tsvetkov, "Transverse optical plasmons in layered superconductors," Czech. J. Phys. **46**, 3165 (1996).

[83] K. M. Kojima, S. Uchida, Y. Fudamoto, and S. Tajima, "New Josephson plasma modes in underdoped $YBa_2Cu_3O_{6.6}$ induced by a parallel magnetic field," Phys. Rev. Lett. **89**, 247001 (2002).

[84] C. C. Homes, T. Timusk, D. A. Bonn, R. Liang, and W. N. Hardy, "Optical properties along the c-axis of $YBa_2Cu_3O_{6+x}$, for x=0.5 $\rightarrow$ 0.95: evolution of the pseudogap," Physica C **254**, 265 (1995).

[85] A. Dubroka, M. Rössle, K. W. Kim, V. K. Malik, *et al.*, "Evidence of a precursor superconducting phase at temperatures as high as 180 K in $RBa_2Cu_3O_{7-\delta}$ (R=Y,Gd,Eu) superconducting crystals from infrared spectroscopy," Phys. Rev. B **76**, 054525 (2007).

[86] D. E. Moncton, J. D. Axe, and F. J. DiSalvo, "Study of Superlattice Formation in 2H-$NbSe_2$ and 2H-$TaSe_2$ by Neutron Scattering," Phys. Rev. Lett. **34**, 734 (1975).

[87] R. Coleman, B. Giambattista, P. Hansma, A. Johnson, W. McNairy, and C. Slough, "Scanning tunnelling microscopy of charge-density waves in transition metal chalcogenides," Adv. in Phys. **37**, 559 (1988).

[88] J. M. Tranquada, B. J. Sternlieb, J. D. Axe, Y. Nakamura, and S. Uchida, "Evidence for stripe correlations of spins and holes in copper oxide superconductors," Nature **375**, 561 (1995).

[89] A. Girlando, M. Masino, J. A. Schlueter, N. Drichko, S. Kaiser, and M. Dressel, "Charge-order fluctuations and superconductivity in two-dimensional organic metals," Phys. Rev. B **89**, 174503 (2014).

[90] K. Kudo, Y. Nishikubo, and M. Nohara, "Coexistence of Superconductivity and Charge Density Wave in $SrPt_2As_2$," J. Phys. Soc. Jpn. **79**, 123710 (2010).

[91] G. Ghiringelli, M. L. Tacon, M. Minola, S. Blanco-Canosa, *et al.*, "Long-range incommensurate charge fluctuations in (Y,Nd)$Ba_2Cu_3O_{6+x}$," Science **337**, 821 (2012).

[92] E. H. da Silva Neto, P. Aynajian, A. Frano, R. Comin, *et al.*, "Ubiquitous Interplay Between Charge Ordering and High-Temperature Superconductivity in Cuprates," Science **343**, 393 (2014).

[93] R. Comin, A. Frano, M. M. Yee, Y. Yoshida, *et al.*, "Charge Order Driven by Fermi-Arc Instability in $Bi_2Sr_{2-x}La_xCu_2O_{6+\delta}$," Science **343**, 390 (2014).

[94] W. Tabis, Y. Li, M. L. Tacon, L. Braicovich, *et al.*, "Charge order and its connection with Fermi-liquid charge transport in a pristine high-T_c cuprate," Nature Comm. **5**, 5875 (2014).

[95] T. Suzuki and T. Fujita, "Structural phase transition in $(La_{1x}Ba_x)_2CuO_{4\delta}$," Physica C **159**, 111 (1989).

[96] M. K. Crawford, R. L. Harlow, E. M. McCarron, W. E. Farneth, J. D. Axe, H. Chou, and Q. Huang, "Lattice instabilities and the effect of copper-oxygen-sheet distortions on superconductivity in doped La_2CuO_4," Phys. Rev. B **44**, 7749 (1991).

[97] V. J. Emery, S. A. Kivelson, and J. M. Tranquada, "Stripe phases in high-temperature superconductors," Proc. Nat. Acad. Sci. **96**, 8814 (1999).

[98] M. Fujita, H. Goka, K. Yamada, and M. Matsuda, "Competition between charge- and spin-density-wave order and superconductivity in $La_{1.875}Ba_{0.125-x}Sr_xCuO_4$," Phys. Rev. Lett. **88**, 167008 (2002).

[99] P. Abbamonte, A. Rusydi, S. Smadici, G. D. Gu, G. A. Sawatzky, and D. L. Feng, "Spatially modulated "Mottness" in $La_{2-x}Ba_xCuO_4$," Nat. Phys. **1**, 155 (2005).

[100] H. H. Klauss, W. Wagener, M. Hillberg, W. Kopmann, *et al.*, "From antiferromagnetic arder to static magnetic stripes: The phase diagram of $(La,Eu)_{2-x}Sr_xCuO_4$," Phys. Rev. Lett. **85**, 4590 (2000).

[101] A. R. Moodenbaugh, Y. Xu, M. Suenaga, T. J. Folkerts, and R. N. Shelton, "Superconducting properties of $La_{2-x}Ba_xCuO_4$," Phys. Rev. B **38**, 4596 (1988).

[102] M. Hücker, M. von Zimmermann, G. D. Gu, Z. J. Xu, *et al.*, "Stripe order in superconducting $La_{2-x}Ba_xCuO_4$ ($0.095 \leq x \leq 0.155$)," Phys. Rev. B **83**, 104506 (2011).

[103] S.-C. Zhang, "Recent developments in the SO(5) theory of high T_c superconductivity," J. Phys. Chem. Solids **59**, 1774 (1998).

[104] A. Himeda, T. Kato, and M. Ogata, "Stripe states with spatially oscillating d-wave superconductivity in the two-dimensional t-t'-J model," Phys. Rev. Lett. **88**, 117001 (2002).

[105] E. Berg, E. Fradkin, E.-A. Kim, S. A. Kivelson, V. Oganesyan, J. M. Tranquada, and S. C. Zhang, "Dynamical layer decoupling in a stripe-ordered high-T_c superconductor," Phys. Rev. Lett. **99**, 127003 (2007).

[106] Q. Li, M. Hücker, G. D. Gu, A. M. Tsvelik, and J. M. Tranquada, "Two-dimensional superconducting fluctuations in stripe-ordered $La_{1.875}Ba_{0.125}CuO_4$," Phys. Rev. Lett. **99**, 067001 (2007).

[107] T. Valla, A. V. Fedorov, J. Lee, J. C. Davis, and G. D. Gu, "The Ground State of the Pseudogap in Cuprate Superconductors," Science **314**, 1914 (2006).

[108] J. Fink, V. Soltwisch, J. Geck, E. Schierle, E. Weschke, and B. Büchner, "Phase diagram of charge order in $La_{1.8x}Eu_{0.2}Sr_xCuO_4$ from resonant soft x-ray diffraction," Phys. Rev. B **83**, 092503 (2011).

[109] J. M. Tranquada, G. D. Gu, M. Hücker, Q. Jie, *et al.*, "Evidence for unusual superconducting correlations coexisting with stripe order in $La_{1.875}Sr_{0.125}CuO_4$," Phys. Rev. B **78**, 174529 (2008).

[110] H.-J. Grafe, N. J. Curro, B. L. Young, A. Vyalikh, *et al.*, "Charge order and low frequency spin dynamics in lanthanum cuprates revealed by nuclear magnetic resonance," Eur. Phys. J. Spec. Top. **188**, 89 (2010).

[111] W. J. Padilla, M. Dumm, S. Komiya, Y. Ando, and D. N. Basov, "Infrared signatures of hole and spin stripes in $La_{2x}Sr_xCuO_4$," Phys. Rev. B **72**, 205101 (2005).

[112] K. K. Gomes, A. N. Pasupathy, A. Pushp, S. Ono, Y. Ando, and A. Yazdani, "Visualizing pair formation on the atomic scale in the high-Tc superconductor $Bi_2Sr_2CaCu_2O_{8+\delta}$," Nature **447**, 569 (2007).

[113] C. C. Homes, M. Hücker, Q. Li, Z. J. Xu, J. S. Wen, G. D. Gu, and J. M. Tranquada, "Determination of the optical properties of $La_{2x}Ba_xCuO_4$ for several dopings, including the anomalous $x = 1/8$ phase," Phys. Rev. B **85**, 134510 (2012).

[114] S. Petit, A. H. Moudden, B. Hennion, A. Vietkin, and A. Revcolevischi, "Spin dynamics study of $La_{2x}Sr_xCuO_4$ by inelastic neutron scattering," Physica B **234-236**, 800 (1997).

[115] C. H. Lee and K. Yamada, "Spin pseudogap in $La_{2x}Sr_xCuO_4$ studied by neutron scattering," Phys. Rev. B **67**, 134521 (2003).

[116] M. Kofu, S.-H. Lee, M. Fujita, H.-J. Kang, H. Eisaki, and K. Yamada, "Hidden quantum spin-gap state in the static stripe phase of high-temperature $La_{2x}Sr_xCuO_4$ superconductors," Phys. Rev. Lett. **102**, 047001 (2009).

[117] J. Wen, Z. Xu, G. Xu, J. M. Tranquada, G. Gu, S. Chang, and H. J. Kang, "Magnetic field induced enhancement of spin-order peak intensity in $La_{1.875}Ba_{0.125}CuO_4$," Phys. Rev. B **78**, 212506 (2008).

[118] H. Němec, L. Fekete, F. Kadlec, P. Kužel, *et al.*, "Ultrafast carrier dynamics in Br^+-bombarded InP studied by time-resolved terahertz spectroscopy," Phys. Rev. B **78**, 235206 (2008).

[119] J. C. Delagnes, P. Mounaix, H. Němec, L. Fekete, *et al.*, "High photocarrier mobility in ultrafast ion-irradiated $In_{0.53}Ga_{0.47}As$ for terahertz applications," J. Phys. D: Appl. Phys. **42**, 195103 (2009).

[120] J. Zielbauer and M. Wegener, "Ultrafast optical pump THz-probe spectroscopy on silicon," Appl. Phys. Lett. **68**, 1223 (1996).

[121] M. C. Beard, G. M. Turner, and C. A. Schmuttenmaer, "Transient photoconductivity in GaAs as measured by time-resolved terahertz spectroscopy," Phys. Rev. B **62**, 15764 (2000).

[122] A. Zettl, C. M. Jackson, and G. Grüner, "Sliding Density Wave in $Sr_{14}Cu_24O_{41}$ Ladder Compounds," Phys. Rev. B **26**, 10 (1982).

[123] G. Blumberg, P. Littlewood, A. Gozar, B. S. Dennis, N. Motoyama, H. Eisaki, and S. Uchida, "Sliding Density Wave in $Sr_{14}Cu_24O_{41}$ Ladder Compounds," Science **297**, 584 (2002).

[124] S. Cox, J. Singleton, R. D. McDonald, A. Migliori, and P. B. Littlewood, "Sliding charge-density wave in manganites," Nat. Mat. **7**, 25 (2007).

[125] E. Berg, E. Fradkin, S. A. Kivelson, and J. M. Tranquada, "Striped superconductors: How spin, charge and superconducting orders intertwine in the cuprates," New J. Phys. **11**, 115004 (2009).

[126] E. Fradkin, S. A. Kivelson, and J. M. Tranquada, "Theory of intertwined orders in high temperature superconductors," arXiv:1407.4480 .

[127] L. E. Hayward, D. G. Hawthorn, R. G. Melko, and S. Sachdev, "Angular fluctuations of a multicomponent order describe the pseudogap of $YBa_2Cu_3O_{6+x}$," Science **343**, 1336 (2014).

[128] P. A. Lee, "Amperean pairing and the pseudogap phase of cuprate superconductors," Phys. Rev. X **4**, 031017 (2014).

[129] T. Timusk and B. Statt, "The pseudogap in high-temperature superconductors: an experimental survey," Rep. Prog. Phys. **62**, 1 (1999).

[130] P. Phillips, "Mottness," Annals Phys. **321**, 1634 (2006).

[131] R. G. Leigh, P. Phillips, and T.-P. Choy, "Hidden charge $2e$ boson in doped Mott insulators," Phys. Rev. Lett. **99**, 046404 (2007).

[132] T. D. Stanescu and P. Phillips, "Pseudogap in doped Mott insulators is the near-neighbor analogue of the Mott gap," Phys. Rev. Lett. **91**, 017002 (2003).

[133] Y. Kohsaka, C. Taylor, P. Wahl, A. Schmidt, *et al.*, "How Cooper pairs vanish approaching the Mott insulator in $Bi_2Sr_2CaCu_2O_{8+\delta}$," Nature **454**, 1072 (2008).

[134] P. W. Anderson, "The resonating valence bond state in La_2CuO_4 and superconductivity," Science **235**, 1196 (1987).

[135] P. W. Anderson, "Physics of the pseudogap phase of high T_c cuprates, or, RVB meets umklapp," Journ. Phys. Chem. Solids **63**, 2145 (2002).

[136] Z. C. Gu, T. Li, and Z. Y. Weng, "Pseudogap phase: Exchange energy driven versus kinetic energy driven," Phys. Rev. B **71**, 064502 (2005).

[137] C. M. Varma, "Non-Fermi-liquid states and pairing instability of a general model of copper oxide metals," Phys. Rev. B **55**, 14554 (1997).

[138] C. M. Varma, "Pseudogap phase and the quantum-critical point in copper-oxide metals," Phys. Rev. Lett. **83**, 3538 (1999).

[139] S. Chakravarty, R. B. Laughlin, D. K. Morr, and C. Nayak, "Hidden order in the cuprates," Phys. Rev. B **63**, 094503 (2001).

[140] R. Daou, J. Chang, D. LeBoeuf, O. Cyr-Choinière, *et al.*, "Broken rotational symmetry in the pseudogap phase of a high-T_c superconductor," Nature **463**, 519 (2010).

[141] S. A. Kivelson, E. Fradkin, and V. J. Emery, "Electronic liquid-crystal phases of a doped Mott insulator," Nature **393**, 550 (1998).

[142] J. Tahir-Kheli and W. A. G. III, "Origin of the pseudogap in high-temperature cuprate superconductors," J. Phys. Chem. Lett. **2**, 2326 (2011).

[143] A. Kaminski, S. Rosenkranz, H. M. Fretwell, J. C. Campuzano, *et al.*, "Spontaneous breaking of time-reversal symmetry in the pseudogap state of a high-T_c superconductor," Nature **416**, 610 (2002).

[144] J. Xia, E. Schemm, G. Deutscher, S. A. Kivelson, *et al.*, "Polar Kerr-effect measurements of the high-temperature $YBa_2Cu_3O_{6+x}$ superconductor: Evidence for broken symmetry near the pseudogap temperature," Phys. Rev. Lett. **100**, 127002 (2008).

[145] V. Hinkov, P. Bourges, S. Pailhès, Y. Sidis, *et al.*, "Spin dynamics in the pseudogap state of a high-temperature superconductor," Nat. Phys. **3**, 780 (2007).

[146] C. Stock, W. J. L. Buyers, R. Liang, D. Peets, *et al.*, "Dynamic stripes and resonance in the superconducting and normal phases of $YBa_2Cu_3O_{6.5}$ ortho-II superconductor," Phys. Rev. B **69**, 014502 (2004).

[147] Y. Wang, L. Li, and N. P. Ong, "Nernst effect in high-T_c superconductors," Phys. Rev. B **73**, 024510 (2006).

[148] L. Li, Y. Wang, S. Komiya, S. Ono, Y. Ando, G. D. Gu, and N. P. Ong, "Diamagnetism and Cooper pairing above T_c in cuprates," Phys. Rev. B **81**, 054510 (2010).

[149] L. E. Hayward, D. G. Hawthorn, R. G. Melko, and S. Sachdev, "Angular Fluctuations of a Multicomponent Order Describe the Pseudogap of $YBa_2Cu_3O_{6+x}$," Science **343**, 1336 (2014).

[150] V. J. Emery and S. A. Kivelson, "Importance of phase fluctuations in superconductors with small superfluid density," Nature **374**, 434 (1994).

[151] T. Valla, A. V. Fedorov, J. Lee, J. C. Davis, and G. D. Gu, "The ground state of the pseudogap in cuprate superconductors," Science **314**, 1914 (2006).

[152] Y. He, Y. Yin, M. Zech, A. Soumyanarayanan, *et al.*, "Fermi surface and pseudogap evolution in a cuprate superconductor," Science **344**, 608 (2014).

[153] E. Pavarini, I. Dasgupta, T. Saha-Dasgupta, O. Jepsen, and O. K. Andersen, "Band-structure trend in hole-doped cuprates and correlation with $T_{c,max}$," Phys. Rev. Lett. **87**, 047003 (2001).

[154] C. Weber, K. Haule, and G. Kotliar, "Apical oxygens and correlation strength in electron- and hole-doped copper oxides," Phys. Rev. B **82**, 125107 (2010).

[155] F. E. Bates, "Normal modes of tetragonal $YBa_2Cu_3O_6$ and orthorhombic $YBa_2Cu_3O_7$," Phys. Rev. B **39**, 322 (1989).

[156] S. Schlachter, U.Tutsch, W.H.Fietz, K.-P.Weiss, *et al.*, "Pressure effect and specific heat of $RBa_2Cu_3O_x$ at distinct charge carrier concenterations: possible influence of stripes," Int. J. Mod. Phys. B **14**, 3673 (2000).

[157] S. Kaiser, C. R. Hunt, D. Nicoletti, W. Hu, *et al.*, "Supplementary: Optically induced coherent transport far above T_c in underdoped $YBa_2Cu_3O_{6+\delta}$," Phys. Rev. B **89**, 184516 (2014).

[158] A. O. Caldeira and A. J. Leggett, "Quantum tunnelling in a dissipative system," Annals of Physics **149**, 374 (1983).

[159] S. V. Dordevic, E. J. Singley, D. N. Basov, S. Komiya, *et al.*, "Global trends in the interplane penetration depth of layered superconductors," Phys. Rev. B **65**, 134511 (2002).

[160] D. Haug, V. Hinkov, Y. Sidis, P. Bourges, *et al.*, "Neutron scattering study of the magnetic phase diagram of underdoped $YBa_2Cu_3O_{6+x}$," New. J. Phys. **12**, 105006 (2010).

[161] V. Hinkov, D. Haug, B. Fauqué, P. Bourges, *et al.*, "Electronic liquid crystal state in the high-temperature superconductor $YBa_2Cu_3O_{6.45}$," Science **319**, 597 (2008).

[162] T. C. Choy, *Effective Medium Thoery: Principles and Applications* (Oxford University Press, 1999).

[163] A. Sihvola, *Electromagnetic Mixing Formulae and Applications* (The Institution of Engineering and Technology, 1999) Chap. 4.

[164] P. W. Anderson and A. H. Dayem, "Radio-frequency effects in superconducting thin film bridges," Phys. Rev. Lett. **13**, 195 (1964).

[165] A. F. G. Wyatt, V. M. Dmitriev, W. S. Moore, and F. W. Sheard, "Microwave-Enhanced Critical Supercurrents in Constricted Tin Films," Phys. Rev. Lett. **16**, 1166 (1966).

[166] S. I. Vedeneev, D. K. Maude, and J. M. Byrne, "Microwave enhancement of superconductivity in $Bi_2Sr_2CaCu_2O_{8+\delta}$ break junctions," Phys. Rev. B **78**, 052509 (2008).

[167] R. Höppner, B. Zhu, T. Rexin, A. Cavalleri, and L. Mathey, "Redistribution of phase fluctuations in a periodically driven cuprate superconductor," Phys. Rev. B **91**, 104507 (2015).

[168] M. Calamiotou, A. Gantis, E. Siranidi, D. Lampakis, J. Karpinski, and E. Liarokapis, "Pressure-induced lattice instabilities and superconductivity in $YBa_2Cu_4O_8$ and optimally doped $YBa_2Cu_3O_{7-\delta}$," Phys. Rev. B **80**, 214517 (2009).

[169] P. Seidel, ed., *Applied Superconductivity: Handbook on Devices and Applications (Vol. 2)* (Wiley and Sons, 2015) Chap. 3.

[170] P. Dai, H. A. Mook, R. D. Hunt, and F. Doğan, "Evolution of the resonance and incommensurate spin fluctuations in superconducting $YBa_2Cu_3O_{6+x}$," Phys. Rev. B **63**, 054525 (2001).

[171] J. Chang, E. Blackburn, A. T. Holmes, N. B. Christensen, *et al.*, "Direct observation of competition between superconductivity and charge density wave order in $YBa_2Cu_3O_{6.67}$," Nat. Phys. **8**, 871 (2012).

[172] S. Blanco-Canosa, A. Frano, T. Loew, Y. Lu, *et al.*, "Momentum-dependent charge correlations in $YBa_2Cu_3O_{6+\delta}$ superconductors probed by resonant x-ray scattering: Evidence for three competing phases," Phys Rev. Lett. **110**, 187001 (2013).

[173] E. Fradkin and S. A. Kivelson, "High-temperature superconductivity: Ineluctable complexity," Nat. Phys. **8**, 864 (2012).

[174] R. J. D. Miller, "The first movie documentary: Nanook of the North," (2014).

[175] P. M. C. Rourke, I. Mouzopoulou, X. Xu, C. Panagopoulos, *et al.*, "Phase-fluctuating superconductivity in overdoped $La_{2-x}Sr_xCuO_4$," Nat. Phys. **7**, 455 (2011).

[176] A. Pimenov, A. Loidl, D. Dulić, D. van der Marel, I. M. Sutjahja, and A. A. Menovsky, "Magnetic field dependence of the transverse plasmon in $SmLa_{0.8}Sr_{0.2}CuO_{4-\delta}$," Phys. Rev. Lett. **87**, 177003 (2001).

[177] A. D. LaForge, W. J. Padilla, K. S. Burch, Z. Q. Li, *et al.*, "Interlayer electrodynamics and unconventional vortex state in $YBa_2Cu_3O_y$," Phys. Rev. B **76**, 054524 (2007).

[178] A. E. Koshelev, "Electrodynamics of the Josephson vortex lattice in high-temperature superconductors," Phys. Rev. B **76**, 054525 (2007).

[179] I. I. Mazin, D. J. Singh, M. D. Johannes, and M. H. Du, "Unconventional superconductivity with a sign reversal in the order parameter of $LaFeAsO_{1x}F_x$," Phys. Rev. Lett. **101**, 057003 (2008).

[180] C. de la Cruz, Q. Huang, J. W. Lynn, J. Li, *et al.*, "Magnetic order close to superconductivity in the iron-based layered $LaO_{1x}F_xFeAs$ systems," Nature **453**, 899 (2008).

[181] D. J. Singh and M.-H. Du, "Density functional study of $LaFeAsO_{1x}F_x$: A low carrier density superconductor near itinerant magnetism," Phys. Rev. Lett. **100**, 237003 (2008).

[182] D. C. Johnson, "The puzzle of high temperature superconductivity in layered iron pnictides and chalcogenides," Adv. in Phys. **59**, 803 (2010).

[183] C.-T. Chen, C. C. Tsuei, M. B. Ketchen, Z.-A. Ren, and Z. X. Zhao, "Integer and half-integer flux-quantum transitions in a niobiumiron pnictide loop," Nat. Phys. **6**, 260 (2010).

[184] T. Hanaguri, S. Niitaka, K. Kuroki, and H. Takagi, "Unconventional s-Wave Superconductivity in Fe(Se,Te)," Science **328**, 474 (2010).

[185] P. Szabò, Z. Pribulovà, G. Pristàš, S. L. Budko, P. C. Canfield, and P. Samuely, "Point contact Andreev reflection spectroscopy of superconducting energy gaps in 122-type family of iron pnictides," Phys. Rev. B **79**, 012503 (2009).

[186] D. Daghero, M. Tortello, R. S. Gonnelli, V. A. Stepanov, N. D. Zhigadlo, and J. Karpinski, "Evidence for two-gap nodeless superconductivity in $SmFeAsO_{1x}F_x$ from point-contact Andreev-reflection spectroscopy," Phys. Rev. B **80**, 060502(R) (2009).

[187] P. Samuely, Z. Pribulovà, P. Szabò, G. Pristàš, S. Bud'ko, and P. Canfield, "Point contact Andreev reflection spectroscopy of superconducting energy gaps in 122-type family of iron pnictides," Physica C **469**, 507 (2009).

[188] R. S. Gonnelli, D. Daghero, M. Tortello, G. A. Ummarino, V. A. Stepanov, J. S. Kim, and R. K. Kremer, "Coexistence of two order parameters and a pseudogaplike feature in the iron-based superconductor $LaFeAsO_{1x}F_x$," Phys. Rev. B **79**, 184526 (2009).

[189] X. Lu, W. K. Park, H. Q. Yuan, G. F. Chen, *et al.*, "Point contact Andreev reflection spectroscopy of superconducting energy gaps in 122-type family of iron pnictides," Supercond. Sci. Technol. **23**, 054009 (2010).

[190] M. Fogelström, W. K. Park, L. H. Greene, G. Goll, and M. J. Graf, "Point-contact spectroscopy in heavy-fermion superconductors," Phys. Rev. B **82**, 014527 (2010).

[191] D. Daghero and R. S. Gonnelli, "Probing multiband superconductivity by point-contact spectroscopy," Supercond. Sci. Technol. **23**, 043001 (2010).

[192] I. K. Yanson and Y. G. Naidyuk, in *Spectroscopy of Emerging Materials*, edited by E. C. Faulques, D. L. Perry, and A. V. Yeremenko (Kluwer Academic Publisher, 2004).

[193] I. K. Yanson and Y. G. Naidyuk, "Advances in point-contact spectroscopy: two-band superconductor MgB_2 (Review)," Low Temp. Phys. **30**, 261 (2004).

[194] Y. G. Naidyuk, O. E. Kvitnitskaya, I. K. Yanson, G. Fuchs, *et al.*, "Point-contact investigations of challenging superconductors: two-band MgB_2, antiferromagnetic $HoNi_2B_2C$, heavy fermion UPd_2Al_3, paramagnetic $MgCNi_3$," Physica B **359-361**, 469 (2005).

[195] W. K. Park and L. H. Greene, "Construction of a Cantilever-Andreev-Tunneling rig and its applications to superconductors," Rev. Sci. Inst. **77**, 023905 (2006).

[196] Y. Kamihara, T. Watanabe, M. Hirano, and H. Hosono, "Iron-Based Layered Superconductor $La[O_{1-x}F_x]FeAs$ (x = 0.05-0.12) with T_c = 26 K," J. Am. Chem. Soc. **130**, 3296 (2008).

[197] L. Boeri, O. V. Dolgov, and A. A. Golubov, "Is $LaFeAsO_{1x}F_x$ an electron-phonon superconductor?" Phys. Rev. Lett. **101**, 026403 (2008).

[198] C. Lester, J.-H. Chu, J. G. Analytis, S. C. Capelli, *et al.*, "Anisotropic charge dynamics in detwinned $Ba(Fe_{1-x}Co_x)_2As_2$," Phys. Rev. B **79**, 144523 (2009).

[199] D. K. Pratt, W. Tian, A. Kreyssig, J. L. Zarestky, *et al.*, "Coexistence of competing antiferromagnetic and superconducting phases in the underdoped $Ba(Fe_{0.953}Co_{0.047})_2As_2$ compound using x-ray and neutron scattering techniques," Phys. Rev. Lett. **103**, 087001 (2009).

[200] T.-M. Chuang, M. P. Allan, J. Lee, Y. Xie, *et al.*, "Nematic electronic structure in the "parent" state of the iron-based superconductor $Ca(Fe_{1x}Co_x)_2As_2$," Science **327**, 5926 (2010).

[201] A. Dusza, A. Lucarelli, F. Pfuner, J.-H. Chu, I. R. Fisher, and L. Degiorgi, "Anisotropic charge dynamics in detwinned $Ba(Fe_{1-x}Co_x)_2As_2$," Euro. Phys. Lett. **93**, 37002 (2011).

[202] L. W. Harriger, H. Q. Luo, M. S. Liu, C. Frost, J. P. Hu, M. R. Norman, and P. Dai, "Nematic spin fluid in the tetragonal phase of $BaFe_2As_2$," Phys. Rev. B **84**, 054544 (2011).

[203] D. C. Johnston, "The puzzle of high temperature superconductivity in layered iron pnictides and chalcogenides," Adv. Phys. **59**, 803 (2010).

[204] D. S. Inosov, J. T. Park, P. Bourges, D. L. Sun, *et al.*, "Normal-state spin dynamics and temperature-dependent spin-resonance energy in optimally doped $BaFe_{1.85}Co_{0.15}As_2$," Nat. Phys. **6**, 178 (2010).

[205] Z. Wei, H. Li, W. Hong, Z. Lv, H. Wu, X. Guo, and K. Ruan, "Superconductivity at 57.3 K in La-doped iron-based layered compound $Sm_{0.95}La_{0.05}O_{0.85}F_{0.15}FeAs$," J. Sup. Nov. Mag. **21**, 213 (2008).

[206] J. Paglione and R. L. Greene, "High-temperature superconductivity in iron-based materials," Nat. Phys. **6**, 645 (2010).

[207] K. Kuroki, H. Usui, S. Onari, R. Arita, and H. Aoki, "Pnictogen height as a possible switch between high-T_c nodeless and low-T_c nodal pairings in the iron-based superconductors," Phys. Rev. B **79**, 224511 (2009).

[208] Y. Mizuguchi, Y. Hara, K. Deguchi, S. Tsuda, *et al.*, "Anion height dependence of T_c for the Fe-based superconductor," Supercond. Sci. Technol. **23**, 054013 (2010).

[209] K. Kuroki, S. Onari, R. Arita, H. Usui, Y. Tanaka, H. Kontani, and H. Aoki, "Unconventional pairing originating from the disconnected Fermi surfaces of superconducting $LaFeAsO_{1x}F_x$," Phys. Rev. Lett. **101**, 087004 (2008).

[210] F. Wang, H. Zhai, Y. Ran, A. Vishwanath, and D.-H. Lee, "Functional renormalization-group study of the pairing symmetry and pairing mechanism of the FeAs-based high-temperature superconductor," Phys. Rev. Lett. **102**, 047005 (2009).

[211] H.-H. Wen and S. Li, "Materials and novel superconductivity in iron pnictide superconductors," Ann. Rev. Cond. Mat. Phys. **2**, 121 (2011).

[212] P. Dai, J. Hu, and E. Dagotto, "Magnetism and its microscopic origin in iron-based high-temperature superconductors," Nat. Phys. **8**, 709 (2012).

[213] J. Wu, P. Phillips, and A. H. C. Neto, "Theory of the magnetic moment in iron pnictides," Phys. Rev. Lett. **101**, 126401 (2008).

[214] W.-C. Lee, W. Lv, J. M. Tranquada, and P. W. Phillips, "Impact of dynamic orbital correlations on magnetic excitations in the normal state of iron-based superconductors," Phys. Rev. B **86**, 094516 (2012).

[215] I. K. Yanson, "Nonlinear effects in the electric conductivity of point junctions and electron-phonon interaction in normal metals," J. Exp. Theor. Phys. **39**, 506 (1974).

[216] Y. G. Naidyuk and I. K. Yanson, *Point Contact Spectroscopy* (New York: Springer, 2005).

[217] A. V. Khotkevich and I. K. Yanson, *Atlas of Point Contact Spectra of Electron-Phonon Interactions In Metals* (Kuwer Academic, 1995).

[218] Y. Tanaka and S. Kashiwaya, "Theory of Tunneling Spectroscopy of d-Wave Superconductors," Phys. Rev. Lett. **74**, 3451 (1995).

[219] W.-C. Lee and P. W. Phillips, "Non-Fermi liquid due to orbital fluctuations in iron pnictide superconductors," Phys. Rev. B **86**, 245113 (2012).

[220] W.-C. Lee, W. Lv, and H. Z. Arham, "Elementary excitations due to orbital degrees of freedom in iron-based superconductors," Int. J. Mod. Phys. B **27**, 1330014 (2013).

[221] W.-C. Lee, W. K. Park, H. Z. Arham, L. H. Greene, and P. Phillips, "Theory of point contact spectroscopy in correlated materials," Proc. Nat. Acad. Sci. **112**, 651 (2014).

[222] M. Maltseva, M. Dzero, and P. Coleman, "Electron cotunneling into a Kondo lattice," Phys. Rev. Lett. **103**, 206402 (2009).

[223] W. K. Park, P. H. Tobash, F. Ronning, E. D. Bauer, J. L. Sarrao, J. D. Thompson, and L. H. Greene, "Observation of the hybridization gap and Fano resonance in the Kondo lattice URu_2Si_2," Phys. Rev. Lett. **108**, 246403 (2012).

[224] L. H. Greene, H. Z. Arham, C. R. Hunt, and W. K. Park, "Design of new superconducting materials, and point-contact spectroscopy as a probe of strong electron correlations," J. Supercond. Novel Mag. **25**, 2121 (2012).

[225] H. Z. Arham, C. R. Hunt, W. K. Park, J. Gillett, *et al.*, "Detection of orbital fluctuations above the structural transition temperature in the iron pnictides and chalcogenides," Phys. Rev. B **85**, 214515 (2012).

[226] W. K. Park, S. M. Narasiwodeyar, E. D. Bauer, P. H. Tobash, *et al.*, "Hidden order and hybridization gap in URu_2Si_2 via quasiparticle scattering spectroscopy," Phyl. Mag. **94**, 3737 (2014).

[227] W. K. Park, S. M. Narasiwodeyar, M. Dwyer, P. C. Canfield, and L. H. Greene, "Hybridization and slow coherence crossover in the intermediate valence compound $YbAl_3$ via quasiparticle scattering spectroscopy," (2015), arXiv:1411.7073 .

[228] G. Wexler, "The size effect and the non-local Boltzmann transport equation in orifice and disk geometry," Proc. Phys. Soc. **89**, 927 (1966).

[229] S. Narasiwodeyar, M. Dwyer, M. Liu, W. K. Park, and L. Greene, "Two-step fabrication technique of gold tips for use in point-contact spectroscopy," Rev. Sci. Inst. **86**, 033903 (2015).

[230] R. Holm and E. Holm, *Electrical Contacts: Theory and Application*, 4th ed. (Berlin:Springer-Verlag, 1967).

[231] A. F. Andreev, "Nonlinear effects in the electric conductivity of point junctions and electron-phonon interaction in normal metals," Sov. Phys. JETP **19**, 1228 (1964).

[232] W. A. Harrison, "Tunneling from an independent-particle point of view," Phys. Rev. **123**, 85 (1961).

[233] A. Pleceník, M. Grajcar, Š. Beňačka, P. Seidel, and A. Pfuch, "Finite-quasiparticle-lifetime effects in the differential conductance of $Bi_2Sr_2CaCu_2O_y$/Au junctions," Phys. Rev. B **49**, 10016 (1994).

[234] W. K. Park, J. L. Sarrao, J. D. Thompson, and L. H. Greene, "Andreev reflection in heavy-fermion superconductors and order parameter symmetry in $CeCoIn_5$," Phys. Rev. Lett. **100**, 177001 (2008).

[235] L. J. Buchholtz and G. Zwicknagl, "Identification of p-wave superconductors," Phys. Rev. B **23**, 5788 (1981).

[236] P. Seneor, C.-T. Chen, N.-C. Yeh, R. P. Vasquez, *et al.*, "Spectroscopic evidence for anisotropic s-wave pairing symmetry in MgB_2," Phys. Rev. B **65**, 012505 (2001).

[237] A. Y. Liu, I. I. Mazin, and J. Kortus, "Beyond eliashberg superconductivity in MgB_2: anharmonicity, two-phonon scattering, and multiple gaps," Phys. Rev. Lett. **87**, 087005 (2001).

[238] A. Brinkman, A. A. Golubov, H. Rogalla, O. V. Dolgov, *et al.*, "Multiband model for tunneling in MgB_2 junctions," Phys. Rev. B **65**, 80517(R) (2002).

[239] T. T. M. Palstra, A. A. Menovsky, J. van den Berg, A. J. Dirkmaat, P. H. Kes, G. J. Nieuwenhuys, and J. A. Mydosh, "Superconducting and magnetic transitions in the heavy-fermion system URu_2Si_2," Phys. Rev. Lett. **55**, 2727 (1985).

[240] T. T. M. Palstra, A. A. Menovsky, J. van den Berg, A. J. Dirkmaat, P. H. Kes, G. J. Nieuwenhuys, and J. A. Mydosh, "Colloquium: Hidden order, superconductivity, and magnetism: The unsolved case of URu_2Si_2," Rev. Mod. Phys. **83**, 1301 (2011).

[241] Y. Dubi and A. V. Balatsky, "Hybridization wave as "hidden order" in URu_2Si_2," Phys. Rev. Lett. **106**, 086401 (2011).

[242] C. R. Wiebe, J. A. Janik, G. J. MacDougall, G. M. Luke, *et al.*, "Magnetic excitations and ordering in the heavy-electron superconductor URu_2Si_2," Nat. Phys. **3**, 96 (2007).

[243] C. Broholm, J. K. Kjems, W. J. L. Buyers, P. Matthews, T. T. M. Palstra, A. A. Menovsky, and J. A. Mydosh, "Magnetic excitations and ordering in the heavy-electron superconductor URu_2Si_2," Phys. Rev. Lett. **58**, 1467 (1987).

[244] J. Figgins and D. K. Morr, "Differential conductance and quantum interference in Kondo systems," Phys. Rev. Lett. **104**, 187202 (2010).

[245] H. Z. Arham and L. H. Greene, "Point contact spectroscopy of Fe pnictides and chalcogenides in the normal state," Curr. Op. in Sol. State Mat. Sci. **2**, 88 (2013).

[246] M. Yia, D. Lu, J.-H. Chu, J. G. Analytis, *et al.*, "Symmetry-breaking orbital anisotropy observed for detwinned $Ba(Fe_{1-x}Co_x)_2As_2$ above the spin density wave transition," Proc. Nat. Acad. Sci. **108**, 6878 (2011).

[247] R. M. Fernandez, A. V. Chubukov, and J. Schmalian, "What drives nematic order in the iron-based superconductors," Nat. Phys. **10**, 97 (2014).

[248] H. Meekes, "Point-contact spectroscopy in incommensurate chromium," Phys. Rev. B **38**, 5924 (1988).

[249] R. Escudero and F. Morales, "Point contact spectroscopy of the Nb_3Sn crystals: Evidence of a CDW gap related to the martensitic transition," Sol. State Comm. **150**, 715 (2010).

[250] S. E. Sebastian, J. Gillett, N. Harrison, P. H. C. Lau, D. J. Singh, C. H. Mielke, and G. G. Lonzarich, "Quantum oscillations in the parent magnetic phase of an iron arsenide high temperature superconductor," J. Phys: Condens. Matt. **20**, 422203 (2008).

[251] W. Malaeb, T. Yoshida, A. Fujimori, M. Kubota, *et al.*, "Three-dimensional electronic structure of superconducting iron pnictides observed by angle-resolved photoemission spectroscopy," J. Phys. Soc. Jpn **78**, 123706 (2009).

[252] M. Tinkham, *Introduction to Superconductivity*, 2nd ed. (New York: Dover, 2004).

[253] J. R. Kirtley, "Inelastic transport through normal-metal—superconductor interfaces," Phys. Rev. B **47**, 11379 (1993).

[254] M. Tortello, D. Daghero, G. A. Ummarino, V. A. Stepanovand, *et al.*, "Multigap superconductivity and strong electron-boson coupling in Fe-based superconductors: A point-contact Andreev-reflection study of $Ba(Fe_{1x}Co_x)_2As_2$ single crystals," Phys. Rev. Lett. **105**, 237002 (2010).

[255] P. Popovich, A. V. Boris, O. V. Dolgov, A. A. Golubov, *et al.*, "Specific heat measurements of $Ba_{0.68}K_{0.32}Fe_2As_2$ single crystals: Evidence for a multiband strong-coupling superconducting state," Phys. Rev. Lett. **105**, 027003 (2010).

[256] S. Chi, S. Grothe, R. Liang, P. Dosanjh, *et al.*, "Scanning tunneling spectroscopy of superconducting LiFeAs single crystals: Evidence for two nodeless energy gaps and coupling to a bosonic mode," Phys. Rev. Lett. **109**, 087002 (2012).

[257] A. M. Zhang and Q. M. Zhang, "Raman scattering in iron-based superconductors," Mod. Phys. Lett. B **26**, 1230020 (2012).

[258] M. Zbiri, R. Mittal, S. Rols, Y. Su, *et al.*, "Magnetic lattice dynamics of the oxygen-free FeAs pnictides: how sensitive are phonons to magnetic ordering?" J. Phys. Condens. Matter **22**, 315701 (2010).

[259] L. Chauvière, Y. Gallais, M. Cazayous, M. A. Méasson, A. Sacuto, D. Colson, and A. Forget, "Raman scattering study of spin-density-wave order and electron-phonon coupling in $Ba(Fe_{1x}Co_x)_2As_2$," Phys. Rev. B **84**, 104508 (2011).

[260] G. Deutscher, N. Hass, Y. Yagil, A. Revcolevschi, and G. Dhalenne, "Evidence for strong electron-phonon interaction in point contact spectroscopy of superconducting oriented $La_{1-x}Sr_xCuO_4$," J. Supercond. **7**, 371 (1994).

[261] C. J. van der Beek, M. Konczykowski, S. Kasahara, T. Terashima, R. Okazaki, T. Shibauchi, and Y. Matsuda, "Quasiparticle scattering induced by charge doping of iron-pnictide superconductors probed by collective vortex pinning," Phys. Rev. Lett. **105**, 267002 (2010).

[262] W. K. Park, C. R. Hunt, H. Z. Arham, Z. J. Xu, *et al.*, "Strong coupling superconductivity in iron-chalcogenide $FeTe_{0.55}Se_{0.45}$," (2010), arXiv:1005.0190 .

[263] N. N. Kovaleva, A. V. Boris, T. Holden, C. Ulrich, *et al.*, "*c*-axis lattice dynamics in Bi-based cuprate superconductors," Phys. Rev. B **69**, 054511 (2004).

[264] T. Motohashi, J. Shimoyama, K. Kitazawa, K. Kishio, K. M. Kojima, S. Uchida, and S. Tajima, "Observation of the Josephson plasma reflectivity edge in the infrared region in Bi-based superconducting cuprates," Phys. Rev. B **61**, R9269(R) (2000).

[265] A. Godard, "Infrared (212 μm) solid-state laser sources: a review," C. R. Physique **8**, 1100 (2007).

[266] S. Komiyama, "Far-infrared emission from population-inverted hot-carrier system in p-Ge," Phys. Rev. Lett. **48**, 271 (1982).

[267] E. Gornik, K. Unterrainer, and C. Kremser, "Tunable far-infrared solid-state lasers based on hot holes in germanium," Opt. Quant. Electr. **23**, S267 (1991).

[268] E. Bründermann, A. M. Linhart, H. P. Röser, O. D. Dubon, W. L. Hansen, and E. E. Haller, "Miniaturization of p-Ge lasers: Progress toward continuous wave operation," Appl. Phys. Lett. **68**, 1359 (1996).

[269] P. R. Bevington and D. K. Robinson, *Data Reduction and Error Analysis* (McGraw-Hill (3rd Ed.), 2003).

[270] R. A. Kaindl, M. Woerner, T. Elsaesser, D. C. Smith, *et al.*, "Ultrafast mid-infrared response of $YBa_2Cu_3O_{7-\delta}$," Science **287**, 470 (2000).

[271] Y. Liu, Y. Toda, K. Shimatake, N. Momono, M. Oda, and M. Ido, "Direct observation of the coexistence of the pseudogap and superconducting quasiparticles in $Bi_2Sr_2CaCu_2O_{8+y}$ by time-resolved optical spectroscopy," Phys. Rev. Lett. **101**, 137003 (2008).

[272] P. Kusar, V. V. Kabanov, J. Demsar, T. Mertelj, S. Sugai, and D. Mihailovic, "Controlled Vaporization of the Superconducting Condensate in Cuprate Superconductors by Femtosecond Photoexcitation," Phys. Rev. Lett. **101**, 227001 (2008).

[273] C. Giannetti, F. Cilento, S. D. Conte, G. Coslovich, *et al.*, "Revealing the high-energy electronic excitations underlying the onset of high-temperature superconductivity in cuprates," Nat. Comm. **2**, 353 (2010).

[274] M. Beyer, D. Städter, M. Beck, H. Schäfer, *et al.*, "Photoinduced melting of superconductivity in the high-T_c superconductor $La_{2+x}Sr_xCuO_4$ probed by time-resolved optical and terahertz techniques," Phys. Rev. B **83**, 214515 (2011).

[275] B. Mansart, J. Lorenzanac, A. Manna, A. Odehb, M. Scarongellab, M. Cherguib, and F. Carbone, "Coupling of a high-energy excitation to superconducting quasiparticles in a cuprate from coherent charge fluctuation spectroscopy," Proc. Natl. Acad. Sci. USA **110**, 4539 (2013).

[276] J. Demsar, K. Biljaković, and D. Mihailovic, "Single particle and collective excitations in the one-dimensional charge density wave solid $K_{0.3}MoO_3$ probed in real time by femtosecond spectroscopy," Phys. Rev. Lett. **83**, 800 (1999).

[277] L. Perfetti, P. A. Loukakos, M. Lisowski, U. Bovensiepen, *et al.*, "Time evolution of the electronic structure of $1T$TaS$_2$ through the insulator-metal transition," Phys. Rev. Lett. **97**, 067402 (2006).

[278] J. C. Petersen, S. Kaiser, N. Dean, A. Simoncig, *et al.*, "Clocking the melting transition of charge and lattice order in $1T$TaS$_2$ with ultrafast extreme-ultraviolet angle-resolved photoemission spectroscopy," Phys. Rev. Lett. **107**, 177402 (2011).

[279] L. Stojchevska, P. Kusar, T. Mertelj, V. V. Kabanov, Y. Toda, X. Yao, and D. Mihailovic, "Mechanisms of nonthermal destruction of the superconducting state and melting of the charge-density-wave state by femtosecond laser pulses," Phys. Rev. B. **84**, 180507(R) (2011).

[280] A. Rothwarf and B. Taylor, "Measurement of recombination lifetimes in superconductors," Phys. Rev. Lett. **19**, 27 (1967).

[281] V. V. Kabanov, J. Demsar, , and D. Mihailovic, "Kinetics of a superconductor excited with a femtosecond optical pulse," Phys. Rev. Lett. **95**, 147002 (2005).

[282] T. Timusk and C. C. Homes, "The role of magnetism in forming the c-axis spectral peak at 400 cm^{-1} in high temperature superconductors," Sol. State Comm. **126**, 63 (2003).

[283] A. R. G. Geoff Burton Smith and A. I. Maaroof, "Metal-insulator nanocomposites which act optically like homogeneous conductors," Journ. of Nanophot. **1**, 013507 (2007).